Experimental Investigation of the Combined Effects of Corrosion and Mean Stress on Fatigue Strength of Low Carbon Steel

PhD Thesis

Marta Morgantini

Weir Advanced Research Centre

Department of Mechanical and Aerospace Engineering

University of Strathclyde

Declaration of author's rights

This thesis is the result of the author's original research. It has been composed by the author and has not been previously submitted for examination which has led to the award of a degree.

The copyright of this thesis belongs to the author under the terms of the United Kingdom Copyright Acts as qualified by University of Strathclyde Regulation 3.50. Due acknowledgement must always be made of the use of any material contained in, or derived from, this thesis.

Marta Morgantini

May 2020

Abstract

This thesis presents an experimental investigation of the combined effects of corrosion and mean stress on the fatigue strength of a low carbon steel.

Corrosion fatigue is a large problem in many engineering fields, which also affects the mining and oil and gas industries, hence the interest from Weir Group. This phenomenon can significantly reduce the fatigue strength of materials by damaging surface structures and accelerating fatigue crack growth. Positive displacement GEHO diaphragm pumps are widely used in mining industries because of the advantage of separating the power end components from the pumped fluid. However, the Fluid End components are operated in harsh environments and are subjected to fatigue and mean stress effects. Understanding the fatigue behaviour of Fluid End components material exposed to freshwater environments and the effects of positive mean stress on the corrosion fatigue strength is of paramount importance to ensure a fatigue life of 10^9 cycles, equals to the design life of GEHO pumps.

The scope of this research work is to evaluate the effect of freshwater environments on the fatigue behaviour of low carbon steel S355J2, the material used to manufacture Fluid End components, and to develop a model to evaluate the effect of mean stresses on the corrosion fatigue strength at elevated fatigue cycles to be applied in the design of GEHO pumps.

This is achieved by developing and performing an experimental programme consisting of corrosion tests on unloaded specimens, uniaxial fatigue tests in air and in the freshwater corrosive environment at different stress ratio conditions. Stress-based experimental results show a decrease in fatigue strength due to the corrosive environment and a continuous decrease of the corrosion fatigue strength with increasing fatigue life. The mean stress effects on corrosion fatigue lives are evaluated by the construction of Haigh diagrams based on experimental results. The sensitivity of S355J2 to mean stress in the corrosive environment is higher at high stress ratios, compared to trends in air. A modified FKM approach is proposed, based on the definition of mean stress sensitivity factor parameters, to predict the allowable stress up to 10^9 fatigue cycles in the freshwater environment.

Industry scale specimens were designed to reproduce critical conditions of Fluid End components of GEHO pumps. Modifications of a test rig available in Weir Minerals Venlo was implemented and two industry scale tests were completed under cyclic pressure loading at different nominal load ratio conditions and results were in good agreement with the proposed predictive model.

Acknowledgements

I would like to express my sincere gratitude to my supervisor Prof. Donald MacKenzie. Your calm, confidence and unwavering support have been the best guidance I could ever require undertaking this research. Thank you for the encouragement you have offered during bright and dark phases. It has truly been an honour to have had the opportunity to benefit from your knowledge over the last four years.

A sincere thanks to my second supervisor, Dr. Yevgen Gorash, for sharing your invaluable expertise in the fatigue behaviour of materials. In your busy agenda, you have always had time for fruitful conversations. A particular recognition goes also to my former second supervisor, Dr. Tugrul Comlekci, who unfortunately left the project during my second year of study. His introduction to the laboratory, passion for material experiments and endless resourcefulness were an excellent kick-off and support during the initial period at the University of Strathclyde.

I would like to thank my Weir Champion, Dr. Ralph van Rijwick for leading the scientific research into resolution of industrial problems. His guidance during the time in Weir Mineral Venlo has added a valuable contribution to the research work. Thanks also to all the members of the Venlo Technology Group for sharing their knowledge during the year and half experience in The Netherlands.

I am thankful to the European Union for funding the APESA project, giving me the opportunity to be part of it, and becoming a member of the, Marie Skłodowska-Curie actions. It has been an amazing experience.

Thank you to the Weir Advanced Research Centre, in particular to Jan Brindley and Dr. Douglas Watson, for their continuous management support. Thanks also to all the colleagues in the Weir Advanced Research Centre, it has been a pleasure to collaborate and share ideas and projects with all of you. Special thoughts to Ali, Alasdair and Daniele, my office squash mates, our tournaments and games have been a great amusement and relaxation after work.

The experimental aspects of this thesis would not have been possible without the technical support staff within the department: Drew Irvine, James Kelly and James Gillespie. Thank you for providing support and help in undertaking the experimental programme and for making the days in the lab even more excited. I am sure understanding your Glaswegian accent has been one of the hardest challenge I have ever faced.

Thanks also to my colleagues and friends, this journey would not have been so spectacular without you. In particular, thanks to my flatmate Janice, for her carefreeness and her ability to make me feel at home. My Glaswegian crew: Alex for his humour, Clara and Filippo for treating me to delicious dishes, Maddalena for her high level of enthusiasm, and Giulia for her ability of being patient, reassuring and for all the support she has offered and she still does from Glasgow. My university friends, Silvia, Francesca, Cecilia and Andrea which, despite the distances, are still fundamental reference points for my personal and professional growth. To my friend Serena, who no matter what, has always been there to welcome me back at home.

A special thanks to my family, who has supported me once again during the long journey resulting in this thesis. To my grandmothers and my grandfather, the best part of my roots. To my parents, who gave me their hospitality and their ability to look at things with curiosity, thanks for being supportive with all my decisions and being present, despite the distance. And to my little brother, who has always taken care of everything and everyone allowing me to breezily enjoy my experiences.

Last but definitively not least, I would like to thank my travel mate, partner in crime and life partner, Francesco. Your encouragement and continuous support throughout this journey has been fundament to arrive to this point. Thanks for your endless patience and for literary pampering me during the last period of writing-up. I am honoured to have you by my side.

Contents

Nomenclature

Equation Variables

ε_a	Strain amplitude
ε_e	Elastic Strain
ε_p	Plastic Strain
$\varepsilon_f^{'}$	Plastic cyclic strain material fitting constant
π	Mathematical real transcendental constant
σ_a	Stress amplitude
σ_a	Corrosion Fatigue Strength defined by Weir for the construction of Haigh Diagram
$\sigma_{a,R}$	Stress amplitude at a particular value of stress ratio
$\sigma_{a,R=-1}$	Stress amplitude in the fully reversed condition
$\sigma_f^{'}$	Fatigue fitting constant

$\tilde{\sigma}_{fB}$	True fracture strength
σ_m	Mean stress
$\sigma_{\max}$	Maximum stress
$\sigma_{\min}$	Minimum stress
σ_{op}	Opening stress
σ_u	Ultimate strength
σ_y	Yield strength
ϕ	Diameter
ΔK	Stress intensity range in a load cycle
ΔK_{eff}	Effective stress intensity range in a load cycle
$\dfrac{da}{dN}$	Fatigue crack propagation rate
a_M	Material constant used in FKM
b_M	Material constant used in FKM
E	Young's modulus
$F_{a,appl}$	Applied amplitude force
$F_{m.appl}$	Applied mean force

J	J-integral
K	Stress intensity factor
K_{eff}	Effective stress intensity factor
$K_{\max}$	Maximum stress intensity factor
$K_{\min}$	Minimum stress intensity factor
K_{AK}	Mean stress factor defined in FKM Guideline
K_f	Fatigue notch factor
K_t	Elastic stress concentration factor
M_σ	Mean stress sensitivity factor
$M_{\sigma,3}$	Mean stress sensitivity factor in Region III
$M_{\sigma,4}$	Mean stress sensitivity factor in Region IV
$M_{\sigma,FKM}$	Mean stress sensitivity factor used in FKM procedure
$M_{\sigma,Schutz}$	Mean stress sensitivity factor based on Schutz definition
N_{cf}	Number of cycles to failure in corrosive environment
N_f	Number of cycles to failure
r	Radius

R	Stress ratio
R_a	Roughness Average of a surfaces
q	Notch sensitivity factor

Abbreviations

CE	Corrosive Environment
CF	Corrosion fatigue
CFS	Corrosion Fatigue Strength
EPFM	Elastic-Plastic fracture mechanics
FCGR	Fatigue crack growth rate
FS	Fatigue Strength
LEFM	Linear elastic fracture mechanics
ppm	Part per million
PD	Positive displacement
SWT	Smith-Watson-Topper

List of Figures

List of Tables

Chapter 1

Introduction

1.1 Motivation and Background

GEHO pumps are a family of positive displacement (PD) pumps designed and manufactured by Weir Mineral Netherlands (WMNL), a subsidiary company of The Weir Group PLC [1] , one of the world's largest producers of equipment for the mining and oil and gas industries. GEHO pumps are used to transport a wide range of ore and mineral slurries. This family of pumps is designed for a long service life of up to 25 years, operating in aggressive environments in which pump components experience a continuous mechanical and chemical attack. Over time, this causes severe material damage in components in contact with the pumped fluid through the combined effect of fatigue and corrosion. Managing the structural integrity of these components is therefore fundamental to guarantee the performance and the safety of the pumps as well as to improve the overall design of GEHO pumps.

The main material used to manufacture Fluid End and Power End components of GEHO pumps is the low carbon steel S355J2, which is used in a variety of industrial applications due to its combination of mechanical properties and relatively low cost. The main problem with the low carbon steel is its susceptibility to corrosive environments, which lead to a degradation of material properties and performances. By enhancing knowledge of the material corrosion fatigue characteristics, evaluation of component fatigue strength at the design stage would be possible with a greater level of confidence.

Although corrosion and fatigue are established disciplines, their combined effects are ongoing research topics. Studies [2, 3] have shown the corrosion fatigue mechanism is a multistage damage process which usually includes pit nucleation and development, pit to crack transition and short and long crack propagation stages. In recent decades, great effort has been spent on understanding and modelling each step. Some of the developed approaches, under certain particular conditions, are able to predict the corrosion fatigue lifetime of the material with a useful accuracy. However, it is not possible to generalise any of the available approaches for direct implementation in industrial fatigue assessment. Many of the available approaches require extensive information regarding the chemical composition of the corrosive environment, the material structure and material properties to be applied effectively. In mineral industries and, more in general, in pumps industries, the Stress-Life approach is usually employed to determine the structural integrity of components designed to work under cyclic repetition of loads, with or without the presence of corrosive environments. Currently, design Codes for fatigue design do not fully represent the corrosion effect [4, 5] and take account of the corrosive environment by application of design factors for the fatigue life of unprotected components [6, 7]. However, even when the corrosion effects are taken into account, no generally accepted guidelines or approaches are available to establish the effect of mean stress on the corrosion fatigue strength or develop Haigh diagrams for materials working in corrosive environments. The objective of the research presented in this thesis is to develop a corrosion fatigue predictive model based on experimental investigation of low alloy carbon steel S355J2, suitable for application in the design of GEHO pumps.

1.2 Aims and Objects

The work presented in this thesis forms part of the wider H2020 APESA Project, which aimed to improve the performance of the GEHO slurry pump product range through better understanding how erosion, corrosion and fatigue mechanisms limit the operating life of the pumps and their components. The aims of the present research work are understanding the fatigue behaviour of low carbon steel S355J2 when exposed to aqueous environments, understanding the effect of positive mean stress on corrosion fatigue strength of the low carbon steel and to develop a predictive model to be applied to GEHO pumps design. To achieve these aims, the main objectives are as follows:

1. To evaluate experimentally the effect of exposure to aqueous solution on unloaded S355J2 material surfaces.
2. To develop experimental information on the fatigue behaviour of S355J2 in air and in corrosive environments under various conditions incorporating tensile mean stress effects.
3. To develop a model for construction of Haigh diagrams at various corrosion fatigue lives for pump design applications.
4. To develop and perform industry scale tests for validation of the corrosion fatigue prediction.

1.3 Thesis Outline

The thesis consists of seven chapters. The industrial background is presented in Chapter 2 and an overview of fatigue life assessments commonly employed by industries is also discussed. A literature review on the main factors influencing the corrosion fatigue behaviour of carbon and low carbon steel is presented in Chapter 3. A review of the main approaches developed to estimate the equivalent stress amplitude, when the fatigue life is affected by the mean stress, is presented in the same chapter. Chapter 4 presents the experimental programme and the experimental procedure descriptions used to investigate the fatigue and corrosion fatigue behaviour of low carbon steel S355J2. The experimental results obtained by uniaxial fatigue testing and the related analyses, developed to predict the corrosion fatigue behaviour at various stress ratios, are the topics of Chapter 5. The development of industry scale tests, including the creation of industry scale specimens and the adaptation of the available test rig, are presented in Chapter 6, together with results of validation tests. A summary of the main findings obtained in the research work and suggestions for further investigations are presented in Chapter 7.

Chapter 2

Industrial Background

The need for investigation of corrosion fatigue behaviour of low carbon steel and development of a fatigue assessment procedure incorporating the effect of mean stress in corrosive environments arose in Weir Minerals in relation to the design of Fluid End components of GEHO pumps, used in the mining and mineral processing industry. Because of their applications, the Fluid End components of GEHO pumps work in cyclic operational conditions in contact with various corrosive environments. Many components of the Fluid End, made by low carbon steel S355, are designed for a full pump fatigue life of 10^9 cycles. During the life of these components, the effect of corrosion degrades the material, resulting in a lowering of strength. The behaviour of low carbon steel subjected to fatigue in corrosive environments is therefore of critical importance to continuous duty of the pumps.

To define the research requirements, the industrial background is presented in this Chapter, including the description of GEHO pumps, the main loads the pumps are subjected to and the current strength assessment used by Weir in the design. In addition, fatigue and corrosion fatigue assessments available to design against fatigue and corrosion fatigue are briefly discussed.

2.1 GEHO Pumps Overview

PD GEHO piston diaphragm pumps are characterised by the presence of a flexible diaphragm, which isolates the pumped fluid from the piston and the power end components. GEHO family pumps are manufactured mainly for the mining and mineral processing industry and, depending on the type of slurry, (a mixture of solids and water), they can be categorised as follows: long-distance pipeline transport, process feed and tailings disposal [8].

Figure 2.1 shows a schematic view of a single-acting piston diaphragm pump [1]. The crankshaft (1) is driven by an external energy source which is often a variable speed motor with gearbox. Through a connecting rod (2), the reciprocating motion of the crosshead (3), the crosshead rod (4), the piston rod (5) and the piston (6) is generated. The piston (6), in turn, displaces the intermediate propelling fluid (7), which is often

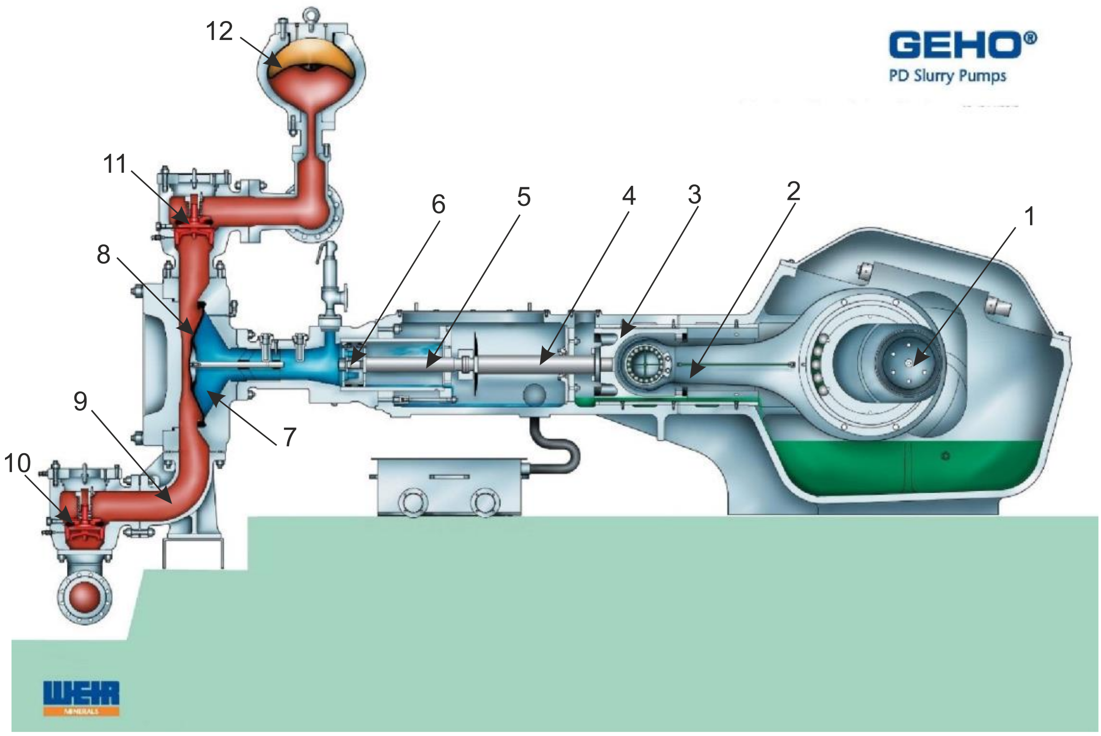

Figure 2.1: Cross-section of GEHO single-acting piston diaphragm pump. *Modified* [8].

a mineral oil. The propelling fluid (7), moved by the piston, displaces an elastomer membrane (8), referred to as the diaphragm, which, on the other side, is in contact with the pumped slurry (9). Through to the presence of the non-return valves, on the suction (10) and discharge (11) side, a positive displacement pump action is enabled. Through the diaphragm movement, the volume of the pump chamber, defined as the volume between the non-return elements and the diaphragm, changes and, as a consequence, the pumped fluid moved to maintain the equilibrium. The part of the pump that handles the pumped fluid, such as valves, connecting pipes, and chamber, is referred to as *Fluid End*. Often, the pump is equipped with dampers (12), filled with gas, on the suction and discharge side to attenuate the residual flow pulsation generated by the pump. A leakage compensation system is also used to keep the volume of the propelling fluid within certain limits, to preserve the diaphragm position within its limits.

The diaphragm hermetically seals the pumped fluid between the pump chamber and the driving mechanism. This characteristic makes the diaphragm pumps particularly appropriate for the mining and mineral process, as the piston and the power ends are isolated from the abrasive and corrosive solids contained in the pumped fluid. The pressure at each side of the diaphragm is approximately equal, due to the hydraulic actuation principle, allowing the generation of relatively high discharge pressures. Applications of piston diaphragm pumps range from small applications, with hydraulic output of a few watts, to high volume applications, with hydraulic output of several megawatts.

2.1.1 Load Distribution in Fluid End Components

The Fluid End components are subjected to cyclic internal pressure loading. The pressure in the pump chamber changes during each pump stroke, from a minimum value almost equivalent to the value of suction pressure, to a maximum value slightly higher than the discharge pressure.

Typical pressure measurements for a triplex single-acting pump (TZPM) are shown in Figure 2.2 [9]. The three curves show variation in suction pressure, discharge pressure and diaphragm chamber pressure over time. Suction pressure and discharge pressure are measured before the suction valve and after the discharge valve respectively. Values of suction and discharge pressure, over time, fluctuate around their mean value.

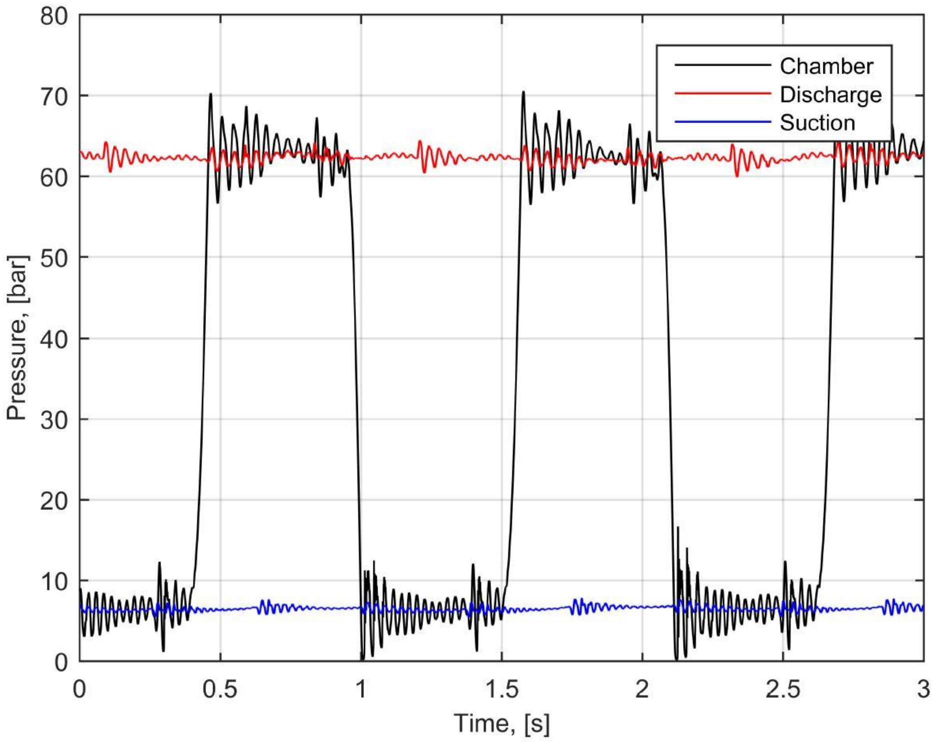

Figure 2.2: Typical pressure measurements on a triplex single-acting piston diaphragm pump. *[9].*

This means that the levels of pressure at the inlet and outlet of the pumps are almost constant during cycles. Usually, the suction pressure, for PD Diaphragm GEHO pumps is around, or slightly higher, than the atmospheric pressure, whereas the discharge pressure is an intrinsic characteristic of the pump and varies between the different models available in the GEHO family. The level of pressure inside the chamber varies during every cycle, according to the position of the diaphragm and, consequently, the opening and closing of the valves. Variation of pressure against the crank angle, for a single cycle, is represented in Figure 2.3, where the status of valves is highlighted for the main variations.

In Figure 2.3, the first half cycle, from 0 to 180 degrees, represents the discharge stroke and the second half, from 180 to 0 degrees, represents the suction stroke. Starting from 0 degrees, the chamber is being compressed, as the diaphragm progressively reduces the chamber volume, up to the condition where the chamber pressure becomes higher than the discharge pressure. This allows the opening of the discharge valve, which enables the passage of the fluid. Then, the pressure inside the chamber decreases, causing the closing of the discharge valve. Simultaneously, because of the backward movement of the diaphragm, the chamber is decompressed. When the chamber pressure goes below the suction pressure, the suction valve opens and the fluid enters the chamber. The chamber fills with the fluid, increasing the chamber pressure. Consequently, the suction valve comes back to its closing position and the fluid passage is blocked. As a consequence of the pressure variation, cyclic stress is induced in all Fluid End components.

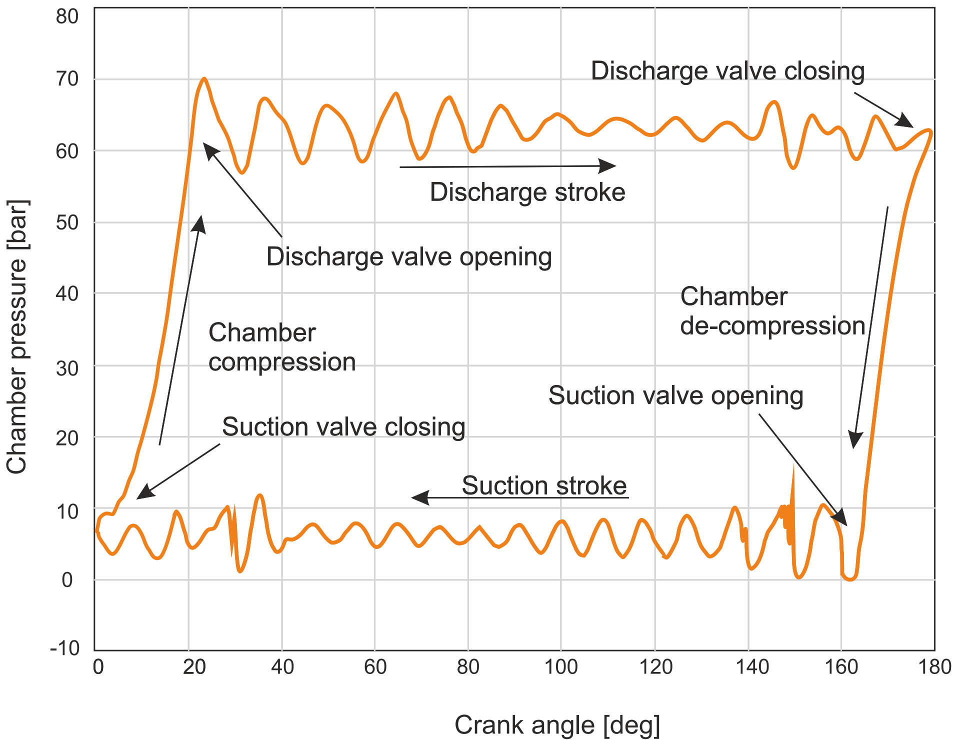

Figure 2.3: Pseudo-indicator diagram of chamber pressure measurement shown in Figure 2.2.

An important aspect that affects the design of the Fluid End component of GEHO pumps is the characteristic of the pumped fluid. By its nature, the slurry transported by the pumps is a mixture of the ore and water which results to be corrosive for the metallic parts in contact with the fluid, such as the transport pipes and Fluid End components. Therefore, the phenomenon of corrosion is taking place on Fluid End components simultaneously to the fatigue loading action.

An additional load component influencing Fluid End parts, comes from pre-tension in bolted joints. Bolt connections are widely used in GEHO PD pumps to connect components, particularly for connections where frequent disassembly as well as high strength are required. In Figure 2.4 different sections of a GEHO pump using bolt connections are shown. In the Fluid End section, the main components connected through bolts are the diaphragm housing cover and the valve housing cover, to the diaphragm house and to the valve house respectively. Bolt pre-loading is a requirement by Standard [10] and it brings the advantages of increasing allowable stress amplitude in bolts, preventing the loosening of the joints and preventing fatigue damage. However, the bolt pre-loading induces a stress distribution in the joint component, proportional to its stiffness, which acts as a constant load during the life of the component. Therefore, particularly for diaphragm house and valve house components, the induced stress caused by the bolt connection has to be taken into account, in addition to the effect of cyclic pressure and the effect of the slurry.

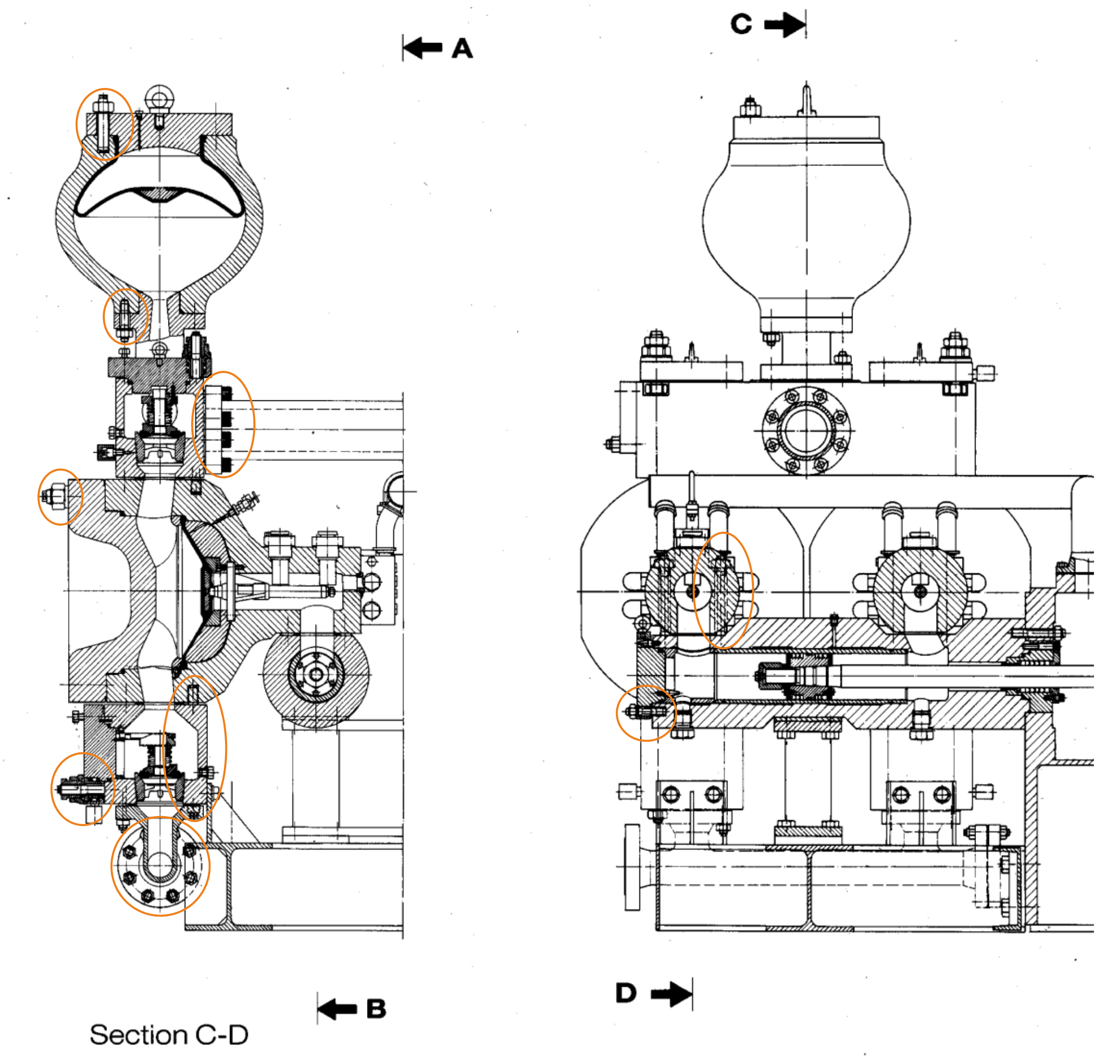

Figure 2.4: Example of bolt joins in PD diaphragm GEHO Pump.

2.1.2 GEHO PD Diaphragm Pumps Strength Assessment

An overview of existing methodologies for the fatigue life prediction available in literature and generally used in industry contexts are presented in Section 2.2. However, the nomenclature used in the fatigue design to define a stress cycles is briefly introduced here to support the description of the strength assessment used for GEHO pumps.

Figure 2.5 shows the nomenclature used in fatigue design, superimposed on the diagram of the constant amplitude stress variation over time.

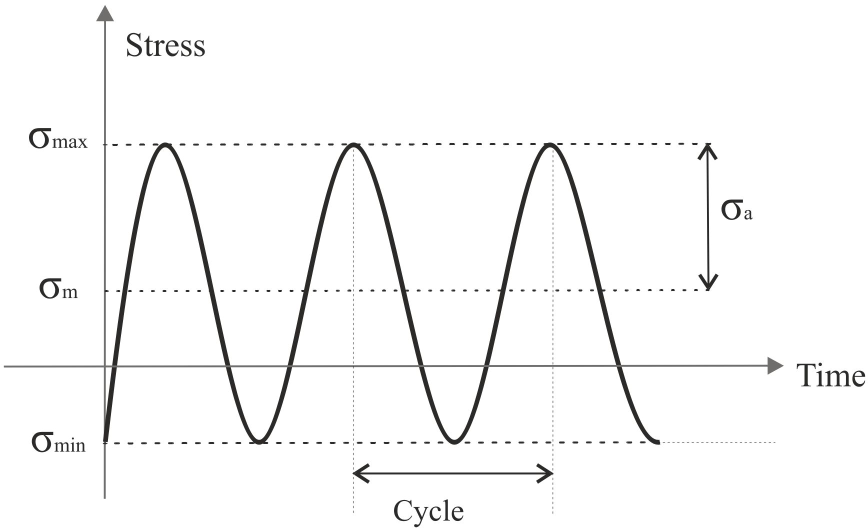

Figure 2.5: Stress cycles around a non-zero mean stress.

Definitions of stress amplitude σ_a, mean stress σ_m, maximum stress σ_{max} and minimum stress σ_{min} are indicated. The algebraic relationships among these quantities are reported in (2.1) to (2.4).

$$\sigma_a = \frac{\sigma_{\max} - \sigma_{\min}}{2} \tag{2.1}$$

$$\sigma_m = \frac{\sigma_{\max} + \sigma_{\min}}{2} \tag{2.2}$$

$$\sigma_{\max} = \sigma_m + \sigma_a \tag{2.3}$$

$$\sigma_{\min} = \sigma_m - \sigma_a \tag{2.4}$$

In GEHO Fluid End components, a fatigue load cycle is defined by the variation of pressure, from discharge to suction values, as presented in Figure 2.3. GEHO diaphragm pumps are designed for continuous duty in mineral applications with a design life of roughly 25 years. This family of pumps are characterized by a relatively low stroke rate to minimize the wear of the self-acting valves in the slurry, usually limited to 60 strokes per minute, or 1 Hz. Based on continuous use, the load cycles at which the pump is subject per year is roughly $30x10^6$. From a strength assessment point of view, this means the maximum allowable stress amplitude in the GEHO design procedure is limited to ensure a design life of 10^9 cycles.

In general, a GEHO pump is based on a combination of main modules selected to obtain the optimum pump configuration based on customer requirements. In the Fluid End section, except for a few elements such as the diaphragm and the valves, the components are designed to ensure a fatigue life of 10^9 cycles. Examples of main modules for the Fluid End section are the diaphragm housing, the valves housing and the corner piece. Each component is designed based on a *nominal pressure* which is selected according to the regulation DIN 323-2 [11]. However, to take into account fluid fluctuation, the stress distribution used to verify the performance of each modular component is based on a level of pressure equal to 110% of the nominal pressure, called *the nominal design pressure*.

The current GEHO design procedure employs the FKM guideline [12] as the default method for strength assessment of both static and dynamic loaded components. The FKM guideline is a widely used guideline for strength assessment within Europe, especially within Germany. The basis for this strength assessment are the static mechanical material property values, as defined in relevant material Standards. It covers a wide range of materials, loading conditions and influencing factors, including high temperature. However, the FKM method is not intended for situations where components are subject to corrosion. In particular, for components subject to corrosion fatigue, the FKM guideline doesn't define a procedure to estimate the corrosion fatigue strength at various stages of the fatigue life, or a procedure to correlate the allowable stress amplitude with mean stress.

For Fluid End components of GEHO pumps, a specific procedure was developed and applied by Weir, based on the definition of a specific value of Corrosion Fatigue allowable Strength $\tilde{\sigma}_a$, for a fatigue life of 10^9 cycles, in the condition of pure tensile loading cycle. This loading condition represents the case in which only the effect of the pressure acts, varying from the minimum value of the ambient pressure to a maximum positive value. The specific value, $\tilde{\sigma}_a$, not given here for confidentiality reasons, applies to a forged steel in a mild corrosion environment. The value is the result of the combination of experimental data from similar materials extrapolated from literature and field experience within Weir Minerals. Starting from this value, the allowable stress amplitude is defined for every combination of stress amplitude and mean stress. To graphically represent the allowable stress amplitudes, the Constant Life Diagram, also known as Haigh Diagram [13], is used. This diagram, widely used in the literature [14] to show the effect of mean stress on the fatigue strength, shows the variation of the allowable stress amplitude as a function of the mean stress, at a fixed number of cycles. Depending on the level of the mean stress, four areas are identified in the Haigh Diagram developed for GEHO pumps and for each region the allowable stress amplitude is defined, as reported in equations (2.5) to (2.8).

1) $\sigma_m \leq 0 \quad \rightarrow \quad \sigma_a \leq 2 \cdot \tilde{\sigma}_a$ (2.5)

2) $0 < \sigma_m \leq \tilde{\sigma}_a \quad \rightarrow \quad \sigma_a \leq \left(2 - \frac{\sigma_m}{\tilde{\sigma}_a}\right) \cdot \tilde{\sigma}_a$ (2.6)

3) $\tilde{\sigma}_a < \sigma_m \leq 2 \cdot \tilde{\sigma}_a \quad \rightarrow \quad \sigma_a \leq \left(1.5 - \frac{\sigma_m}{2 \cdot \tilde{\sigma}_a}\right) \cdot \tilde{\sigma}_a$ (2.7)

4) $\sigma_m > 2 \cdot \tilde{\sigma}_a \quad \rightarrow \quad \sigma_a \leq \frac{\tilde{\sigma}_a}{2}$ (2.8)

To define the relations between the allowable stress and the mean stress, and consequently to design the Haigh diagram, the four regions were chosen arbitrarily as no experimental data were available for S355J2 in freshwater conditions at the time in which Weir developed this procedure. However, the concept of division in regions is taken from the FKM Haigh Diagram developed for metals under fatigue stress in air, and from its definition of mean stress sensitivity factor.

Figure 2.6 shows the Haigh diagram designed by Weir Mineral for low carbon steel S355J2 in freshwater conditions, including the construction lines from which the allowable stress is defined.

To perform the strength assessment, the state of stress and its variation over time must be evaluated to be compared with the allowable stress state defined in the Haigh diagram.

Based on the description of pressure variation in the diaphragm housing of GEHO pumps, illustrated in Section 2.1.1, the load cycle can be schematized as a constant variation from a minimum, identified with the suction pressure, to a maximum, represented by the discharge pressure. The maximum discharge pressure required by the client is defined as the *Design Pressure*.

During the life service of a pump, the pressure load may change its intensity, for example by changing the flow rate in tailing and pipeline transport. This aspect may be taken into account by defining the load probability which evaluates the probability that a specific customer will operate the pump at its maximum design pressure continuously. Weir design assessment always considers a high load probability. This means the minimum pressure which the pump is required to work continuously is equivalent to the Design pressure, thus the maximum pressure required by the client. From a structural point of view, this implies a conservative design for some applications.

All the modular components of the Fluid End section are selected in order that the nominal design pressure is equal or higher than the design pressure. The state of stress for the pump is calculated using the design pressure and the pre-tension of bolt joints when required. The result, usually obtained from an FE analysis, is used for the fatigue strength to evaluate the amplitude and mean stress in the surface of the components. Each point must lie within the limits of the Haigh diagram to have a successful design. This should guarantee a fatigue life of 10^9 cycles, in the corrosive environment.

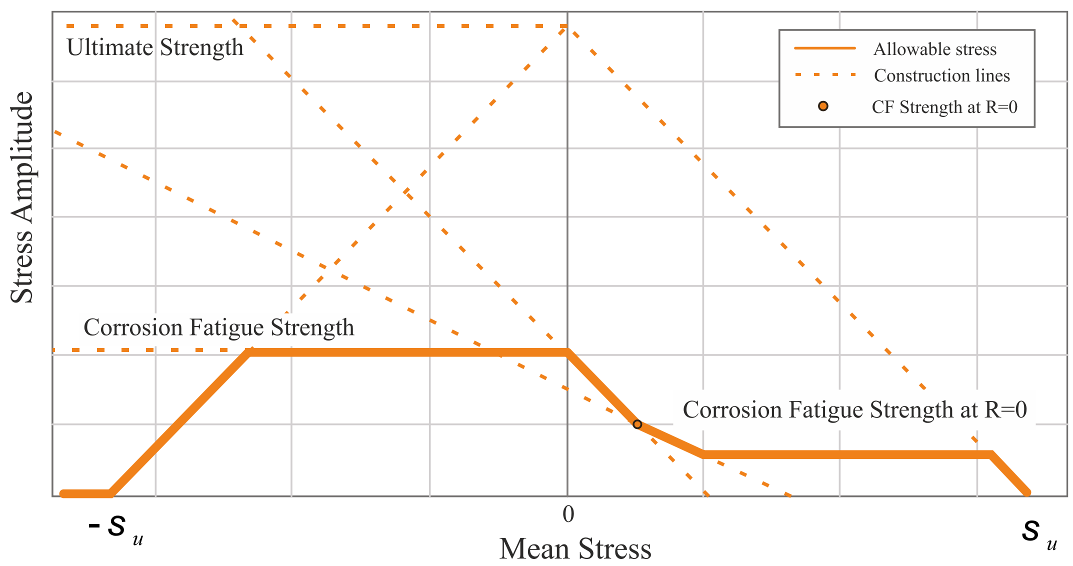

Figure 2.6: Haigh diagram for GEHO Fluid End components.

2.1.3 Identification of Industrial Problem

Fluid End components are subjected to cyclic pressure loading by the pumped liquid, which also causes corrosive degradation of the material. The cyclic pressure therefore causes corrosion fatigue degradation of Fluid End components, which can be represented as a rectangular or sine wave, as shown in Figure 2.7 a). A second fundamental loading condition, which affects only some components on the Fluid End section, is caused by the pre-tension of bolted joints and it is almost constant over time, as shown in Figure 2.7 b). When both loading conditions are present, components are affected by a state of corrosion fatigue characterised by a positive mean stress, as shown in Figure 2.7 c).

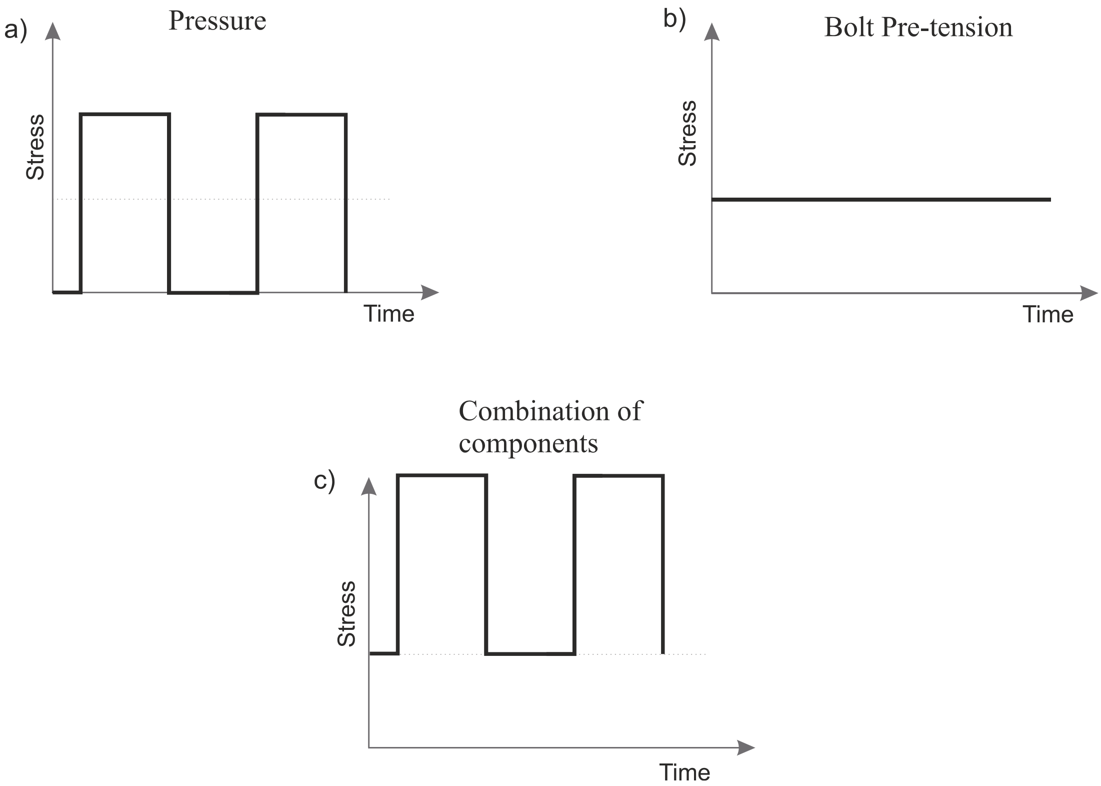

Figure 2.7: Schematic representation of load conditions. *a) cyclic pressure; b) bolt pre-tension; c) combination of bolt pre-tension and pressure.*

Modular Fluid End components, subject to corrosion fatigue stress under positive mean stress, such as the diaphragm housing and valves housing, are designed to ensure a fatigue life equal to the life of the pump. These components are not expected to be replaced within the life of the pumps, such as, for example, the diaphragm or the valves. The failure of one of these modular components and the consequent replacement would incur high cost, including machine downtime, inspection at the mining site by qualified Weir Engineers, production of a new component and installation. For these reasons, the strength assessment adopted in the design of Fluid End components is required to be conservative both in the analysis of the loads and in the choice of modular components. However, occasional unexpected and premature corrosion fatigue can occur, particularly for diaphragm houses.

The extent of the corrosion mechanism in fatigue failure can be observed for a diaphragm house in Figure 2.8. In this case, it was found that two distinct cracks propagated through the entire thickness of the diaphragm house, causing pump downtime.

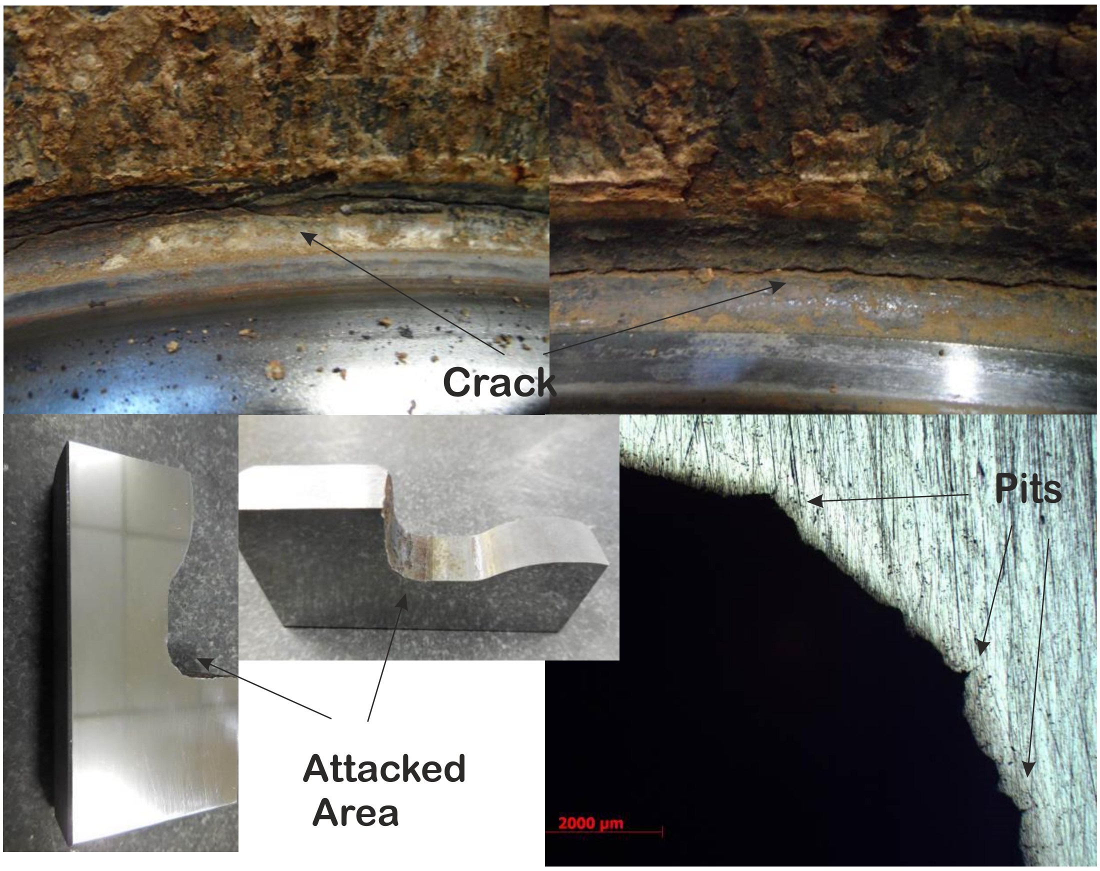

Figure 2.8: Example of propagated cracks in a diaphragm house.

The procedure adopted by Weir is based on a combination of field experience, experimental information for different materials in various corrosive environments and the utilization of scaling factors. A more accurate and robust procedure would require corrosion fatigue data for the steel used in manufacture of the main modular components and a detailed understanding of the effect of tensile mean stress on corrosion fatigue life.

2.2 Overview of Fatigue Life Assessment

Prediction of the fatigue lifetime of material is a fundamental requirement for safe and reliable design of components. For design and troubleshooting related to service failures in machines, pumps, and structures, there are three major approaches for estimating fatigue lives of components, the applicability of which is depending on different factors such as material characterisation, design requirements, loading conditions and other aspects [14].

The longest established approach to analyse and design against fatigue failure is the nominal *stress-based* approach, which employs stress versus number of cycles to failure curves, commonly called S-N curves. This approach has been used since the fatigue problem arose and initial experimental data, published by Wöhler [15], were based on this. Under this approach, the analysis considers the nominal (average) stress in the affected region of engineering components.

In late 1950, another approach was developed, based on the local strain at a point in a component as the governing fatigue parameter, commonly known as the *strain-based* method. This involves a more detailed analysis of localized yielding that may occur in the region of interest during the load cycle. This approach was developed to meet the need to analyse fatigue problems where high stress was required at relatively short lives, particularly for nuclear and motor engineering components [16]. Life estimates are based on materials properties from tests on unnotched specimens, axially loaded specimens, specifically cyclic stress-strain curve and strain versus life curve.

Fracture mechanics is currently used to estimate the fatigue life of machine components. In contrast to stress-based and strain-based approaches, cracks are assumed to exist in material components and structures within the context of fracture mechanics. This approach allows estimation of the residual lifetime of a component containing a flaw and is useful in situations where cracks are known to exist or when a periodic inspection is scheduled and cracks found.

To predict the fatigue life of notched components linear elastic fracture mechanics may be employed to evaluate the propagation of the crack, where the extent of plasticity is small compared with other geometrical dimensions, such as the crack length. To predict the number of cycles required for crack initiation, considered as developing and growing small cracks, the local-strain approach is applicable. Usually, total cycles to failure of a small unnotched axial specimen are used and, in combination with a relationship between nominal stress and notch root strains, the strain life curve provides an estimate of the initiation life of the notched member. Thus, the total life of the component is given by the two contributions [17].

2.2.1 Stress-based Approach

The stress-based approach has been the most widely used method of fatigue analysis since the introduction of the fatigue concept in the mid-1800s, [16]. The major strength of this approach is the ability to provide both quantitative and qualitative estimates of fatigue life with the need for minimal material properties information.

The stress-based approach is generally presented in terms of stress cycle, defined as a variation of the load between a maximum and minimum stress level. Description of parameters that define a load cycle are shown in Figure 2.5 in Section 2.1.2. To characterise the condition of a load cycle, the stress ratio *R* is employed, defined as the ratio between the minimum and the maximum stress (2.9).

$$R = \frac{\sigma_{\min}}{\sigma_{\max}} \tag{2.9}$$

The term *completely reversed cycling* is used to describe the situation at which $\sigma_m=0$, or *R=-1*, additionally, *zero-to-tension cycling* refers to situation at which $\sigma_{min}=0$ or *R=0*.

The prediction of a component life, the number of cycles to failure, is obtained by comparing the stress amplitude the component is subjected to with the S-N curve for the same material obtained from tests on uniaxial stressed specimens under the same loading conditions. When the stress state in a body is not uniaxial, or when one component in the stress tensor is not predominant over the others, the stress amplitude is evaluated using a multiaxial criterion, such as Maximum Principal stress, Tresca or Von Mises [16]. Typical S-N curves for an alloy steel obtained from fatigue tests at different R values in air and plotted on a log-log diagram are shown in Figure 2.9.

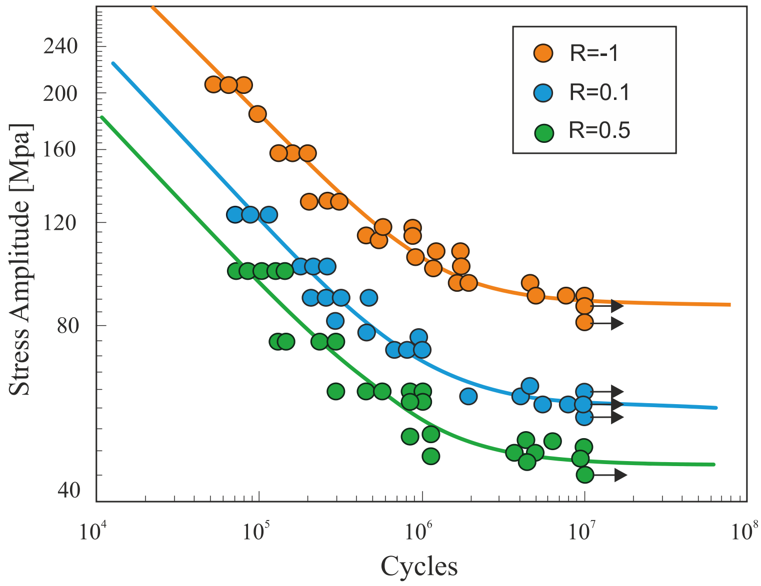

Figure 2.9: Effects of mean stress on S-N curves. *Data from [18].*

The curves describe the variation of the fatigue strength of a material over the number of fatigue cycles. The fatigue life of an alloy steels increases at decreasing the applied amplitude stress. Many alloy steels exhibit a distinct *fatigue limit* around 10^6 to 10^7 cycles range. In a log-log S-N diagram the relationship between the applied stress and the fatigue limit is usually described by Basquin's power law, equation (2.10) [19],where σ_f' is a fitting constant which represents the intercept with the y-axis, N_f is the number of cycles and b is a fitting constant which graphically represents the slope of the curve. In the same scale diagram the fatigue limit is represented by a line parallel to the x-axis.

$$\sigma_a = \sigma_f^{'}(2N_f)^b \tag{2.10}$$

Recent fatigue tests carried out in air [20] have shown that, in the region of very high number of cycles (from 10^9 to 10^{12}), the fatigue strength may reduce below the fatigue limit, due to fatigue crack initiation at internal non-metallic inclusions. Hence, the concept of a fatigue limit may not be valid for very high cycles. In this thesis, *fatigue limit* is used to denote the value of fatigue strength in the region between 10^6 and 10^7 cycles.

When the stress-based approach is applied in the design of notched members, a *fatigue notch factor* K_f is applied to represent the reduction in fatigue strength due to local stress concentration effects. The notch factor is dependent on material characteristics and geometrical parameters, such as notch dimensions, notch positions and component geometry [19]. To relate material properties and notch geometry to the fatigue notch factor, the *notch sensitivity factor q* was introduced by Neuber [21] and later by Peterson [22]. To determine the fatigue strength at the notch, the notch sensitivity factor can be applied in the empirical form proposed by Peterson (2.11) and the notch factor calculated (2.12):

$$q = \frac{1}{1 + \frac{\alpha}{\rho}} \tag{2.11}$$

$$K_f = 1 + q(K_t - 1) \tag{2.12}$$

where α is a material-dependent parameter, ρ is the notch radius and K_t is the elastic stress concentration factor, defined as the ratio of the maximum stress at the notch to the nominal stress. An extensive collection of tables proposed by Peterson [22] is available to estimate empirically the fatigue notch factor for various geometries and notch shapes. However, in the recent decades, especially in industrial applications, the stress distribution is more commonly estimated through a Finite Element (FE) Analysis and results are then compared with S-N curves.

A fundamental aspect of the stress-based approach is the effect of the mean stress on fatigue life. Generally, compressive mean stress is known to increase the fatigue life of metals, while tensile mean stress is detrimental [23]. A common way to represent the mean stress effect on fatigue strength is employing the *Constant-life diagram*, often known as *Haigh diagram*, from the name of the author [13] who first proposed the diagram in the form employed in engineering design. The Constant-life diagram shows the admissible stress amplitude region with respect to the mean stress, at a fixed number of cycles, that corresponds to the fatigue limit. Several empirical equations and approaches have been proposed to correlate the admissible stress amplitude as a function of the applied mean stress to limit the amount of experimental data required to calculate fatigue life for different stress ratios, R.

In industrial practice, two relationships are commonly employed to describe the profile of the combination of static and alternating stress: the Geber approach [24] and the modified Goodman approach [25]. Both relate the stress amplitude to mean stress, Geber through a parabolic dependency (2.13) and modified Goodman through a linear dependency (2.14).

$$\frac{\sigma_{a,R}}{\sigma_{a,R=-1}}+\left(\frac{\sigma_m}{\sigma_u}\right)^2=1 \tag{2.13}$$

$$\frac{\sigma_{a,R}}{\sigma_{a,R=-1}}+\frac{\sigma_m}{\sigma_u}=1 \tag{2.14}$$

The two approaches are based on the assumption that, for a high value of stress ratio, the mean stress is limited by the ultimate strength σ_u. Because of the parabolic dependency, the Geber approach incorrectly predicts the compressive mean stress effect.

A more recent analytical approach was developed by Haibach in the FKM Guideline for analytical strength assessment of mechanical components [12]. This approach has acquired an increasing interest in industry because it describes a general procedure, easy to apply, based on the following relation (2.15):

$$\sigma_{a,R}=K_{AK}\times\sigma_{a,R=-1} \tag{2.15}$$

where K_{AK} is the *mean stress factor*, which is a function of mean stress ratio and of the mean stress sensitivity factor, M_σ. The mean stress sensitivity factor, M_σ, describes to what extent the mean stress affects the fatigue strength of a component [12]. In the FKM, a relationship between the mean stress sensitivity factor and material properties is proposed as (2.16):

$$M_\sigma=a_M\times10^{-3}\times\sigma_u+b_M \tag{2.16}$$

where a_M and b_M are material dependent constants. For structural steel, FKM suggests the following values of constants:

$$\begin{cases}a_M=0.35\\ b_M=-0.1\end{cases} \tag{2.17}$$

In determining the mean stress factor K_{AK}, the Constant-Life Diagram is divided into four areas depending on the stress ratio. For each of these areas, a relationship between mean stress factor and mean stress sensitivity factor is proposed. Field I is defined for R>1, where the maximum and minimum stress of the cycle are always under compression. In this area, the value of the mean stress factor is defined (2.18):

$$K_{AK} = \frac{1}{(1 - M_\sigma)} \tag{2.18}$$

Field II is the region within -∞≤*R*≤*0*: in this field, the maximum stress is positive, except for the left limit case in which it is zero, whereas the minimum is negative, except for the right limit case in which it is zero. In this field, the mean stress factor is defined (2.19):

$$K_{AK} = \frac{1}{1 + M_\sigma \cdot \left[\frac{1+R}{1-R}\right]} \tag{2.19}$$

Field III is the region within 0<R<0.5, where mean stress is always in tension. Mean stress factor in this area is described by equation (2.20):

$$K_{AK} = \frac{\dfrac{1 + M_\sigma / 3}{1 + M_\sigma}}{1 + \dfrac{M_\sigma}{3} \cdot \left[\dfrac{1+R}{1-R}\right]} \tag{2.20}$$

Field IV is defined for R>0.5, as for Field III, mean stress is always positive. In this region the mean stress factor, given by the equation (2.21), is independent of the stress ratio R, providing a constant stress amplitude in the entire region.

$$K_{AK} = \frac{3 + M_\sigma}{3 \times (1 + M_\sigma)^2} \tag{2.21}$$

A graphical comparison between the Geber, modified Goodman and FKM approaches is shown in Figure 2.10, based on a mild steel data for fatigue in air. From a fatigue design point of view, these equations are used to calculate the equivalent stress amplitude giving the same fatigue life as the actual stress amplitude and mean stress. This is then applied to an R=-1 S-N curve to determine the fatigue life.

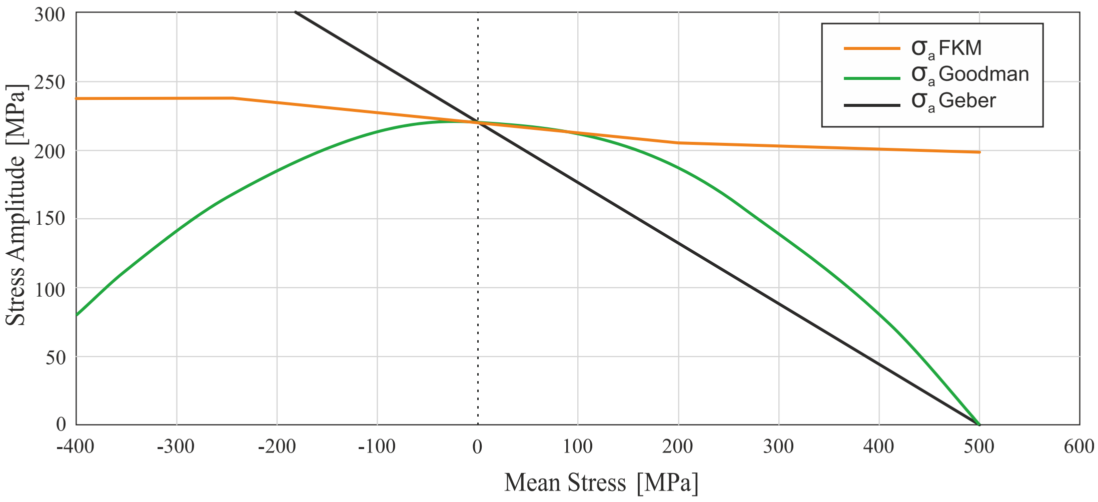

__Figure 2.10: Constant-Life Diagram.__ Representation of FKM, Goodman, and Geber approaches for steel in air.

2.2.2 Strain-based Approach

The strain-based approach considers the plastic deformation that may occur in localized regions where fatigue cracks begin. In such regions, to estimate the fatigue life, local stresses and strains are analysed. This approach employs cyclic stress strain curves and strain versus life curves which allow a more detailed analysis of the local yielding and an improved approximation of the short fatigue lives when compared with the approximation obtained with stress-based approach.

An example of cyclic stress-strain curves is shown in Figure 2.11a), where the difference between the behaviour obtained from monotonic and cyclic tests is highlighted.

Figure 2.11 b) shows an example of a Strain versus Life curve [16].

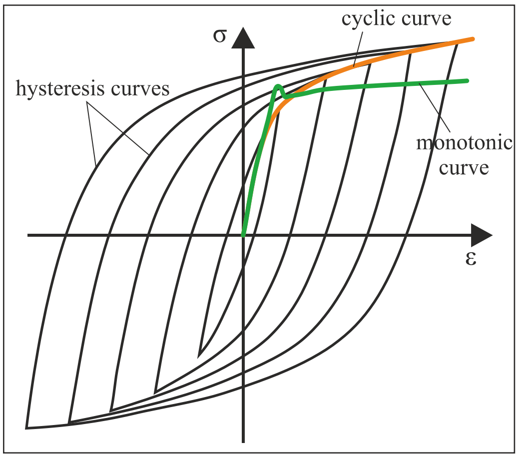

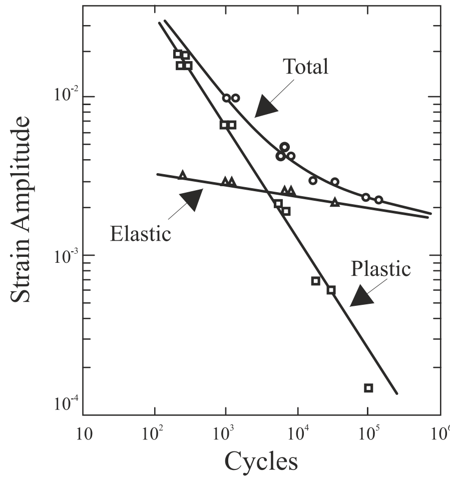

__Figure 2.11: Example of Stress-Strain curves (left) and Strain–Life curve (right).__ Modified from [16].

The total strain amplitude, as shown in Figure 2.11 b), can be divided into the elastic and plastic components and described as the contribution of the two separate components (2.22).

$$\varepsilon_a = \varepsilon_e + \varepsilon_p \tag{2.22}$$

The elastic behaviour can be described using Basquin's law, as for the stress-based approach, which in terms of deformation can be written as (2.23), where *b* is a material parameter.

$$\varepsilon_e = \frac{\sigma_f^{'}}{E}\left(2N_f\right)^b \tag{2.23}$$

To related the plastic component of the cyclic strain with the fatigue life, Coffin and Manson [26, 27] independently found the following relation (2.24), where ε_f' and *c* are both material related parameters.

$$\varepsilon_p = \varepsilon_f^{'}\left(2N_f\right)^c \tag{2.24}$$

Although this approach is considered more accurate than the stress-based approach when plastic deformation is involved, usually components with a short fatigue life less than 10^5 cycles, it offers no significant advantage in analysis of high cycle fatigue and is not usually the first choice in such application.

2.2.3 Fracture Mechanics Approach

The Fracture mechanics approach may be employed to estimate the fatigue life of a component that already contains a flaw or a crack. This approach is particularly useful in situations where cracks are known to occur or when a periodic inspection is scheduled and cracks may be found, as it is focused on the propagation of the cracks. It is, for example, widely used in aeronautical industries to calculate the time required between two inspections.

As a general characterisation, fracture mechanics can be divided into two main groups: *Linear Elastic Fracture Mechanics* (LEFM) and *Elastic-Plastic Fracture Mechanics* (EPFM) [28]. Linear elastic fracture mechanics is based on the assumption that cracks propagate under elastic behaviour and plastic deformation at the crack tip is small compared to the dimensions of the crack itself. When this assumption is not valid, an elastic-plastic criterion is employed which takes into account the effect of plastic deformation around the crack tip.

The fracture mechanics approach is based on the *stress intensity factor K*, which characterises the stress field near the advancing crack tip in the material. In particular, *K* is considered a measure of the severity of a crack and is dependent on the crack size, loading, and geometry. The definition of *K* is based on the assumption that the material behaves in a linear-elastic manner and it is expressed in the form of equation (2.25), where *a* is the crack length and *Y* is a dimensionless factor which depends on the loading mode, the geometry of the components and crack. Empirical formulae for Y for different geometries and crack positions are available in the literature [29, 30]. Different stress intensity factor solutions with respect to geometry and loading conditions are gathered in Murakami's handbook [31].

$$K = Y\sigma\sqrt{\pi a} \tag{2.25}$$

By definition, the stress intensity factor can be employed if the small scale yielding criterion is satisfied, when the crack is already developed and is much bigger than the plastic deformation around its tip. This concept is employed in LEFM to evaluate whether an existing crack will grow under the applied stress [32].

Conversely, when the crack is smaller than the yield deformation zone, EPFM is applied to fatigue problem prediction. In these kind of problems, the J-Integral, defined in equation (2.26), is used [33], where Γ is a curve surrounding the notch tip, *W* is the strain-energy density, *T* is the traction vector defined according to the external normal along Γ, $T_i=\sigma_{ij}n_j$, u is the displacement vector and *ds* is an element of arc length along Γ. The value of *J* is independent of the selected curve. For the case of linear elastic behaviour, the relation can be written as (2.27), where $E^*=E$ for plane stress and $E^*=E/(1-\gamma^2)$ for plane strain [34].

$$J = \int_{\Gamma}\left(W dy - T\frac{\partial u}{\partial x} ds\right) \tag{2.26}$$

$$J = \frac{K^2}{E^*} \tag{2.27}$$

From experimental data conducted in air, the growth of a crack caused by loading cycles can be evaluated through the fatigue crack growth rate (FCGR). The most popular relationship to describe the FCGR was proposed by Paris [35, 36] as a function of the stress intensity range (2.28).

$$\frac{da}{dN} = C\left(\Delta K\right)^{m} \tag{2.28}$$

The stress intensity range is the difference between the maximum and minimum stress intensity factors in a load cycle (2.29), *m* and *C* are material properties.

$$\Delta K = K_{max} - K_{\min} \tag{2.29}$$

According to Paris's law (2.28), the relationship between crack propagation and stress intensity is linear. This equation describes region II of the fatigue crack propagation behaviour, shown in Figure 2.12.

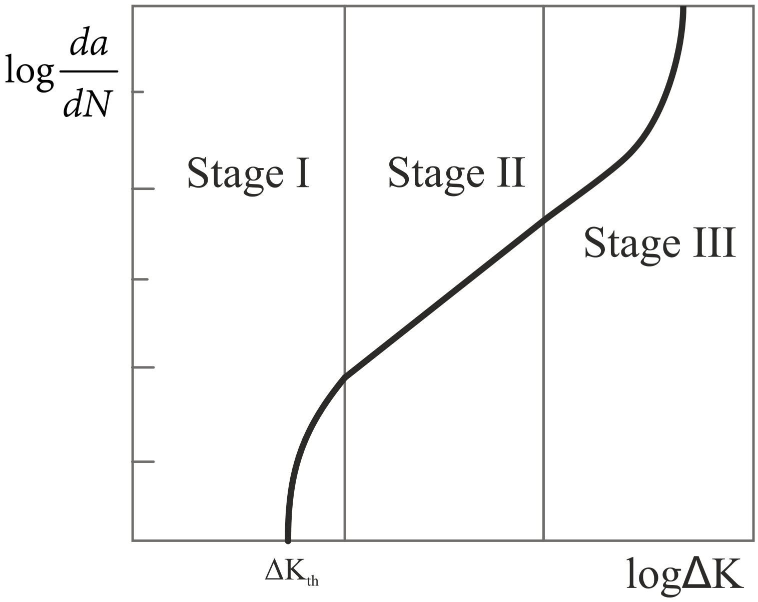

Figure 2.12: Fatigue crack propagation. *Typical behaviour of steel in air.*

To obtain the number of cycles to grow a crack from a given initial length a_i to another length a_f the integration of the fatigue crack growth rate equation (2.28) (or similar models) employing the stress intensity factor, is required. The number of cycles *N* are obtained as (2.30):

$$N = \int_{a_i}^{a_f} \frac{da}{C(\Delta K)^{m}} \tag{2.30}$$

An important contribution to the study of crack propagation was the introduction of the crack closure effect concept, by Elber [37], which is based on the assumption that in a loading cycle a crack propagates only when is open. It was experimentally demonstrated [38] that during unloading the crack closure occurs at stress levels above zero for positive stress ratio R, or below zero when the cycling loads are in compression (negative stress ratio). Three major mechanisms have been recognized behind the crack closure effect: plasticity induced crack closure [39], roughness induced crack closure [40] and oxide-induced crack closure [41].

The applied load stress at which the contact between crack surfaces is lost is designated as crack opening stress σ_{op}. Accordingly, an effective stress intensity factor range is defined as (2.31):

$$\Delta K_{eff} = K_{\max} - K_{op} \tag{2.31}$$

The effective stress intensity range replaces the stress range ΔK (2.29) in Paris's equation (2.28) to evaluate the crack growth rate based on the effective stress. When the crack growth rate is plotted against the effective stress intensity factor, the effect of load ratio is included in the definition of ΔK_{eff} and, therefore, all experimental data ideally converge into the same trend, as shown in Figure 2.13.

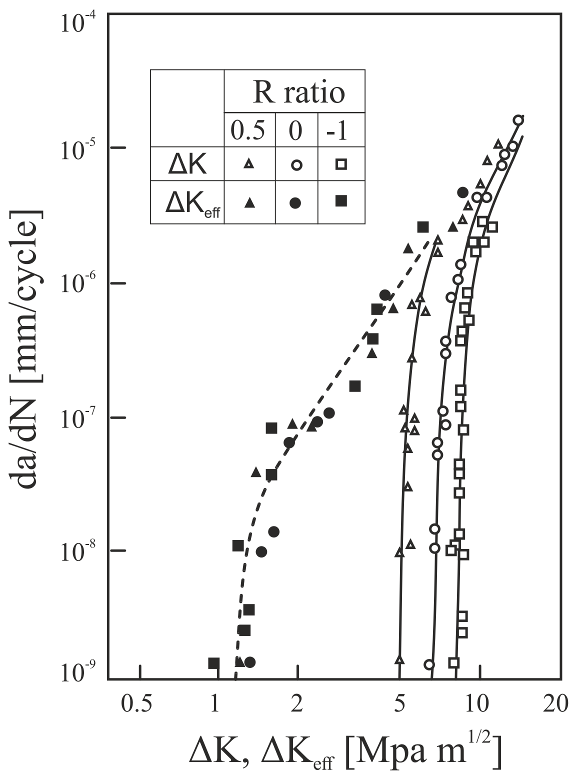

Figure 2.13: Effects of the stress ratio on the fatigue crack propagation of mild steel. *Data from [42].*

The fracture mechanics approach estimates the number of cycles required for a crack to grow from an initial length to a final length, usually the length at which fracture occurs. When used in conjunction with information on the existing initial crack size, this can be considered as the total fatigue life. Although the stress-based approach gives good agreement with experimental data from flaw-free specimens uniformly stressed, fracture mechanics results appear more accurate in the fatigue prediction of components that present already cracks, evaluating the stress status close to the crack tip area.

2.2.4 Corrosion Fatigue Approach

The effect of corrosion during component operation can have a catastrophic impact if not properly taken into account. From studies performed regarding the causes of failure of engineering structures and components, fatigue has been found to be the major failure mechanism in aircraft, chemical and offshore plant and pressure vessels [43]. The corrosion mechanism has also been recognized as a major mechanism leading to failure, with a direct cost per year in the U.S. higher than $250 billion, based on a study conducted in 2002 [44]. The synergetic effect of corrosion and fatigue is detrimental to the life of components and precautions should be considered and accounted for during the design process. Depending on the application, it may be possible to improve the corrosion-resistance of material by adding alloying elements [45]. Other methods include cathodic protection [46], coating [47] and metal cladding [48]. However, these methods are not always applicable and/or effective. Therefore, knowledge of material fatigue behaviour in the corrosive environment and definition of an appropriate methodology is fundamental to properly design against corrosion fatigue.

To safely assess the fatigue life of engineering components subject to a corrosive environment, the reduction of time to fracture should be considered in life prediction. For this purpose, similar assessments to those described for fatigue in air can be used, such as the stress-life approach and fracture mechanics.

The stress-life approach is often employed to investigate corrosion fatigue strength, based on S-N curves obtained in corrosive environment. A large number of factors are known to influence fatigue failure in a corrosive environment, including loading conditions, stress ratio, cyclic frequency, dissolved oxygen in the corrosive solution, material properties, and composition, fluid temperature and flow rate around specimens [49]. Typical S-N curves for low carbon steel obtained in corrosive environment are shown in Figure 2.14 [50]. The synergetic effect of corrosion and fatigue leads to failure even when the repeated stress is far below the value of fatigue strength in air.

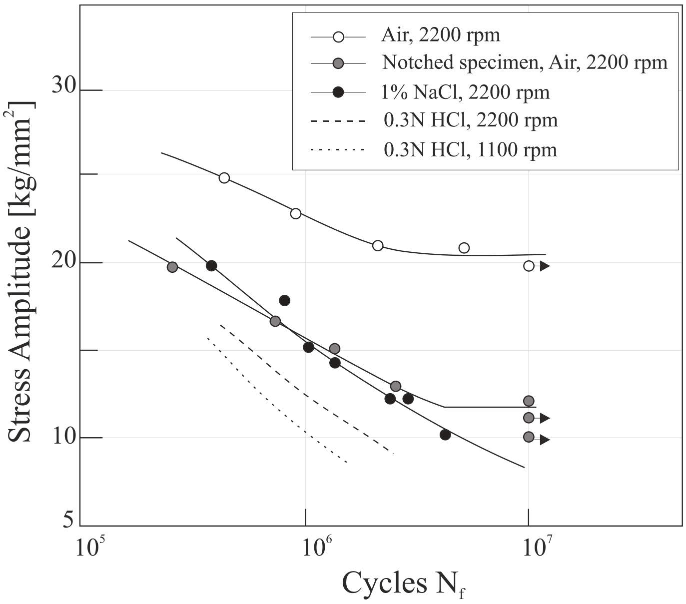

Figure 2.14: S-N curves in air and in corrosive environments*.Data from [50].*

The propagation time of a crack stressed in corrosive environment can be evaluated by fracture mechanics approach. Typical variations of fatigue crack growth rate with stress intensity factor range in corrosive environment are shown in Figure 2.15 [51] for high tensile steel. The propagation of the crack, at a given stress intensity range, is faster in corrosive environment compared to its propagation in air.

In a corrosive environment under cycling loading, cracks mainly start from corrosion pits that arise from local galvanic activity. In this situation, pits on the surface grow continuously until a transition to crack occurs. An environmentally assisted crack growth phase then follows until the final failure occurs. Figure 2.16 shows schematically these development stages. Recently, corrosion fatigue models have been developed [52], based on the combination of some of these stages: usually pit growth and crack growth. The total life of the component is divided in at least two steps that include the pit growth, driven by Faraday’s law, and the crack growth, driven by fracture mechanics. The delimitation between the two stages is determined by a critical pit depth from which a fatigue crack can develop [53].

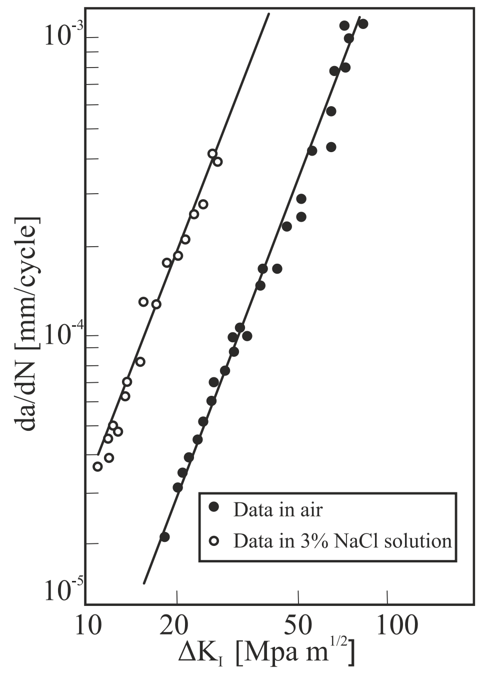

Figure 2.15: Effects of the seawater environment on fatigue crack growth rate. *Data from [51].*

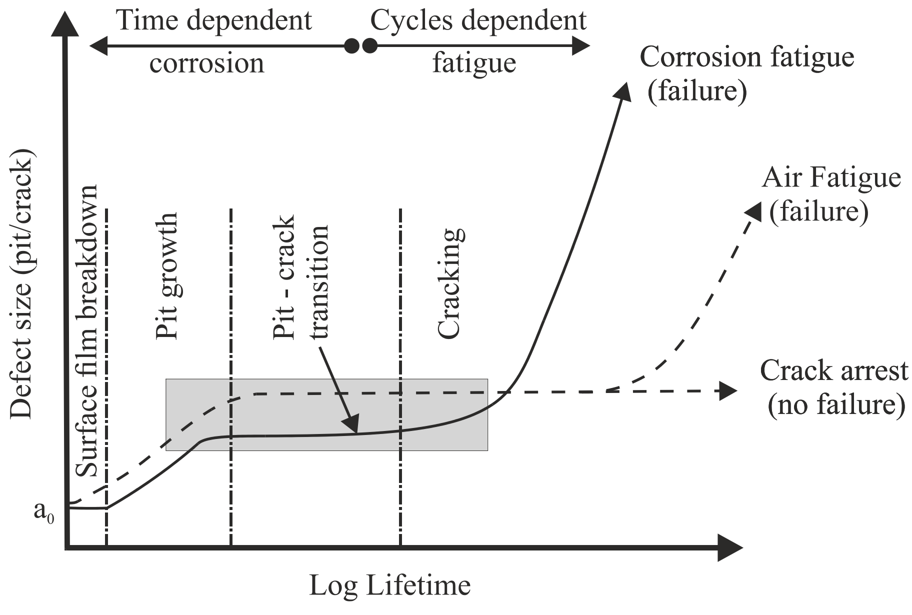

Figure 2.16: Schematic representation of defect size development stages during the corrosion fatigue lifetime. *Modified [53].*

In a recent review of corrosion fatigue damage modelling, Larrosa et al. [54] presented an overview of the corrosion fatigue problem in different industrial contexts, such as oil and gas, aerospace and power generation, investigating on current approaches employed by industries. It appears that there is no a commonly accepted methodology to assess the problem. In some cases, S-N curves obtained in air are scaled using a safety factor. In others, the FCGR is accelerated by employing a scale factor. The design codes resulted from the corrosion fatigue damage models includes the marine environment, more aggressive than the freshwater environment.

In addition, the main design codes of structural engineering, which include corrosion fatigue, are developed for the marine environment, which is more aggressive than freshwater environment, because it is the most common environment where the problem of corrosion fatigue arises.

2.3 Conclusion

The overview of the operation of GEHO piston diaphragm pumps and its fatigue strength assessment illustrates the industrial background of this thesis and the limitation that industry-strength assessment currently faces.

The effect of the corrosive environment must be taken into account during the fatigue design of Fluid End components to evaluate the reduction of fatigue strength, particularly for those components which are working under positive mean stress. Premature failure of modular components, designed to work for the entire life of the pump, can lead to catastrophic consequences from both economical and environmental points of view. However, an overly-conservative design is not desirable because of material waste and detrimental pump performance.

Through the overview of fatigue and corrosion fatigue assessments, the main methodologies employed to assess the fatigue life of engineering components were briefly introduced. Prediction of fatigue life of components working in a non-aggressive environment is well established in industry and many guidelines are available. However, the problem of corrosion fatigue is still an open research topic and a general approach to the problem is not agreed yet upon within the industrial context.

Based on this overview, the following research points are identified as being of primary interest to properly assess the corrosion fatigue design of GEHO’s pumps:

- Understanding the behaviour of corrosion fatigue strength of low carbon steel S355J2 in the freshwater environment.
- Understanding how the allowable amplitude stress changes with reference to the applied mean stress.

The knowledge of corrosion fatigue strength of S355J2 is fundamental to validate the current fatigue strength assessment employed by Weir. Particularly important is the understanding of the variation of fatigue strength with reference to number of cycles and the behaviour at high number of cycles, up to 10^9 cycles.

Chapter 3

Corrosion Fatigue Overview

3.1 Introduction

Fatigue of metals has been studied for more than 160 years and a good understanding of metal fatigue mechanisms in air has been achieved [16]. One of the more recent definitions of metal fatigue has been proposed by Pook [55], as the '*failure of metal under a repeated or otherwise varying load which never reaches a level sufficient to cause failure in a single application*'. A significant feature of the fatigue phenomenon is that the loading is not large enough to cause a static (or immediate) failure. Danger in fatigue failure is the lack of deformation in the region of the fracture, even in materials that are quite ductile when broken by a static load [56].

The whole fatigue life of metals consists of three phenomena: crack initiation, crack propagation and final fracture [19]. Fatigue cracks in components cycled in air usually start from slip lines that appear on the surface of the component, usually where any type of discontinuity is already present. These slip lines create protuberances on the surface, leaving the surface in a rough condition, acting as a localised stress raiser.

The continuous repetition of loads gives the fatigue slip a particular feature, creating extrusion and intrusion on the interest portion of surface that facilitates the slip bands progression. In this phase of fatigue, damage nucleates and, cycle by cycle, it evolves until the formation of microcracks also called microstructurally short cracks [57]. Further cycles increase the damage that grows to the grain boundaries. Then, the microcracks in each single grain join to form a macrocrack. The transition between crack initiation and crack propagation is usually determined by the dimension of the crack.

In terms of size, cracks can be categorised in three groups [39]: microstructurally short cracks, mechanically short cracks and mechanically long cracks. Each type of crack presents a different behaviour in propagation that may be described by different theories. In Figure 3.1, a schematic Stress-Life diagram shows the evolution of damage highlighting the phases from crack initiation to final fracture, which is the Wöhler's curve. It is interesting to note that, the formation of microstructurally short cracks and mechanically short cracks don't always lead to failure. It has been established that short cracks can propagate under small values of stress, even lower than the fatigue limit, and in addition cracks can arrest after a deceleration in the crack propagation [39]. This behaviour can be graphically illustrated as a function of the applied stress intensity range, as shown in Figure 3.2.

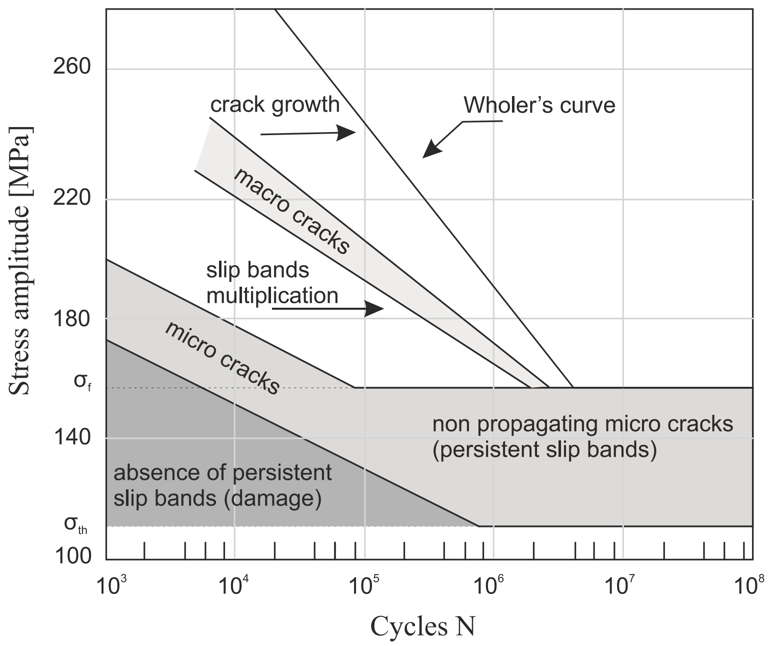

Figure 3.1: Fatigue diagram with marked phases of the damage evolution.*Modified [19].*

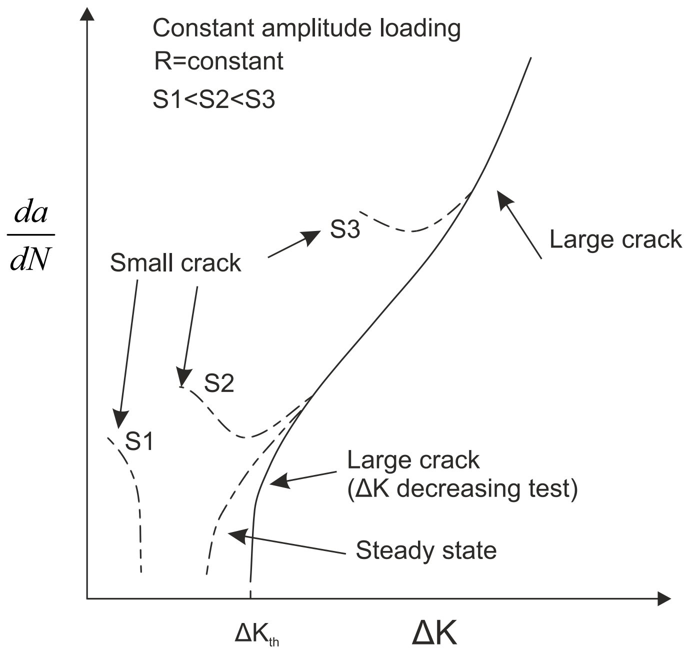

Figure 3.2: Fatigue crack growth behaviour of small cracks. *Modified [58].*

An additional important feature in the damage evolution is the portion of life spent on crack initiation and crack propagation. It is recognized that the fatigue life of a smooth component subjected to cycling load in an inert environment in absence of macroscopic damage is dominated by the crack initiation phase, including propagation of short cracks, for up to 80% of the total life [58]. Consequently, the part of the lifetime spent on crack propagation, that can be estimate applying LEFM, is relatively small. However, factors such as the geometry, the applied stress and the environment may accelerate or slow down this phase. Moreover, when a component is loaded in a corrosive environment, the crack initiation stage of fatigue life is also affected, resulting in a lower total lifetime of the component.

A review of the main factors which influence the corrosion fatigue strength and the corrosion fatigue life of materials is presented in this Chapter, to understand the behaviour of low carbon steel in aggressive environments.

In addition, special attention is spent on the review of existing models to account for the mean stress effect on fatigue life. The well-known Goodman and Geber approaches currently employed in many industrial fatigue assessment and more advanced methodologies are evaluated.

3.2 Corrosion Fatigue

Corrosion is defined as metal degradation by the electrochemical or chemical attack and its influence can drastically affect the fatigue behaviour of many metals [19]. It has been demonstrated that the synergetic effect of the corrosive environment and cyclic loads is more detrimental than the single action of each phenomenon acting individually [53]. Many research studies have been performed to identify the factors that affect the corrosion fatigue strength of components and the relation between those factors and the fatigue life. However, the effect of corrosion fatigue on structural integrity is still not fully understood, as the fatigue strength of material is affected by many parameters that often cannot be evaluated separately.

One of the first features identified in corrosion fatigue investigations was the connection between pitting and cracking and the time-dependency effects due to corrosion, reported by McAdam [59] and Gough [60]. The corrosion mechanism is a time-dependent process and, consequently, corrosion fatigue is time-related. The higher the frequency of tests, the shorter the time the specimens are immersed in corrosive solution before failure. Results of numerous investigations show the fatigue strength of unnotched specimens in air is almost unaffected by increasing the loading frequency because the fatigue phenomenon is cycle-dependent and not time-related [61]. Nikolin and Karpenko [62] tested a Grade 45 steel in 3% NaCl solution at frequencies from 0.4 Hz to 2.6 Hz, showing that the corrosion fatigue strength, at the same fatigue life, increases at higher frequency of a factor of 2.6. Similar results were obtained by Endo [63] for three different structural steels tested from 4Hz to 44 Hz in air, tap water and corrosive solution of 1% NaCl dripped onto the central part of specimens. Related experimental results are plotted in S-N diagrams and S-t (stress-time) diagrams, shown in Figure 3.3. The results show that for a relatively short fatigue life, increasing the loading frequency increases the corrosion fatigue life of material, both in tap water and saline solution. In the same region, S-N curves obtained at different loading frequencies appear to be parallel to each other, which suggests that the effect of frequency may be described by a translation of a single curve. However, at higher numbers of cycles for materials tested in a tap water environment, the distance between curves at various loading frequencies decreases, which implies that the effect of loading frequency on fatigue behaviour diminishes. This tendency is even more clear from the analysis of S-t curves for all three cases, which show a convergence of the curves at a long testing-time. From the available data, the same trend is not visible for corrosion fatigue trends in saline solutions.

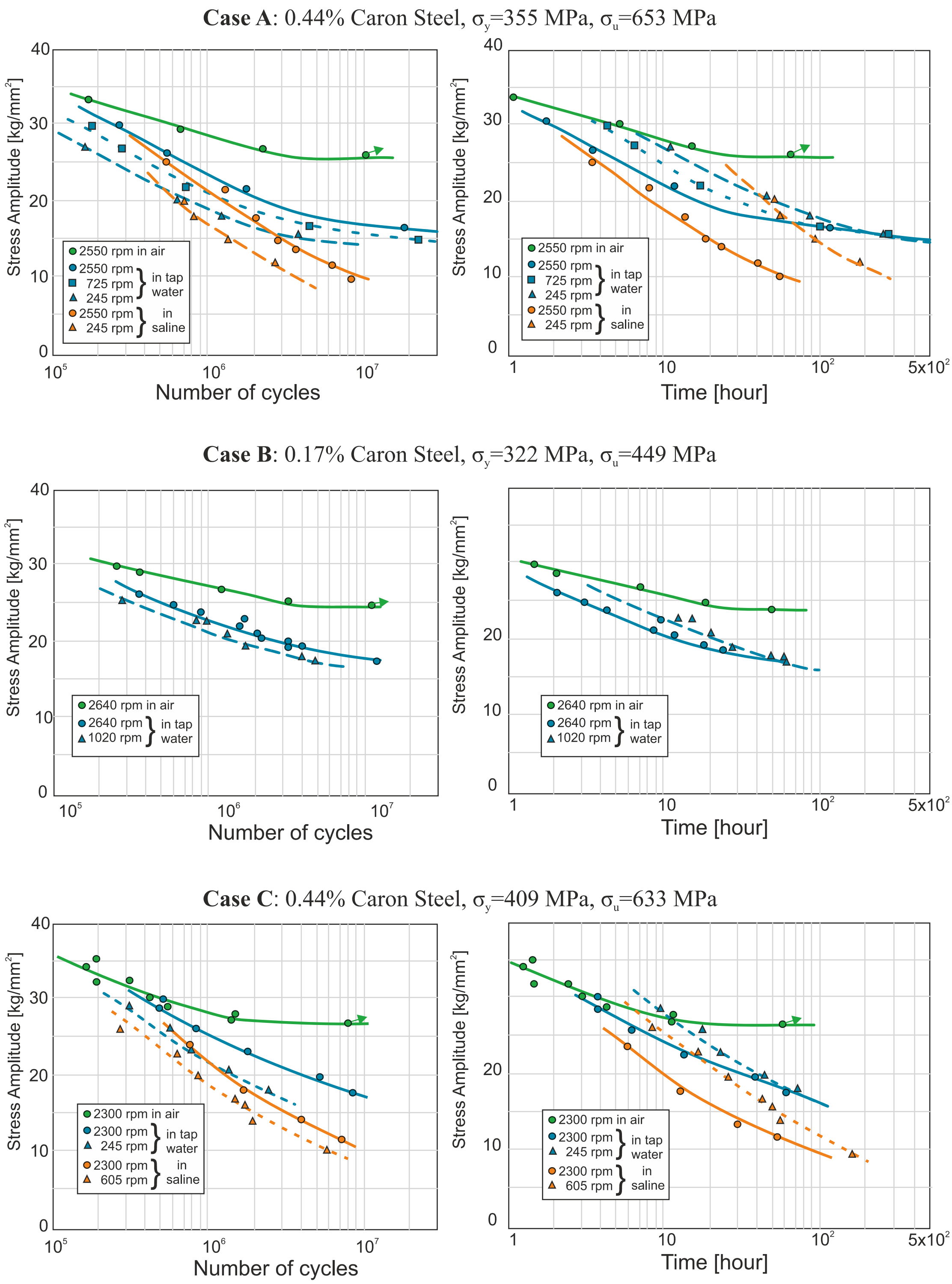

Figure 3.3: Effects of the load frequency on the corrosion fatigue strength. *S-N diagram (right) and Stress-Time diagram (left). Data from [63].*

Another characteristic to be highlighted is that the rate at which the corrosion fatigue strength increases with the increasing frequency is not uniform. In Nikolin experimental data [62], the ratio between the corrosion fatigue strength obtained at 2.6 Hz and at 0.4 Hz is 2.6, measured at 5 million cycles. However, in Endo's results where the gap is much higher, case C, the ratio between corrosion fatigue strength at 38 Hz and 4 Hz is around 1.3, estimated at 5 million cycles. This behaviour is in line with Barson's findings [64], reported in Figure 3.4, where the effect of frequency on the fatigue crack propagation rate of 4340 steel in vapour water environment is investigated. The effect of frequency is higher at low frequencies than at high frequencies: fatigue crack growth at 1 Hz is almost 7 times slower than at 0.1 Hz, but with the same factor in increasing frequency, at 10 Hz, fatigue crack growth is only 3 times slower than at 1 Hz. This trend suggests that the effect of frequency is stronger at low frequency but it becomes less severe at higher frequencies.

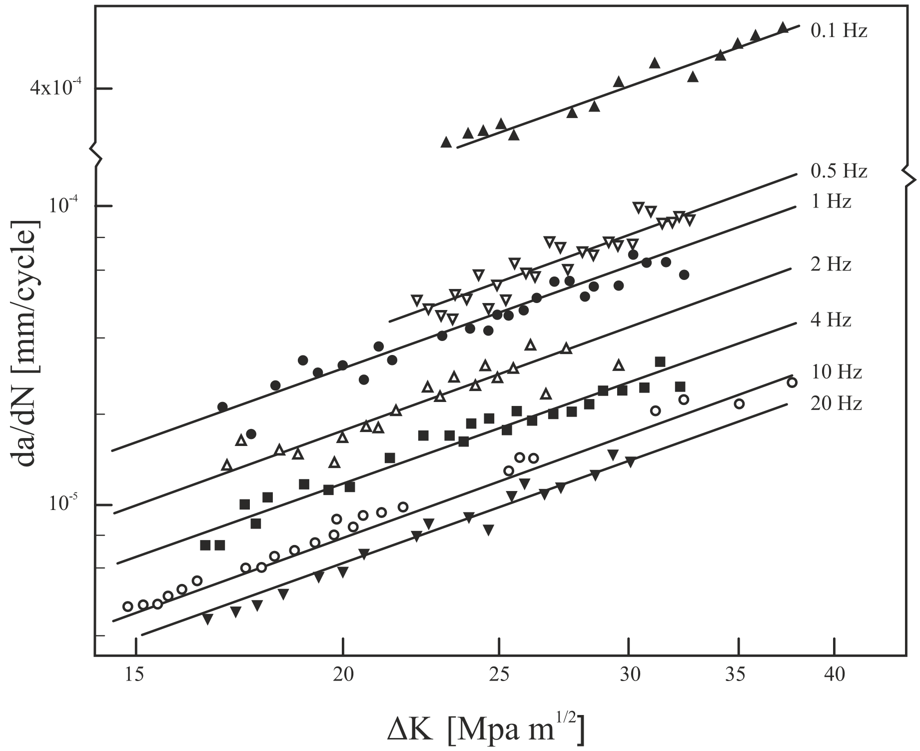

Figure 3.4: Fatigue crack propagation of martensitic steel AISI 4340 .*The effects of the load frequency on fatigue crack growth in the water solution. Modified [19, 65].*

McAdams [59] also investigated the relationship between fatigue strength in a corrosive environment and increased tensile strength due to heat treatment. In air, fatigue strength at high number of cycles can be correlated with tensile strength of materials: the higher the tensile strength, the higher the fatigue strength [66]. In the corrosive environment, fatigue strength appears independent of the tensile strength of the material. This behaviour is clearly shown in Speidel's work [67], where fatigue life tests in air and aerated water are carried out for low strength and high strength carbon steel, G10050 and K08500 respectively, reported in Figure 3.5. At elevated number of cycles, higher than 10^7, S-N curves obtained for the two carbon steels in a corrosive environment almost converge, whereas in air the materials show a distinct fatigue strength value, related to tensile strength. Therefore, as a general deduction, it could be assumed that increase in tensile strength of alloys characterised by a low-corrosion resistance is associated with a decreased resistant to corrosion fatigue [53].

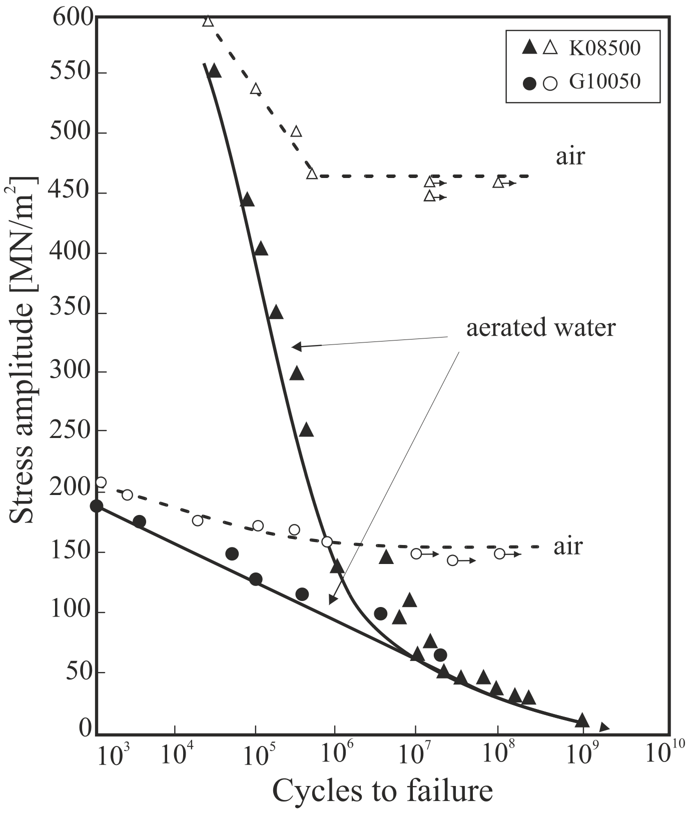

Figure 3.5: S-N curves for low strength and high strength carbon steel in air and aerated water. *Modified [67].*

The effect of the environment on fatigue life can be evaluated by plotting the relationship between the stress amplitude, or applied stress, against the number of cycles on the S-N diagram. In literature, the majority of stress-life data are in the range of low cycle fatigue, especially when tests are conducted under low frequency, as they are time-consuming and achieving results at high number of cycles would be extremely long and expensive. A selection of experimental data characterizing the high cycle fatigue life is considered below for low and medium carbon steel in various corrosive environments.

Ragab et al. [68] investigated the behaviour of low and medium carbon steel, AISI 1018 and AISI 4340, in various environments at room temperature: air, tap water, natural seawater, and 4% NaCl tap water (artificial seawater). Experimental results are shown in Figure 3.6. At elevated numbers of cycles, a decrease of fatigue strength occurs for both materials in all the test environments in comparison with fatigue strength in air. There is no notable difference in the effect of natural seawater and artificial seawater on fatigue strength, and experimental data are plotted fitting a single curve, both for low and medium steel. At 10^7 cycles, low carbon steel shows a reduction in fatigue strength of a factor of roughly 2.9 when tested in seawater and of 2.8 when tested in tap water, and for the medium steel, the reduction is around 2 and 1.6 respectively. At low number of cycles, the effect of the corrosive environment is slightly visible in seawater solution and almost absent in tap water environment. This result should be evaluated considering that tests run at a fixed frequency of 47.5 Hz require just around 30 minutes to achieve 10^5 cycles. Nevertheless, different authors [19, 53, 69] have pointed out that the most significant impact of the environment is visible at stress amplitude below the fatigue limit in air.

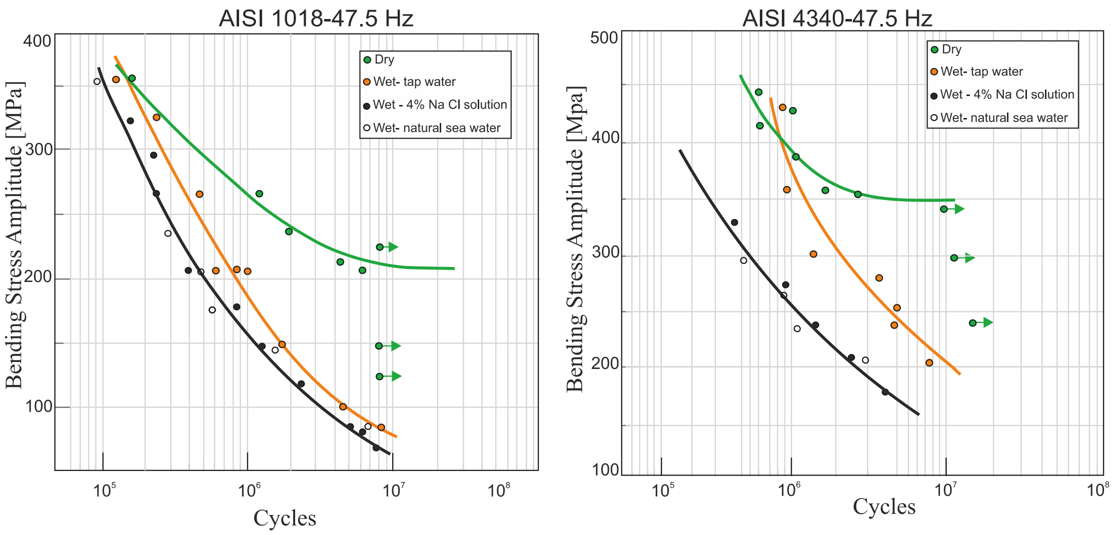

Figure 3.6: S-N curves in air, freshwater, artificial and natural seawater.*(a) low carbon steel (b) medium carbon steel. Data from [68].*

Palin-Luc et al [70] studied the effect of corrosion on giga-cycle fatigue strength of R5 rolled steel performing tests in air, in air after pre-corrosion and under a constant flow of artificial seawater solution at 20 kHz. Experimental results plotted in S-N curves are illustrated in Figure 3.7. At 300 million cycles, corrosion fatigue strength is reduced almost by a factor of 5 compared to data obtained in air for virgin specimens and, in general, fatigue strength is continuously decreasing with fatigue life. From the fractography analysis, it was noticed that crack initiation areas were located all around the surface for specimens tested under the water flow, and not internal as typically happens in very high cycle fatigue in air [20].

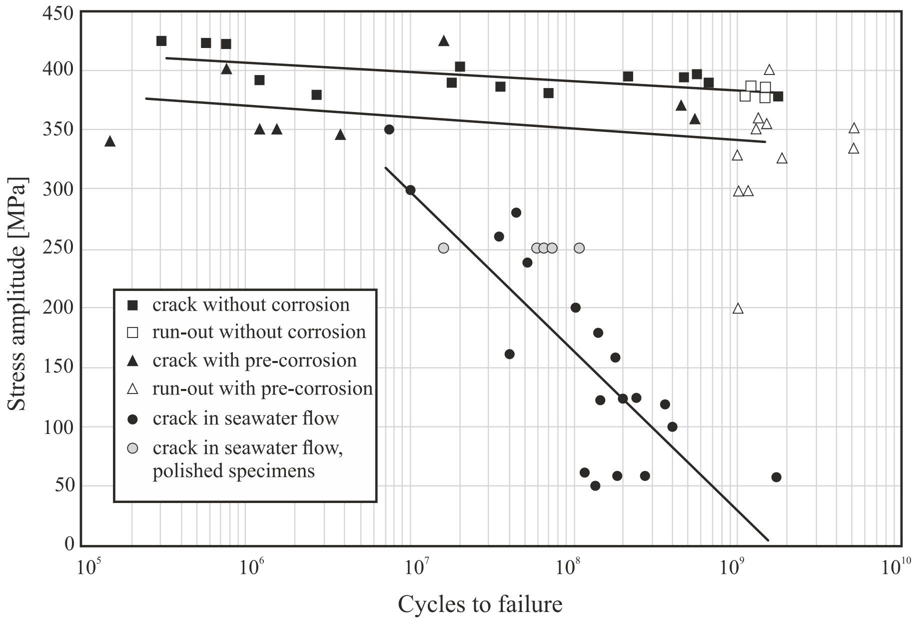

Figure 3.7: S-N curves of R5 steel. *Data obtained in air, in air after pre-corrosion and in seawater environment. Data from [70].*

A further interesting feature in Palin-Luc's work [70] is the behaviour of specimens corroded for 600 hours in a salt fog environment and tested under cycling load in air, referred to as 'pre-corroded'. Many corrosion pits were found on the surfaces of the material, caused by fog, with dimensions between 30 and 100 µm. Comparison between pit dimensions for pre-corroded specimens and pits on specimen tested under cycling load in corrosive environment shows that in the second case the pits are bigger. A similar investigation, that concerns the relationship between the pits development and growth in a corrosive environment with the applied stress is also investigated by Murtaza and Akid [71]. This research shows the growing progress of pits in silicon-manganese spring steel as a function of the applied stress. The higher the applied stress, the faster the pit growth. Rollins et al. [69] studied the mechanism of corrosion fatigue of high carbon steel showing that the environments mainly affect the early stage of fatigue life as it facilitates and enhances the crack initiation. Similarly, Goto [72] investigated the fatigue damage of carbon steel in 3% NaCl solution, highlighting the mechanism of fracture. In the corrosive environment, cracks initiate from corrosion pits which are generated in the initial phase of fatigue life. When the applied stress is relatively high, close to or higher than the fatigue limit in air, pits initiate from slip band sites. However, slip bands do not occur, or at least are not visible, at lower stress amplitude, and pits are generated all around the wet surface. Cracks develop from pits and propagate trough boundary grains: as defined for fracture in air, cracks are divided into three categories, depending on the size. Many pits occur on material surfaces when subjected to corrosive solution, however not all pits evolve into cracks. Murtaza and Akid [73] studied the behaviour of short crack growth in high strength steel in aerated NaCl solution and observed that the transition between short and long cracks in a corrosive environment occurs at a lower number of cycles compared to an inert environment.

Ebara et al. [74] investigated the effect of different corrosive solutions on the very high cycle fatigue life of stainless steel. Tests were performed at 16 kHz, in distilled water and in three different compositions percentage of sodium chloride aqueous solutions: $3x10^{-4}$, $3x10^{-2}$ and 3. S-N curves obtained from these tests are reported in Figure 3.8.

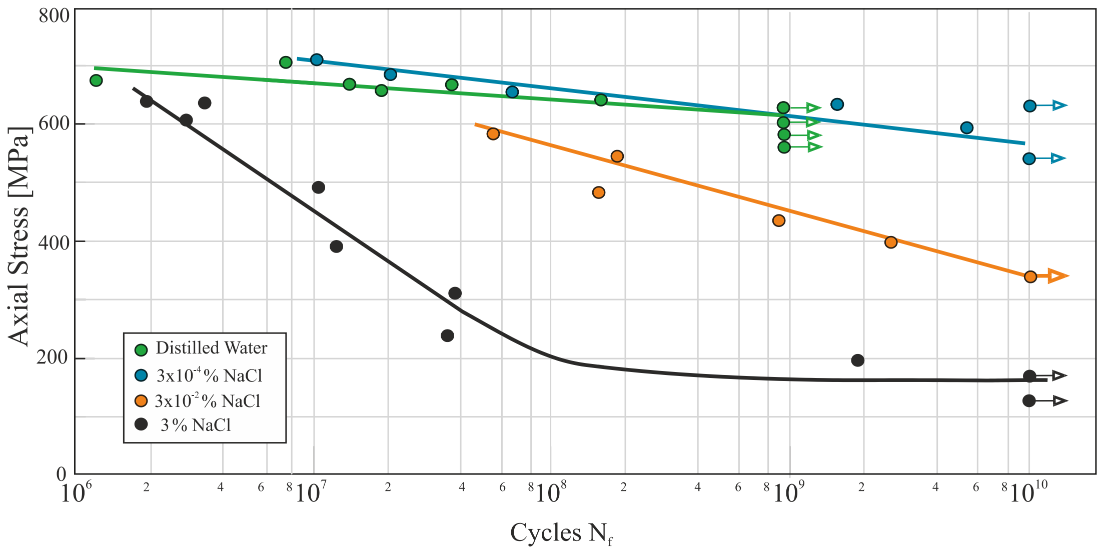

Figure 3.8: S-N curves of 12Cr stainless steel. *Data obtained in different aqueous solutions performed at 16 kHz. Data from [75].*

It was found that the corrosion fatigue strength of 12Cr Stainless steel is particularly dependent on the concentration of sodium chloride. At the same level of stress, the higher the contents of NaCl the shorter the life. From fractography analysis of corrosion fatigue cracking [76], corrosion pits were identified at the initiation region of the fracture surface. For this material, the authors found that the dimensions of pits were independent on the applied stress and in the majority of cases, pits depth were between 10 and 30 µm. From fractography analysis, the depth of corrosion pits was measured from samples tested at different sodium-chloride contents: the depth of pits appears independent of the solution composition.

The trend of results obtained in 3% Na Cl show a change in the slope at very high numbers of cycles, whereas S-N curves for the other environments constantly decrease with number of cycles. However, the amount of experimental data in corrosive environment at very high numbers of cycles (greater than 10^8) are insufficient to properly understand any possible changing on the slope.

3.3 Mean Stress Approaches and Constant Life Diagram

The importance of mean stresses and its effect on fatigue life was recognized almost immediately after the study of fatigue was introduced by August Wöhler in 1870 [15]. Commonly, asymmetric cycling about zero stress is encountered in many engineering applications, which results in mean stress superimposed on alternating stress. Therefore, for a specific fatigue life, the component must be designed to assure the working stresses due to loading are within established limits.

The most practical way to represent limits of the allowable working stress is through the Constant Life Diagram, commonly known as Haigh diagram. The alternating stress amplitude is plotted on the ordinate against the static tensile (or compressive) stress. The curve joining the two points represents the contour of combinations of static and alternating stress giving the same endurance [77].

The most popular models representing the safe contour in the Constant Life diagram are the Geber parabola and the modified Goodman line. In both cases, the allowable area is limited by the ultimate strength of the material. A more conservative approach was proposed by Soderberg [78], equation (3.1), mainly for brittle materials, in which the static strength is limited to the yield stress σ_y.

$$\sigma_{a,R} = \sigma_{a,R=-1} \times \left[1 - \left(\frac{\sigma_m}{\sigma_y}\right)\right] \tag{3.1}$$

Another development of the modified Goodman equation was proposed by J. Morrow [79] for ductile metals, replacing the ultimate strength σ_u with the corrected true fracture strength $\tilde{\sigma}_{fB}$ (3.2) of the material. It was shown by Landgraf [80] that, for steels, the true fracture strength can be approximated with the fitting constant σ_f' that is the intercept stress for σ_m=0 of the unnotched axial S-N curve, according to Basquin's law. From a practical point of view, it is easier using the form with the fitting constant as it can be derived from the knowledge of S-N curve obtained at R=-1, whereas the true fracture strength is often not available.

$$\sigma_{a,R} = \sigma_{a,R=-1} \times \left[1 - \frac{\sigma_m}{\tilde{\sigma}_{fB}} \right] \tag{3.2}$$

In a comparative study by Watson [81], mild steel and low alloy steel experimental data were used to compare the Goodman, Geber, Soderberg and Morrow approaches. The Morrow equation appears to correlate mean stress data better than the other relationships. However, it was shown by Dowling [82] that for a large number of steels, Morrow's equation is not safe in the area of high values of stress ratio, as the limit for static tensile stress is higher than the ultimate strength.

Kececioglu et al. [83, 84] showed through a probabilistic approach that for carbon steel the experimental fatigue failure surface follows the failure line defined in equation (3.3), where a is a material constant, depending on material composition, the process of material forming, the ultimate strength, and the stress gradient.

$$\sigma_{a,R} = \sigma_{a,R=-1} \times \left[1 - \left(\frac{\sigma_m}{\sigma_u} \right)^2 \right]^{1/a} \tag{3.3}$$

This approach was indeed formulated based on notched samples. Because of the lack of information on the material constant a, Kececioglu's equation has not become popular in industrial design methodologies. However, this approach has been employed as a reference for further development. Recently Sekercioglu [85] applied Kececioglu's to unnotched samples, proposing the value of the constant $1/a = 0.8$ for low carbon steel, based on experimental results.

Bagci [86], inspired by Geber parabola, proposed a fourth-order line, limited by the yield strength of the material (3.4).

$$\sigma_{a,R} = \sigma_{a,R=-1} \times \left[1 - \left(\frac{\sigma_m}{\sigma_y} \right)^4 \right] \tag{3.4}$$

However, the Bagci line includes the possibility of yielding when the ratio of the endurance limit to the yield strength is greater than 0.25, as indicated by Orthwein [87]. Further development was proposed by Wang et al. [88] that introduced a new boundary condition to keep the fatigue criterion below the yield line for any ratios of endurance limit to yield strength of material. The corresponding equation is known as Clemson approach (3.5).

$$\sigma_{a,R} = \sigma_{a,R=-1} \times \left[1 - \left(\frac{\sigma_m}{\sigma_y} \right)^{S_y / S_{a,R=-1}} \right] \tag{3.5}$$

Kwofie [89] proposed an exponential stress function to relate the fatigue strength and the mean stress at a certain fatigue life. This approach is based on the premise that the mean stress directly affects the fatigue strength coefficient σ_f' of the Basquin's stress-life equation. The corresponding equation (3.6) is a function of a numerical parameter α, which represents the mean stress sensitivity of the material.

$$\sigma_{a,R} = \sigma_{a,R=-1} \times \exp\left[-\alpha \left(\frac{\sigma_m}{\sigma_u} \right) \right] \tag{3.6}$$

The parameter α gives the equation a degree of freedom: the value can be estimated as the one that minimizes the scatter using experimental data. It is important to notice that, for particular values of α, equation (3.6) becomes equal to a number of previous approaches, such as (3.2). However, as noted by Papuga [90], validation of this model considered only a few different steels and further investigation is required to generalise it.

A different form from the previous approaches was proposed in 1970 by Smith, Watson and Topper [91]. They demonstrated a relationship, valid for metallic material, between a stress-strain parameter $\sigma_{\max}\varepsilon_a$ and fatigue life of small smooth specimens. In particular, they assumed a constant product of these two terms for a given life. From this, the SWT (Smith Watson Topper) approach was developed in the form of the equation (3.7). This formulation appears independent of material characteristics. This means the same effect is predicted at a selected stress amplitude, no matter the material.

$$\sigma_{a,R=-1} = \sigma_a \sqrt{\frac{2}{1-R}} \tag{3.7}$$

Although the SWT parameter has been generally successful in predicting the effects of mean stress in low and high-cycle fatigue for many materials [23], later works showed a better correlation with experimental data by proposing a modification of the constant function. Bergmann [92] introduced a material-dependent factor, *k*, and defined the function P_k, equation (3.8), constant for the fatigue life:

$$P_k = \sqrt{(\sigma_a + k\sigma_m)\varepsilon_a E} \tag{3.8}$$

Similarly, Robert and Erdogan [93] introduced a material-dependent factor γ defining the damage parameter P_{eff}, constant for a given life, as (3.9):

$$P_{eff} = \left(\sigma_a^{\gamma}\sigma_{\max}^{\gamma}\varepsilon_a E\right)^{1/2} \tag{3.9}$$

Walker [94], based on the definition of the damage parameter P_{eff}, proposed the stress-based relation for mean stress (3.10), known as Walker approach. Values of γ for metals ranges from 0 to 1. Lower values of γ indicate a stronger influence of R on fatigue life and vice versa.

$$\sigma_{a,R=-1} = \sigma_a \left(\frac{2}{1-R}\right)^{1-\gamma} \tag{3.10}$$

Nihei [95] evaluated the mean stress effect on cast steels, structural steels and aluminium alloys fatigue lives, using damage parameters, showing that P_{eff}, and P_k, have the best estimation accuracy with no significant difference between them. It was also highlighted that these two parameters allow an individual fit to material data sets.

A similar conclusion was reached by Dowling [82], who proposed an extensive comparison between the Goodman, Morrow, SWT and Walker approaches, in the stress-based forms. The comparison is based on experimental data for structural steels, stainless steels, aluminium alloys and titanium alloy. It was shown that the Walker approach gives superior results when there are available data to calculate the value of the fitting parameter γ. In more recent work, Dowling [96] also proposed a relationship between the ultimate strength and the parameter γ, reported in equation (3.11), valid for steels. However, Papuga [90] showed that the scatter in mean stress prediction increases considerably when Dowling's γ estimation is employed.

$$\gamma = -0.0002 \times \sigma_u + 0.8818 \tag{3.11}$$

The FKM strength assessment, which employs a mean stress sensitivity factor M introduced by Schultz [97], is popular among industry procedures, but it is not often included in comparison works or in fatigue handbooks, except for particular cases in which there is an explicit interest in practice [98]. Kœchlin [99], McKelvey and Lee [100] pointed out the lack of comparison to experimental results in the FKM Guideline. Burger and Lee [101] examined the mean stress sensitivity factor model by comparing the Walker mean-stress correlation equation to the best fitting parameters for steels, aluminium alloys and titanium alloys. Using the Walker relationship as the method of comparison, as it is the best fit to experimental data, it was concluded that the FKM Guideline has the least amount of stress deviation and, overall, FKM method can produce acceptable results.

3.3.1 Comparison of Mean Stress Approaches Based on Experimental Data

A dataset for four different low carbon steels is used here to further evaluate the effect of mean stress on the reduction of fatigue strength. Mechanical properties, fatigue strength and data source for each of the four steels are summarised in Table 3.1.

Table 3.1: Mechanical properties of materials used for comparison and sources.

	σ_u (MPa)	σ_y (MPa)	$\sigma_{a,R=-1}$ (MPa)	α	γ	Source
0.12% C Mild Steel	347	260	180	0.7	0.55	[77]
St50 Steel	538	400	210	0.5	0.55	[102]
0.10% C Mild Steel	376	283	198	0.3	0.75	[[103]
0.13% C Carbon Steel	347	289	179	0.75	0.4	[88]

A Haigh diagram is plotted for each data set and comparisons between Goodman, Soderberg, Geber, Bagci, Clemson, Kowfie SWT and Walker's approaches are shown in Figure 3.9 to Figure 3.12.

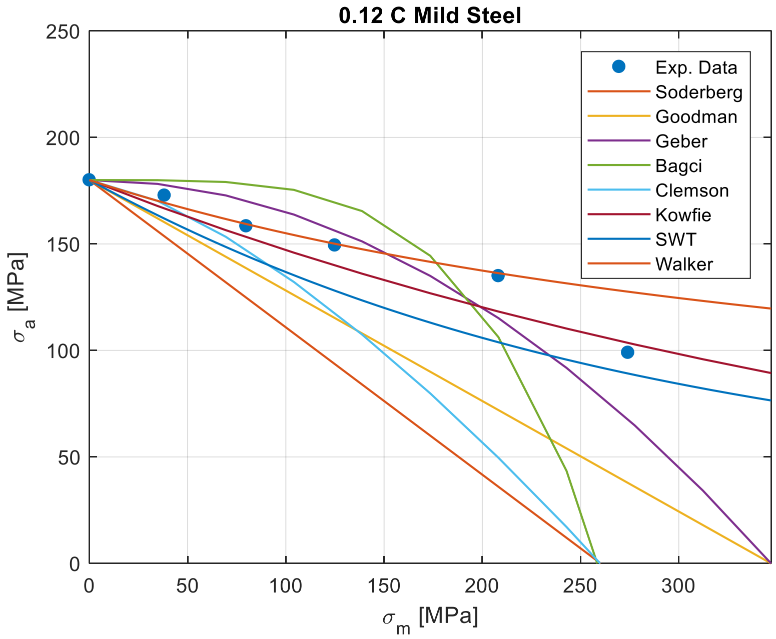

Figure 3.9: Haigh diagram of 0.12C Mild Steel. *Comparison of mean stress approaches.*

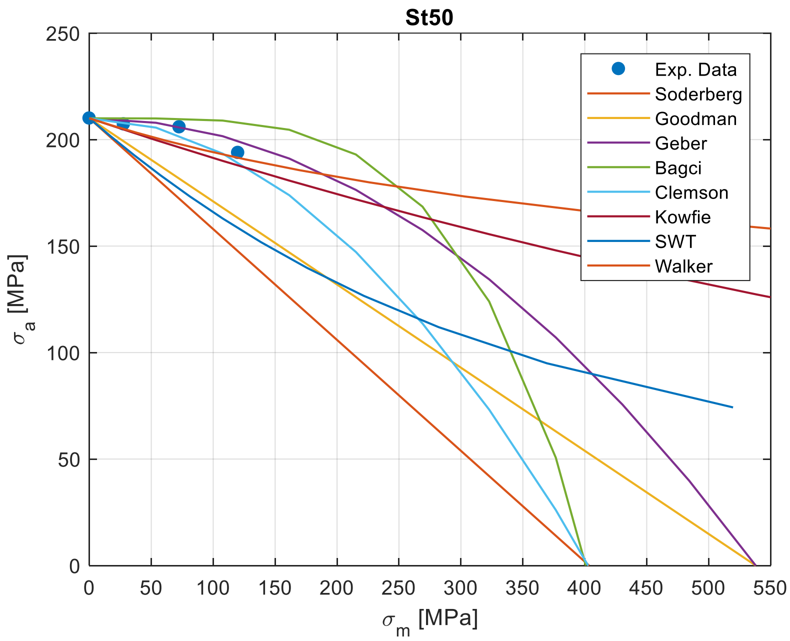

Figure 3.10: Haigh diagram of St50. *Comparison of mean stress approaches.*

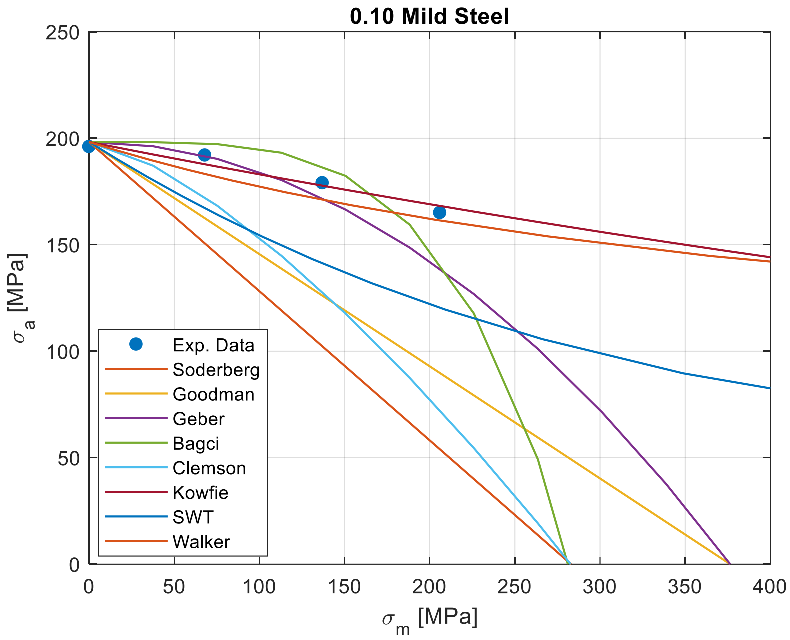

Figure 3.11: Haigh diagram of 0.10%C Mild Steel. *Comparison of mean stress approaches.*

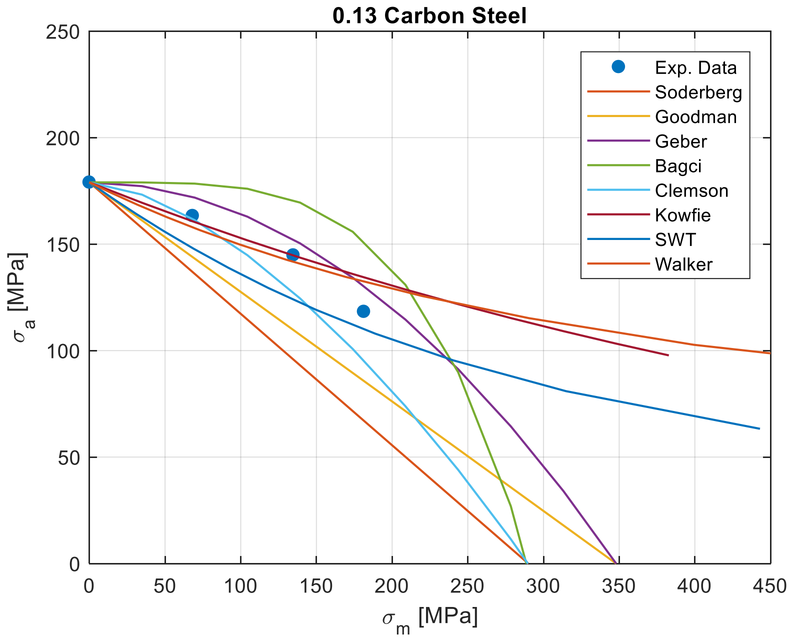

Figure 3.12: Haigh diagram of 0.13%C Steel. *Comparison of mean stress approaches.*

For the four data sets, the Bagci approach underestimates the effect of mean stress at relatively low values of stress ratio, (R<0) and doesn't properly represent the behaviour for higher stress ratios. It appears to be not a safe solution for predicting the mean stress effect. Conversely, Soderberg and Goodman approaches are always too conservative. Clemson's approach also tends to be too conservative for high stress ratios, and in some case, also for low values. The Geber parabola predicts the mean stress effect reasonably well but may err on the unsafe side at low values of stress ratio. The best approach without adjustable parameters, which shows a conservative prediction, is the SWT equation. Kowfie and Walker approaches, which depend on an experimentally determined parameter, show superior agreement with experimental results compared to the other approaches. In both cases, based on the experimental data sets, it seems that these two models underestimate the effect of mean stress at high value of stress ratio. Although the two approaches are based on different relationship, the identified allowable areas are similar, making no tangible difference between the two.

Based on the proposed data sets, a comparison of the Walker approach employing Dowling estimation of the parameter γ (3.11) and employing experimental data to extrapolate the value of the parameter γ is made. Graphical representations of the two equations obtained for each set of data are shown in Figure 3.13 - Figure 3.16.

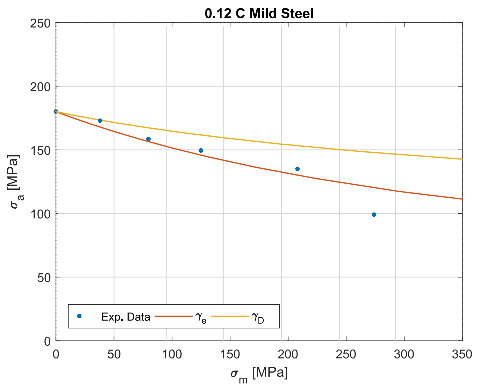

Figure 3.13: Haigh diagram of 0.12C Mild Steel. *Walker and Dowling comparison.*

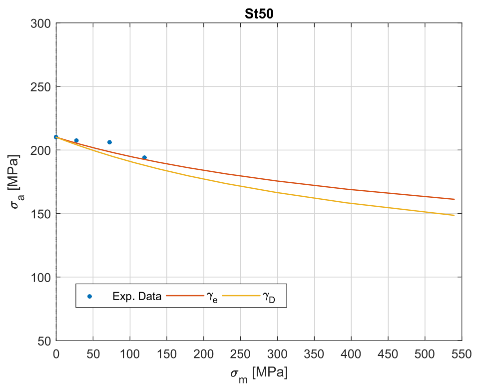

Figure 3.14: Haigh diagram of St50. *Walker and Dowling comparison.*

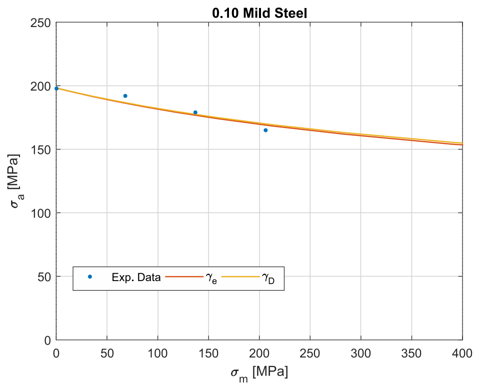

Figure 3.15: Haigh diagram of 0.10 Mild Steel. *Walker and Dowling comparison.*

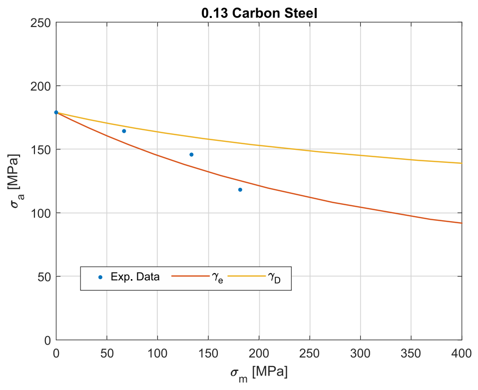

Figure 3.16: Haigh diagram of 0.13 Carbon Steel. *Walker and Dowling comparison.*

In the case of 0.10%C Carbon steel, Figure 3.15, the prediction obtained through Dowling's estimate agrees with the best fit extrapolation and in the other cases, the prediction through Dowling's relationship is also similar to the values obtained through the experimental data. However, all the curves obtained with Dowling prediction, Figure 3.13, Figure 3.14, and Figure 3.16, lie on the unsafe side of the best fits, predicting a lower effect of mean stress. Therefore, in the absence of experimental data, although Walker's approach is the one that best predicts the effect of mean stress, it would be safer to opt for a different solution rather than employing Dowling's prediction to evaluate the parameter γ.

A comparison between the FKM mean-stress sensitivity factor approach and the Walker equation is proposed, using the same experimental datasets and material information. Figure 3.17 to Figure 3.20 show the allowable amplitude stress obtained from the two approaches plotted in the Haigh diagrams.

To obtain the allowable stress amplitude according to the FKM approach, the procedure summarised in Section 2.2.1 is used. The FKM Guideline [12] also includes an assessment on how to obtain the fatigue limit of materials in the fully reversed condition. However here this value is taken directly from the experimental data set, for each of the evaluated materials. The mean stress sensitivity factor, which the FKM diagram is based on, is a linear function of the ultimate strength of the material (2.16) the higher the ultimate strength, the steeper the slope of the curve. In other words, materials with higher strength are more sensitive to the mean stress, which implies that the reduction of fatigue strength, because of the mean stress, is higher. This behaviour is shown in Figure 3.17 and Figure 3.20, for the 0.12%C mild steel and for the 0.13%C carbon steel, whose ultimate strengths are below 350MPa. In these cases, the difference between the fatigue strength at R=-1 and at R=0 is only a few units, whereas there is a more pronounced difference in the case of St50 steel Figure 3.18.

Based on experimental data sets, the FKM approach underestimate the effect of mean stress in Field II of the Haigh diagram for those materials which show a low ultimate strength. In Field III the slope proposed by the FKM approach becomes one-third of that in Field II. The comparison with experimental results suggests that in this region the FKM approach is inappropriate for these materials: the allowable area is largely overestimated. Field IV, which is defined by values of stress ratio higher than 0.5, is characterised by a constant value of allowable stress, represented by a line parallel to x-axis. For low strength steels, such as those included in the data sets, it is not feasible to define the allowable stress amplitude in this field because the stress amplitude would be higher than the ultimate strength.

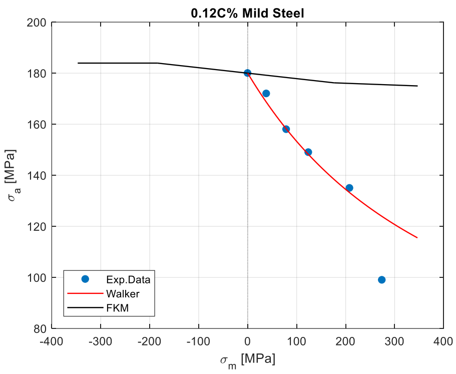

Figure 3.17: FKM and Walker Haigh diagram, 0.12 Mild Steel.

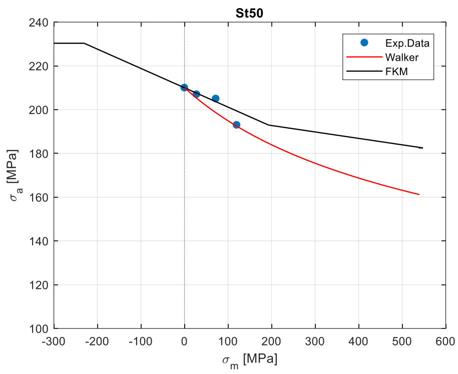

Figure 3.18: FKM and Walker Haigh diagram, St50.

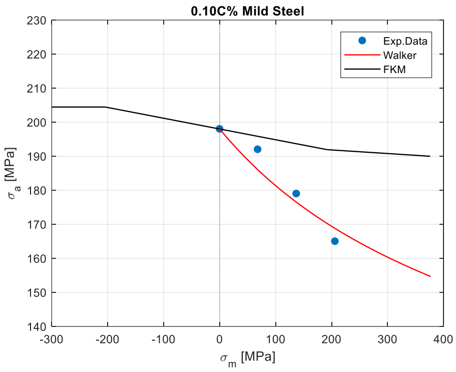

Figure 3.19: FKM and Walker Haigh diagram, 0.10 Mild Steel.

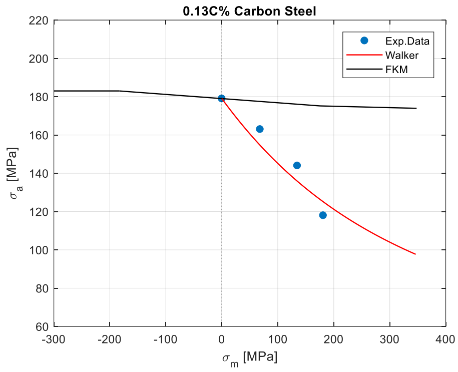

Figure 3.20: FKM and Walker Haigh diagram, 0.13 Carbon Steel.

Overall, the comparisons between the FKM and Walker approaches show that Walker exhibits a better correlation with experimental data.

The representation of allowable stress amplitude as a function of mean stress using a Haigh diagram is the most common practice employed in research and to design components in industry. Based on the review presented here, many approaches on how to define the allowable stress have been developed and experimental data support some of these. However, all the approaches have been verified using experimental data obtained in air. To define the allowable stress amplitude for components working in corrosive environments, further investigation is required or other methods should be considered.

3.4 Conclusion

The problem of corrosion fatigue was reviewed, highlighting the mechanisms which characterise corrosion fatigue behaviour and the main parameters which affect the corrosion fatigue strength of material.

Based on available experimental data, it is clear that corrosive environments have a fundamental effect on the fatigue strength of structural materials: fatigue strength decreases compared to the behaviour in air and this effect is more pronounced at elevated numbers of cycles. Although numerous research works available in the literature describe the mechanism of corrosion pits and propagation of pits and cracks, more experimental data are required to understand the level of decrease of corrosion fatigue strength. There are no general rules to predict the S-N curves in corrosive environment as a function of material properties or fatigue behaviour in air and in general, the corrosion mechanisms are usually studied from a chemistry prospective and for their influence on a microscopic level but no measurements applicable to the corrosion fatigue design are provided. Moreover, it was shown that corrosion fatigue strength is susceptible to the nature of the corrosive environment and testing conditions.

A review of the various approaches available to determine the reduction in fatigue strength caused by the presence of mean stress, has been presented. Experimental data on fatigue behaviour in air for four different structural steels are used to compare the effectiveness of the mean stress approaches. Among the available models, the Walker approach provides a superior match with experimental data. However, this approach requires a set of experimental data to be defined, as it is dependent on an empirical parameter.

To gain a better understanding of corrosion fatigue behaviour of low carbon steel S355J2 in freshwater environments, to be applied to GEHO pump design, an experimental investigation, which simulates the real condition at which Fluid End components are commonly working, is required. Experimental investigation should include corrosion fatigue tests at various stress ratio conditions to be compared with available approaches.

Chapter 4

Experimental Investigation of Fatigue and Corrosion Fatigue of S355

4.1 Introduction

The motivation for an experimental investigation to evaluate the effect of corrosive environment on the fatigue behaviour of low carbon steel S355J2, used for Fluid End components in GEHO pumps, and to establish the effect of mean stress in design is highlighted in Chapter 2 and Chapter 3. In this Chapter, the characterisation of the material, experimental programme and experimental procedure used throughout the project are presented and discussed.

Fatigue testing procedures and description of test equipment capability are important aspects in ensuring the proper performance of fatigue and corrosion fatigue tests and the analysis of experimental results. For uniaxial fatigue tests in air, Standards [104, 105] have been developed to ensure that experimental results are not affected by the way the tests are performed or samples manufactured. In aggressive environments, more parameters can influence the fatigue test results, such as test frequency, solution composition, and type of corrosion [106, 107]. Standards [108-110] usually suggest setting these parameters as close as possible to the real application conditions. Specimen characteristics, test equipment, and test conditions are discussed here to highlight the main parameters that influence the experimental results. A corrosion testing method is developed and implemented to investigate the effect of exposure to an aggressive environment on unloaded low carbon steel and an analysis programme performed. This includes measurements of surface roughness and pits depth of the corroded surface of samples through the use of a 3D surface measurement system.

4.2 Characterisation of Material

The material investigated is a low carbon forged steel, grade S355J2G3+N. Specimens were obtained from a single 610 mm diameter and 1600 mm length of material. The chemical composition of the block was provided by the supplier and details are reported in Table 4.1. Initially, twelve transverse slices were cut out from the bar to produce specimens for the initial phase of the experimental investigation, shared within the APESA Project. The remaining part of the block was used to produce industrial scale specimens for testing in the Weir Mineral dynamic pump test rig in The Netherlands, as described in Chapter 6. Twenty rectangular blanks were extracted from each transverse slice, using a water jet cutter. The core of the block, equal to a third of the diameter, was not used in manufacturing samples as the mechanical properties of this part are less affected by the forging process the block was subjected to. Dimensions of the initial block and cutting plans, for the slices and blanks, are shown in Figure 4.1.

Table 4.1: Chemical composition of the investigated material.

C	Mn	Si	P	S	Cr	Ni	Mo	Al
0.2	1.32	0.34	0.009	0.002	0.01	0.03	0.01	0.042

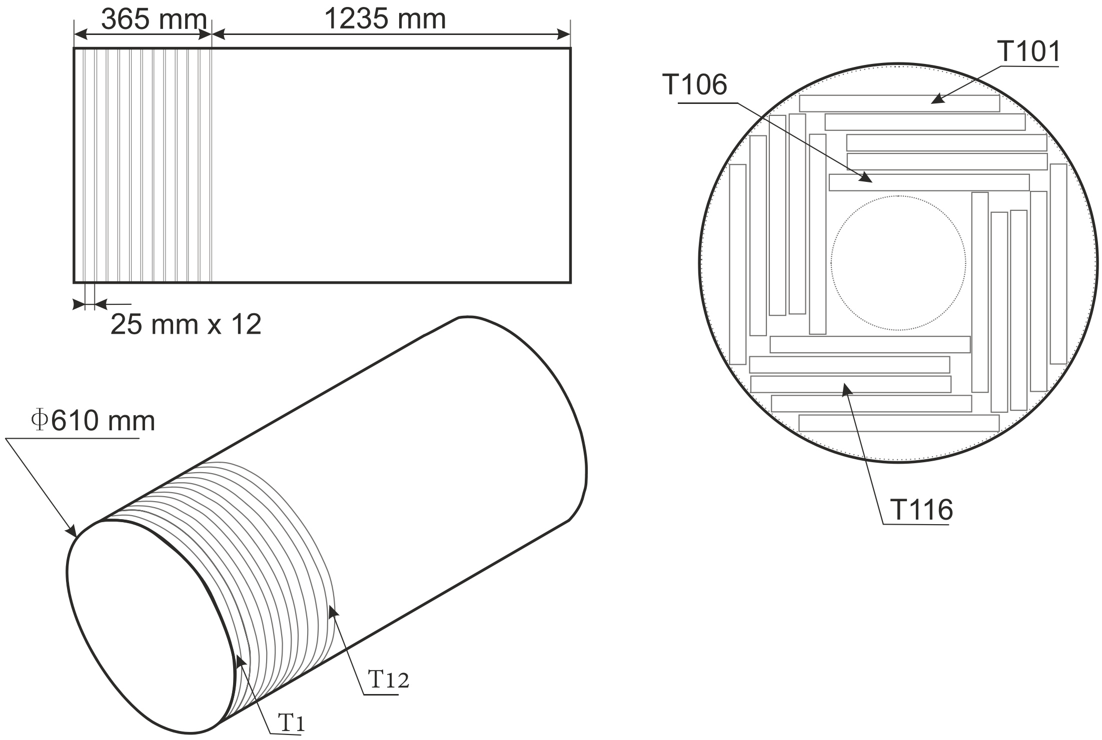

Figure 4.1: Shape, dimensions, and cutting plan of S355J2 block.

4.2.1 Tensile Testing

To verify mechanical properties of low carbon steel S355J2, tensile tests were conducted, using a 250 kN Instron machine under displacement control at a rate of 1mm/min. The specimen geometry, manufactured according to E8/E8M-16a Standard [111], is shown in Figure 4.2. Three tensile tests were performed using specimens from different locations in the slice, as shown in Figure 4.1, to evaluate possible differences in behaviour caused by the local characteristics of the material.

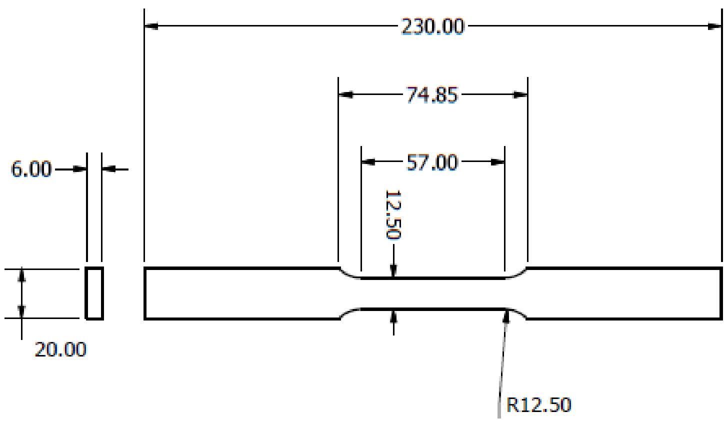

Figure 4.2: Specimen dimensions for tensile tests. *Dimensions are expressed in mm.*

The three stress-strain curves, obtained from the tensile testing, are plotted in Figure 4.3.

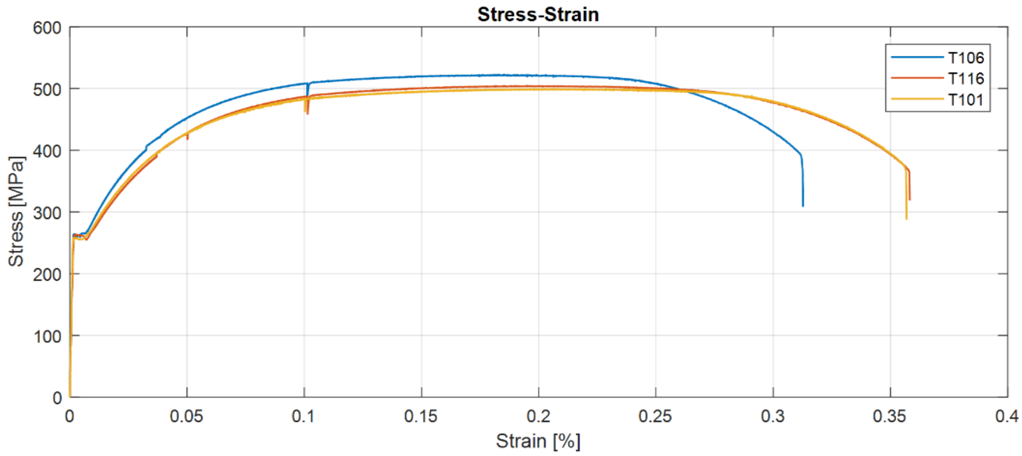

Figure 4.3: Stress-Strain curve of S355J2. *Data obtained from tensile tests on S355J2 specimens.*

The mechanical properties obtained from each test are summarised in Table 4.2.

Table 4.2: Mechanical properties of S355J2. *Data from tensile tests on S355J2 specimens.*

	Young's Modulus	Yield Stress	Ultimate Stress	Elongation
T101*	198 GPa	258 MPa	500MPa	35.7%
T106	187 GPa	262 MPa	522.7 MPa	32%
T116*	172 GPa	261 MPa	504.6 MPa	35.9%

*Test run by Okorokov [112]

The results show a good agreement between the three tests and the material certificate issued by the supplier. Differences in results are within the expected scatter [113] and the location in the slice, from which samples are extracted, is not considered an influencing parameter in the programme. Values obtained for specimen T101, that show the lowest yield and ultimate tensile stress, are chosen as reference values.

4.3 Fatigue Testing in Air

Investigation of the fatigue behaviour of S355J2 in air was performed for two reasons: using in air S-N curves as a reference to understand the effects of corrosive environments on fatigue strength and for evaluating the effect of mean stress on fatigue in air.

Among the models available to predict the effect of mean stress on fatigue strength at a fixed number of cycles, discussed in Chapter 3, the one that better correlates available experimental data of similar low carbon steel is Walker's model prediction. This model is a function of a material constant, which is estimated on the basis of test data. A minimum of two families of S-N curves are required to apply this methodology.

Low carbon steel S355 is a non-alloy European Standard (EN10025) structural steel, widely used in the construction, manufacturing and offshore industries. Depending on the sub-grade associated with the S355 category, the toughness of the material and, consequently, the fatigue behaviour is different [114]. Little information on the fatigue behaviour of the sub-grade of S355 investigated is available in the literature. The n-Code DesignLife fatigue code, incorporated in the ANSYS Workbench environment, includes the S355J2G3 grade in the Materials Manager library. Table 4.3 summarises the mechanical properties and fatigue in air information available in n-Code DesignLife, which is based on the FKM Guideline [5].

Table 4.3: Mechanical properties and fatigue information of S355J2G3 from n-Code [12].

Yield Strength	355 MPa
Ultimate Tensile Strength	510 MP)
Elastic Modulus	2E5 MPa
Stress Range Intercept	7290.51 MPa
First fatigue Strength Exponent	-0.2
Fatigue Transition Point	1E6 cycles
R-ratio of Test	-1

From this information, the fatigue strength range at 10^6 cycles, the fatigue limit in air according to the n-Code DesignLife, can be calculated using the power-law relation between the coordinate of intercept with the y-axes and the transition point (4.1):

$$\frac{N_2}{N_1} = \left(\frac{S_2}{S_1}\right)^b \tag{4.1}$$

Figure 4.4 shows the extrapolated stress-life curve. The ordinate axis represents the stress range, such that when the stress ratio is R=-1, the stress amplitude is half of the stress range.

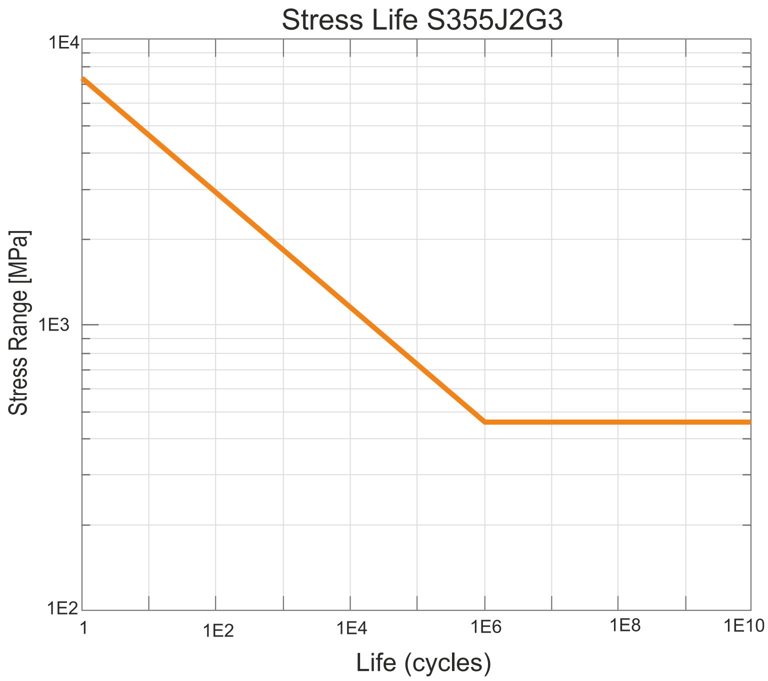

Figure 4.4: S-N curve in air at R=-1 obtained from data of n-Code.

It is not possible to estimate the material parameter required in the Walker equation from this information, as no information about behaviour at different stress ratio conditions is available in n-Code DesignLife. Therefore, an experimental program including positive mean stress was designed to determine the fatigue behaviour in air of S355J2.

4.3.1 Specimen Manufacture

Specimens with tangentially blending fillets between the test section and the ends were selected for uniaxial fatigue tests according to ASTM E466-07 [104]. A requirement on the surface roughness, of 0.2 µm maximum value, is imposed by the Standard. Longitudinal surface polishing was applied in the central part of the specimens to obtain a maximum roughness of 0.2 µm. The dimensions and geometry of the specimens are shown in Figure 4.5

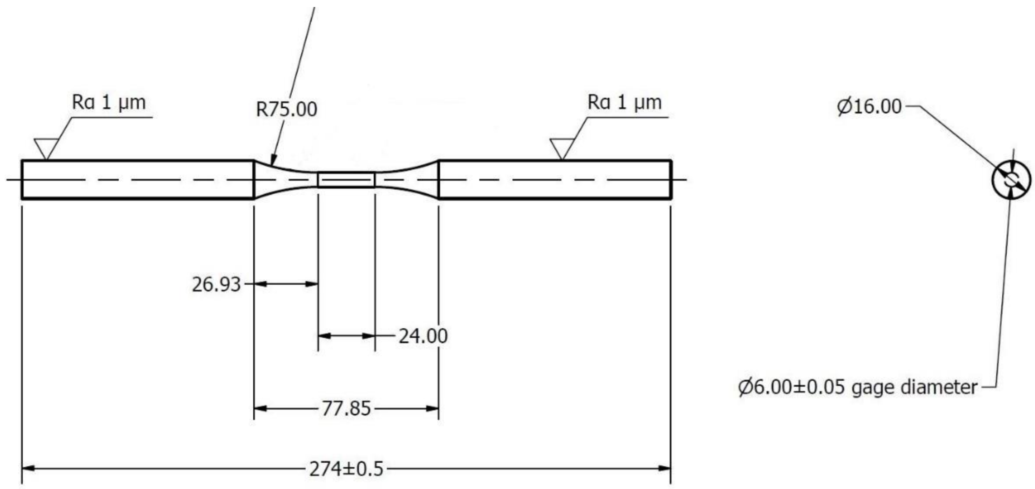

Figure 4.5: Specimen dimensions for uniaxial fatigue testing. *Dimensions are in mm if not differently specified.*

To allow proper calculation of load to be applied in order to achieve the required stress during fatigue testing, the central diameter of each specimen was measured using a Digital Micrometer with accuracy ±0.002 mm. The average of three central diameter measurements was obtained for each sample and utilized as a reference for the calculation of stress. The minimum and maximum values of diameter measured among the family of samples, reported in Table 4.4, show that the required tolerance was met. The exact value of each diameter was then considered for each test to calculate the force to be applied.

Table 4.4: Minimum and maximum values of the measured specimen diameters.

ϕ_{min}	5.962 mm
ϕ_{max}	6.023 mm

4.3.2 Roughness Measurements

A Mitutoyo Surftest SV-2000 machine was used to measure values of the arithmetic mean roughness R_a of virgin specimens after the manufacturing. A specimen assembled on the measuring equipment is shown in Figure 4.6. Readings were obtained across sixteen 0.8 mm segments in the test section, which is the central region of the specimen, at angles of 0º, 90º, 180º and 270º around the centre. An example of R_a profile across 8 segments is shown in Figure 4.7. Fixed speed measurement of 0.5

mm/s was used. The final value of roughness, associated with each specimen, is the arithmetic mean obtained from the four measurements at every 90º.

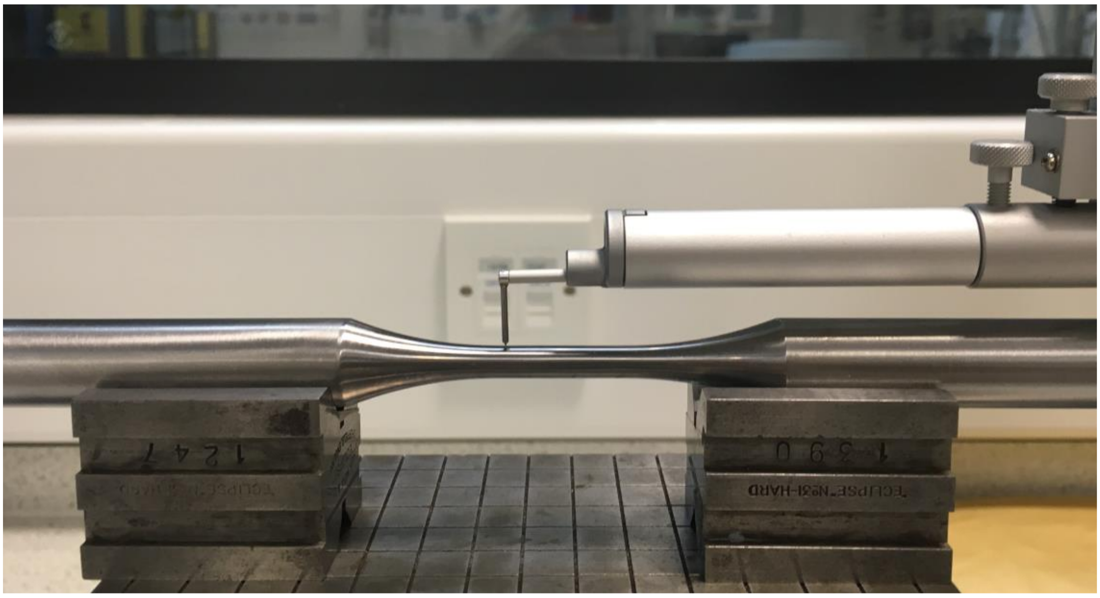

Figure 4.6: Surface roughness measurements of tangentially bending fillets fatigue specimen. *Measurements obtained with Mitutoyo Surftest SV-2000.*

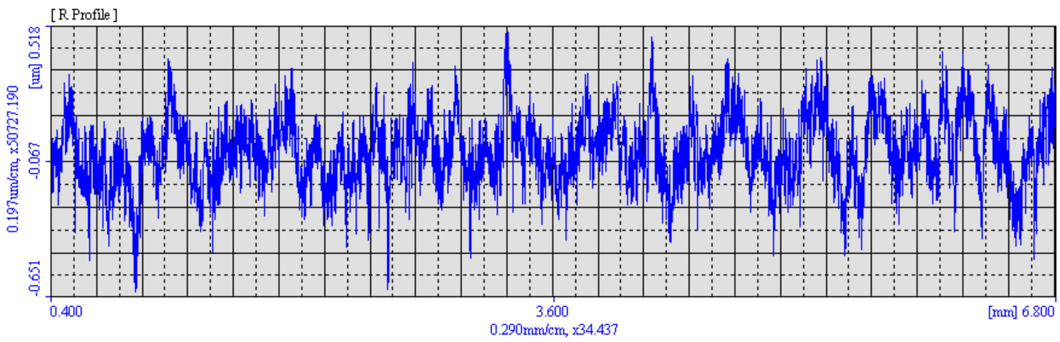

Figure 4.7: Roughness profile of S355J2 specimen after manufacture. *Measurement obtained on 6.4 mm length path.*

The histogram in Figure 4.8 shows R_a values for the fifty-four manufactured samples, used for fatigue tests in air and corrosive environment. The values of surface roughness are between 0.09 to 0.16 µm. One specimen was discarded as the arithmetic mean roughness was higher than 0.2 µm.

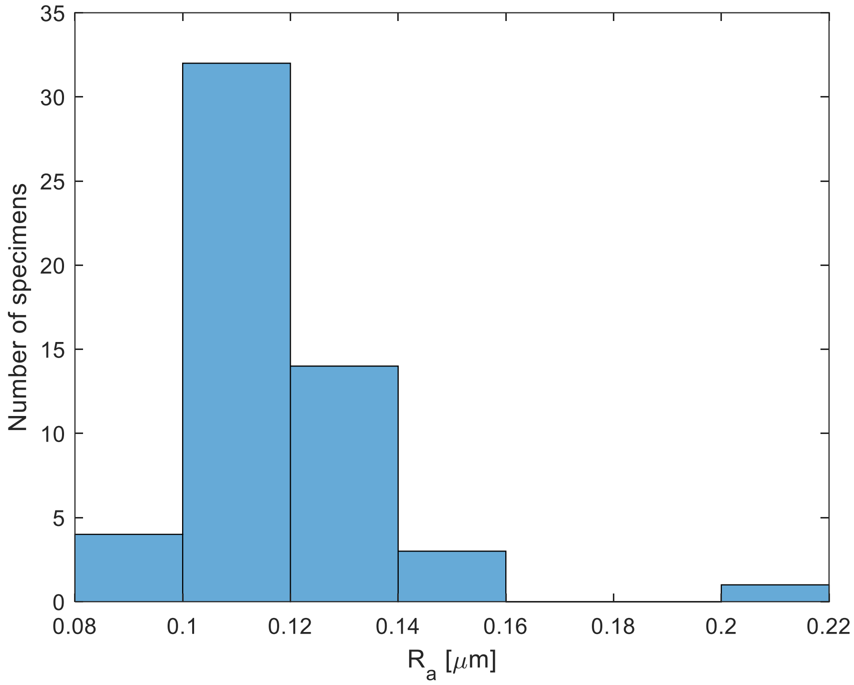

Figure 4.8: Values of measured arithmetic mean roughness of axial fatigue specimens.

4.3.3 Equipment Setup and Loading Conditions for Testing

Fatigue tests in air were performed using servo-hydraulic Instron 8801 100kN and Instron 8802 250kN tensile test machines. Tests were carried out under axial loading and under load control at 15 Hz. In Figure 4.9 the installation of a uniaxial sample for a fatigue test on Instron 8802 is shown.

Figure 4.9: Installation of specimen on the Instron 8802 testing machine for the fatigue test in air.

Instron Wave Matrix™ software was used to define test conditions. Two load steps were chosen for fatigue tests in air: the first step reproduces a linear increase (or decrease) of the applied load and the second step is a cyclic variation of the applied load. The first load step is applied to pass from the condition in which the specimen is fixed to the machine to the initial condition of the fatigue test, which is the mean load F_m. Two inputs are required for this step: the value of load to be achieved, the mean load F_m, and the duration of the step, the time to achieve this load condition. For all of the tests, the duration of the first step Δt was selected as 10 seconds. A sinusoidal distribution was selected to fatigue the specimen in the second step load. The inputs to define the distribution are the mean load F_m, which is equal to the value chosen for the first step, the amplitude load F_a, the frequency in Hz and the total duration of this step, in terms of fatigue cycles. For all tests in air, 6 million cycles were selected as the maximum duration for the second step. If the specimen didn't fail within these cycles, it was taken off the test rig and recorded as a run-out.

The relation between amplitude and mean load depends on the stress ratio R. Two values of stress ratio were evaluated for fatigue tests in air:

- Fully reversed loading, R=-1;
- Positive mean load with minimum load always equal to zero, R=0.

The applied load amplitude $F_{a,appl}$ and the mean load $F_{m,appl}$ were calculated for each specimen using the equations (4.2) and (4.3), taking into account the diameter of each specimen and the required test stress in the central region of the specimen. In both equations, r represents the radius of the specimen, which value came from the measurement of the central diameter for each test.

$$\sigma_{a,test} = \frac{F_{a,appl}}{\pi r^2} \tag{4.2}$$

$$\sigma_{m,test} = \frac{F_{m,appl}}{\pi r^2} \tag{4.3}$$

To obtain fatigue failure between 10^5 cycles up to the fatigue limit, amplitude test stresses were estimated based on mechanical properties and FKM information. Characteristics of stresses, fatigue cycles and outcomes for stress ratio R=-1 and R=0 are reported in Table 4.5 and Table 4.6 respectively.

Table 4.5: Conditions of fatigue tests in air at fixed stress ratio R=-1.

Sample	*Amplitude Stress (MPa)*	*%* σ_y	*Mean Stress (MPa)*	*Cycles*	*Results*
T109	232.2	90	0	$2.49\ 10^5$	Failed
T224	232.2	90	0	$3.57\ 10^5$	Failed
T105	219.3	85	0	$1.75\ 10^6$	Failed
T112	219.3	85	0	$1.37\ 10^6$	Failed
T204	214.1	83	0	$2.04\ 10^6$	Failed
T520	214.1	83	0	$1.63\ 10^6$	Failed
T403	209	81	0	$6.00\ 10^6$	Intact

Table 4.6: Conditions of fatigue tests in air at fixed stress ratio R=0.

Sample	*Amplitude Stress (MPa)*	*%* σ_y	*Mean Stress (MPa)*	*Cycles*	*Results*
T122	196.3	76	196.3	$2.55\ 10^5$	Failed
T518	196.3	76	196.3	$3.70\ 10^5$	Failed
T203	188.2	73	188.2	$8.31\ 10^5$	Failed
T402	188.2	73	188.2	$7.00\ 10^5$	Failed
T612	188.2	73	188.2	$6.04\ 10^5$	Failed
T103	188.2	73	188.2	$4.36\ 10^5$	Failed
T316	184.8	71.5	184.8	$8.19\ 10^5$	Failed
T151	184.8	71.5	184.8	$5.37\ 10^5$	Failed
T514	180	69.7	180	$8.72\ 10^5$	Failed
T409	180	69.7	180	$6.00\ 10^6$	Intact
T117	174.5	67.5	174.5	$6.00\ 10^6$	Intact

4.4 Corrosion Testing

The degradation effect of corrosion on fatigue strength, by accelerating both the crack initiation and crack propagation, was considered in Chapter 3. Crack initiation mechanisms are usually studied in connection to pitting corrosion. The development of a pit, the appearance on the surface of small localized material damage from the characteristic morphology, can occur both in metals characterised by an active electrochemical behaviour, such as ferrous alloys, and in metals characterised by a passive electrochemical behaviour, such as stainless steels and aluminium alloys. Usually, pitting corrosion is regarded as a corrosion mechanism that occurs in materials that show a protected stubborn oxide film in environments that contain an aggressive species, such as chlorides. This type of corrosion is an extremely localised phenomenon that triggers when the passivating layer is broken as a result of the electrochemical mechanism. In contrast, materials that show an active electrochemical behaviour when subject to aggressive environment, such as carbon steels, don't form a passivating oxide film but they give origin to insoluble corrosive products, such as rust, that, once deposit on the material, form a spongy and not very compact film, which is unsuitable to prevent the anodic process. In these metals, general corrosion on the surface in contact with the environment occurs, which causes general surface degradation and material loss. In these cases, the development of pits occurs together with the general degradation, but it is not a localised phenomenon, in the sense that it is not occurring only where the passivating layer is broken, and therefore it is important to be distinguished from the typical corrosion pitting behaviour.

In the literature, various models are available to describe the corrosion fatigue interaction by considering corrosion pits as surface cracks whose growth rates can be determined by the pitting kinematics [54, 115-119]. However, less effort has been spent on the effect of general corrosion as the cause of the crack nucleation in fatigue.

Several investigations of corrosion effects in low carbon steel have been conducted in the last few decades because of the increasing utilization of this family of steel on offshore wind energy power plants. However, the corrosive environment investigated is the marine environment or the artificial marine environment [120], typical for these applications. Corrosion mechanisms on low carbon steel are usually studied from a chemistry perspective, highlighting its effect at a microscopic level. Correlation with parameters relevant to fatigue design is not provided by these investigations. The analysis of corrosion testing presented here identifies and investigates measurable parameters that can be associated with the effect of exposure to corrosive environments.

A corrosion testing procedure was developed and implemented for unloaded low carbon steel S355J2 specimens to investigate the superficial effect on carbon steel caused by the exposure to freshwater.

4.4.1 Corrosion Test Rig Equipment and Testing Conditions

Rectangular specimens of 25x25x8 mm, shown in Figure 4.10, were manufactured from the same S355J2 carbon steel used for fatigue test specimens. A small dot of silicon was applied on the surface of each specimen to protect that area from corrosion with the aim, after the exposure to the corrosive environment, to measure material loss using this non-corroded surface as a reference.

Figure 4.10: Specimens for corrosion testing.

Corrosion tests were performed by placing the specimens in a test chamber, shown in Figure 4.11, connected to an external water tank. The water in the tank was aerated by an air pump and continuously circulated through the chamber during the test.

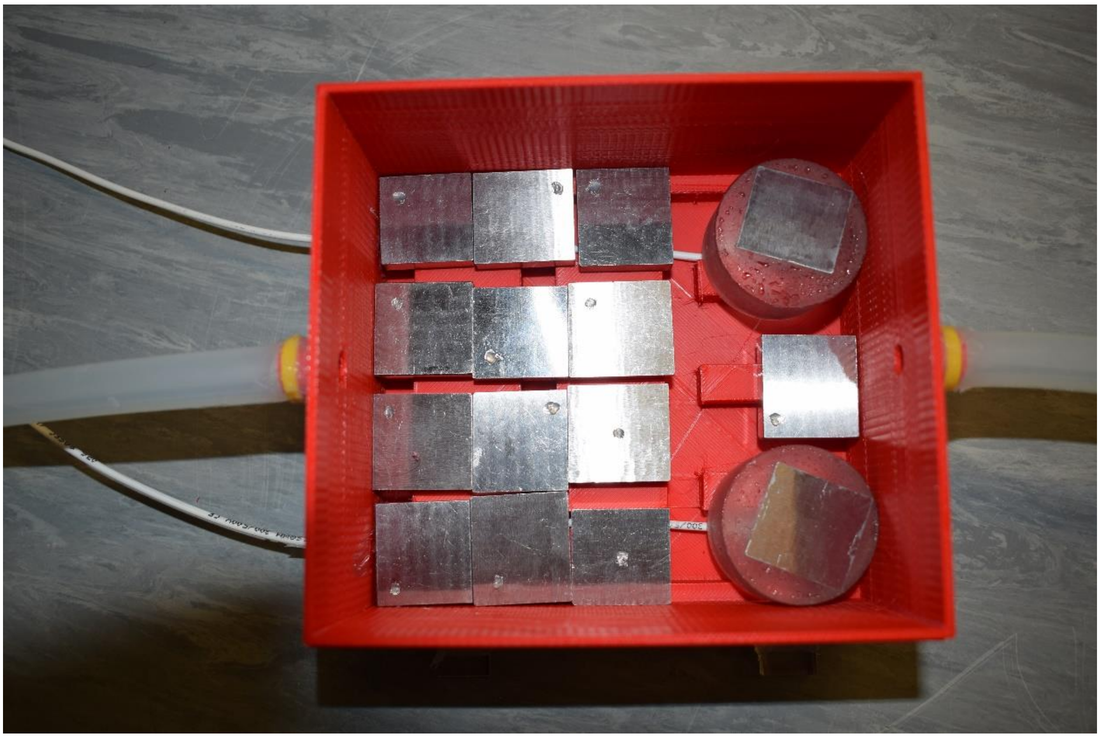

Figure 4.11: Corrosion test chamber with marked specimens.

The characteristics of the aqueous solution, reported in Table 4.7, were chosen to be representative of GEHO pump applications. GEHO pumps experience different slurry solutions, which mainly depends on the region where the pumps are installed. The characteristics of the selected solution are representative of corrosion conditions pumps are commonly subjected to. In more aggressive environments, different materials may be used in manufacturing Fluid End components or corrosion protection solutions may be applied to limit or prevent corrosion effects.

Table 4.7: Characteristics of aqueous solution used for corrosion tests.

Temperature	*ppm*	Conductivity	pH
25±1 ºC	884 NaCl	2.0 ± 0.2 mS	6.9 ± 0.1

The overall duration of corrosion testing was 40 days. To evaluate the corrosion effect and the material loss throughout the period, each specimen was held in the solution for a different time. From day 2 to 8, one specimen was removed from the testing chamber each day. Then, one specimen every two days until day 22. The last specimen was held in the flow solution until day 40. One specimen was not exposed to the freshwater environment and this served as a reference for initial roughness.

4.4.2 Surface Analysis After Corrosion

An Alicona Infinite Focus IFM G4 system was employed to analyse the surface of corroded specimens and measure the arithmetic mean roughness and the depth of corrosion damage. Alicona Infinite Focus is a three-dimensional optical measurement system that is able to scan a surface and reproduce a true 3D image. This system combines dimensional metrology and surfaces roughness measurement. It is provided with four lenses with a magnification of 5x, 20x, 50x and 100x.

Examples of surface degradations after 4, 16 and 22 days of testing are shown in Figure 4.12. After specimen removal from the test rig, corrosion products, such as rust, were present on the surface of the specimen. To allow proper visualisation of the surface and the use of the Alicona, when each specimen was removed from the corroded solution, it was cleaned using a soft hand brushes under tap water and then quickly dried using hot air flow and stored in a plastic bag with silica gel bubbles to prevent further degradation. At this stage, the silicon protection, applied to a small region of the surface, was removed.

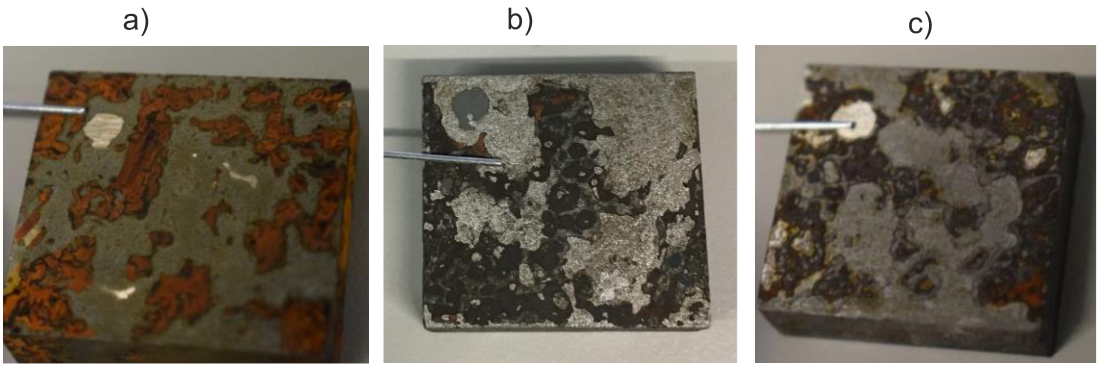

Figure 4.12: Corroded specimens. *a) after 4 days, b) after 16 days, c) after 22 days.*

To scan the surface of the specimen, an area is selected by the coordinates of 4 points. For each specimen, two areas in different regions of the surface were scanned. In at least one of the two areas, a corner of the non-corroded spot was included, to allow comparison of roughness and evaluate the material loss in terms of depth. The maximum dimensions of each scanned area are 3.2x3.2 mm, but in some cases, the scanned surface was much smaller. The scanning process is time-consuming and it was not feasible to scan the whole surface. The duration of the scan process also depends on the magnification: the higher the magnification, the longer the duration.

Based on the characteristics of the corroded specimen, it was found the most suitable magnification was 20x. This lens was selected for the analysis of all the samples.

Figure 4.13, Figure 4.14, and Figure 4.15 show examples of 2D texture for specimen corroded for 2, 7 and 16 days respectively. In all three surfaces the non-corroded portion of the area, protected by the silicon and indicated on the pictures, and the corroded portions can be seen and distinguished. Comparison between protected areas and the rest of the surface gives an indication of the surface degradation caused by corrosion and the progress of corrosive attack can be identified visually. After 2 days of corrosion, the surface exhibits degradation, with some area less rough than others. Although the surface is not yet uniformly affected, the degradation is present in most of the surface: no specific local attack can be identified. After 7 days of corrosion, the degradation appears more uniform and deeper and, except for the protected area, no part is left without corrosion effects. After 16 days the degradation has completely and uniformly affected the surface. These scans confirm the tendency of low carbon steel to being affected by general corrosion degradation when exposed to the freshwater environment.

To better qualify the degradation of surfaces, the 3D area scans and their corresponding colour maps are shown for surface corroded for 7, 18, 22 and 40 days in Figure 4.16, Figure 4.17, Figure 4.18, and Figure 4.19 respectively. Analysis of these scans shows in detail the effect of the freshwater environment on the surface of the metal. The colour map helps in the identification of morphology, the presence of pits and the general degradation. Pits appear randomly distributed over the whole surface of the specimens, as showed in Figure 4.16 and Figure 4.17. To measure the differences in height, the Alicona software automatically calculates the average height of each corroded surface as the reference from which to take the measurements. Therefore, the colour scale in each figure is not equivalent for all scans. The measure of the heights is an important parameter in the evaluation of the effect of corrosion on the material surface, as it indicates the severity of degradation. It also shows the amount of material loss, in terms of depth, for surfaces that contained a non-corroded area, as shown, for example, in Figure 4.16, Figure 4.18 and Figure 4.19. From the same examples, the range of height is increasing over time of corrosion exposure. This is in agreement with Faraday’s law, commonly utilized to estimate the material loss due to a corrosion electrochemical reaction.

Figure 4.13: The 2D texture of the specimen surface corroded for 2 days. *Non-corroded area is encircled.*

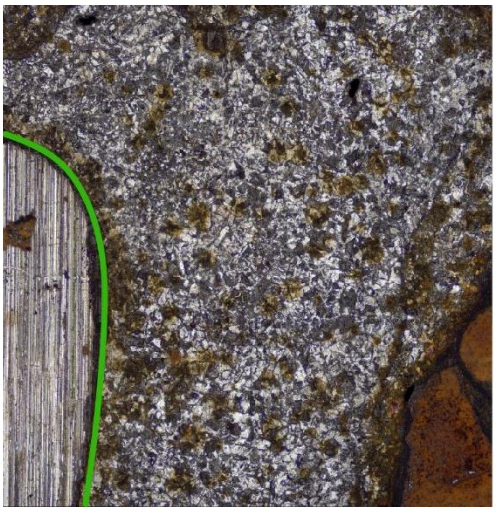

Figure 4.14: The 2D texture of the specimen surface corroded for 7 days. *Non-corroded area is encircled.*

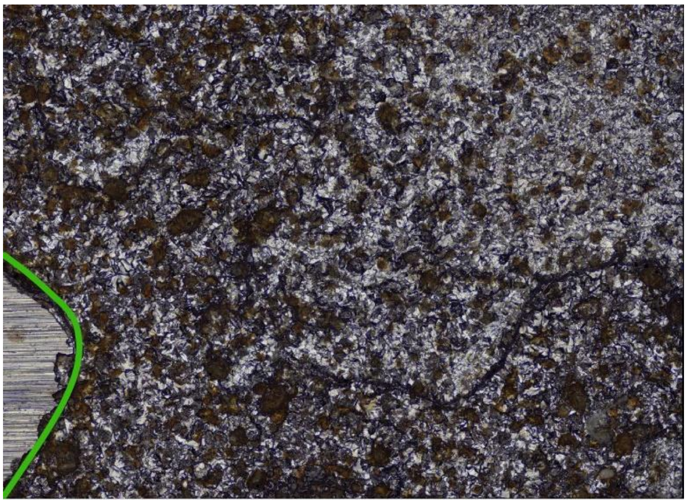

Figure 4.15: The 2D texture of the specimen surface corroded for 16 days. *Non-corroded area is encircled.*

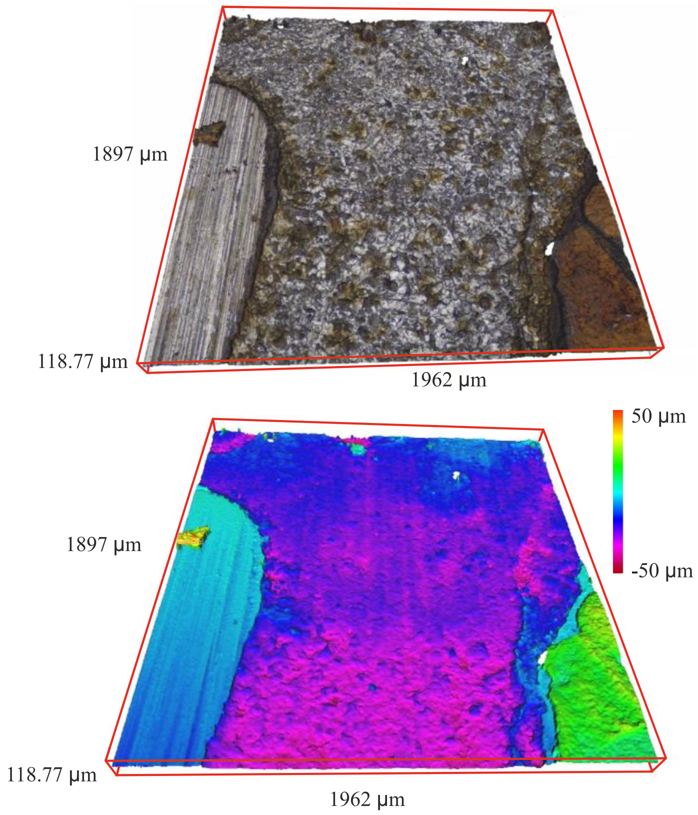

Figure 4.16: The 3D scan of 7 days corroded surface and the 3D colour map.

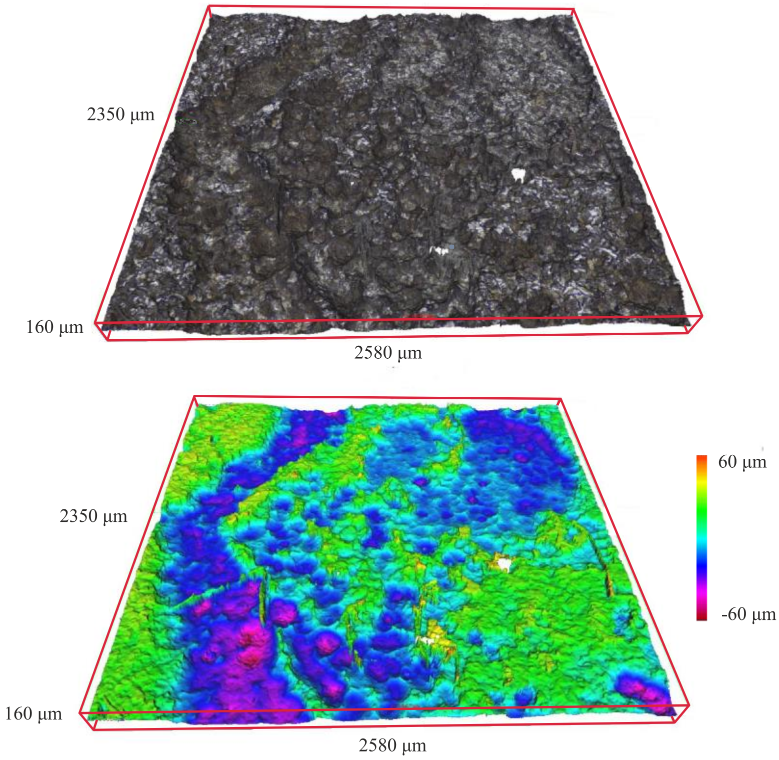

Figure 4.17: The 3D scan of 18 days corroded surface and the 3D colour map.

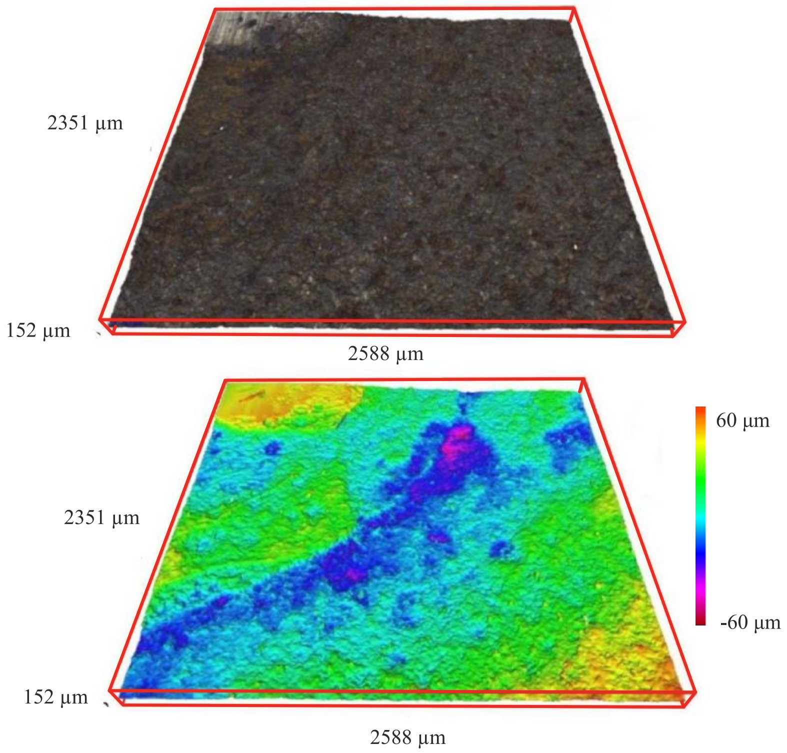

Figure 4.18: The 3D scan of 22 days corroded surface and the 3D colour map.

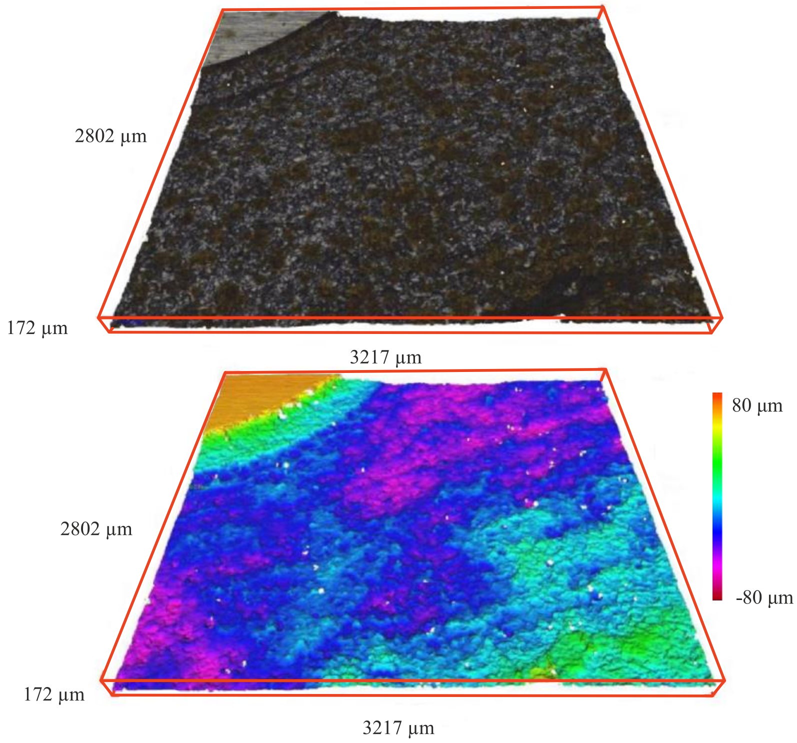

Figure 4.19: The 3D scan of 40 days corroded surface and the 3D colour map.

The Alicona software includes a tool to measure, after the scanning of surfaces, the depth profile of a selected path. This is used to analyse pit shape and depth, starting from the 2D representation of the surface. Figure 4.20 and Figure 4.21 show examples of pit profiles in a 2D graph where the depth profile is plotted against the length of the path of surfaces corroded for 12 and 16 days respectively. From this analysis, the maximum relative depth can be measured for the selected path. This dimension is an important surface parameter as it gives an indication of the stress concentration at the pit.

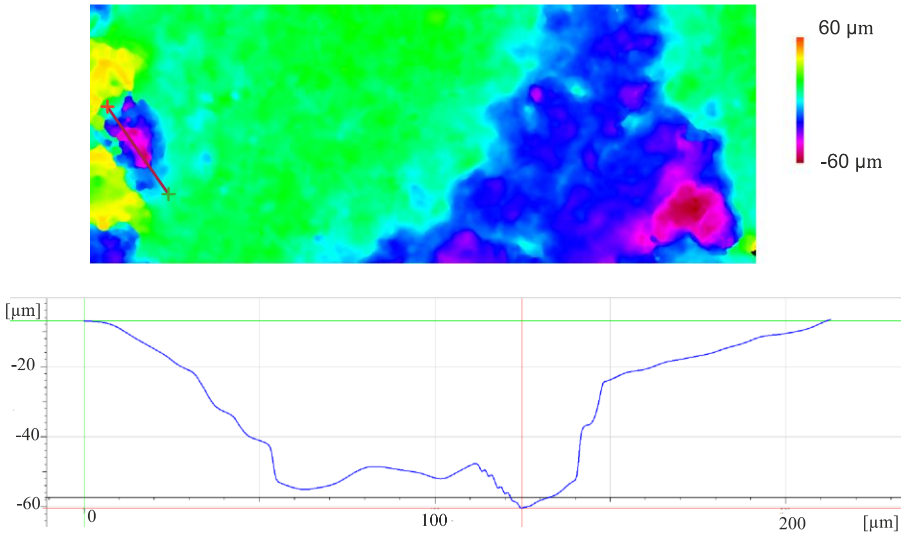

Figure 4.20: The profile of a pit on 12 days corroded specimen.

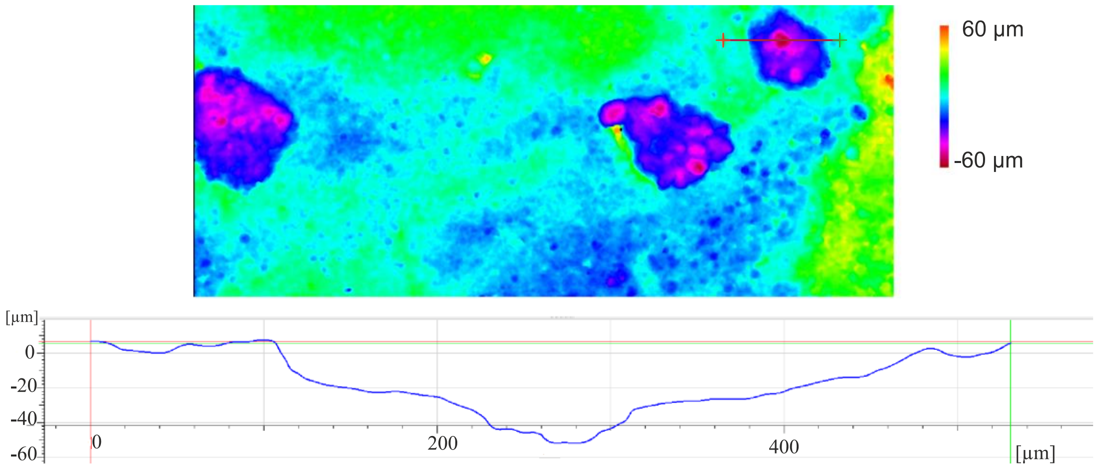

Figure 4.21: The profile of a pit on 16 days corroded specimen.

Analysis carried out on around 200 pits on all the corroded surfaces indicated that they have an irregular semi-elliptical profile. From the same analysis, corrosion pit depth was measured and the three maximum pith depths for each sample were plotted against the number of corrosion days.

The trend in results, reported in Figure 4.22, shows that the pit depth grows faster at the early stage of exposure, up to 10 days. Subsequently, the pits still grow in the depth direction but the growth rate decreases until the maximum depth becomes almost constant and independent of the exposure time. This transition can be identified after 12 to15 days of exposure.

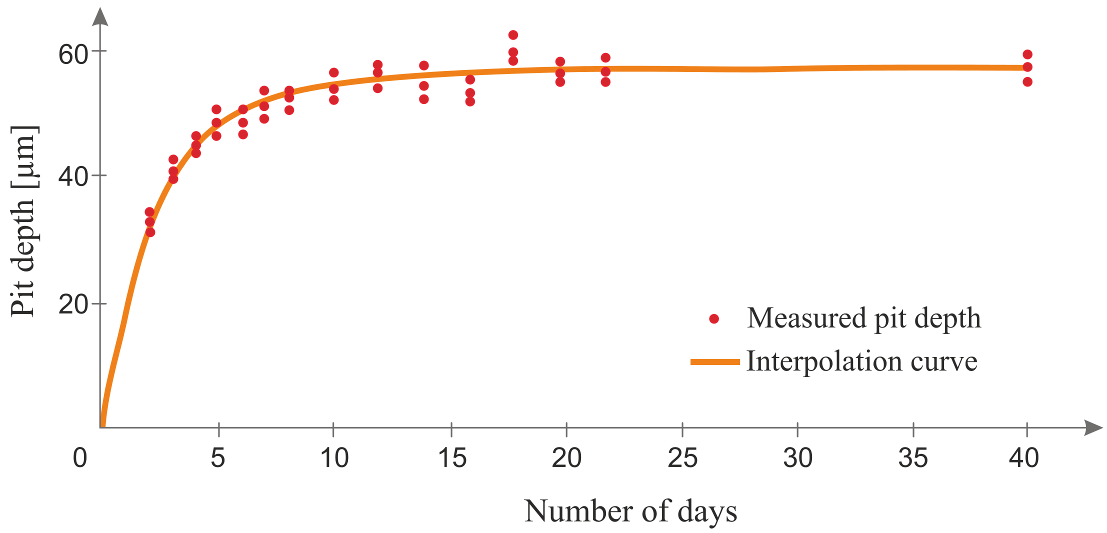

Figure 4.22: Maximum pit depth against corrosion exposure length.

A similar analysis was developed to assess the surface mean roughness of the corroded sample. The Alicona software includes a tool to automatically calculate the roughness based on the arithmetical mean deviation of the selected profile, according to the equation (4.4) and to standard BS EN ISO 4287:2000.

$$R_a = \frac{1}{n}\sum_{i=1}^{n} | z_i | \tag{4.4}$$

Figure 4.23 shows an example of surface roughness estimation of non-corroded specimens. The roughness is estimated along a path perpendicular to the machining direction, as shown. Similarly, in Figure 4.24 the surface profile of roughness is shown for a 2 day corroded surface along the highlighted path. The value of roughness measured for the non-corroded sample is 0.280 µm, whereas for sample corroded for 2 days is 1.0907 µm. After two days of immersion in aqueous solution, the surface roughness of S355J2 is already highly degraded, increasing by a factor of four.

The surface roughness of each specimen was calculated as the mean value of the measurements obtained along paths. The obtained values are plotted in a graph against the number of days of exposure to corrosion, shown in Figure 4.25. Similar to the trend of maximum pit depth, the surface roughness strongly increases at the early stage of corrosion exposure, however, after around 15 days, the value of surface roughness is almost constant at R_a=3.5 µm.

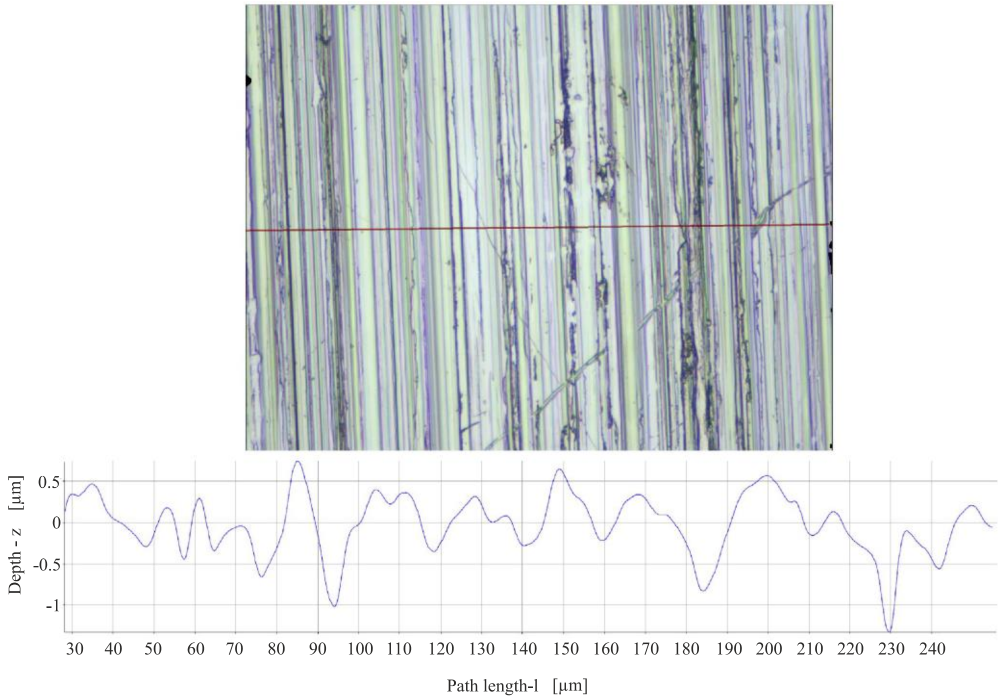

Figure 4.23:A roughness profile of non-corroded specimen.

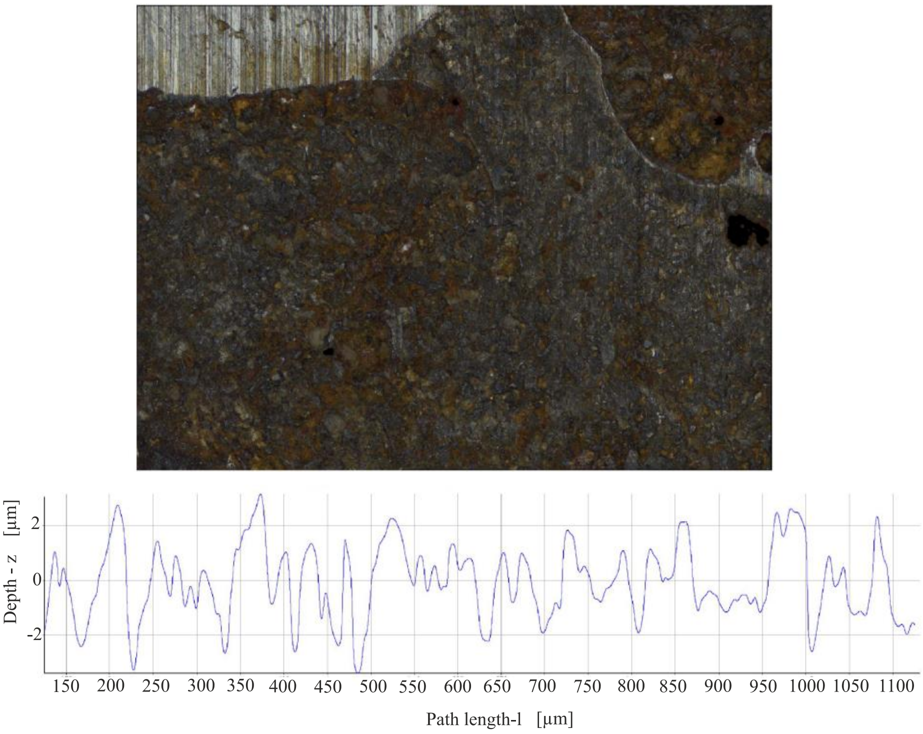

Figure 4.24: A roughness profile of 2 days corroded specimen.

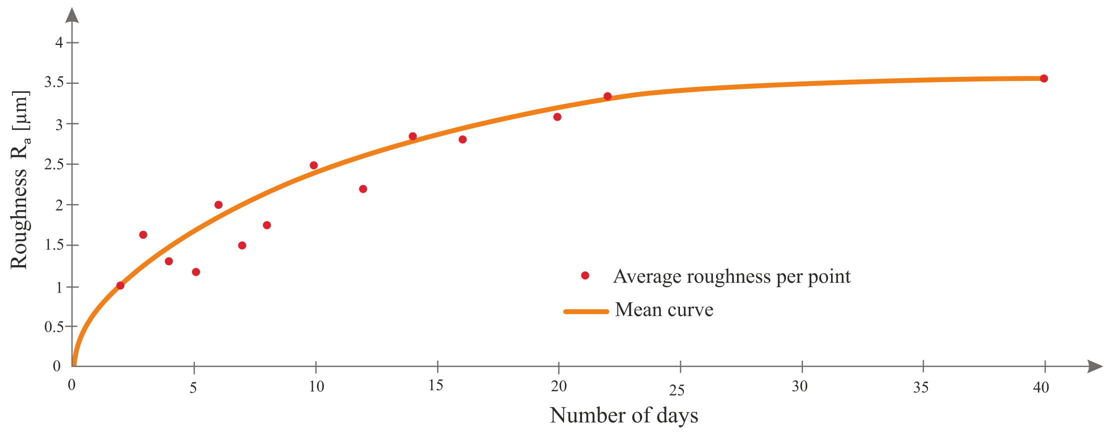

Figure 4.25: Average of the surface roughness against days of corrosion.

4.4.3 Summary

The experimental procedure developed to understand the effect of the freshwater solution on the surface of low carbon steel S355J2 shows that the material is affected by general corrosion over the whole surface. The effect of corrosion also induces the formation of pits, randomly distributed over the surface. The analysis of the maximum pit depths and the surface roughness over the duration of corrosion exposure show an asymptotic behaviour: after a consistent growth of properties during the first period of corrosion immersion, occurring in the first twelve to fifteen days, the characteristics tend to stabilise and both values remain constant for the rest of the test. This behaviour indicates that, after a certain amount of time, the characteristics of corroded surfaces become independent of the time of exposure, except for material loss, which increases with time.

4.5 Corrosion Fatigue Testing Methodology

The corrosion fatigue testing programme was designed with the aim of understanding the fatigue behaviour of S355J2 in the freshwater environment in the high and very high cycle fatigue regions and defining S-N curves to be used to evaluate the effect of the positive mean stress on fatigue strength. Therefore, uniaxial fatigue tests at different fixed stress ratios were conducted on S355J2 specimens to investigate the corrosion fatigue life. For each imposed stress ratio, at least two distinct stress amplitude values are required to obtain the minimum information required to extrapolate the fatigue behaviour of the material. The region in which information is sought is around 10^9 cycles, which is the design fatigue life of GEHO pumps. Based on the frequency at which tests are run, the test time to achieve 10^9 cycles could be particularly long. The effect of frequency on corrosion fatigue strength reviewed in Chapter 2, identified the need to run tests at the same frequency of the application for which tests are designed, to avoid any discrepancy between the real application and experimental data. Based on this conclusion, the frequency used to run uniaxial fatigue tests would be 1 Hz. However, at this frequency, a single fatigue test would last for 25 years. Therefore, as pointed out by Palin-Luc et al [70], it is practically impossible to investigate the behaviour in the region of high and very high cycles fatigue regime if a low frequency is chosen. A higher value of loading frequency should then be considered when experimental data in the high cycle fatigue region are required.

Three fatigue machines were selected for the purpose of this experimental investigation: servo-hydraulic testing system Instron 8011 and Instron 8802 of 100kN and of 250kN capacity respectively, and oil-free linear motor technology Instron EletroPuls™ E3000 with a maximum dynamic capability of ±3000N.

The servo-hydraulic machines share a cooling system, which was the main limitation in frequency for fatigue testing. From preliminary tests, it was found that the maximum frequency at which both machines are able to run simultaneously for consecutive days without losing precision in controlling the applied load is 10 Hz.

The ElectroPuls E3000 provides a high-frequency range for fatigue testing with the limitation of a maximum capability of 3000 N. According to the standard E466-15 [121], the minimum diameter of a tests section of a specimen with tangentially blended fillets between test section and ends should be 5.08 mm. Based on these limitations, the maximum nominal stress that can be produced with the maximum available load is σ_{max}=60 MPa, calculated using equation (4.2). This stress level is limited and it would not cover many combinations of mean stress conditions. Therefore, based on these limitations, two sets of tests were performed: one using servo-hydraulic testing machines, at frequency 10 Hz, and one using ElectroPuls E3000, at a higher frequency. For the first set, the region of interest is limited from 10^5 to 10^7 cycles which is, in the longer scenario, equivalent to almost 12 days of continuous testing. This set of data is aimed at the construction of S-N curves in the identified region and to the investigation of mean stress effects. The second set of data, performed at a higher frequency, is aimed to define fatigue strength of S355J2 in the freshwater solution at very high cycles.

Many studies have been developed to understand the influence of the applied load on the corrosion rate [122]. It is known that dynamic stress increases the corrosion rate of passive metallic materials, such as Al-alloys and stainless steel. However, agreement on the role of cyclic stress on pit development on low carbon steel is still a current topic of debate. Evans et al [123] demonstrated that the corrosion rate of low carbon steel increases with cyclic stress in the presence of plastic strains. However, Linder et al [124] showed that for high carbon steel under short exposure to corrosion, the pit growth rate appears independent of applied mechanical loads. Melchers [125] proposed that at high strains corrosion rate is affected by cyclic strain as the rust layer is periodically removed. However, this behaviour doesn't occur at low strain, close to or lower than the fatigue limit in air, and no direct relation between corrosion rate and applied load is found in this condition. Results obtained from the corrosion tests presented in Section 4.4 suggest that surface conditions due to corrosion exposure, such as surface roughness and depth of pits, become constant after an initial exposure period. In terms of corrosion fatigue, when the stress amplitude is below the fatigue limit in air, the development of corrosion and the connected degradation may not be being affected by the applied stress. In this scenario, the development of corrosion degradation can follow the trend obtained from the corrosion test on unloaded specimens, proposed in Section 4.4. This would mean that the initial phase of corrosion fatigue life, equivalent in length to the unsteady phase of the corrosion trend, is strongly affected by the corrosion environment as it is known that the crack initiated from a pit in the corrosion environment. Whereas, after this initial phase, it is expected the role of the applied stress would be the one more relevant and the corrosion fatigue life characterised by the crack growth stage. To evaluate this hypothesis experimentally, a further condition was included in the test investigation plan, which consists of corrosion fatigue testing on pre-corroded S355J2 specimens. This set of corrosion fatigue testing were performed using Instron 8801 and 8802 testing machines.

4.6 Corrosion Fatigue Tests at Frequency 10 Hz

All the corrosion fatigue tests run at the loading frequency 10 Hz were performed on S355J2 specimens from the same batches used for fatigue testing in air with geometry and characteristics shown in Figure 4.5. Analysis of surface roughness was included in the analysis of specimens in air, Section 4.3.2. Mean and amplitude forces were calculated for each test based on the measured diameter of the selected specimens, using equations (4.2) and (4.3). This procedure was used for all corrosion fatigue tests regardless of the frequency or the type of machine unless otherwise specified.

4.6.1 Testing Equipment

One technique that is often described in literature to achieve corrosion exposure during the application of dynamic loads consists of the dripping mechanism [70, 126]. The specimen is fatigued in air and corrosive solution drips or flows over the central area of the specimen. Usually, this technique is employed in tests that simulate a corrosion process in presence of abundant oxygen, such as the effect of rain dropping on aeronautical or railway structures or the zone of a pylon just above the surface of the sea where water splashes up. The test equipment to produce this effect usually is not complex and doesn't require any sealing. Therefore, it is often a desirable solution. However, the surface effects this technique produces are usually more aggressive and localized than complete immersion of the sample because the amount of available oxygen promotes a quicker corrosion process. Therefore, for application in which the components are fully immersed during the loading cycles, such as Fluid End components or pressured pipes, this technique is not suitable as it would simulate an excessively detrimental effect.

Another method, less popular because of its complexity, consists of complete immersion of the specimen, while the cycling loads are applied, using a corrosion chamber that fully encases the specimen. In this experimental investigation, a corrosion chamber was developed, based on a previous design of Anagnostakis [127], designed to be compatible with Instron 8801 and 8802 testing machines. The corrosion chamber consists of the following components: two half parts, manufactured using 1.75 mm Poly-Lactic Acid filaments suitable for 3D printing, two windows made using transparent Plexiglas, two 3D printed seals manufactured with Black Tango elastic material. The seals have the function of sealing the chamber and preventing leaks and also of stabilizing and connecting the specimen to the chamber. The two half parts of the chamber are assembled through a threaded connection and sealed using silicon around the border.

In this configuration, the chamber completely encloses the central part of the sample, providing corrosive solution around this central area during the fatigue test, leaving the grip sides of the specimen free of corrosion, allowing a proper grip to the testing machine. An example of the final assembly of a specimen and chamber is shown in Figure 4.26.

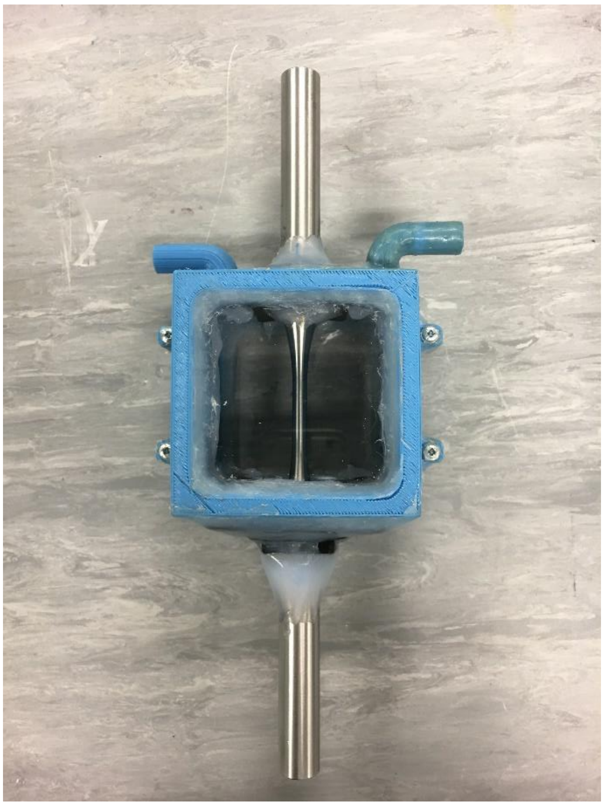

Figure 4.26: Corrosion fatigue chamber assembled to and uniaxial specimen.

On the top part of the chamber, two 7 mm diameter holes are placed, one on each side of the specimen, to allow a continuous flow of the solution through the chamber. A closed system was created using a water pump placed inside a 20 L tank, connected through plastic pipes to the chamber. The pump provided a flow rate of 130 L/h at the inlet and outlet pipes of the chamber. The flow conditions inside the chamber were not monitored during the tests. However, based on the preliminary study of Anagnostakis [127], the top position of the inlet and outlet should create a homogeneous flow inside the chamber that allows the corrosion of the central part, avoiding preference sites. An air pump was placed inside the tank to oxygenate the solution for the duration of the tests and maintain the same level of oxygen. Each specimen is provided with a single water supply system and the tank of water is never shared. The experimental set up is shown in Figure 4.27.

After each test, the sample was removed from the chamber and the equipment was cleaned and re-assembled for the next test.

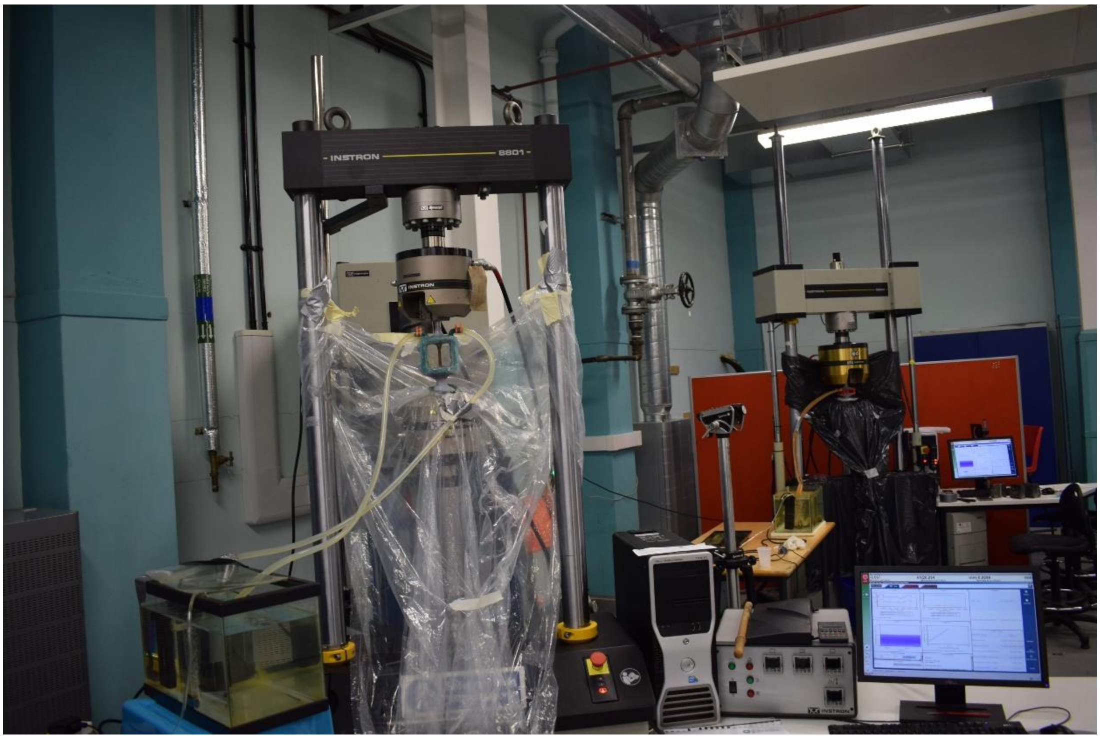

Figure 4.27: Equipment set up in AMRL for corrosion fatigue tests.

4.6.2 Testing Conditions in the Freshwater Environment

Fatigue tests in the corrosive environment were carried out using the same setup of WaveMatrix™ software described for fatigue in air, except for the duration of the second step. In this case, as a fatigue limit was not expected, tests were not stopped until the specimen was broken.

The corrosive solution selected for corrosion fatigue tests had the same compositions of the solution used for corrosion tests, reported in Table 4.7. Unless specified, these characteristics are representative of all corrosion fatigue experimental investigation.

Three stress ratio families were performed at the loading frequency of 10 Hz on virgin specimens: R=-1, R=0, and R=0.5. The investigation only considers the effect of positive mean stress on the fatigue life of carbon steel in the corrosive environment, as this is the condition GEHO pumps are subjected to. Values of mean and amplitude stresses for each test and the corresponding number of cycles to failure are reported in Table 4.8, Table 4.9, and Table 4.10 respectively for R=-1, R=0, and R=0.5 stress ratio values.

Table 4.8: Conditions of corrosion fatigue tests at R=-1 and 10Hz.

Sample	***Amplitude Stress (MPa)***	***%*** σ_y	***Mean Stress (MPa)***	***Cycles***	***Results***
T108	209	81	0	$3.47\ 10^{5}$	Failed
T614	167.7	65	0	$1.05\ 10^{6}$	Failed
T407	167.7	65	0	$1.36\ 10^{6}$	Failed
T205	129	50	0	$2.93\ 10^{6}$	Failed
T209	129	50	0	$2.73\ 10^{6}$	Failed
T123	116.1	45	0	$4.56\ 10^{6}$	Failed
T111	100	38.7	0	$6.43\ 10^{6}$	Failed

Table 4.9: Conditions of corrosion fatigue tests at R=0 and 10 Hz.

Sample	***Amplitude Stress (MPa)***	***%*** σ_y	***Mean Stress (MPa)***	***Cycles***	***Results***
T414*	188.2	73	188.2	$2.22\ 10^{5}$	Failed
T415*	188.2	73	188.2	$2.05\ 10^{5}$	Failed
T412*	180	70	180	$2.85\ 10^{5}$	Failed
T413*	180	70	180	$2.61\ 10^{5}$	Failed
T223	129	50	129	$1.01\ 10^{6}$	Failed
T609	102	39.5	102	$3.00\ 10^{6}$	Failed
T519	90	35	90	$4.14\ 10^{6}$	Failed

*Test run by Tsergas E. [128]

Table 4.10: Conditions of corrosion fatigue tests at R=0.5 and 10 Hz.

Sample	*Amplitude Stress (MPa)*	*% σ_y*	*Mean Stress (MPa)*	*Cycles*	*Results*
T613	115	44.5	345	$9.40\ 10^{5}$	Failed
T314	95	36.8	285	$1.98\ 10^{6}$	Failed
T517	75	29	225	$3.87\ 10^{6}$	Failed
T617	75	29	225	$4.29\ 10^{6}$	Failed

Figure 4.28 shows the progress of corrosion, during the corrosion fatigue tests, on the surface of specimen T205 tested at R=-1. Small traces of rust were visible on the surface after 1:15 h (a). One hour later (c) more rust dots occurred and spread over the surface of the sample. After five hours (e) the dots expanded creating small rusty areas, clearly visible on the surface. Twenty-one hours from the beginning of test (f), a spongy layer of rust covered more than half of the surface. The rusty layer expanded (g and h) occupying the uncorroded areas and, after two days (i), it covered the whole surface. The progression of corrosion is conformed with the results obtained from corrosion testing. Because of the flow inside the chamber, some corrosion products, such as small portions of the rusty layer, detached from the sample and dissolved in the solution. This feature can be observed by comparing the colour of the solution that, over time, becomes more yellowish. However, an analysis of sample surfaces after corrosion fatigue testing would better quantify the level of degradation and surface characteristics.

a) b) c) d) e) f)

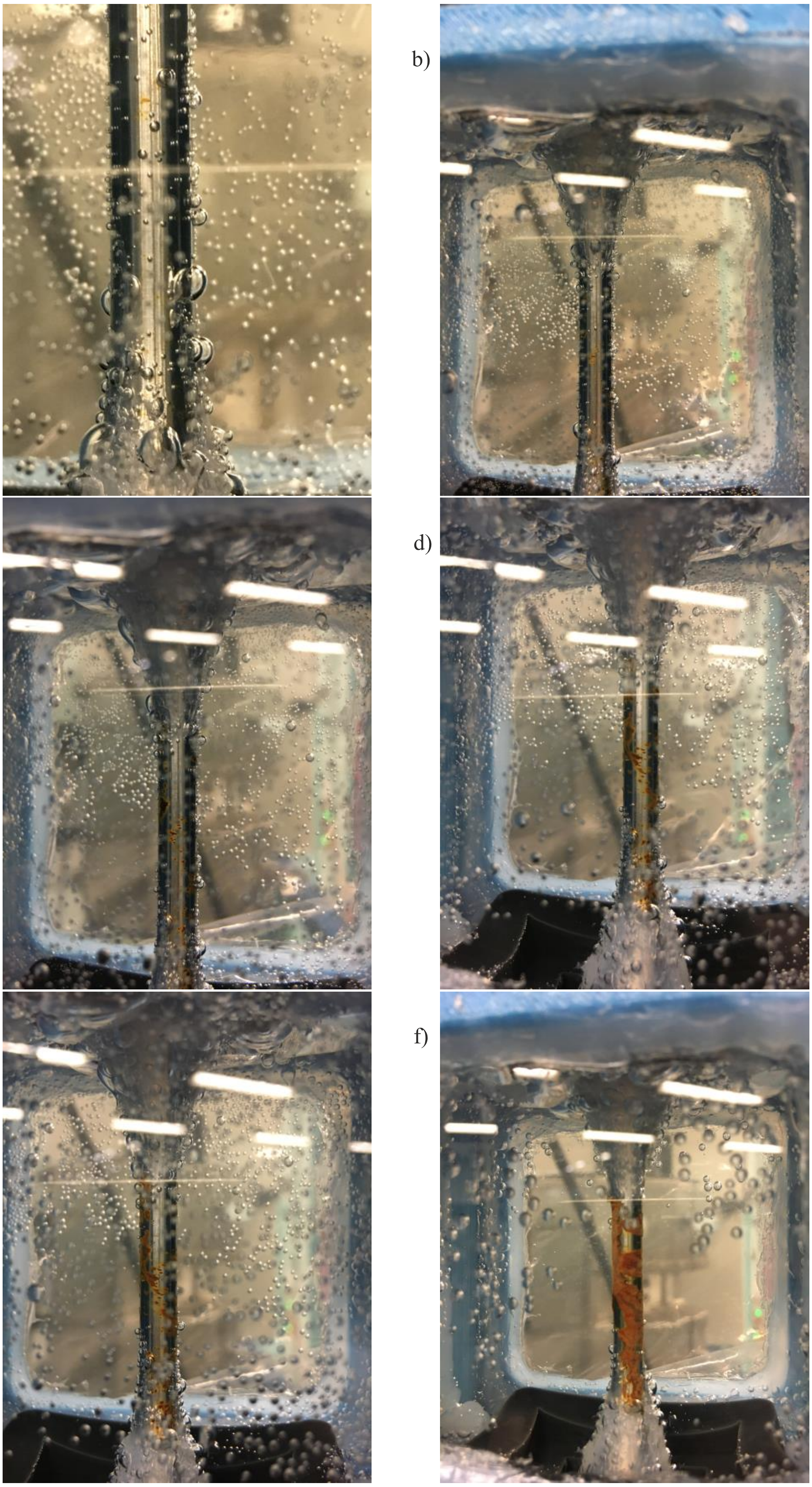

Figure 4.28: Progression of corrosion on specimen T205. *Continued to the next page.*

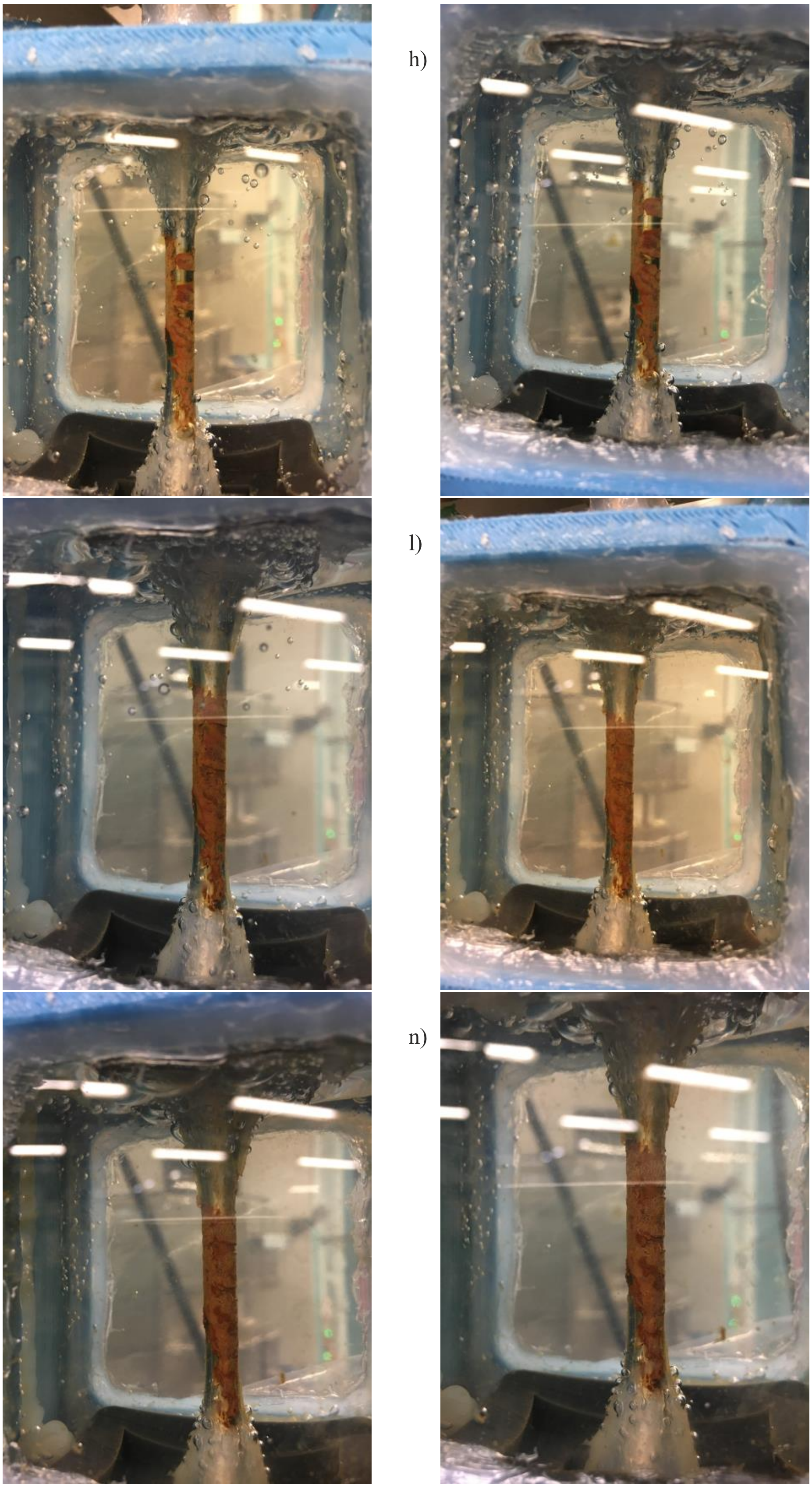

Figure 4.28: Progression of corrosion on specimen T205. *Corrosion after: a) 1:15h, b) 1:45 h, c) 2:15 h, d) 4:15 h, e) 5 h, f) 21h, g) 28 h, h) 29:15h, i) 47 h, l) 50:45 h, m) 72:15 h, n) 76:45 h.*

4.6.3 Pre-Corroded Specimens and Testing Conditions

Specimens corroded before corrosion-fatigue tests were placed in a 20 L tank of solution, with the same freshwater characteristics used for corrosion fatigue tests, and left under the solution flow for 21 days. An air pump was placed inside the tank to provide the constant oxygenation for the duration of the pre-corrosion process. To guarantee good grip during the successive fatigue test, silicon was placed all around the grip area of the specimen, as shown in Figure 4.29. Two supports were placed inside the tank which specimens were propped against, to maintain the central part of the specimens completely surrounded by the solution. When the specimens were removed from the solution, the central part of all specimens appeared corroded and a spongy layer of rust surrounded this area, as shown in Figure 4.30. Specimens were cleaned using a soft hand brush and cold water and immediately dried with hot airflow. Figure 4.31 shows the central area of a pre-corroded specimen compared with a specimen where no further treatments were applied after the manufacture, here defined *virgin specimen*.

Corrosion fatigue tests were performed, using the same corrosion cell and equipment described in Section 4.6.1 for corrosion fatigue tests on virgin specimens.

The aim of this experimental investigation is to understand whether the initial surface conditions affect the total fatigue life when the stress level is of the order or lower than the fatigue limit in air. Although the mean stress effect is not studied for this condition, to be able to generalise the results obtained from this procedure, two stress ratios were selected for the pre-corroded corrosion fatigue tests: R=-1 and R=0.5. Characteristics of stresses and fatigue cycles are summarised in Table 4.11 and Table 4.12 respectively for R=-1 and R=0.5.

Figure 4.29: Pre-corrosion of fatigue specimens.

Figure 4.30: Detail of specimen surface after 21 days of immersion in the corrosive solution.

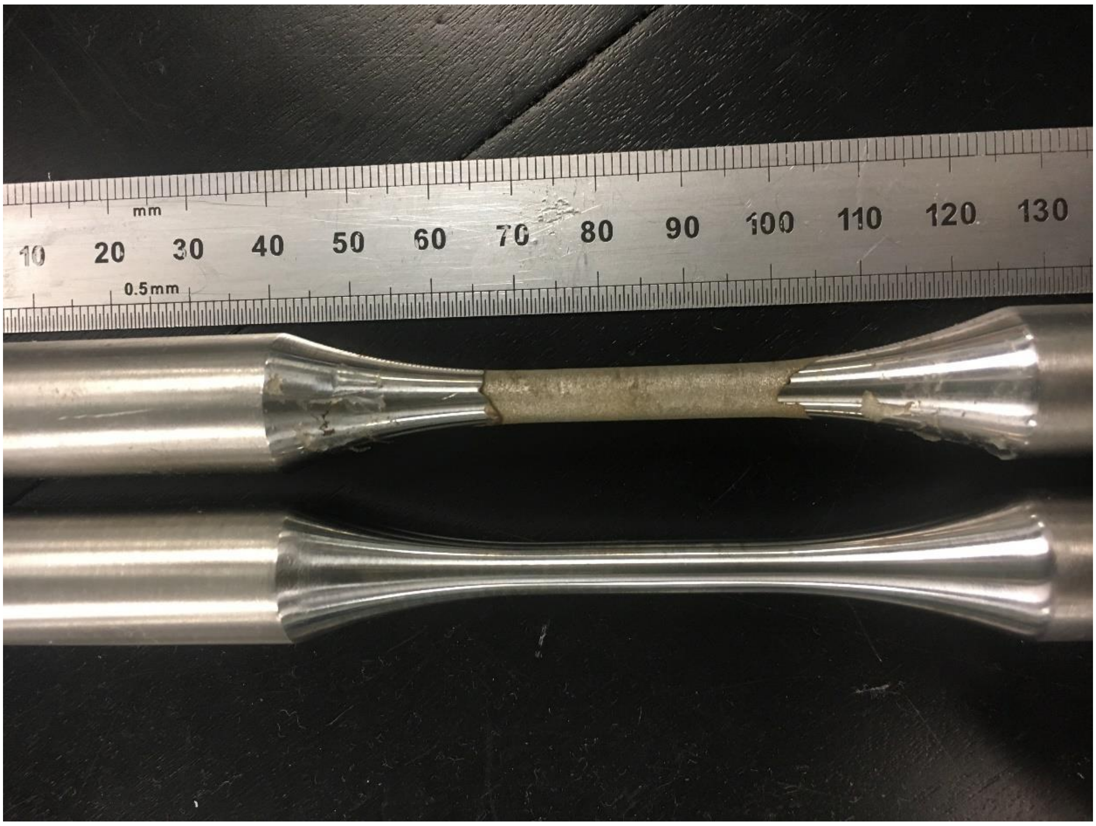

Figure 4.31: Comparison between surface after manufacture and a 21 day corroded surface.

Table 4.11: Conditions of pre-corroded corrosion fatigue tests at R=-1 and 10 Hz.

Sample	***Amplitude Stress (MPa)***	$\%\sigma_y$	***Mean Stress (MPa)***	***Cycles***	***Results***
T301	120	46.5	0	$1.92\ 10^6$	Failed
T419	97	37.6	0	$5.55\ 10^6$	Failed
T420	92	35.6	0	$7.06\ 10^6$	Failed

Table 4.12: Conditions of pre-corroded corrosion fatigue tests at R=0.5 and 10 Hz.

Sample	***Amplitude Stress (MPa)***	$\%\sigma_y$	***Mean Stress (MPa)***	***Cycles***	***Results***
T303	75.8	29.3	227.4	$2.36\ 10^6$	Failed
T315	54.6	21.1	163.8	$1.31\ 10^7$	Failed
T417	50.8	19.6	152.4	$1.51\ 10^7$	Failed

4.7 External Corrosion Fatigue Tests at Frequency 10 Hz

Due to a cooling system failure of the local AMRL hydraulic fatigue testing machine, the Exova laboratory, Daventry (UK), was engaged to perform further corrosion fatigue testing of S355J2 in the freshwater solution. Exova was instructed to perform endurance fatigue tests in aerated 824 ppm NaCl solution and in air. Servo hydraulic test machines TZCF-10 and TZCF-11 with a maximum capacity of 100 kN were used to conduct load controlled tests after calibration in accordance with BS EN 7500 and ASTM E4. A separate corrosion cell was built for each machine, which completely encased the central part of specimens, but a single circulation system for the two cells was used, differently from corrosion fatigue testing performed in the University, where each test was completely independent. A schematic representation of the system is shown in Figure 4.32. Corrosion cells were designed by Exova and manufactured using PBC plastic with inlet and outlet allowing the circulation of the solution between the solution tank and the corrosion cell. It is important to note that the inlet hole is placed on the bottom and the outlet hole on the top of the corrosion cell and both of them are on the same side of the sample. Inlet and outlet diameter is 6.35 mm. Comparing the equipment utilised for testing in AMRL and in Exova, the main differences are the dimension and position of inlet and outlet holes and the circulation system.

Technical drawings of the corrosion chamber are shown in the Annexe.

The corrosive solution, contained in a 10 L tank, was aerated during tests by an air pump and circulated using a peristaltic pump with a flow rate of approximately 100 L/h. Equipment set up for corrosive solution circulation and details of the corrosion cell assembled to the sample during the fatigue test are shown respectively on the left and right sides of Figure 4.33.

Nine samples were provided, from the same batch of specimens tested in air and corrosive environment in AMRL laboratory, to be loaded axially. Specimen diameters were measured again in Exova and the mean and the amplitude loads were calculated according to these dimensions, which agreed with the ones obtained in AMRL. Application of loads followed a sine wave shape and all tests were performed at a frequency of 10 Hz. The maximum and minimum values of loads and displacements were monitored and recorded during the testing.

Corrosion fatigue tests were performed at three different stress ratio conditions: R=0, R=0.5, and R=0.65. Whereas, a single test in air at R=0 was performed to compare the scatter in the result that may occur because of differences in fatigue machines.

Characteristics of stress and number of cycles are reported in Table 4.13, Table 4.14, Table 4.15, and Table 4.16 respectively for R=0 in air, and R=0, R=0.5 and R=0.65 in corrosive solution.

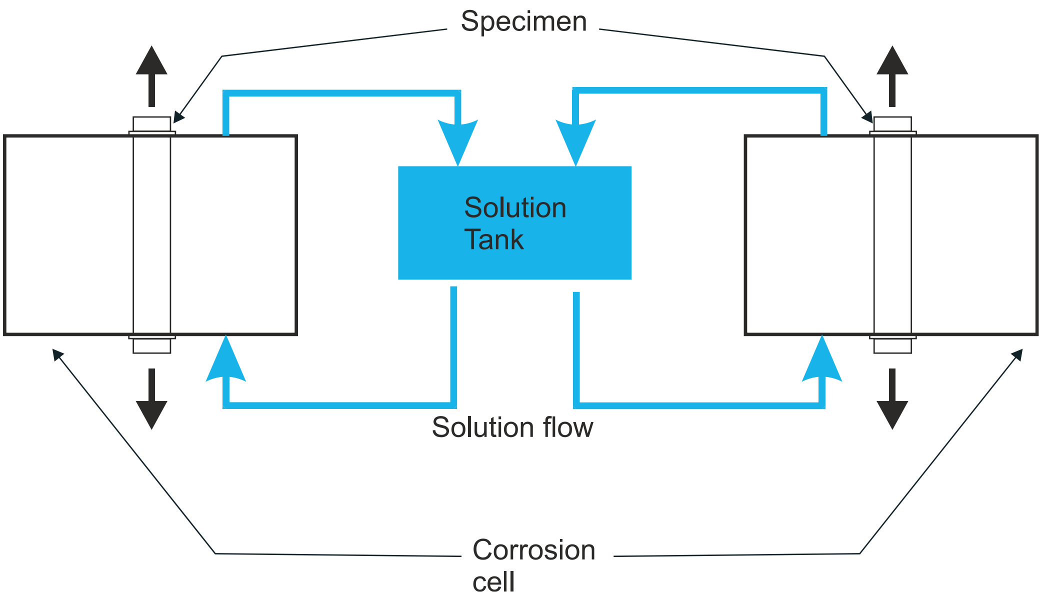

Figure 4.32: Corrosion circulation system used at Exova to perform corrosion fatigue testing.

Figure 4.33: Exova testing equipment. *Left) Details of the circulation system in Exova laboratory; Right) Corrosion fatigue cell assembled at fatigue machine.*

Table 4.13: Conditions of fatigue test in air at R=0 performed in Exova.

Sample	*Amplitude Stress (MPa)*	*% σ_y*	*Mean Stress (MPa)*	*Cycles*	*Results*
T615	184	71	184	5.95 10^5	Failed

Table 4.14: Conditions of corrosion fatigue tests at R=0 performed in Exova.

Sample	*Amplitude Stress (MPa)*	*% σ_y*	*Mean Stress (MPa)*	*Cycles*	*Results*
T408	129	50	129	1.22 10^6	Failed
T405	85	33	85	1.73 10^7	Failed

Table 4.15: Conditions of corrosion fatigue tests at R=0.5 performed in Exova.

Sample	*Amplitude Stress (MPa)*	*% σ_y*	*Mean Stress (MPa)*	*Cycles*	*Results*
T620	115	44.5	345	1.15 10^6	Failed
T104	95	36.8	285	2.88 10^6	Failed
T406	75	29	225	1.17 10^7	Failed
T619	75	29	225	8.99 10^6	Failed

Table 4.16: Conditions of corrosion fatigue tests at R=0.65 performed in Exova.

Sample	*Amplitude Stress (MPa)*	*% σ_y*	*Mean Stress (MPa)*	*Cycles*	*Results*
T124	78.75	30	371.25	3.49 10^6	Failed
T404	60	23	282.85	1.14 10^7	Failed

4.8 Corrosion Fatigue Tests at Frequency 100 Hz

The second set of experimental data was obtained by performing corrosion fatigue tests at higher frequency using the Instron EletroPuls E3000 in the AMRL facility. Specimens suitable for this smaller machine were designed according to Standard E466-15 [121]: the geometry and dimensions are shown in Figure 4.34. Specimens were manufactured from one of the slices from the low carbon steel S355J2 block, described in Section 4.2.

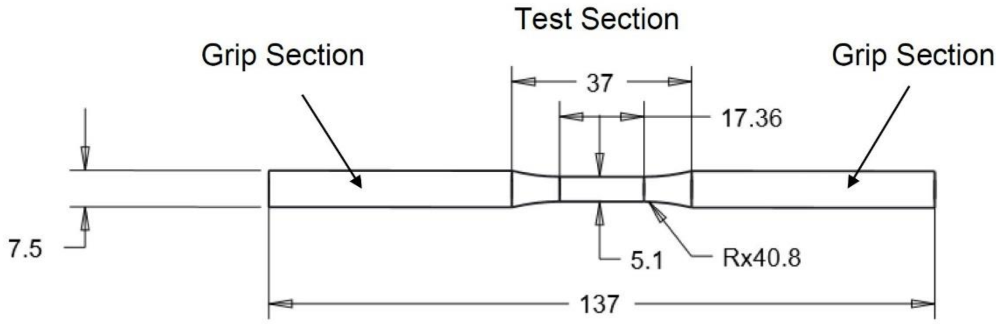

Figure 4.34: Specimen dimensions for uniaxial corrosion fatigue tests at 100 Hz.

The roughness of the test section was measured using the Mitutoyo Surftest SV-2000 machine with the same set up as in Section 4.3.2. Readings were obtained across eight 0.8 mm segments in the test section at angles of 0º and 180º around the centre. The values of surface roughness were between 0.18 µm and 0.26 µm. Although these values are higher than the previous sets of specimens, polishing was not required as all of these samples were designed to be used in the corrosive environment.

A corrosion cell, completely enclosing the specimen during loading, was designed in accordance with Instron E3000 dimensions. The corrosion cell design was based on the same considerations described in Section 4.6.1. The chamber's components and seals were manufactured by 3D printing, using the same materials employed for the larger chamber. Inlet and outlet holes, of 7 mm diameter, are located on the top of the chamber, one on each side of the sample. Details of the corrosion cell and experimental setup are shown in Figure 4.35.

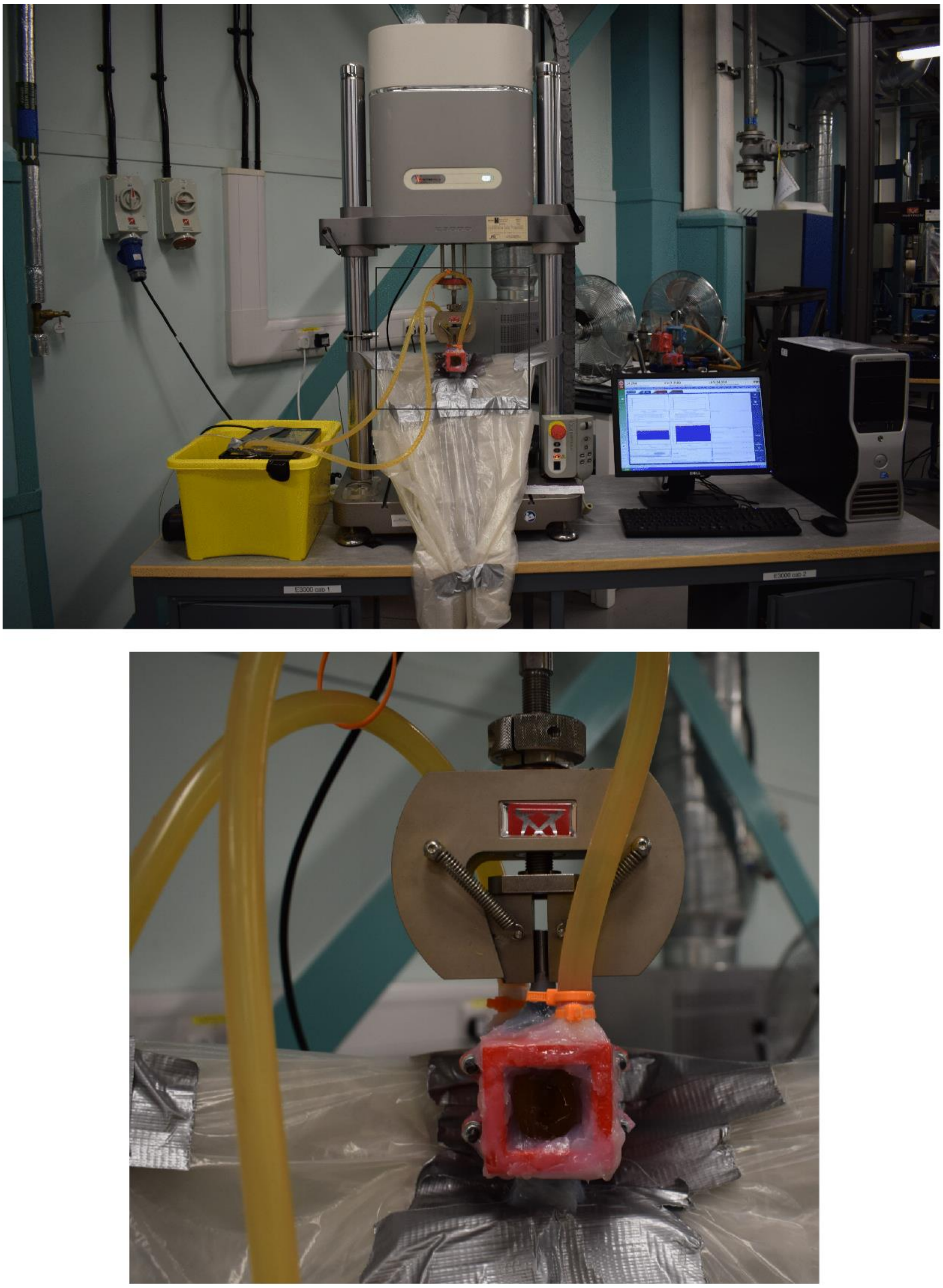

Figure 4.35: Equipment setup for high-frequency tests.

The ElectroPuls E3000 testing machine offers a high-frequency performance with the limitation of maximum dynamic loading. Preliminary tests were performed, using S355J2 steel, to determine the maximum applicable force in relation to the maximum frequency. The maximum obtained frequency to perform a reasonable control of the applied load was 100 Hz. However, in a few cases at this frequency, the applied load monitored and recorded through the WaveMatrix™ software disagreed with the nominal value picked in the setup. It appeared that the difference between the imposed and the applied load is of a maximum of 100 N. Since the aim of this set of tests was to investigate the fatigue strength at very high fatigue cycles, the higher frequency of 100 Hz, was chosen at load precision expense. Consequently, in this set of experiments, each experimental test resulted to be performed at a value of stress ratio slightly different from the nominal value, as it depends on the maximum and minimum applied loads. During corrosion-fatigue testing, WaveMatrix™ was set to save data constantly, following instructions reported in Table 4.17. Data monitored during testing and recorded are the maximum and minimum loads and the maximum and minimum position of grip. It was required to save the last 10000 data before the end of the tests. History values of maximum and minimum loads was used to calculate the actual maximum and minimum stress the specimens were subject to. Values of maximum and minimum stress were obtained as the arithmetic mean of the load history. It was noted that the maximum difference between the arithmetic mean value and recorded data is 20 N, which based on the sample area, is less than 1 MPa. Stress amplitude and mean stress, calculated from the load history, and respective fatigue life for each specimen are summarised in Table 4.18.

Table 4.17: Data save programme during corrosion fatigue tests.

Data saved	***Saving frequency (cycles)***	***Range of saving (cycles)***
1	100	1000
1	1000	10000
1	10000	100000
1	100000	End of test

Table 4.18: Conditions of corrosion fatigue tests at 100 Hz.

Sample	*Amplitude Stress (MPa)*	*Mean Stress (MPa)*	*Stress Ratio R*	*Cycles*	*Results*
T705	36.4	69.1	0.31	$5.44\ 10^{7}$	Failed
T716	36.7	65.2	0.28	$1.11\ 10^{8}$	Failed
T720	30.2	58.6	0.32	$2.05\ 10^{8}$	Failed
T721	30.0	58.2	0.32	$1.16\ 10^{8}$	Failed
T722	29.7	57.6	0.32	$1.19\ 10^{8}$	Failed
T723	26.1	52.9	0.34	$2.69\ 10^{8}$	Failed

4.9 Summary

To investigate the fatigue behaviour of low carbon steel S355J2 in a corrosive environment and to evaluate the effect of mean stress on fatigue strength, an experimental programme consisting of corrosion tests on unloaded specimens, uniaxial fatigue tests in air and in the corrosive environment was performed. In addition, results obtained from tensile testing define the mechanical characteristics of S355J2.

Corrosion fatigue life is usually modelled as a combination of the different contributing mechanisms, such as crack nucleation and crack growth stages. Crack nucleation is closely connected to the surface condition of the material. In aggressive environments, it is mainly affected by the corrosion effect on the surface. Corrosion tests were designed and implemented on small rectangular samples to investigate the degradation caused by the exposition to the freshwater solution. The effect of corrosion exposure on specimen surfaces was analysed over a maximum period of 40 days. Uniform attack corrosion over the surface was found, showing extensive formation of rust after the first few days. 3D surface analysis was performed by laser scan to evaluate the roughness and measure dimensions of pits and defects. It was found that both the pit depth and value of surface roughness increase during the immersion time up to approximately 12 days of exposure. After this time, although the loss of material caused by corrosion continued, the relative depth of defects and the surface roughness remained constant.

For corrosion fatigue testing, corrosion chambers were designed and manufactured to completely enclose the specimen during the application of loads to allow simultaneous corrosion of the central region.

The effect of positive mean stress was investigated in the region 10^5 to 10^7 cycles and, for each stress ratio, various stress amplitudes were tested with the aim of extrapolating the fatigue behaviour to higher numbers of cycles. In addition, some specimens were corroded for 21 days before being used for simultaneous corrosion fatigue testing at two distinct stress ratios, to evaluate which effect the pre-corrosion provokes on the overall corrosion fatigue life.

To identify the fatigue strength at high fatigue cycles, a set of experimental data was performed at elevated loading frequency in the corrosive environment.

Analysis of all fatigue experimental results, in terms of fatigue life, reductions of fatigue strength, fractography of fracture surfaces, and the effect of mean stress on fatigue behaviour is the topic of the next Chapter.

Chapter 5

Experimental Data Analysis

This chapter analyses the experimental results obtained by uniaxial fatigue testing for the conditions presented in Chapter 4. The related analysis leads to the evaluation of S-N curves in the freshwater environment and to the design of constant-life diagrams in the same corrosive environment.

Comparisons between the different test conditions are evaluated through the study of the specimen's fracture surface that allows the investigation of different mechanisms that occurred during the fatigue and corrosion fatigue life of the S355J2 low carbon steel specimens. By the examination of the external surface of specimens and measurement of corroded degradation, an analogy between pre-corroded specimens tested in the freshwater environment under cycling loads and virgin specimens loaded at high frequency in the same corrosive environment is highlighted. Owing to the elevated cost and time-consuming characteristics of corrosion fatigue testing, the majority of the sets of experimental results are in the region of fatigue life up to 10 million cycles. Consequently, the definition of S-N curves at higher cycles and the related estimation of corrosion fatigue strength in the different conditions of mean stress is obtained by the predictive model gathered by these analyses.

To evaluate the mean stress effect on corrosion fatigue strength of low carbon steel experimental results are plotted in the form of Haigh diagrams and, for each length of fatigue life, the allowable stress is calculated. The approach to analyse the mean stress effect on corrosion fatigue strength is based on the FKM definition of the Haigh diagram both because a similar methodology is employed by Weir to estimate the allowable stress in Fluid End components and because the FKM approach is versatile and can be easily adapted to different environments. Starting from the design of the Haigh diagram in air, the mean stress sensitivity factor is calculated and comparisons with values obtained in the corrosive environment for different fatigue lives are discussed. Definitions of new parameters, based on the physical meaning of the mean stress sensitivity factor, are proposed to describe the allowable stress limits in a corrosive environment at values of stress ratio higher than R=0. Based on these parameters, comparison between results obtained in different corrosive aqueous solution flows permits the extrapolation of mean stress effect at values of stress ratio higher than R=0.5. From the mean stress analysis on corrosion fatigue experimental results in the fatigue life-region up to 20 million cycles and through the estimation of fatigue strength at higher fatigue life, the allowable stress in the Haigh diagram at 10^9 cycles can be predicted.

The diagram in Figure 5.1 shows the outcomes from each set of experimental data analysis.

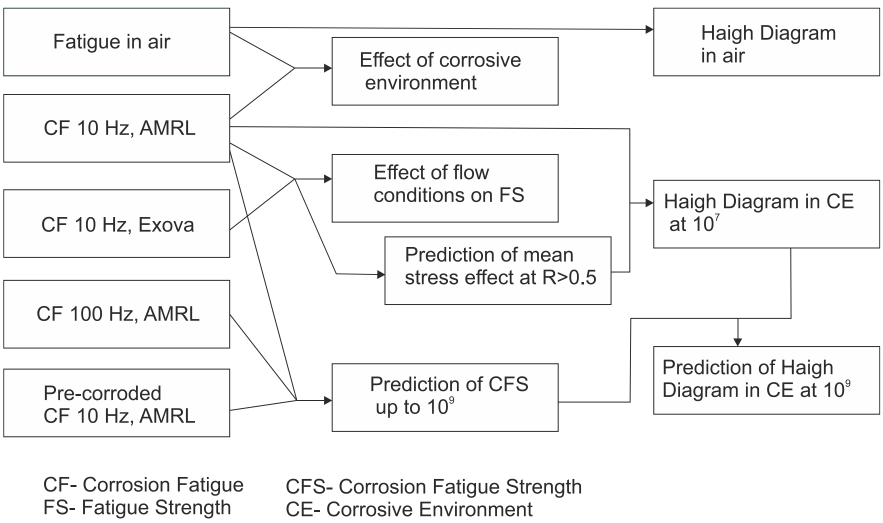

Figure 5.1: Outcomes of experimental data analysis.

5.1 Evaluation of Fatigue Properties in Air

Experimental investigation in air was performed with the aim of determining the fatigue properties of S355J2 in an inert environment. In particular, tests were designed to obtain information on fatigue strength to be compared to results obtained in the corrosive solution. In addition, a positive mean stress loading condition was included in the investigation to evaluate the effect of mean stress on fatigue strength in air.

The two sets of experimental results obtained from uniaxial fatigue tests conducted in air, for stress ratio R=-1 and R=0, are shown in the log-log S-N diagram in Figure 5.2. Approximation of S-N curves for each set of stress ratio was obtained by linear regression using Basquin’s power law up to 3 million cycles for R=-1, and up to 1 million cycles for R=0. After these fatigue lives, based on experimental data of run-out specimens, the fatigue strength of the material is considered constant with cycles and is represented by a straight line on the S-N diagram. Table 5.1 shows values of the fatigue strength in the plateau region and the two constants of the power-law equation for both stress ratio conditions. Under positive mean stresses, fatigue strength decreases compared to the fully reversed condition and the plateau region appears at a lower number of cycles. This is a typical behaviour observed in alloy steels subject to positive mean stress conditions [129].

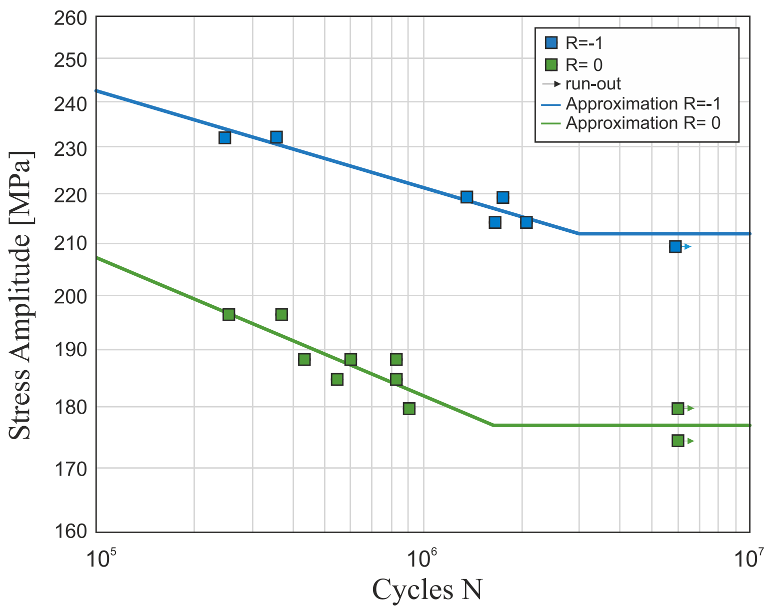

Figure 5.2: log-log S-N curves from experimental data in air.

Table 5.1: Constant values for S-N curves in air.

Type of loading	$\sigma_f^{'}$ MPa	b	σ_f MPa
R=-1	392.5	-0.0395	212
R=0	417.2	-0.0573	176

Another fatigue test in air, at stress ratio R=0, was performed in the Exova facility. The aim of this single test was to evaluate any difference in results, caused by the use of two different fatigue testing machines. The result is plotted in a log-log S-N diagram, shown in Figure 5.3, together with the fatigue results obtained from the AMRL facility. The fatigue result is in agreement with the trend obtained in AMRL: the cycles at which the specimen failed are within values obtained from AMRL tests, at the same stress amplitude. Therefore, based on this result, it was assumed that experimental results obtained in Exova were not affected by the testing machine and setup.

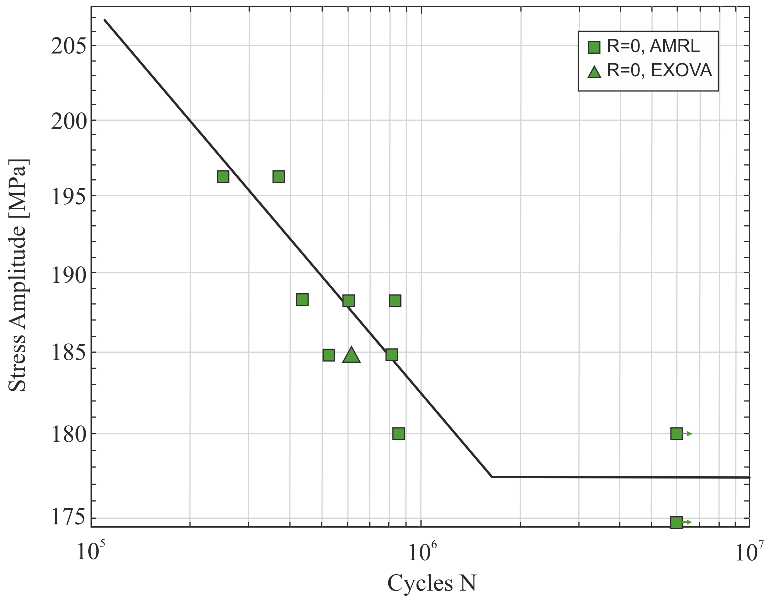

Figure 5.3: log-log S-N curve in air at stress ratio R=0. *Comparison between results obtained in AMRL and the result obtained in Exova.*

The fatigue crack nucleation occurred on the external surface of specimens and propagated perpendicular to the direction of the applied stress, both in specimens fatigued in the fully reversed loading and in those subjected to positive mean stresses. In specimens under fully reversed loading, the fracture surface, shown in Figure 5.4

and Figure 5.5, can be divided into three regions: a semi-elliptical shaped area, an intermediate region, characterised by a fibrous appearance, and the region where final ductile fracture took place. The semi-elliptical shaped area consists of the crack nucleation site and the initial part of crack propagation. Therefore, most of the fatigue life was spent creating this fractured portion. The part of the surface, created in a relatively short period of the total fatigue life, is characterised by a fibrous appearance with radial lines almost perpendicular to the perimeter of the semielliptical zone, sometimes called a river [17]. This radial pattern is recognised to be typical in the region where the final fracture is approaching. Finally, the last small part of the surface is characterised by a ductile fracture, where the stress in the remained area approached the ultimate strength of the material.

Figure 5.6 and Figure 5.7show the fracture surface of specimens failed under positive mean stress conditions at a lower and higher number of cycles respectively. In both cases, two regions are visible: the fibrous appearance area, where the final stage of propagation took place and the final ductile fracture area. In these cases, the final ductile area occupies a surface that is roughly more than a half of the total surface of the specimens, that means the propagation of crack ended at almost half of the specimen thickness and, after this, the specimen separated because of the high stress. This is caused by the fact that the maximum force, as well as the maximum stress, is two times the amplitude stress. Therefore, the ultimate strength of the material is achieved at a shorter length of crack propagation.

Figure 5.4: The fracture surface of specimen T520 tested at R=-1.

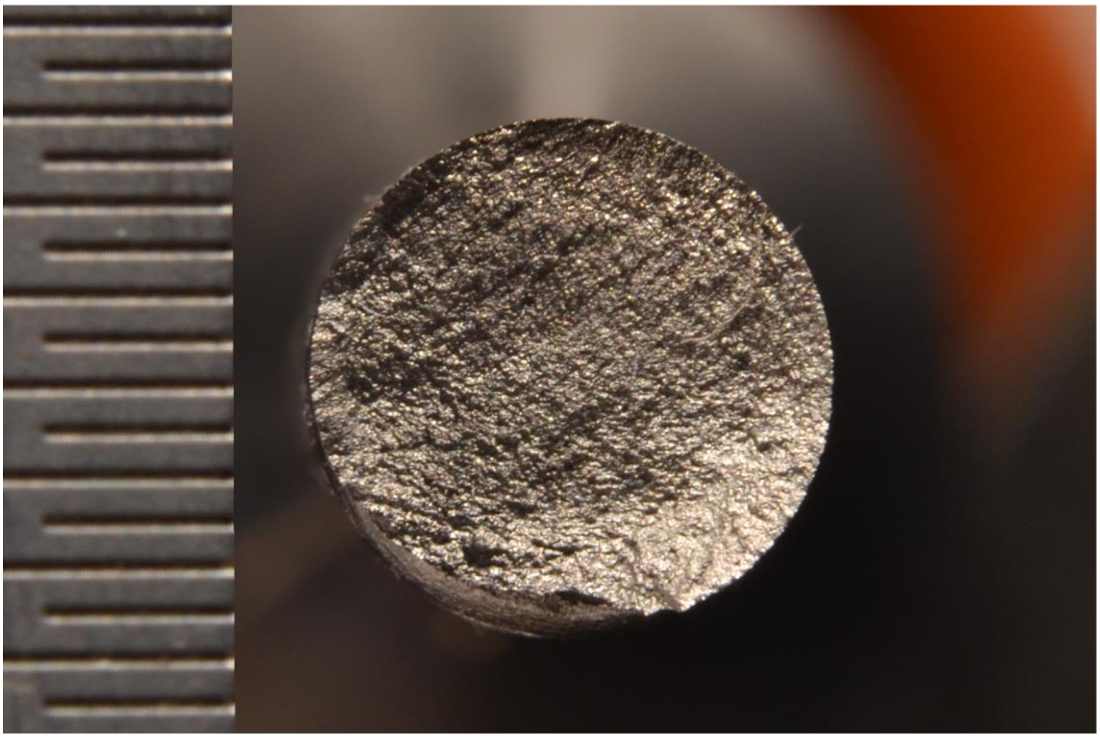

Figure 5.5: The fracture surface of specimen T224 tested at R=-1.

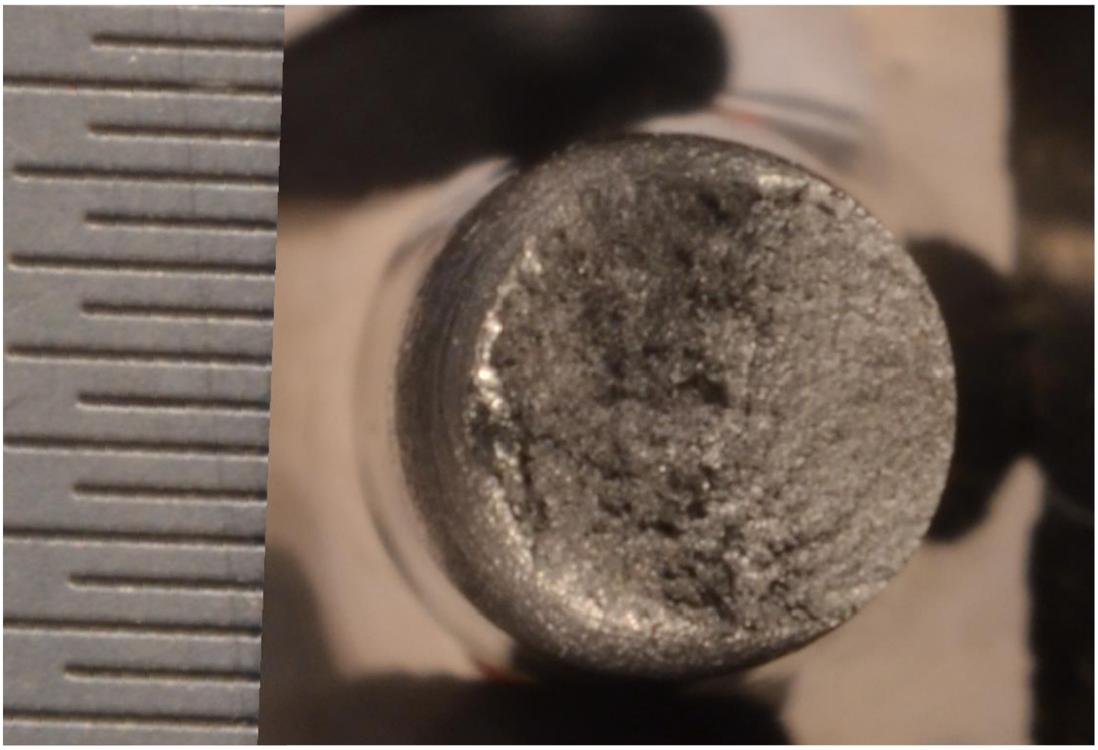

Figure 5.6: The fracture surface of specimen T515, tested at R=0.

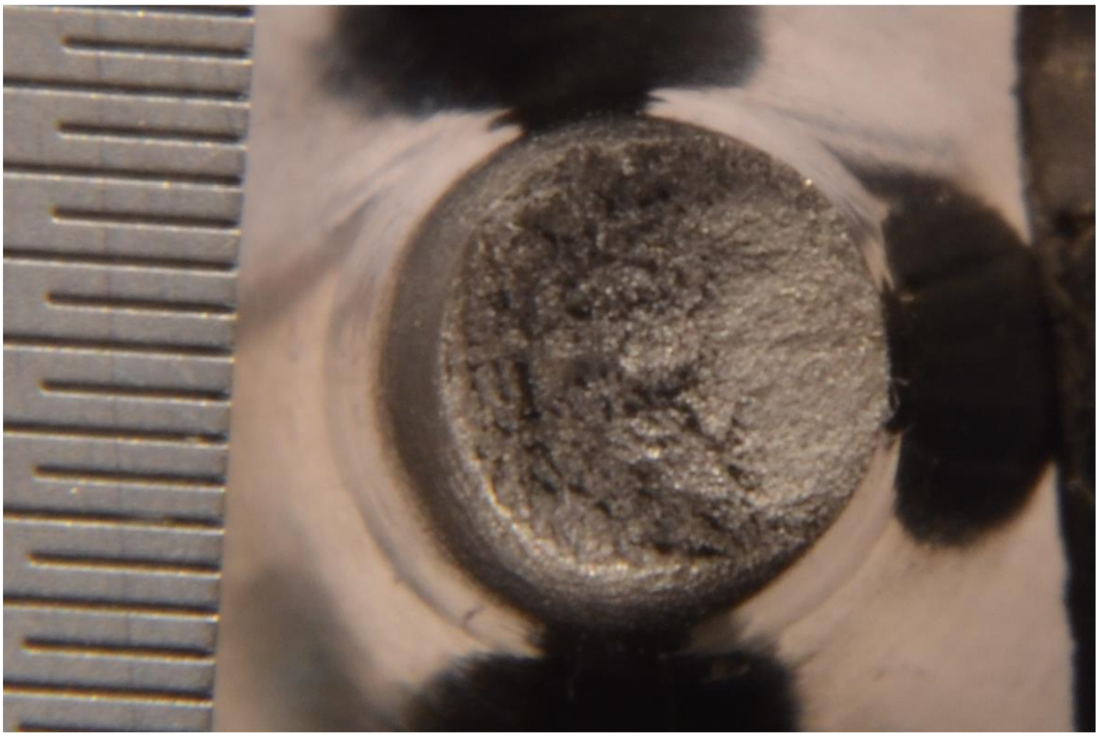

Figure 5.7: The fracture surface of specimen T230 specimen tested at R=0.

5.2 Experimental Results in Corrosive Environment and Fractography Analysis

5.2.1 Results of Corrosion Fatigue Tests at Loading Frequency 10 Hz

The results of uniaxial corrosion fatigue testing obtained at load frequency 10 Hz in the AMRL facility are plotted in the log-log S-N diagram, shown in Figure 5.8. On the same diagram, S-N curves obtained as the best fit of Basquin's equation are drawn for each stress ratio data set. The two constant values that described the S-N curve, for each stress ratio, are summarised in Table 5.2.

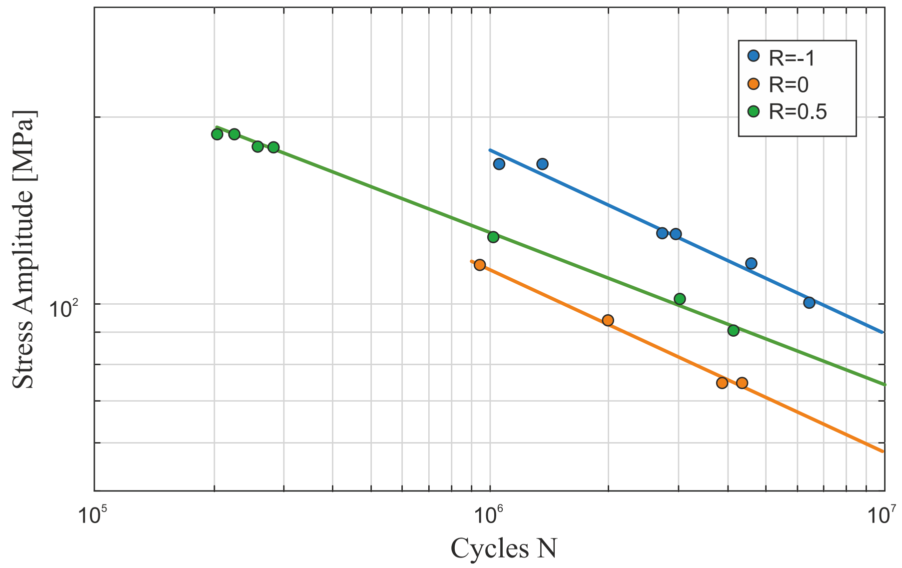

Figure 5.8: log-log S-N curves from data obtained in AMRL at 10 Hz.

Table 5.2: Constant values for S-N curves in the freshwater environment. *Data obtained by linear regression of experimental results at 10 Hz, performed in AMRL.*

Type of loading	σ'_f, MPa	b
R=-1	1.2516 10^4	-0.2937
R=0	4.4815 10^3	-0.2439
R=0.5	8.0651 10^3	-0.2935

In the region of fatigue life between 10^5 and 10^7 cycles, the fatigue strength in the corrosive environment continuously decreases regardless of the stress ratio conditions. Consequently, the gap between the fatigue strength in air and in the corrosive environment increases with the fatigue life. Based on these trends of fatigue life, there is no indication that a fatigue limit occurs in the corrosive environment. However, to properly identify how the fatigue strength decreases with the fatigue life, corrosion fatigue data at high cycles are considered in the next sections.

To better understand the corrosion fatigue phenomenon and to investigate its features, fracture specimens were inspected using an optical microscope with various magnification lenses.

Figure 5.9 and Figure 5.10 show the fracture surface of corroded fatigue specimens, failed after 2.9 and 3.8 million cycles respectively. Fracture surfaces are characterized by the propagation of multiple cracks that join together to lead to the final fracture of the specimens. This characteristic is observed in the majority of failed specimens under the combined effect of the corrosive environment and the cyclic loading. Consequently, the appearance of the surface is less smooth than the fracture surface of specimens tested in air, and only the portion where the final fracture occurred can be easily distinguished. Multiple cracks and flaws are also visible on the external surface of specimens, as shown in Figure 5.11 and Figure 5.12 for specimens failed after 9.4×10^5 cycles and 3×10^6 cycles, respectively. All flaws and cracks developed and propagated perpendicular to the loading direction, that is on the plane of maximum normal stress. Crack initiation sites, for all of the identified cracks, are located all around the specimen surface and no internal site was identified.

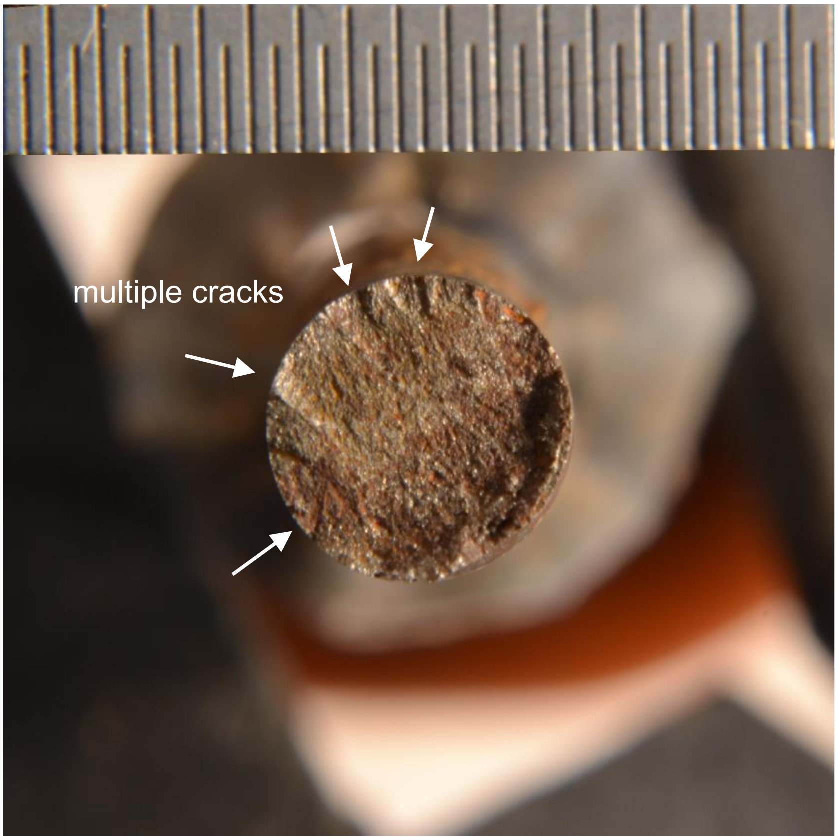

Figure 5.9: Fracture surface of specimen T205. *Number of cycles at failure 2.9 x* 10^6.

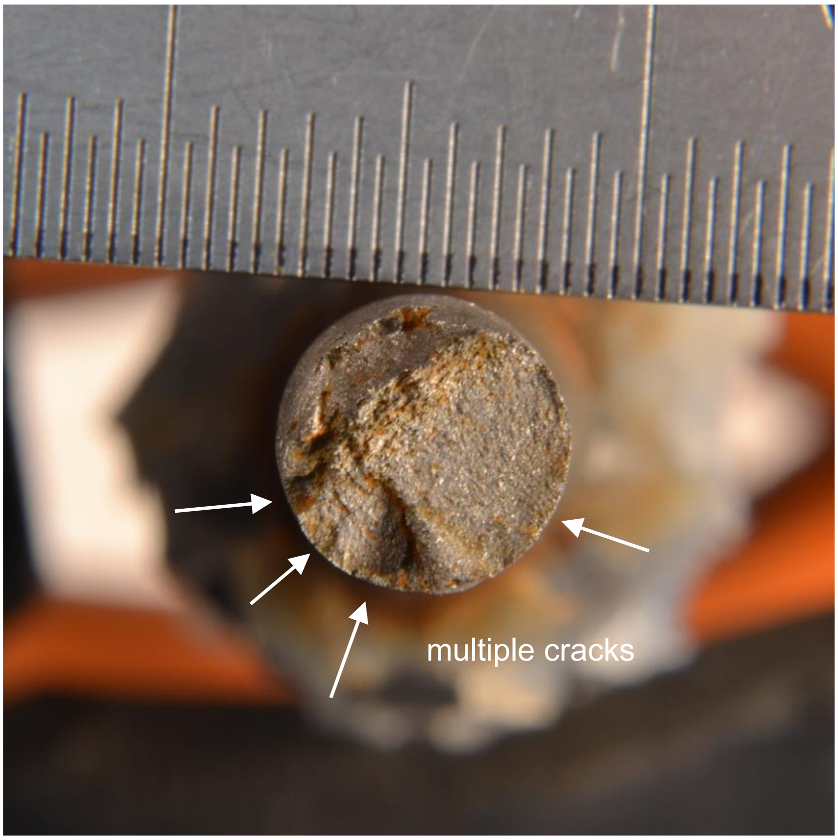

Figure 5.10: Fracture surface of specimen T519. *Number of cycles at failure 3.8 x* 10^6.

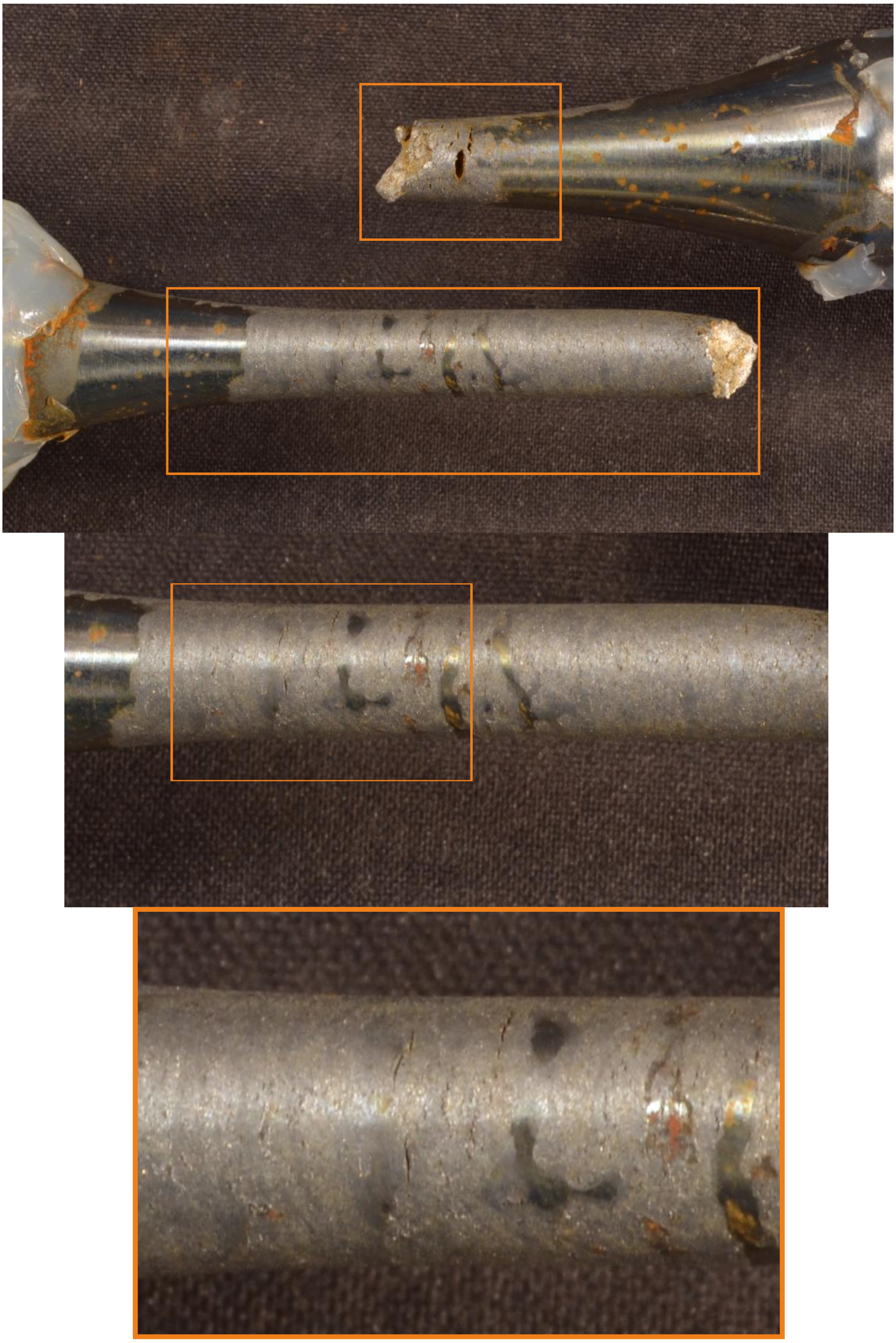

Figure 5.11: Details of multiple cracks on the surface of specimen T613. *Number of cycles at failure 9.4 x 10^5.*

Figure 5.12: Details of multiple crack sites on the corroded surface of specimen T609. *Number of cycles at failed 3 million.*

To further understand the crack initiation and propagation mechanism, specimens were cut into two halves along an axial plane to analyse the extension of cracks through the surface. The part of the cut specimen is prepared and assembled to a mounted specimen to allow to be handled easily. Using this procedure, features of the corroded surfaces, such as pits and the profile of surface roughness caused by corrosion effects, as well as cracks and flaws can be identified.

Figure 5.13 shows the section of corroded fatigue specimen failed at 2.7 million cycles, obtained using a magnification x50, and details of two cracks propagated from the external surface, obtained with magnification x200. From the surface section, two propagated cracks are visible: both of them initiated on the external surface of the specimen and propagate almost perpendicular to this surface. The portions of the area that surrounded the crack initiation site, for both cracks, are coarse and corrugated due to the detrimental effect of corrosion. Based on the shape of material around the cracks, it is reasonable to suppose that cracks initiated from a corrosion pit. A further example of a crack initiated from a corrosion pit on the external surface is shown in Figure 5.14 for specimen T205, magnification x100. In this case, multiple cracks are also present in the selected sections. The larger pit from this section is semi-elliptical shaped with depth and width of 26 μm and 57 μm respectively.

Different authors [130, 131] have recognised that dimensions of pits remained almost unchanged after the transition from a pit to a crack has occurred. Based on this observation it can be assumed that dimensions of pits visible on the section surfaces are almost the same from which cracks had started to propagated.

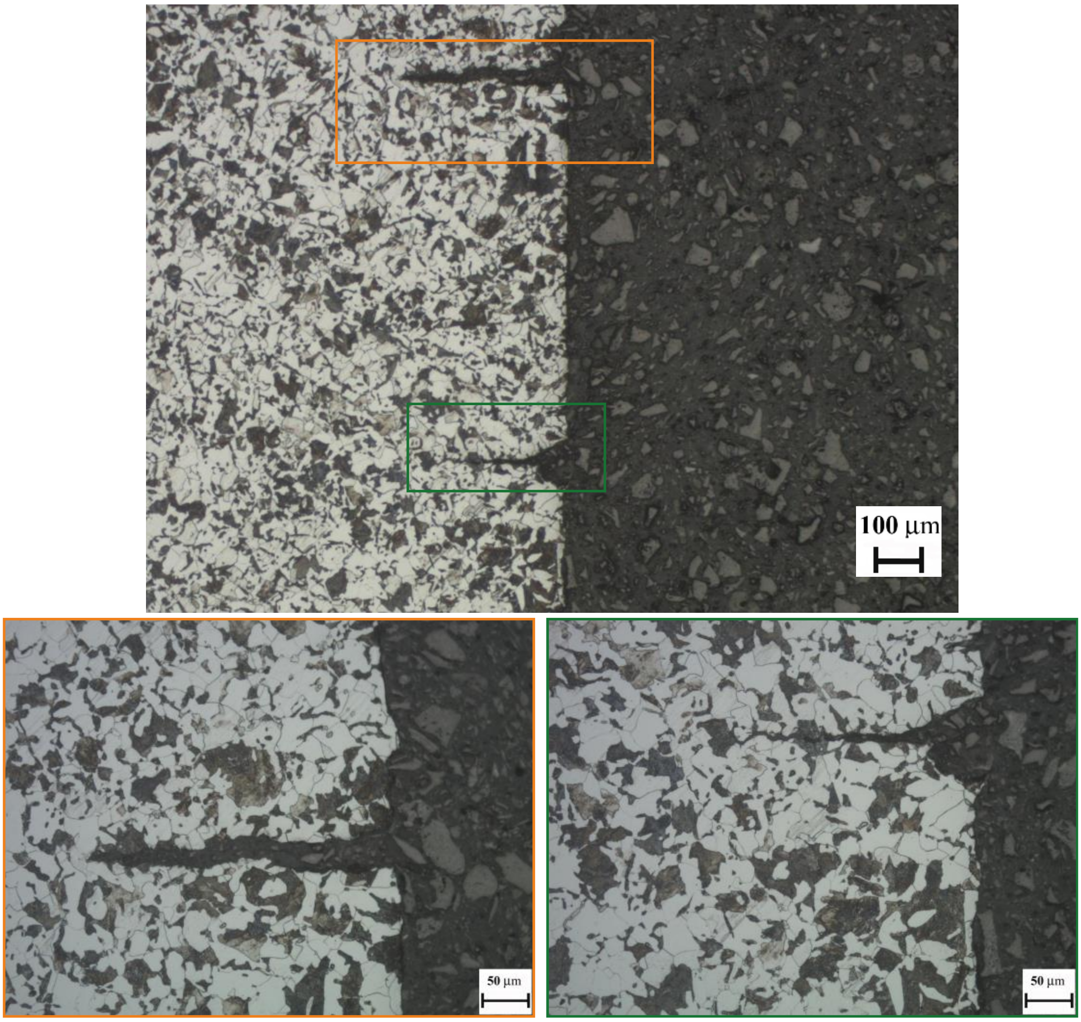

Figure 5.13: Details of corroded surface of specimen T209. *Number of cycles at failure 2.7 x 10^6.The dark area on the right is the mounting material, which has only the function to support the portion of the analysed specimen.*

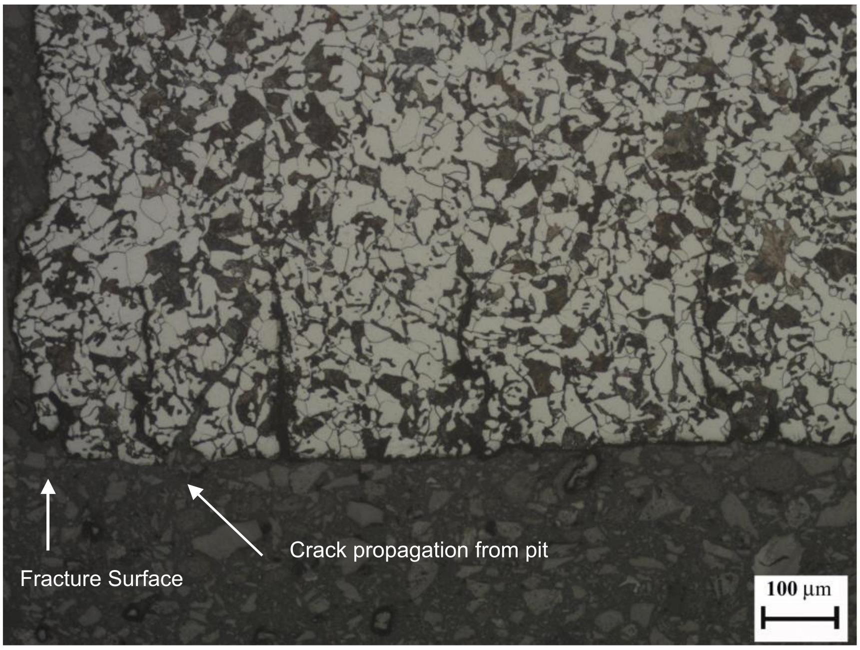

Figure 5.14: Section of the fracture surface of specimen T205. *Details of rough surface appearance and propagated cracks. The dark area on the bottom is the mounting material, which has only the function to support the portion of the analysed specimen.*

5.2.2 Results of Corrosion Fatigue Tests in Exova

To further investigate the behaviour of low carbon steel S355J2, additional corrosion fatigue tests were performed in the Exova facility. Experimental results are plotted in log-log S-N diagram with results obtained in AMRL under the same conditions, shown in Figure 5.15. In each laboratory, three values of stress ratio R were considered: in AMRL specimen were tested at R=-1, R=0 and R=0.5, whereas in Exova stress ratio conditions were R=0, R=0.5 and R=0.65. Constant values to describe Basquin's law, for each set of stress ratio condition, were obtained from linear regression and are reported in Table 5.3.

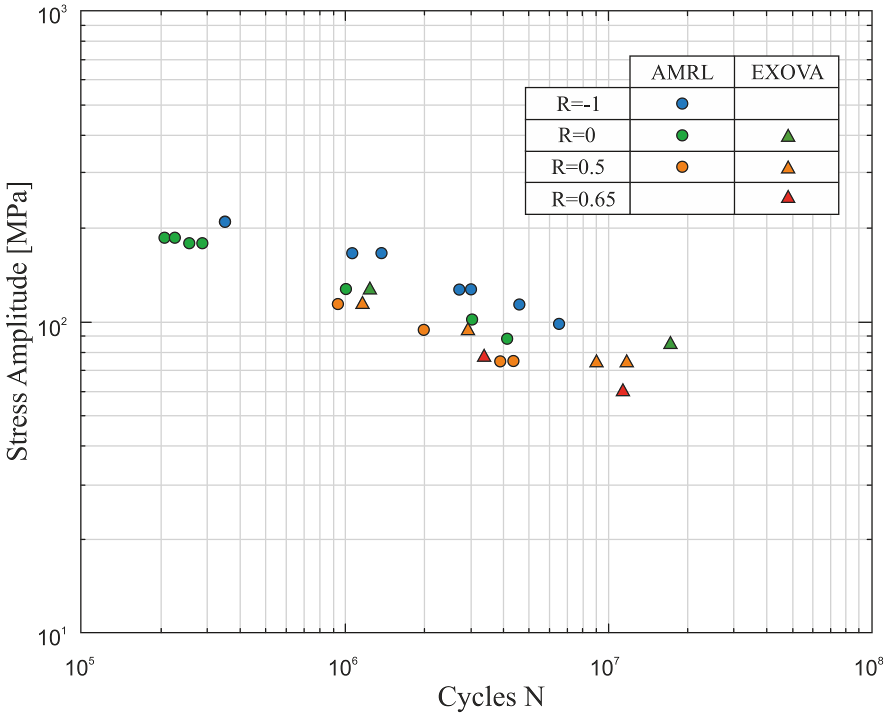

Figure 5.15: log-log S-N diagram of corrosion fatigue data at 10 Hz. *Experimental results of simultaneous corrosion fatigue obtained in AMRL and Exova facilities.*

Table 5.3: Constant values for S-N curves performed in Exova. *Data obtained by linear regression of corrosion fatigue experimental results.*

Type of loading	σ_f' (MPa)	b
R=0	1.3147 10^3	-0.1577
R=0.5	1.9639 10^3	-0.1938
R=0.65	2.9565 10^3	-0.2300

5.2.3 Comparison of Corrosion Fatigue Results at 10 Hz

From the results obtained in air for uniaxial specimens tested in Exova, no differences were expected in corrosion fatigue results from the two laboratories, for each family of stress ratio R, as shown in Figure 5.3. This was supported by the fact that the test equipment to simulate the corrosive effect during fatigue tests was designed to be as similar as possible to the one developed in AMRL and the corrosive environment and tests frequency were exactly the same for both cases. However, the differences, in terms of fatigue life, between tests performed in AMRL and Exova laboratory are too large to be considered as scatter in results. Details of this behaviour are shown in

Figure 5.16 and Figure 5.17 where only the data for the single stress ratio condition R=0 and R=0.5 are represented respectively. The differences between the two sets of results increase with decreasing the stress amplitude, as highlighted by the approximate S-N curve obtained by linear regression of experimental data. Hence, at stress amplitude of 50% of the yield stress, the difference in fatigue life is less than 150000 cycles, that is 1.1 times higher than the fatigue life obtained in AMRL. However, at stress amplitude equal to 33% of the yield stress, the fatigue life obtained by tests in Exova is 3 times higher than that shown by specimens tested in AMRL. A similar trend occurs also in the comparison between corrosion fatigue testing at stress ratio R=0.5 obtained in the two facilities.

The trends in experimental results in air and in the corrosive environment, obtained in the two facilities, suggest that inequality in results arises from the corrosion mechanism and in the interaction between corrosion and fatigue. There is no evidence which suggests that the inequality may be connected to the type of machine used for the fatigue tests. If the inequality had been caused by fatigue testing equipment, the same difference in fatigue cycles would have been expected, regardless of the value of stress amplitude at which tests were performed.

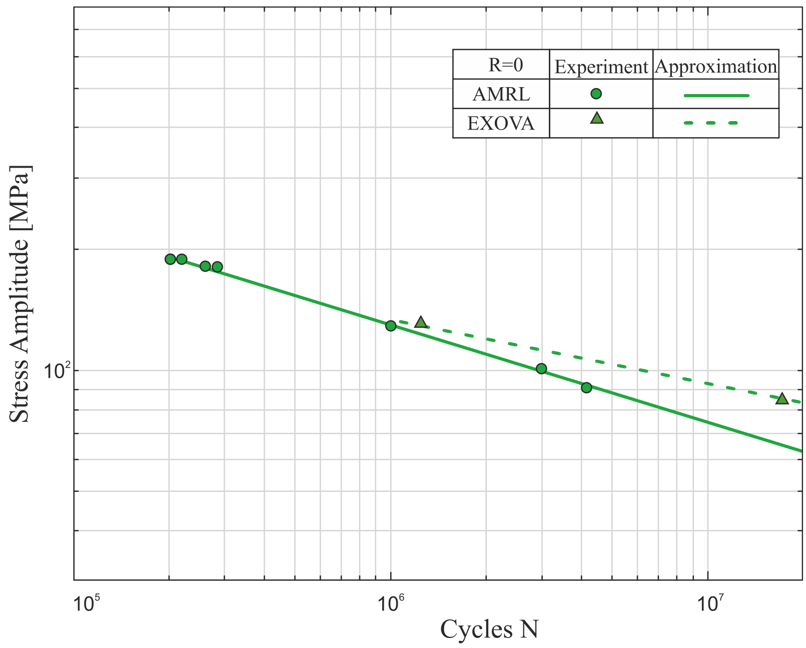

Figure 5.16: log-log S-N curves obtained from experimental corrosion fatigue data at R=0. *Comparison between Exova and AMRL trends.*

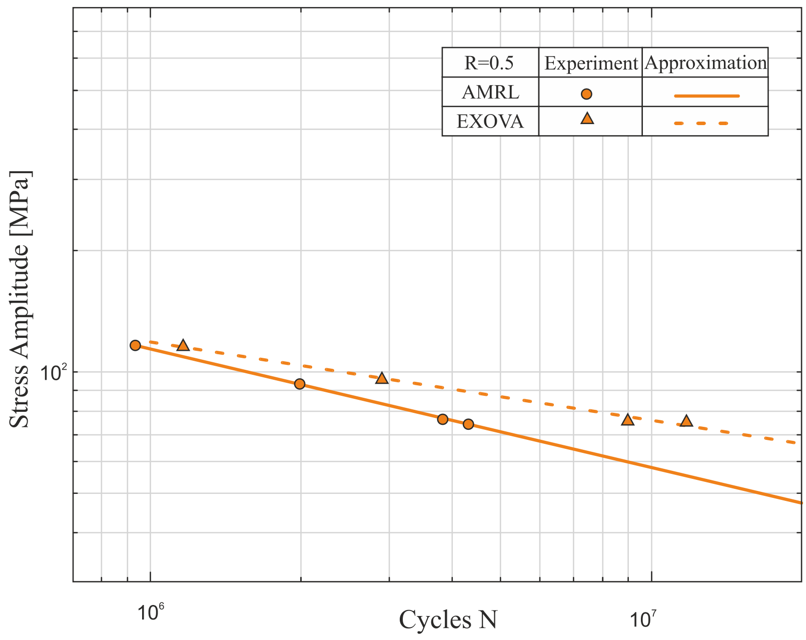

***Figure 5.17: log-log S-N curves obtained from experimental corrosion fatigue data at R=0.5**. Comparison between Exova and AMRL trends.*

At higher amplitude stresses, when the overall length of tests is around 25-30 hours, fatigue strength can be less susceptible to variation in corrosive flow distribution or velocity of the flow, as long as the chemical composition of the solution is the same. However, at lower stress amplitude, fatigue strength is easily influenced and small variations in the corrosive environment may cause a significant change in fatigue life. Ebara [132] showed that both the effect of frequency and chemical composition of the corrosive solution are stronger at low stress amplitudes where fatigue failure required a longer time. This tendency can be explained by the fact that the critical dimension of a defect, from which a crack begins to grow, can be related to the stress intensity factor K and consequently to the applied stress: when the stress is higher, a smaller size defect allows the growth of a flaw into a crack. Conversely, the lower is the applied stress, the more the defect needs to grow to become critical [130]. Moreover, as summarised by Li [131], a further condition that should be satisfied to allow the transition from pit to crack is that the corrosion fatigue crack growth rate should overtake the pit growth rate. As the defect size is mainly controlled by the chemical reaction in the corrosive environment, changes in the chemical composition of the corrosive solution or in the duration and procedure of exposure to the corrosive environment can affect the chemical reaction and consequently the overall time spent on crack initiation and crack growth.

To better understand the reason why inequality occurred in fatigue results and understand the role of the corrosion mechanism in this scenario, analysis of the corroded surfaces of tested specimens was carried out. It was observed that all specimens tested in Exova facility show a non-homogeneous degradation of the surface. If the specimen is ideally divided into two parts, along the longitudinal axis, the surface of one of the half part is barely corroded whereas the other half presents a more uniform deterioration, appearing much more degraded than the other. Evidences of this irregularity are shown in Figure 5.18, Figure 5.19, Figure 5.20, and Figure 5.21 for various lengths of fatigue life. For each specimen, the less corroded side, shown in a), is represented next to the complementary more damaged side, shown in b) obtained turning the specimen of roughly 180º. All tested specimens present this feature, regardless of the stress amplitude and the stress ratio at which the test was performed and consequently regardless of the length of the fatigue test.

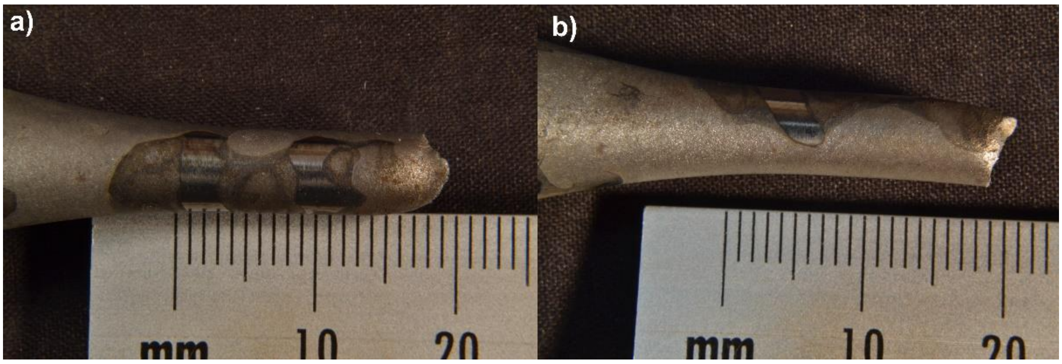

Figure 5.18: Surface of tested specimen T104, failed at 2.88 10^6 cycles. *a) surface less corroded, b) surface more corroded.*

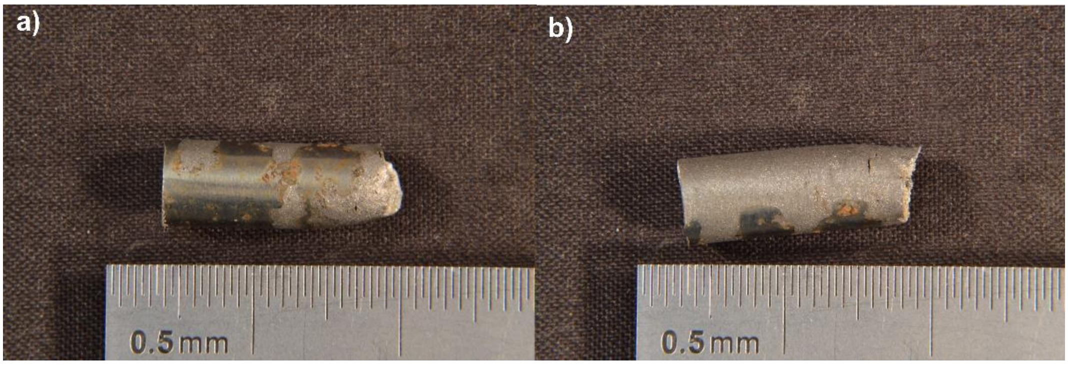

Figure 5.19: Surface of tested specimen T124, failed at 3.49 10^6 cycles. *a) surface less corroded, b) surface more corroded.*

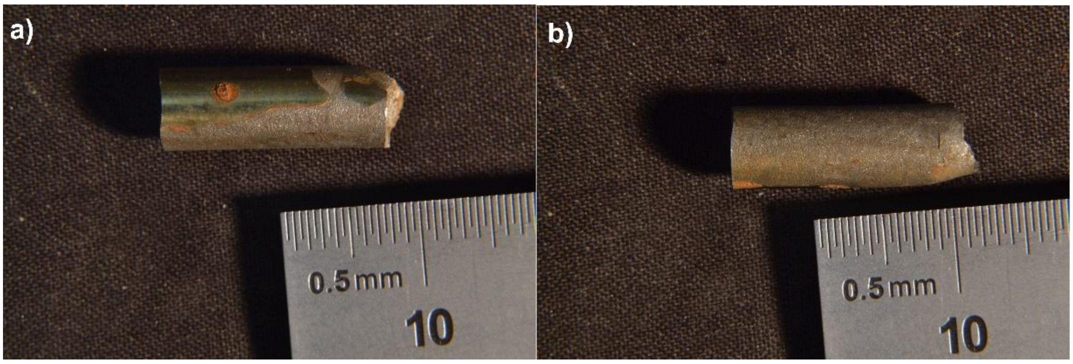

Figure 5.20: Surface of tested specimen T619, failed at 8.99 10^6 cycles. *a) surface less corroded, b) surface more corroded.*

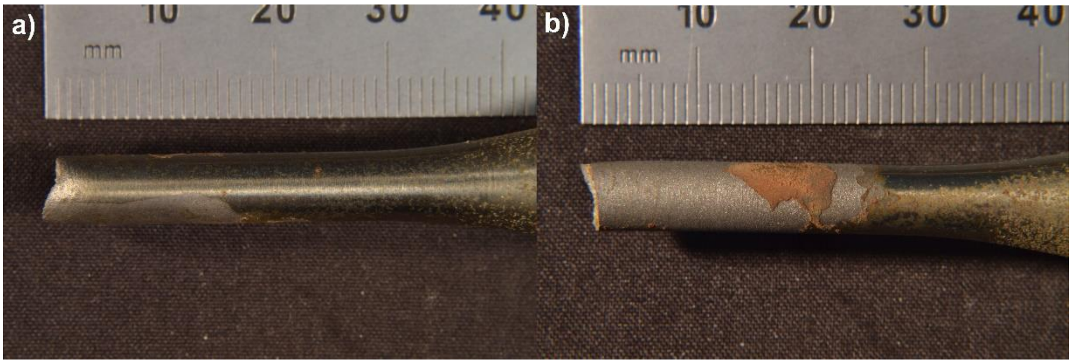

Figure 5.21: Surface of tested specimen T406, failed at 1.17 10^7 cycles. *a) surface less corroded, b) surface more corroded.*

The Alicona Infinite Focus IFM G4 system was employed to scan portions of specimen surface, in both halves, with scan magnification 20x.

Figure 5.22, Figure 5.23, and Figure 5.24 show the texture of a portion of the surface of the specimens T104, T619 and T406 which fatigue lives were 2.8 million, 8 million and 11 million cycles respectively. Through a deeper visualisation of these less corroded sections, small corroded spots are visible on the surfaces which increase in number with time of exposure, but overall these less corroded portions have maintained the polished appearance. This is a peculiar feature, especially for low stressed specimens, such as T619 and T406, for which the total duration of the test, and consequently of immersion in the corrosive solution, was more than 10 days and 13 days respectively. In these cases, a more intense degradation was expected based on the duration of the tests.

In contrast, the other surfaces show general corrosion over the whole part. In particular, for the low stressed specimens, the polished appearance completely disappeared and no unaffected regions are visible. Examples of textures of the more corroded half sections are shown in Figure 5.25 and Figure 5.26 for the test duration of 3 and 13 days respectively.

Visual analysis of the surface of specimens tested in corrosive environment in the AMRL facility was performed to evaluate if a similar feature occurred. Surfaces of specimen tested for 1 million and 4.1 million cycles are shown in Figure 5.27 and Figure 5.28 respectively. In these cases, no discontinuity in corrosion degradation occurred: a general degradation affected uniformly the surface of specimens. For the higher stressed specimen T223, which duration of tests was roughly 27 hours, the degradation appears less heavy and few isolated polished areas are still visible. This is in line with corrosion test findings, where after 2 days of exposure in corrosive environment the surface was not yet completely corroded. For lower stressed specimen T519, subjected to corrosion exposure for almost 5 days, the quality of surface appears rougher and only a few isolate small areas present a sort of polished appearance. However, in all cases, the less corroded areas are not oriented in any particular direction and no net division can be identified on the surface of the specimens.

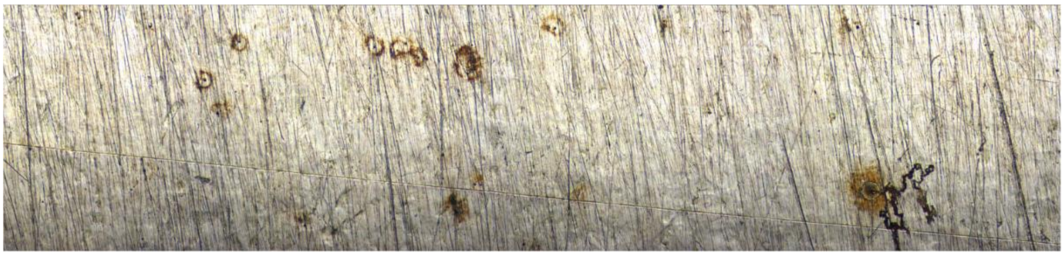

Figure 5.22: The 2D texture of the less corroded portion of the specimen surface T104.

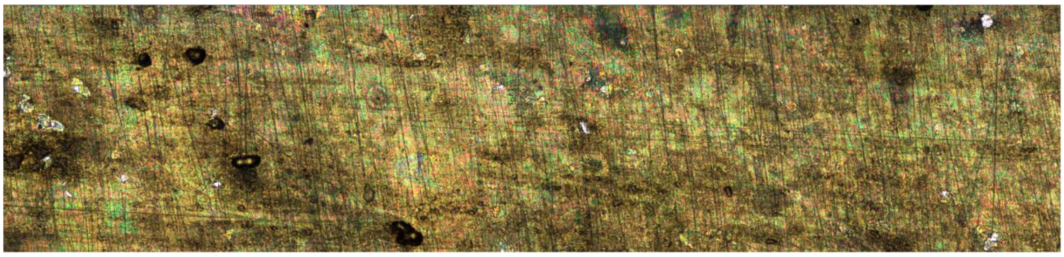

Figure 5.23: The 2D texture of the less corroded portion of the specimen surface T619.

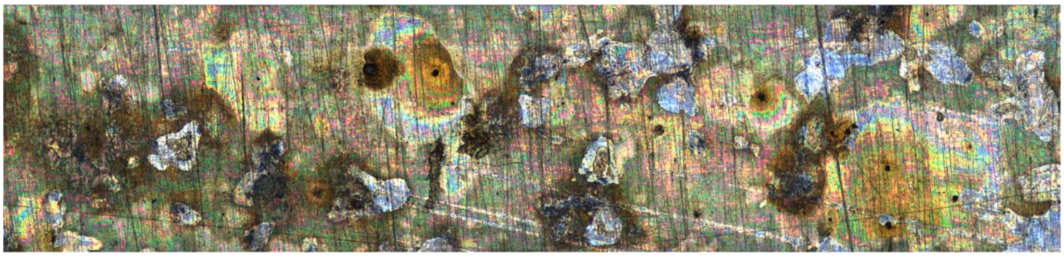

Figure 5.24: The 2D texture of the less corroded portion of the specimen surface T406.

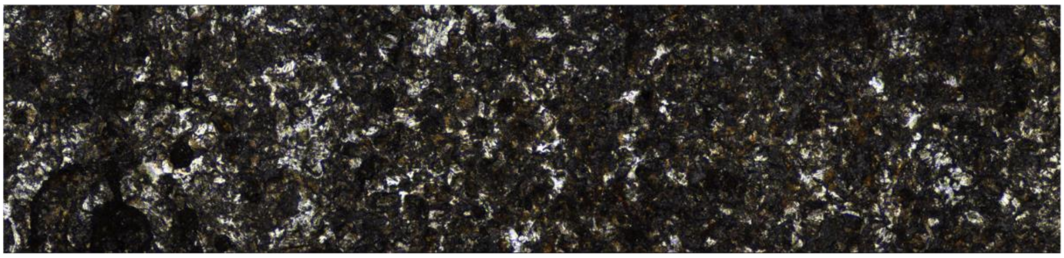

Figure 5.25: The 2D texture of the more corroded portion of the specimen surface T104.

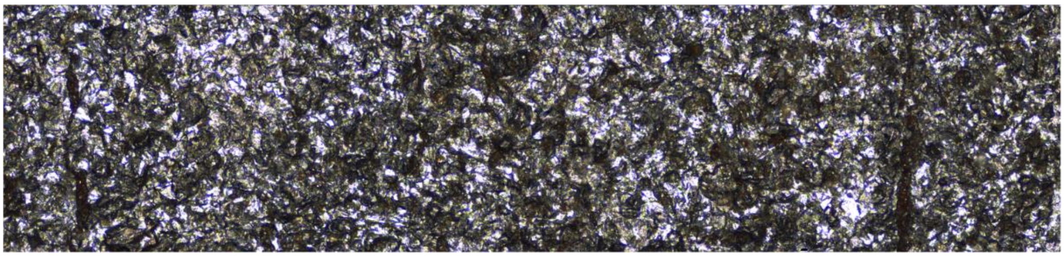

Figure 5.26: The 2D texture of the more corroded portion of the specimen surface T406.

Figure 5.27: Surface of tested specimen T223. *Fatigue life 1.01 10^6 cycles, tested in AMRL.*

Figure 5.28: Surface of tested specimen T519. *Fatigue life 4.14 10^6 cycles, tested in AMRL.*

To quantify these discrepancies in how the corrosion mechanism affects the specimen surface, the surface roughness of five specimens, with fatigue life range from 1.1 million to 11.7 million cycles, was evaluated using the Alicona software in both half sections.

Examples of roughness profile are shown in Figure 5.29 and Figure 5.30, for the less corroded and the more corroded half section respectively. The average value of roughness for each section was calculated as the arithmetic mean value of roughness obtained along several paths.

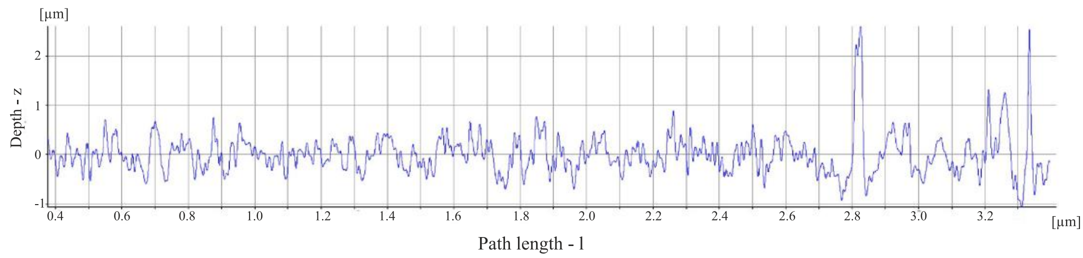

Figure 5.29: Roughness profile of the less corroded section of specimen T406.

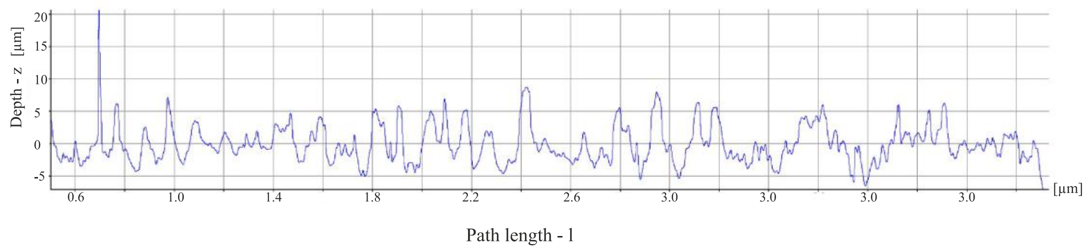

Figure 5.30: Roughness profile of the more corroded section of specimen T619.

Values of surface roughness, obtained for the less corroded sections, range from 0.18 µm to 0.82 µm, regardless of the fatigue life of the specimen. These values of surface roughness confirm that these portions of surfaces are barely affected by the corrosive environment. Indeed, the maximum surface roughness measured in virgin specimens was 0.16 µm. Whereas, the surface roughness of the complementary portions ranges from 1.17 µm, for the fatigue life of 1.1 million cycles, to 2.43 µm, for the fatigue life of 11.7 million cycles. In this case, surface roughness increased with the exposure time, following a trend similar to the one obtained for corrosion tests. However, these values, on average, are lower than the values obtained for corrosion tests for the same exposure period, particularly in the high cycle range.

A possible explanation of this inequality in the development of surface degradation due to the corrosive environment may be the nature of the aqueous solution flow around the specimen during the fatigue test. The inlet and outlet on the corrosion chamber employed for tests in Exova facility, shown in Figure 4.32, were both placed on the same side with respect to the specimen position. In other words, if the chamber is ideally divided into two halves, following the longitudinal axis of the specimen, inlet and outlet are both placed in the same half of the section, one on the bottom and one on the top of the chamber. This lack of symmetry may create an inhomogeneity between the two sides of the chamber, in terms of flow distribution and fluid dynamics. Considering the circulation system, it may be that the use of a single circulation pump for two corrosion fatigue units, combined with the possible pressure drops in pipes junctions, could have also reduced the flow velocity. However, this suggestion cannot be verified after the fact, as neither the AMRL nor the Exova corrosion flow velocity was measured.

The inlet and outlet location with respect to the specimen, along with the possible effect of the flow velocity decrease, may have restricted the flow to the half section where inlet and outlet were placed, with stagnant conditions, or similar, in the other half where a lower level of oxygenation would have occurred. This may explain the lower degradation and surface roughness found on half of the surface. Additionally, the flow decrease could have induced a lower pit development on the surface of the specimens, compared to AMRL tests, which would explain the longer fatigue life of the Exova set of experiments.

5.2.4 Results of Pre-Corroded Specimens Tested at 10 Hz

Experimental results obtained from uniaxial corrosion fatigue tests at a frequency 10 Hz on specimens previously exposed to the corrosive solution for 21 days are plotted in a log-log S-N diagram, in Figure 5.31. Two conditions of stress ratio were selected for these tests: R=-1 and R=0.5. Approximation of the S-N curve, for each set of stress ratio, is described by Basquin’s law, for which constants were obtained by linear regression, summarised in Table 5.4. The comparison between the pre-corroded experimental results and results obtained from simultaneous corrosion fatigue on virgin specimens are discussed later, in Section 5.3.

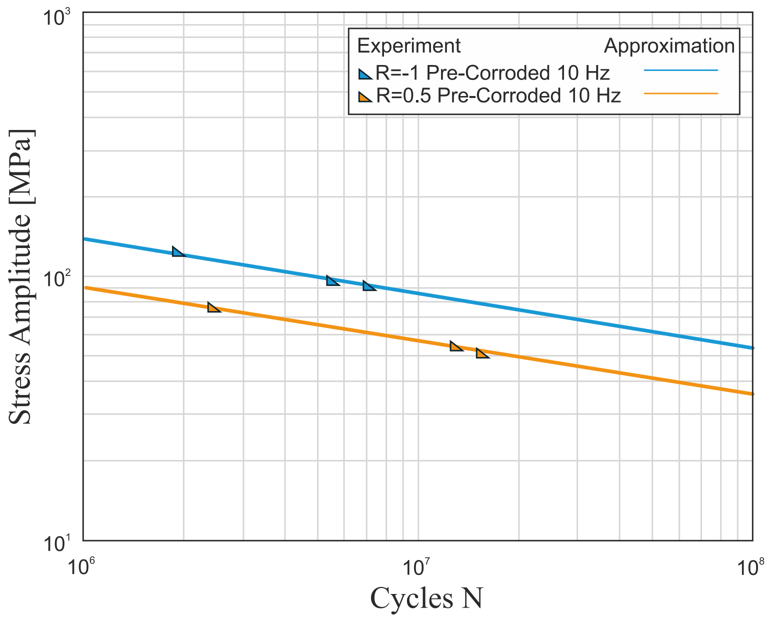

Figure 5.31: log-log S-N curves obtained from pre-corroded specimens tested at 10 Hz in the corrosive environment.

Table 5.4: Constant values for S-N curves of pre-corroded specimens.

Type of loading	σ_f' , MPa	b
R=-1	2606	-0.2030
R=0.5	1775	-0.2051

Analysis of fracture surfaces of pre-corroded specimens tested in corrosion fatigue conditions was performed to evaluate if any different features were visible in comparison to fracture surfaces of specimens without the pre-corrosion treatment.

Figure 5.32 shows the fracture surface of specimen T419, failed after 5.5 million cycles. From this surface, multiple propagation cracks are visible on slightly different planes that converged before final fracture. All cracks, as previously seen for synchronous corrosion fatigue fracture surfaces, initiated from the surface of the specimens. The presence of multiple cracks is even more likely to occur than in simultaneous corrosion fatigue on virgin specimens as pre-corroded specimens have a rough surface at the beginning of corrosion fatigue tests from which cracks may initiate.

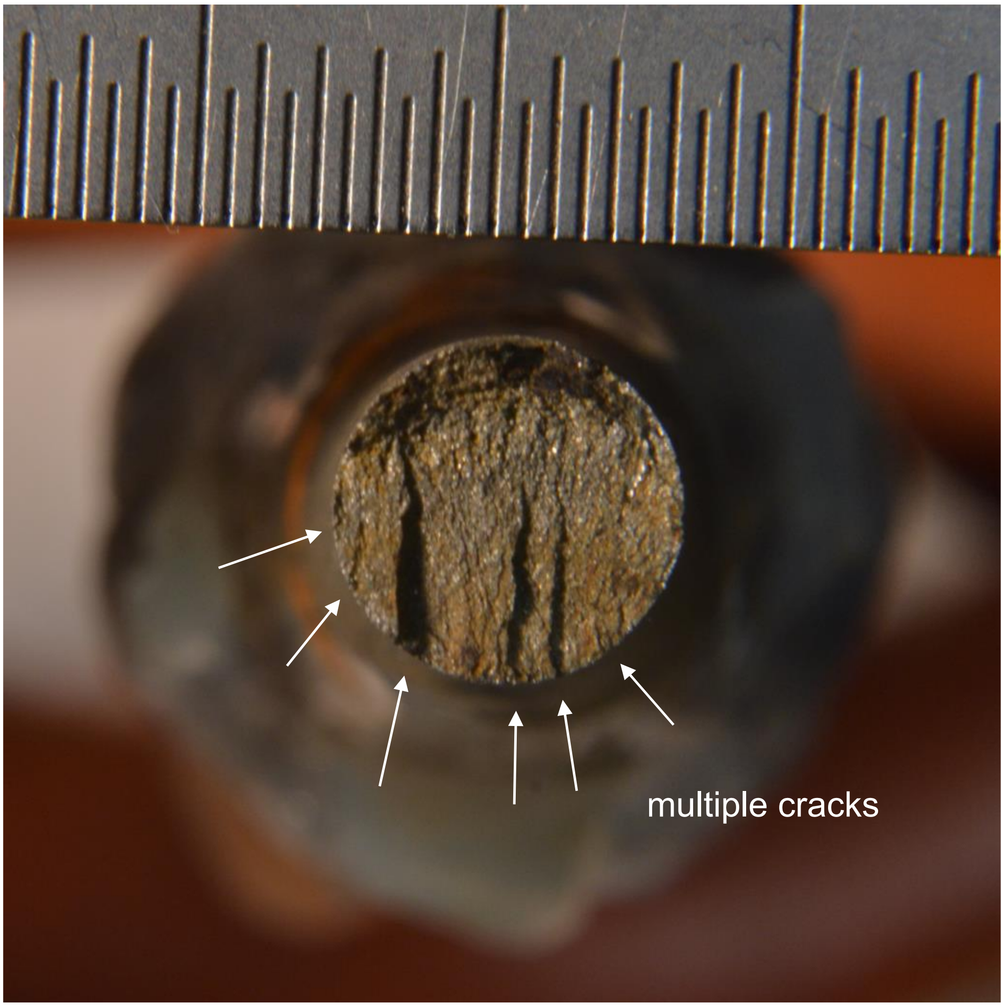

Figure 5.32: The fracture surface of pre-corroded specimen T419. *Corrosion fatigue life 5.5 million cycles.*

Optical visualisations were performed on specimens, sectioned along the longitudinal axis.

Figure 5.33 and Figure 5.34 show the surface profile of pre-corroded specimens failed after 7 million and 13 million cycles respectively. Degradation of the external edge is visible in both sections and, particularly in the case of specimen T315 in Figure 5.34, the rough profile of the surface indicates a loss of material due to corrosion exposure. The overall exposure to the corrosive environment in this test was 36 days. Various pits were spotted on the analysed surfaces of pre-corroded corrosion fatigue specimen. All pits present a semi-elliptical shape. Dimensions of the bigger pit, found among the pre-corroded specimens, are 88 µm depth and 135 µm width.

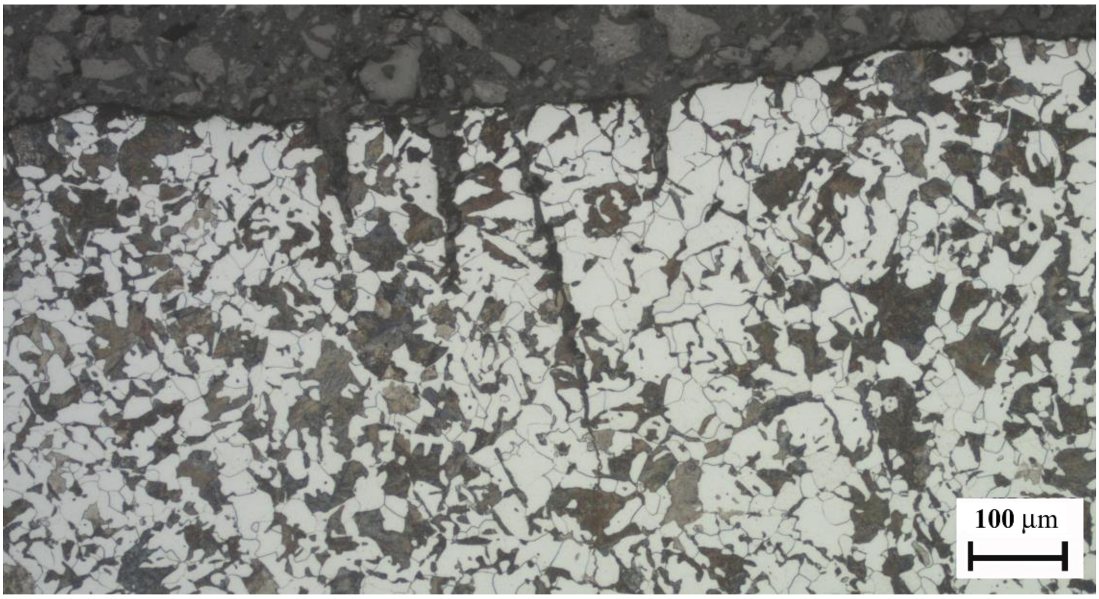

Figure 5.33: Longitudinal section of specimen T420, failed at 7 million cycles. *Detail of external surface profile. Magnification x100.*

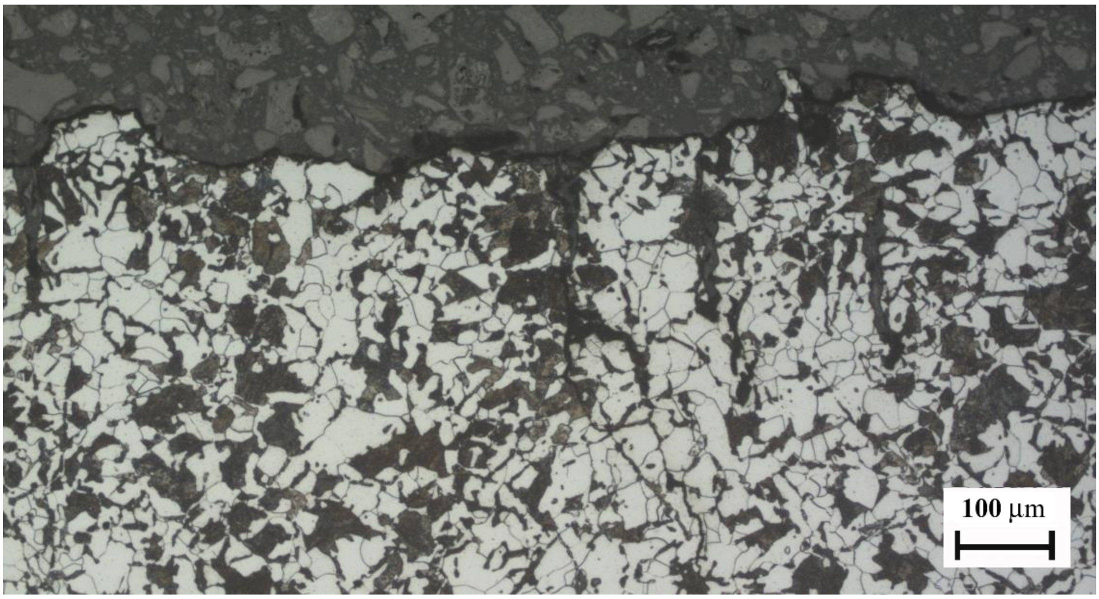

Figure 5.34: Longitudinal section of specimen T315, failed at 13 million cycles. *Detail of external surface profile. Magnification x100.*

5.2.5 Results of High Frequency Corrosion Fatigue Tests

The experimental results obtained from uniaxial fatigue tests in the corrosive environment performed at 100 Hz in the AMRL facility are plotted in a log-log S-N diagram in Figure 5.35. At this elevated frequency, because of test machine characteristics, it was impossible to maintain a fixed value of stress ratio within all tests. All stress ratio values were around R=0.3, with a minimum of R=0.28 and a maximum of R=0.34. In Figure 5.35 the various stress ratio conditions are highlighted by different colours. Although the number of experiments is not sufficient to perform a statistical analysis, comparing high-frequency results with data obtained in the region up to 10^7 cycles, shows the scatter at higher fatigue cycles is wider. This feature could be associated with the difference in the stress ratio conditions.

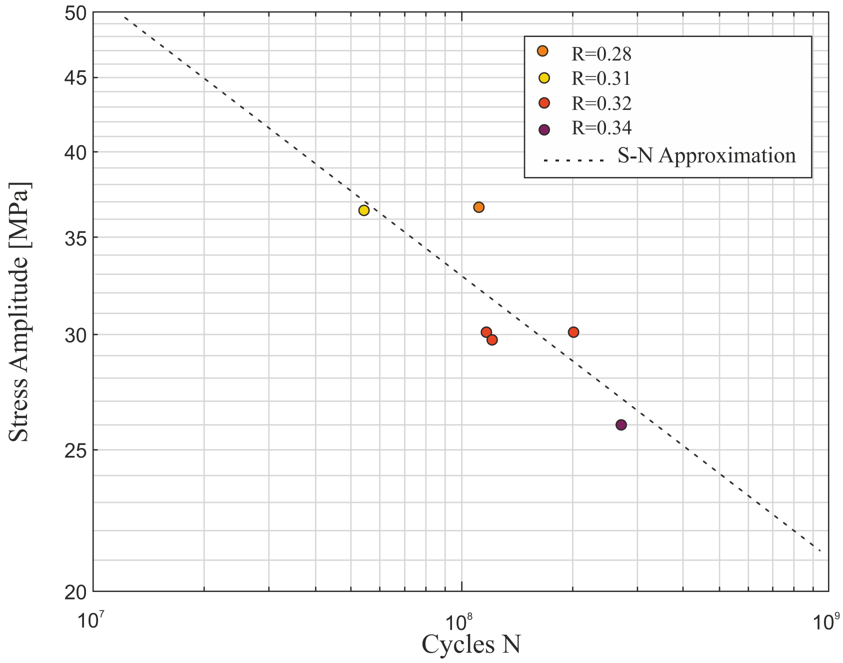

Figure 5.35: log-log S-N diagram of corrosion fatigue results at 100 Hz.

In the case of about 36 MPa of stress amplitude, there is a difference in the maximum stress of 3.5 MPa between the two stress ratio conditions, R=0.28 and R=0.31. A similar scatter in data is found also within results obtained at the same stress ratio condition R=0.32. Moreover, S-N experimental data available in literature, both in corrosive environment and in air [133-135] show that in the region of fatigue cycles higher than 10^8, divergence in experimental data is larger than in the region at higher stress amplitudes, for tests obtained under the same stress ratio condition and with the same loading equipment.

Based on these observations, the set of data at a load frequency of 100 Hz is grouped in the same family, nominally classified as R=0.3. Although a possible inaccuracy may be introduced with this procedure, the aim is to understand the trend of S-N curves, and the behaviour of S355J2, in the very high cycle fatigue region in the freshwater environment. Therefore, all experimental results from this set were used to calculate the best-fit equation through linear regression, to describe the behaviour of

S355J2 in this region and to extrapolate the curve to 10^9. Constant values that describe the Basquin's equation are summarised in Table 5.5.

Table 5.5: Constant values for S-N curve obtained at frequency 100Hz.

Type of loading	$\sigma_f^{'}$, MPa	b
R=0.3	1340.1	-0.1940

It is noted that because of the higher frequency, the characteristics of surfaces, and therefore the conditions for which cracks are initiated, may be different from those that would have occurred if tests were run at 10 Hz, which would mean a longer corrosion exposure time. The fatigue failure for most specimens run at 100 Hz occurred between 100 and 230 million cycles. This region corresponds to corrosion fatigue test lengths of roughly 12 to 27 days, equivalent to the time in which specimens were subjected to corrosion exposure. This means that, at the time of fatigue failure, the surface features of roughness and pits dimensions, caused by corrosion exposure, are expected to be aligned with the steady values obtained from corrosion testing shown in Figure 4.22 and Figure 4.25. To verify this suggestion, an analysis of specimen surfaces after corrosion fatigue tests were performed using various magnification lenses.

Figure 5.36 and Figure 5.37 show the section of specimen T716 and T722 respectively, obtained with magnification x50. In both examples, general degradation, caused by the effect of corrosion, can be identified throughout the external surface, as well as thanks to the presence of pits.

Figure 5.38 and Figure 5.39 show details of pit developed from the surface of specimen T722 and T720 respectively, obtained with magnification x100.

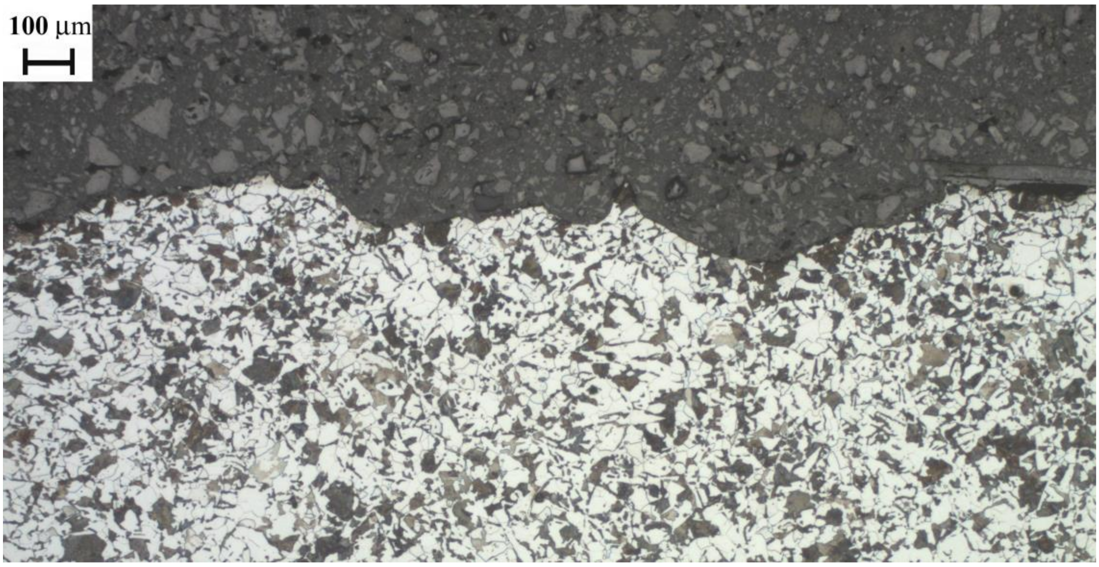

Figure 5.36: Longitudinal section of specimen T716, 1.11 10^8 cycles. *Magnification x50.*

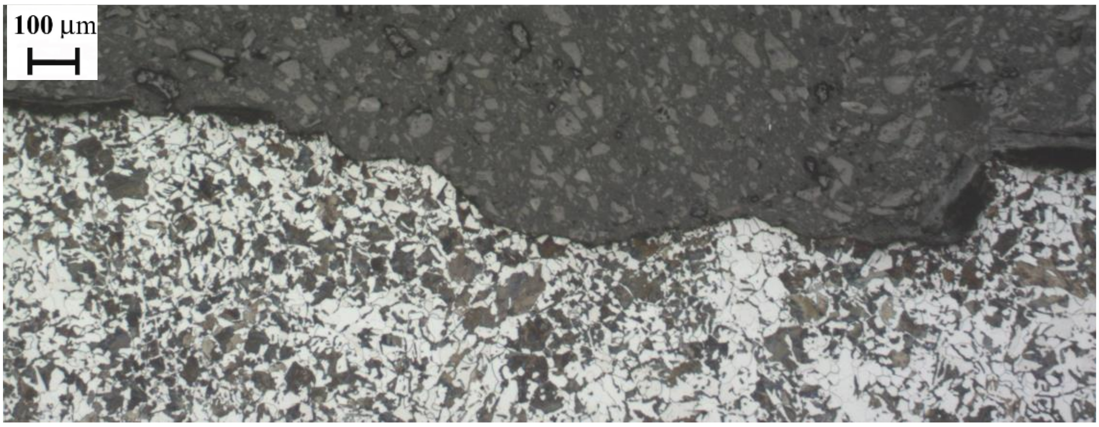

Figure 5.37: Longitudinal section of specimen T722, 1.19 10^8 cycles. *Magnification x50.*

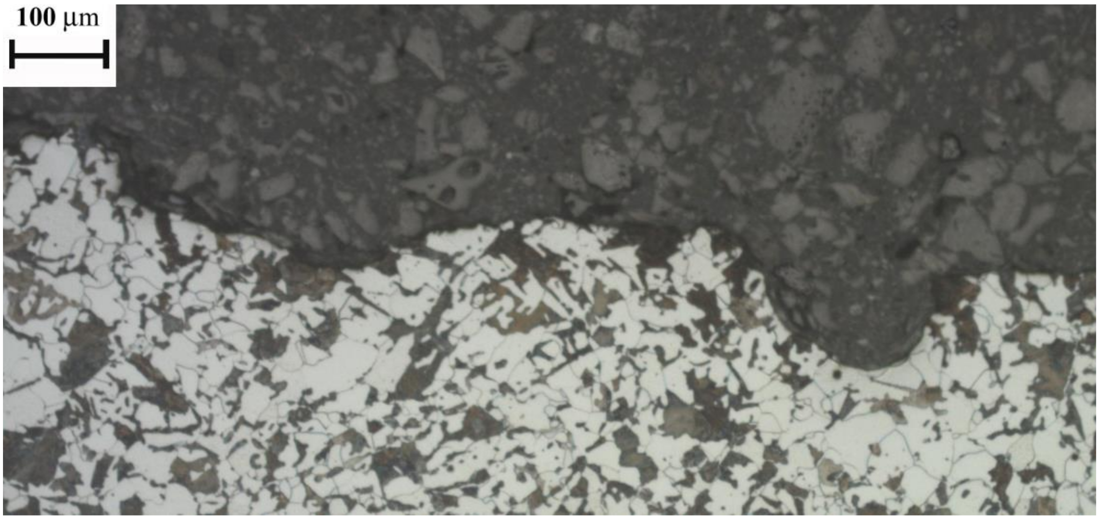

Figure 5.38: Longitudinal section of specimen T722, 1.19 10^8 cycles. *Magnification x100.*

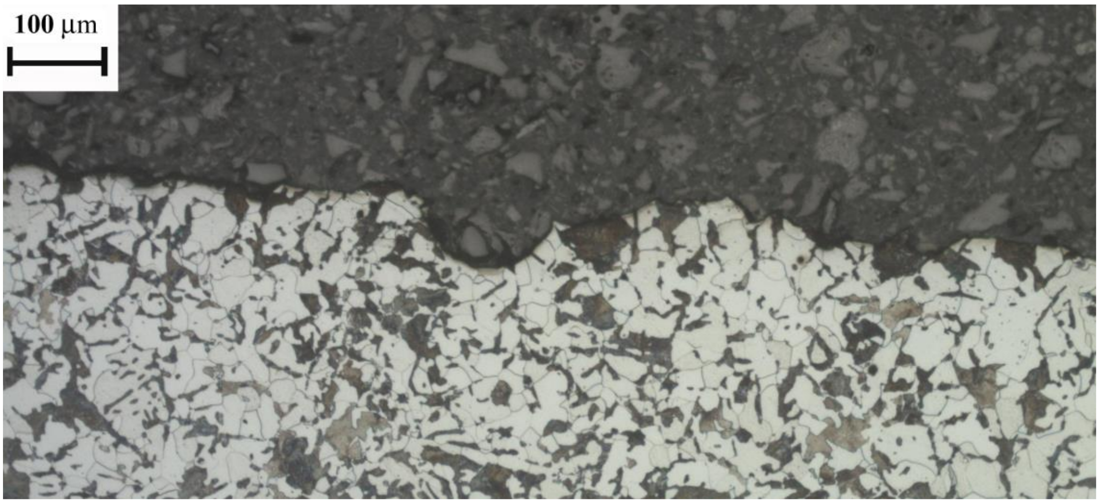

Figure 5.39: Longitudinal section of specimen T720, 2.05 10^8 cycles. *Magnification x100.*

It is interesting to compare the characteristics of the surface of specimens tested at high frequency and pre-corroded specimens tested at lower frequency. In terms of exposure to the corrosive environment, these two conditions are similar, since the overall time of pre-corrosion and corrosion fatigue testing, in one case, and the time of corrosion fatigue test, in the other case, are in some cases of the same length. From this comparison, two main aspects are highlighted. The quality of surface in the case of high frequency tested specimens is strongly affected by corrosion effect, as expected the general surface roughness and pit dimensions are of the same order identified on the surface of tested corrosion fatigued. This confirms the trends found in corrosion tests results. It can be concluded, consequently, that the initial phase of corrosion fatigue life is mainly dominated by the corrosion mechanism, that it is time-dependent. However, after a certain amount of time, the effect of corrosion doesn't alter the characteristics of the surface, such as pits depth and surface roughness, but is only the cause of a general material loss. The second aspect that distinguished the two sets of surfaces is the almost absence of propagated cracks from pits on the lateral surface, in the high-frequency set of specimens, whereas multiple cracks are found in pre-corroded specimens. This feature is connected to the level of stress amplitude at which tests are performed. High-frequency tests are characterised by fatigue failure at elevated cycles achieved through a low level of stress amplitude. The pre-corroded specimens are tested at higher stress amplitude which is responsible for the fatigue failure at lower cycles. In this higher condition of loads, the critical dimension for which cracks started to propagate is achieved in multiple points, potentially at different times.

5.3 Evaluation of Corrosion Fatigue Strength

To evaluate the fatigue strength of low carbon steel and to estimate the degradation due to aqueous solution, experimental results from uniaxial fatigue tests are analysed. Fatigue data obtained in air were used to define properties of S355J2 in non-aggressive conditions, Section 5.1, to be used as a reference to evaluate the effects of the interaction between corrosion and fatigue phenomena.

From the experimental results fractography of specimens tested at Exova and at AMRL, many differences were identified and discussed in Section 5.2.2. On the basis of this discussion, the two sets of data cannot be considered to belong to the same family. The corrosion inequality occurring on the Exova specimens surface is not representative of the corrosive degradation that affects Fluid End components in GEHO pumps where no preferential corrosion sites have been identified. Therefore, the Exova data are not used here in the prediction of the corrosion fatigue strength of S355J2 at high cycles in the corrosive environment. However, they are considered when evaluating the mean stress effect in corrosive environment to understand if different corrosive environments can change the relation between allowable amplitude stress and mean stress at a fixed fatigue life.

A comparison between experimental results obtained for uniaxial fatigue tests in air and in the freshwater corrosion environment, performed at 10 Hz in AMRL, is undertaken to evaluate the detrimental effect of the corrosive environment on fatigue strength. Experimental results in both environments and approximation of S-N curves from Basquin's equation for each set are reported in the log-log S-N diagram shown in Figure 5.40.

The degradation of fatigue strength due to the corrosive environment of the S355J2 low carbon steel is already tangible at low numbers of cycles. Around 300000 cycles, approximately 8 hours of testing at 10 Hz, the fatigue strength of S355J2 at stress ratio R=0 decreased by 11% compared to behaviour in air, from 194 MPa to 174 MPa. At longer fatigue lives, the effect of the environment is more significant. The difference between fatigue life values obtained in air and in the aqueous environment is larger at a higher number of cycles, as shown by experimental results in Figure 5.40. At 6 million cycles, almost seven days of testing, fatigue strength decreased of more than 50% both for stress ratio R=-1 and R=0 when compared to the same loading condition in air. The fatigue strength for R=0.5 in corrosive solution at 6 million cycles is 38% of fatigue strength in air at R=0 and 31% of fatigue strength at R=-1. The fatigue strength reduction in this case is due to the combined effect of the corrosive environment and positive mean stress.

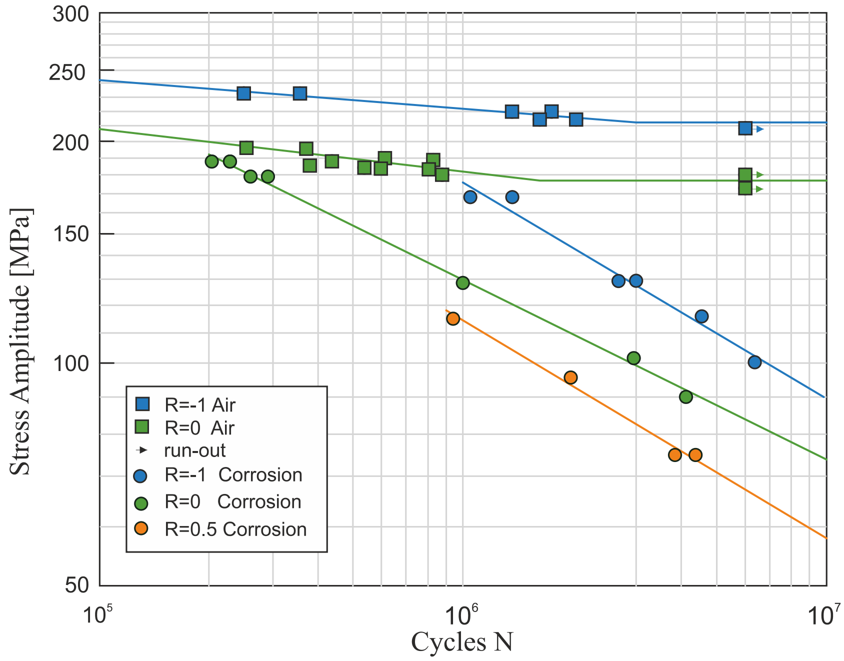

Figure 5.40: Fatigue and corrosion fatigue results on uniaxial specimens tested in AMRL at 10Hz. *log-log S-N curves.*

To further evaluate the degradation of corrosive environment on fatigue life and the interaction between corrosion and fatigue, the corrosion fatigue results obtained from pre-corroded specimens are compared to results obtained from simultaneous corrosion fatigue tests on virgin specimens. Data are plotted in the log-log S-N diagram for the two stress ratio conditions in Figure 5.41.

The effect of a previous corrosion exposure on corrosion fatigue life is greater at higher stress amplitudes and it decreases when the stress is lower, for both stress ratio conditions. At stress amplitude equal to 45% of the yield stress, for R=-1, the fatigue life of pre-corroded specimens decreases by a factor of 1.9 compared to simultaneous corrosion fatigue on virgin specimens. At a stress amplitude of 35% of the yield stress, the decrease in fatigue strength is of a factor of 1.3. Similar trends are also visible for the stress ratio condition R=0.5. At stress amplitude 75 MPa, the fatigue life of the pre-corroded set of specimens is 1.75 times shorter than the corrosion fatigue life of virgin specimens. However, at lower amplitude stresses, it appears that the fatigue life

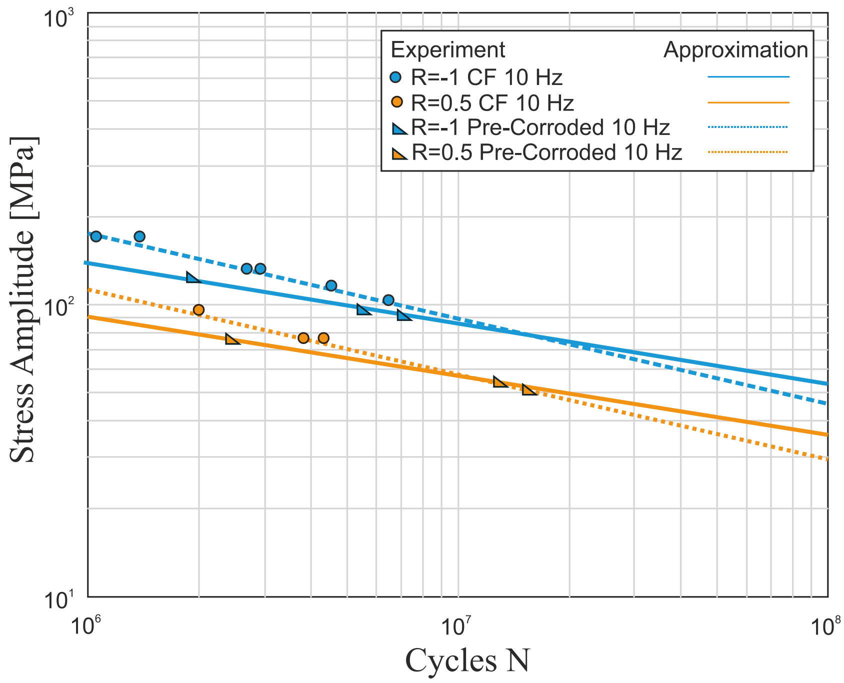

Figure 5.41: Comparison of log-log S-N curves in two different conditions of induced corrosion.

of pre-corroded specimens is almost the same as simultaneous corrosion fatigue testing on virgin specimens, based on the extrapolation of the S-N curve.

The difference in fatigue life at low cycles can be explained by the effect of the period of non-steady corrosion on the specimen surface, identified through corrosion testing. In specimens where the corrosion effect started simultaneously with the cyclic loads, some time was needed for the corrosive solution to start the process of deterioration on the specimen surface, leading to a longer overall corrosion fatigue life. In contrast, in the pre-corroded, the surface already presented the characteristics of roughness and pit depth, described in Section 3.4, that is distinctive for the steady phase, as they were exposed to the corrosive environment for 21 days. Therefore, pre-corroded specimens showed a shorter fatigue life in the region up to approximately 10 million cycles.

Figure 5.41 shows that the difference, in term of corrosion fatigue lives, between the two conditions decrease with the fatigue cycles until the two S-N curves intersect, for both stress ratio conditions. The intersection occurs at a corrosion fatigue life higher than 10^7 cycles. For both conditions, this intersection corresponds to a test length around 16 days, which is the steady phase of corrosion degradation, according to corrosion tests on unloaded specimens. It is proposed that in this condition of intersection between the two curves, the surface characteristics of the specimens from different initial conditions are aligned. This suggestion is supported by other researches [130, 136, 137] showing that pit growth is not uniform during the corrosion fatigue life of various low carbon steels. The pit growth rate decreases with increasing cycles, up to the condition in which the pit achieves a critical dimension from which the transition from pit to crack occurs. This means that, when the material is tested under corrosion fatigue conditions, initially, the pits grow quickly, then the rate of growth decreases. It can be supposed that after a certain amount of time, in which pit grows with different rates based on the two initial conditions, the dimension of pit and the consequent transition to crack would be led by the cyclic effect of the load in combination with the surface properties of the material. Characteristics of the surface of pre-corroded specimens at the beginning of corrosion fatigue testing are such that pits are already developed. Consequently, the growth rate of pits in corrosion fatigue testing on pre-corroded specimens should be lower than the growth rate on virgin specimens. Therefore, at higher fatigue cycles, the rough conditions of the surface align for both conditions, and the corrosion fatigue failure is led by cycling stress conditions.

This would suggest that once the two conditions are aligned, the corrosion fatigue life of both will also aligned and described by the same S-N curve. In particular, the curve that describes the behaviour is the one obtained as the best fit of pre-corroded data, as shown in Figure 5.42.

The suggestion that a single curve which describes the behaviour at high cycles for both pre-corroded and virgin initial conditions is supported by the corrosion fatigue data obtained at the loading frequency of 100 Hz in the AMRL. Figure 5.42 shows experimental results obtained at 10 Hz for pre-corroded specimens and virgin specimens at stress ratio R=0.5, and the results obtained at 100 Hz. The S-N curves obtained from linear regression for each data set, are shown up to 10^9 cycles. At fatigue cycles higher than 20 million, the approximation obtained by the extrapolation of S-N curve of pre-corroded specimens is similar to the one obtained for corrosion fatigue testing at 100 Hz, whereas the approximation of simultaneous corrosion fatigue at 10 Hz on virgin specimen predicts a shorter fatigue life. It should be noted that the two curves (high frequency and pre-corroded) are the results of two different stress ratio conditions. The differences between the prediction (R=0.5) and experimental data (R=0.3) are believed to be caused by the effect of mean stress.

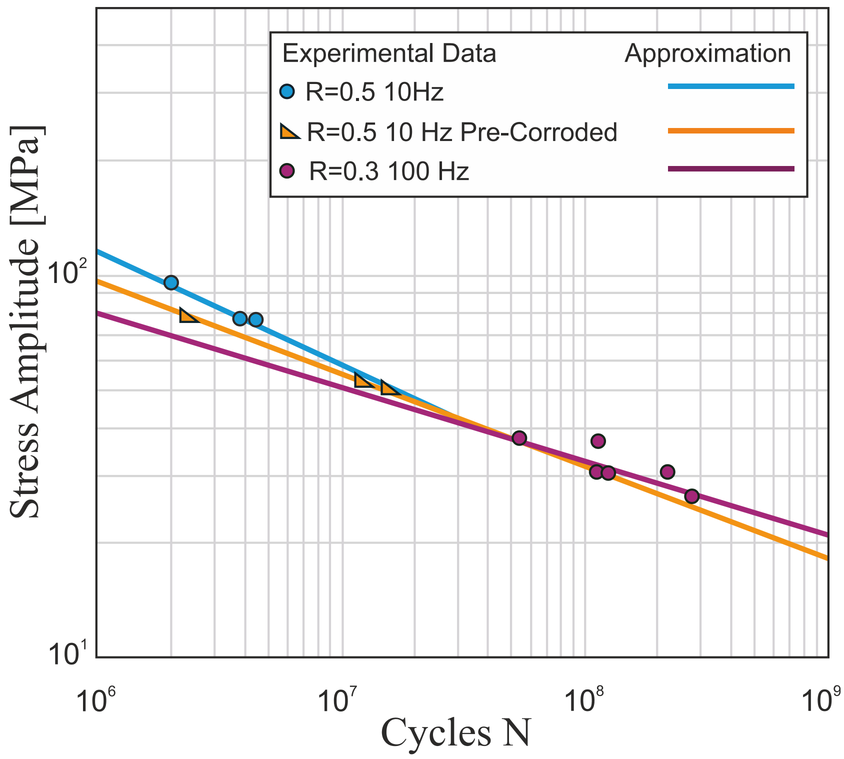

Figure 5.42: log-log S-N curves of S355J2 in the freshwater environment. *Comparison of experimental data at 10Hz, 100Hz and pre-corroded.*

The corrosion fatigue data obtained at 100 Hz may have been affected by the frequency and, consequently, the fatigue strength may be higher than that for tests at lower frequency. Although it has been shown that materials tested in air show an increase in fatigue strength proportional to the increasing of loading frequency [61, 138, 139], this effect occurs after a certain value of frequency. Nicholas [61] has shown that below 300 Hz the difference in fatigue strength is negligible, for the most materials. The range of frequency that mainly affects fatigue properties is between 1000 Hz and 3000 Hz. Therefore, no frequency effect is considered in the evaluation of fatigue strength for tests performed at 100 Hz.

From Figure 5.42, there is not a linear correlation between behaviour in the region around 10^6 and 10^8 cycles. The fatigue strength in the very-high cycles regime cannot be predicted by the same Basquin's law used in the range of lower fatigue cycles ($\approx 10^6$) for simultaneous corrosion fatigue tests on virgin specimens. The comparison between high-frequency tests and pre-corroded corrosion fatigue tests leads also to another interesting aspect. Once the cracks start to propagate, the fatigue life is cycle dependent and not time dependant. This characteristic also applies in the steady corrosion phase. This is significant, as the effect of frequency in this region does not affect the corrosion fatigue life. Therefore, for applications working in a corrosive environment designed for an expected life in the very high cycle fatigue region, it would be convenient from an experimental point of view to use pre-corroded specimens and perform the tests at high frequency.

To summarize, the corrosion fatigue life of S355J2 in the region between 10^5 and 10^9 cycles can be described by the combination of two trends. In the non-steady corrosion region, where the influence of corrosion is predominant, the behaviour is better described by Basquin's law obtained from simultaneous corrosion fatigue tests on virgin specimens. Ideally, experimental data to characterise this region should be performed at the same frequency of the real application. The second region, when the characteristics of degraded surfaces become steady, can be described by Basquin's law obtained from higher frequency tests as the behaviour is mainly influenced by the cyclic loads instead of the time of exposure to the corrosion. In general, if the whole life is described by the extrapolation of S-N curve obtained from the linear interpolation of experimental data at 10 Hz (low-frequency), a conservative error would be introduced in the prediction.

5.4 Mean Stress Analysis

5.4.1 Evaluation of Mean Stress Effects on Fatigue Strength in Air

To evaluate the effect of positive mean stress on fatigue performance in air, the experimental results, obtained from the two stress ratios, are used to define a Haigh diagram and to calculate the value of the constant parameter γ required in Walker's equation (3.10). From the analysis of the mean stress approaches available in the literature, presented in Chapter 3, Walker approach gave the best prediction of the variation of fatigue strength in air of carbon and low carbon steels. Therefore, this method is initially employed to define the allowable stress amplitude in the Haigh diagram.

The best fit value of the parameter γ, found using the least-squares method, is 0.7214. To understand the difference between the predicted equivalent stress amplitude, obtained through Walker equation, and the stress amplitude obtained from uniaxial fatigue tests, a graph is proposed where these values are compared with an ideal zero-error line, for various number of cycles from 300000 to 1.8 million, shown in Figure

5.43. The distance between each point and the non-error line indicates the difference, in MPa, between the amplitude stress obtained through Walker's approach and the amplitude stress obtained from the experimental investigation. The predictive model tends to be more conservative at higher cycles, close to the fatigue limit, where all points lie below the zero-error line.

Using the Walker equation, the Haigh diagram for positive mean stress is defined and the limit for allowable fatigue strength can be identified for every number of cycles. Figure 5.44 shows the Haigh diagram at three extensions of fatigue life.

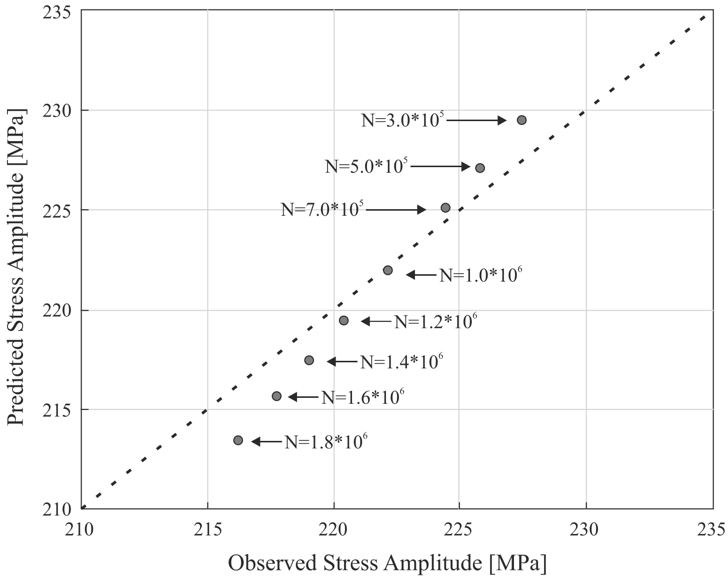

Figure 5.43: Predicted stress amplitude using Walker criterion versus observed stress amplitude.

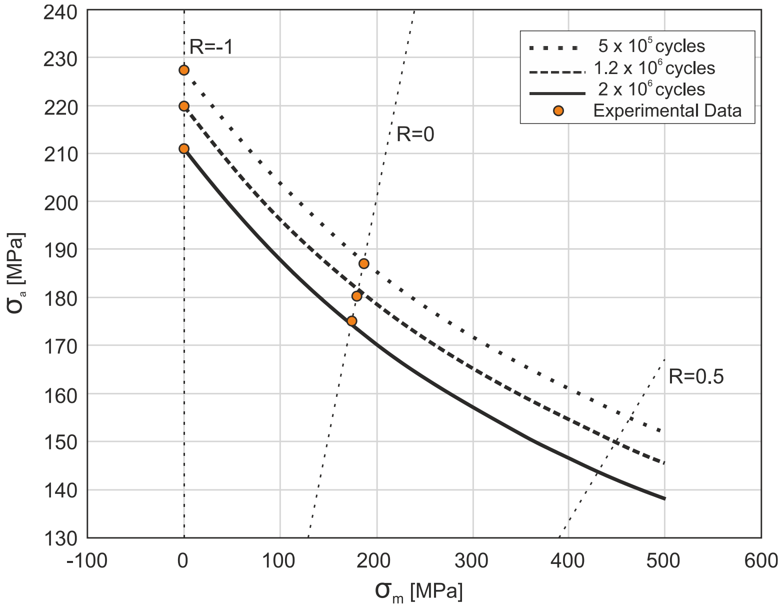

Figure 5.44: Haigh diagram for data in air at various number of cycles.

Comparative analysis between the Walker approach and the FKM approach is proposed to highlight advantages and limitations of these approaches in the prediction of allowable fatigue strength of S355J2. To define the fatigue strength according to FKM guideline, the mean stress sensitivity factor M_σ must be calculated. Two calculations are proposed for this analysis. In one case, the mean stress sensitivity factor is calculated using the definition available in the FKM guideline, (2.16), and the material constants proposed for steels, summarised in Table 5.6. In the second case, the mean stress sensitivity factor is obtained using its general definition proposed by Schutz [140], reported in equation (5.1), which is the absolute value of the slope of the constant life plot [101].

$$M_\sigma = \frac{\sigma_{a,R=-1}}{\sigma_{a,R=0}} - 1 \tag{5.1}$$

The values of stress amplitude, required in the definition, are taken from the experimental results, of Table 5.7. The graphical comparison between the three approaches is plotted in the Haigh diagram, shown in Figure 5.45.

Table 5.6: Values used to calculate the mean stress sensitivity factor M_σ in air, proposed by FKM.

a_M	b_M	σ_U (MPa)	$M_{\sigma,FKM}$
0.35	-0.1	500	0.0750

Table 5.7: Values used to calculate the mean stress sensitivity factor M_σ in air, proposed by Schutz.

$\sigma_{a,R=-1}$ (MPa)	$\sigma_{a,R=0}$ (MPa)	$M_{\sigma,Schutz}$
211	176	0.1989

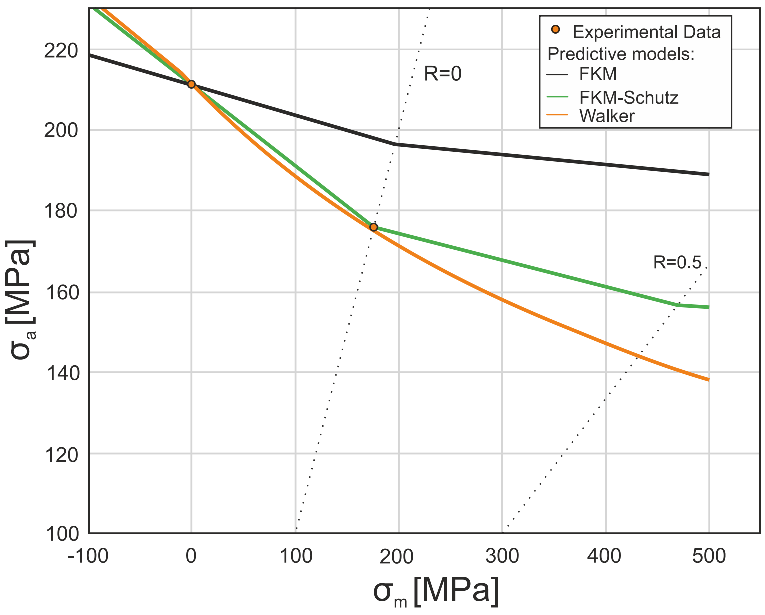

Figure 5.45: Haigh diagram in air. *Comparison between experimental data and FKM, Schutz and Walker prediction.*

The allowable stress limits predicted using the mean stress sensitivity factor proposed by FKM guideline, compared to Walker's approach and in general with experimental data, are visibly not conservative, particularly in Region III and Region IV, for values of stress ratio R higher than zero. At R=0 the FKM predicted allowable stress is more than 20 MPa higher than the one obtained experimentally and, since the mean stress sensitivity factor value is particularly low, at higher values of stress ratio R, the difference becomes larger and the model less accurate. However, when allowable stress limits are obtained through the FKM procedure, using the mean stress sensitivity factor by Schutz definition and experimental data, the difference with Walker approach is negligible at low value of stress ratio and a maximum of 15 MPa at values of mean stress close to the ultimate strength.

From a practical point of view, to design the Haigh diagram in air at least two sets of experimental data, at stress ratio R=-1 and R=0, are required to estimate the parameter required in the Walker approach and for the calculation of the mean stress sensitivity factor used in FKM procedure. To better understand which of the two approaches give a better prediction of the allowable stress at values of stress ratio greater than 0.5, another set of experimental investigation would be required.

5.4.2 Evaluation of Mean Stress Effects in the Corrosive Environment

Three sets of corrosion fatigue experimental results are used to analyse the effect of positive mean stress on corrosion fatigue strength and to design constant life diagrams. In the corrosive environment, the fatigue strength of S355J2 continuously decreases with number of cycles and a fatigue limit is not present. Here, constant life diagrams are evaluated at 0.9 million, 2 million, 5 million and 10 million cycles to failure. The corresponding values of stress amplitude are calculated using Basquin's law equations obtained by interpolation of corrosion fatigue experimental results for stress ratios R=-1, R=0 and R=0.5, tested in AMRL at 10 Hz. Using the relations between the stress amplitude and stress ratio, the values of mean stress at the same fatigue life are obtained for all three stress ratios and are plotted in the Haigh diagram shown in Figure 5.46.

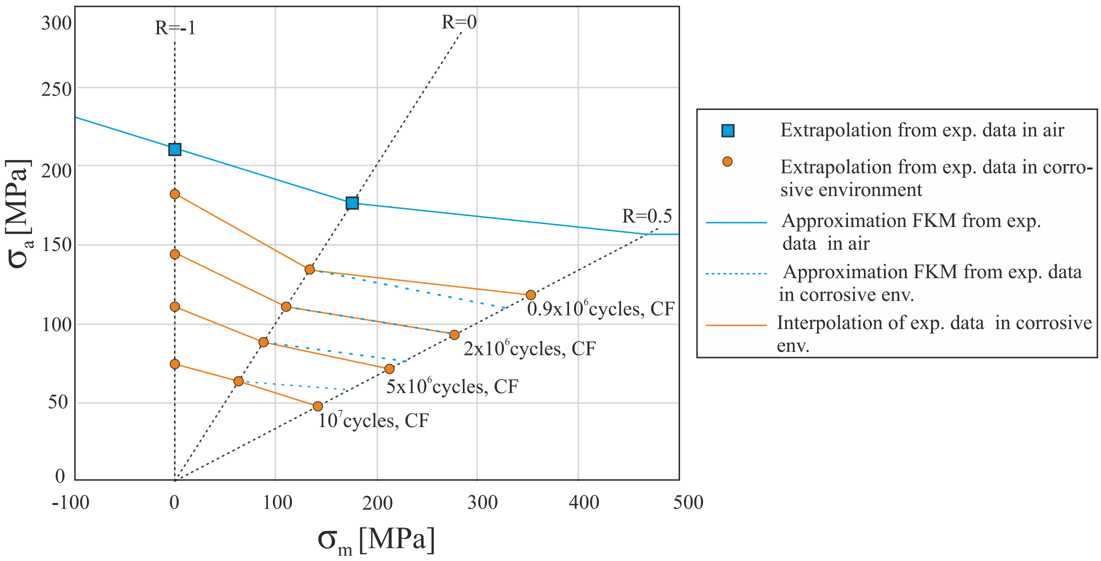

Figure 5.46: Haigh diagram for experimental data in air and in corrosive environment.

This illustrates the progressive effects of mean stress on corrosion fatigue strength. Experimental values for fatigue strength in air for R=-1 and R=0 are also shown. The allowable fatigue strength in air is defined by the FKM approach, where the Schutz mean stress sensitivity factor is calculated directly from experimental results. Similarly, the Schutz definition is used to calculate the allowable corrosion fatigue strength. Consequently, values of mean stress sensitivity factor M_σ are defined for each selected fatigue life and numerical values reported in Table 5.8. The variation of mean stress sensitivity factor with the corrosion fatigue life, valid in the range of fatigue life described by the S-N curves obtained through simultaneous corrosion fatigue of virgin specimens, was found to be given by equation (5.2):

$$M(N_{cf}) = -0.064\ln(N_{cf}) + 1.2394 \tag{5.2}$$

Table 5.8: Values of mean stress sensitivity factor from data at 10Hz, AMRL.

Number of Cycles	M_σ
0.9 million	0.363
2 million	0.310
5 million	0.251
10 million	0.207

Figure 5.46 shows that the sensitivity of the tested low carbon steel to mean stress in the freshwater environment approaches the behaviour in air only at high numbers of cycles to failure. The mean stress sensitivity factors tend to decreases with increasing of fatigue life. At lower numbers of cycles, less than 1 million, the slope of the joining line from R=-1 and R=0 is steeper, with a value of M_σ higher almost twice that at 10 million cycles. This trend suggests that the corrosive environment influences both the fatigue strength of S355J2 and the mean stress effect.

According to the FKM procedure, to define the allowable fatigue strength in the region in between R=0 and R=0.5, the slope of the line joining R=0 with R=0.5 is 1/3 of the slope in the region in between R=-1 and R=0, that is 1/3 M_σ. When this definition is employed, the predicted values of stress amplitude at stress ratio R=0.5 do not match with the experimental results. This difference is shown in Figure 5.46. At fatigue lives less than 1 million cycles, the FKM approach predicts a conservative value of allowable stress amplitude. However, at higher fatigue cycles, the trend changes and the allowable stress predicted by the FKM approach is higher than the fatigue strength obtained experimentally and, consequently, is not a safe prediction.

This comparison suggests that the effect of positive mean stress on corrosion fatigue life cannot be studied without taking into account the corrosive effect. The shape of the Haigh diagram describing the behaviour of the material in the corrosive environment is not a scaled version of the Haigh diagram in air. Therefore, a different approach needs to be considered to evaluate the effect of mean stress in the freshwater environment.

To properly predict the allowable corrosion fatigue strength in between R=0 and R=0.5, experimental data are taken into account and the slope of the line that joins these two points on the constant life diagram is calculated. Using a similar approach to FKM, a new parameter $M_{\sigma,3}$ is defined in this region (5.3):

$$M_{\sigma,3} = \frac{\sigma_{a,R=0} - \sigma_{a,R=0.5}}{\sigma_{m,R=0.5} - \sigma_{m,R=0}} \tag{5.3}$$

The physical meaning of this parameter is similar to the mean stress sensitivity factor defined by Schutz with the difference that $M_{\sigma,3}$ is evaluated in the region of the Haigh Diagram between R=0 and R=0.5, FKM Region III. This gives the absolute value of the slope of the line that joins R=0 and R=0.5 on the diagram and is a measure the extent to which the mean stress affects the corrosion fatigue life in this region. The relationship between the mean stress sensitivity factor $M_{\sigma,3}$ and the corrosion fatigue life was determined as equation (5.4).

$$M_{\sigma,3}(N_{cf}) = 0.0372\ln(N_{cf}) - 0.439 \tag{5.4}$$

Equation (5.4) is valid in the fatigue life range described by the S-N curve for simultaneous corrosion fatigue life of virgin specimens.

Mean stress sensitivity factors $M_{\sigma,3}$ at various number of cycles are reported in Table 5.9: In the same table, the ratio between the mean stress sensitivity factor in Region II and in Region III is calculated. Schematic representation the variation between R=-1 and R=0.5, as fatigue life changes, is shown in Figure 5.47. This shows that for increasing corrosion fatigue life, the low carbon steel in Region III becomes more sensitive to the mean stress and values of $M_{\sigma,3}$ tend to the mean stress sensitivity factors of Region II. Thus, at longer corrosion fatigue lives, the slope of the line in Region III becomes closer to the slope in Region II. At 15 million cycles $M_{\sigma,3}$ is almost the same value of M_{σ}. This means that the effect of positive stress ratio, for values of stress ratio higher than zero, is stronger in the corrosive environment than in air in the range of high cycle fatigue.

Table 5.9: Values of mean stress sensitivity factor in Region III. *Calculation based on simultaneous corrosion fatigue data obtained in AMRL at 10Hz and the comparison with Region II.*

Number of Cycles	$M_{\sigma,3}$	$M_{\sigma}/M_{\sigma,3}$
0.9 million	0.073	4.945
2 million	0.100	3.081
5 million	0.135	1.863
10 million	0.163	1.277
15 million	0.181	1.018

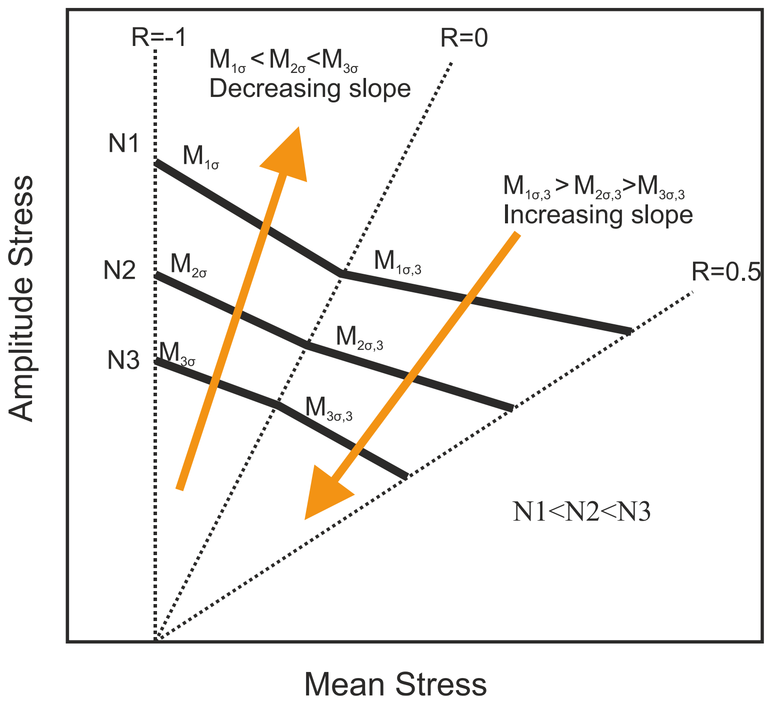

Figure 5.47: Trend of mean stress sensitivity factors in Region II and Region III with increasing corrosion fatigue life.

This same tendency is shown by the sets of data obtained in the corrosive environment developed by Exova. Figure 5.48 illustrates the Haigh diagram, at different corrosion fatigue lives, obtained using Exova experimental results using the same procedure as for AMRL results. For this experimental programme, the stress ratio conditions were R=0, R=0.5 and R=0.65, which define the borders in between Region II, Region III and Region IV. According to the FKM procedure, the allowable fatigue strength in Region IV is independent of the stress ratio. This means, for R≥0.5, the maximum allowable stress amplitude is a constant up to the ultimate strength of the material. However, as clearly shown by the S-N curves from Exova data, Figure 5.15, and from the corresponding Haigh diagram, Figure 5.48, the fatigue strength at R=0.65 is lower than the fatigue strength at R=0.5, for the same corrosion fatigue life.

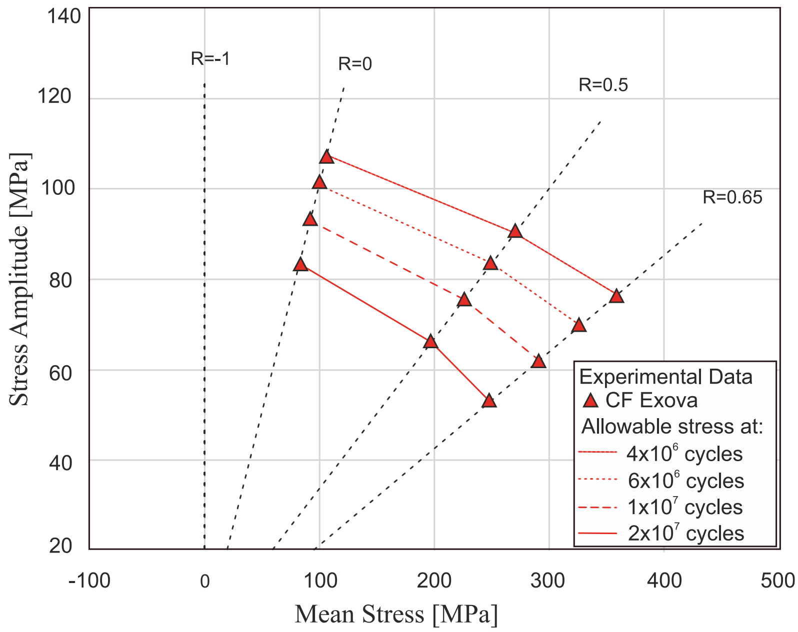

Figure 5.48: Haigh diagram for Exova experimental data in corrosive environment.

To take into account the decrease of fatigue strength in Region IV, the parameter $M_{\sigma,4}$ is defined as the absolute value of the slope of the line joining R=0.5 and R=0.65 in the diagram, equation (5.5). This parameter is the measure of the mean stress sensitivity in the Region IV.

$$M_{\sigma,4} = \frac{\sigma_{a,R=0.5} - \sigma_{a,R=0.65}}{\sigma_{m,R=0.65} - \sigma_{m,R=0.5}} \tag{5.5}$$

Values of mean stress sensitivity factor in Region III and Region IV are summarised in Table 5.10, for corrosion fatigue lives from 4 to 20 million cycles. These values are calculated using the values of stress amplitude and mean stress predicted from Basquin's equations.

Mean stress sensitivity factors in Region IV, $M_{\sigma,4}$, are higher than values in Region III, differing from the prediction of FKM. This confirms the trends that in the corrosive environment, the effect of mean stress on fatigue strength is more severe at high values of stress ratio. At longer fatigue life, values of mean stress sensitivity factor in both regions increase progressively, showing a higher effect at longer fatigue life. Interesting to notice is that the growth rates of mean stress sensitivity factor are different in the two regions: the higher the stress ratio, the faster the growth rate of mean stress sensitivity factor.

Table 5.10: Values of Mean Stress Sensitivity factor in Region III and Region IV. *Calculation based on simultaneous corrosion fatigue data obtained in Exova at 10Hz and comparison with Region III.*

Number of Cycles	$M_{\sigma,3}$	$M_{\sigma,4}$	$M_{\sigma,3}/M_{\sigma,4}$
4 million	0.103	0.154	0.672
6 million	0.114	0.177	0.646
10 million	0.128	0.209	0.613
20 million	0.149	0.262	0.567

A comparison between trends obtained from experimental results from Exova and AMRL was performed to assess the effect of the different corrosive conditions on mean stress sensitivity of low carbon steel. It was already discussed in the previous Section that the corrosion fatigue strength is tangibly influenced by the flow distribution of corrosive solution around the test specimen. Therefore, at the same fatigue life, the allowable corrosion fatigue stress in the Haigh diagram based on Exova experimental data is higher than the limits defined for AMRL. However, the aim of this comparison is to evaluate the influence of the corrosive flow conditions on the material's resistance to mean stress. For this purpose, the allowable corrosion fatigue strength for the two sets of data is calculated at fatigue life of 2 million, 5million, 10 million, and 20 million cycles and plotted on the same Haigh diagram, shown in Figure 5.49.

The only region on the Haigh diagram in which both conditions are completely defined by the experimental data is Region III, between R=0 and R=0.5. Values of stress sensitivity factor $M_{\sigma 3}$ for the two conditions are reported in Table 5.11. In both cases, the material tends to become more susceptible to mean stress with increasing fatigue life and therefore values of $M_{\sigma 3}$ increase with the fatigue lifetime. S-N curves obtained from AMRL data show a faster decrease of fatigue strength, compared to Exova. As a consequence, the increment of stress sensitivity factor for Exova data over the fatigue life is less than the increments shown for AMRL data and the ratio between these two parameters decreases with fatigue lifetime.

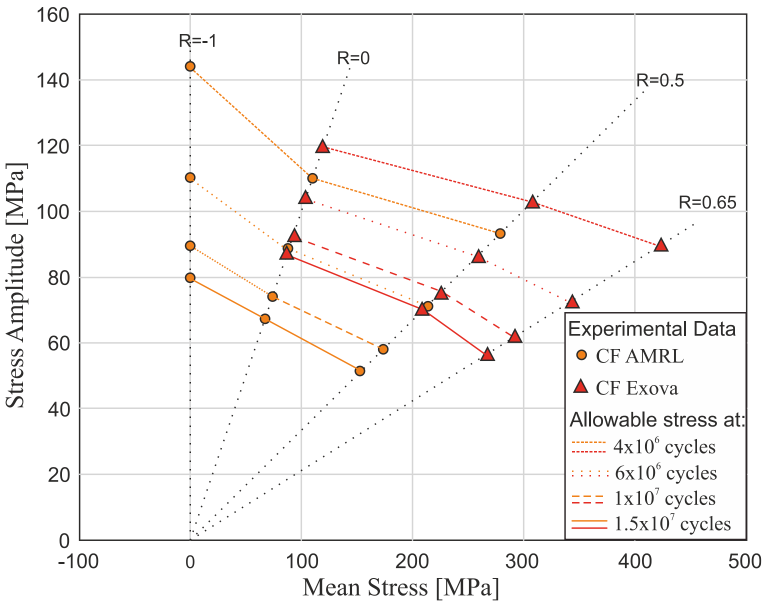

Figure 5.49: Haigh diagram in corrosive environments. *Comparison of allowable stress regions between data from AMRL and Exova.*

Table 5.11: Mean stress sensitivity factors calculated in Region III. *Calculation based on simultaneous corrosion fatigue experimental data in Exova and in AMRL at 10 Hz.*

Number of Cycles	$M_{\sigma,3}$ Exova	$M_{\sigma,3}$ AMRL	$M_{\sigma,3\_Ex.}/M_{\sigma,3\_AM.}$
4 million	0.086	0.099	0.866
6 million	0.109	0.133	0.820
10 million	0.128	0.162	0.793
15 million	0.140	0.181	0.779

The two values of mean stress sensitivity factor are of the same order of magnitude, for each of the selected fatigue lives, but values calculated with Exova results are smaller compared to the AMRL. This means, from a mean stress point of view, that in the corrosive flow conditions obtained in AMRL the material is more sensitive to mean stress than in Exova flow conditions, at the same fatigue life. Therefore, the corrosive flow characteristics influenced not only the fatigue strength of the S355J2 but also the relation of allowable amplitude stress and mean stress, at a fixed corrosion fatigue life.

From the same comparison between Exova and AMRL corrosion fatigue data, a second analysis was carried out. The aim of this analysis is to understand if any relation exists between the two sets to generalize the mean stress behaviour. It has been shown that the mean stress sensitivity factor is not constant over fatigue life and, in the case of Region III, it decreases. Because of the nature of the Haigh diagram, the values of mean stress sensitivity factor are compared at the same corrosion fatigue life and, based on the S-N curves in the two corrosive situations, the stress amplitude are always different for each comparison. It is interesting to compare the mean stress sensitivity factors obtained at the same level of stress, which are at different corrosion fatigue lives. Values of stress amplitude, at stress ratio R=0, were selected and the corresponding fatigue cycles, using Basquin's laws, calculated for both conditions. From the fatigue cycles, still using Basquin's laws, values of stress amplitudes at stress ratio R=0.5 were calculated and summarised in Table 5.12

Table 5.12: Values of mean stress sensitivity factor for AMRL and Exova conditions. *Data obtained at fixed values of stress amplitude.*

$\sigma_{a,R=0}$ MPa	$N_{f,AMRL}$	$N_{f,Exova}$	$\sigma_{a,R=0.5\_AMRL}$	$\sigma_{a,R=0.5\_Exova}$	$M_{\sigma,3\_AMRL}$	$M_{\sigma,3\_Exova}$
130	1.006×10^6	1.177×10^6	113.88	114.34	0.076	0.073
100	2.950×10^6	6.217×10^6	83.05	82.82	0.113	0.115
90	4.544×10^6	1.212×10^7	73.16	72.76	0.130	0.134
80	7.365×10^6	2.559×10^7	63.49	62.96	0.149	0.156

Results of this comparison show that the mean stress sensitivity factors in Region III are almost equivalent when calculated from the same value of stress amplitude in the two flow conditions. This shows that the flow conditions play an active role in the corrosion fatigue strength of the material, but do not affect directly the mean stress sensitivity. Thus, the corrosion fatigue strength in the two different environments is strongly affected by the corrosive conditions, as shown in the S-N curves, but the relationship between the stress amplitude and mean stress is almost equivalent for the same stress conditions.

This result can be considered from a fracture mechanism point of view. Specimens in Exova and in AMRL were tested in the same corrosive solution, in terms of chemical compositions, but in different flow conditions. The flow condition can be considered mainly responsible for the time spent on crack initiation whereas the stress condition determines the dimension from which the defect starts to propagate. However, during crack propagation, the main role is played by the level of stress which defined the loading cycles. This interpretation would explain why the mean stress sensitivity factors appear equivalent under the same stress amplitude, but not at the same corrosion fatigue life. If the two corrosive solutions had been different, in chemical composition, the crack propagation mechanism would have been affected by this and, consequently, the mean stress sensitivity would probably not be of the same order.

On the base of this comparative analysis, the relationship between stress amplitude and mean stress in Region IV, obtained through Exova experimental results, can be extrapolated to describe AMRL behaviour and to complete the Haigh diagram in the corrosive condition. To do this, a relation between the mean stress sensitivity factor, $M_{\sigma,4}$, and the stress amplitude at stress ratio R=0.5, $\sigma_{a,R=0.5}$, was determined as equation (5.6), from the best fit of experimental data.

$$M_{\sigma,4} = 1.1785 \bullet e^{-0.023\sigma_{a,R-0.5}} \tag{5.6}$$

The allowable stress amplitude in the corrosive environment, which is characteristics of GEHO pumps working environment, is now defined in all the regions of positive mean stress up to the stress ratio R=0.65. Since there are no experimental data for stress ratio values higher than R=0.65, it is difficult to predict what happens for higher values of mean stress.

In Figure 5.50 the allowable stress amplitude is represented in the Haigh diagram for the corrosion fatigue life at 15 million cycles, using the proposed mean stress sensitivity factor for each region. For conservative reasons, it is considered that the material behaviour in Region IV follows the behaviour between R=0.5 and R=0.65, defined by the mean stress sensitivity factor $M_{\sigma,4}$.

From a practical point of view, it is very unusual for Fluid End components to operate under condition with stress ratio higher than R=0.5. To achieve this condition, the mean stress should be at least 3 times higher than the stress amplitude and, in the case of R=0.65, the ratio between the mean and the stress amplitude would be four times higher.

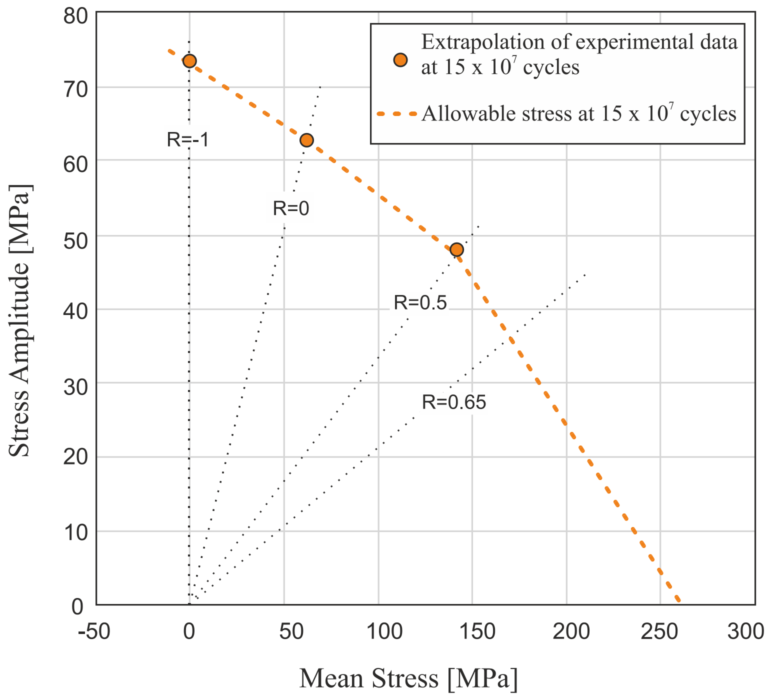

Figure 5.50: Haigh diagram at 15 million cycles in the freshwater environment. *Experimental results obtained in AMRL.*

5.4.3 Comparison of Haigh Diagram Limits with Models Available in Literature

Various models are available in the literature based on the stress-life approach, as discussed in Section 3.3, to predict the effect of mean stress on fatigue life in air. However, in corrosive environment, the use of the stress-life approach is less widely used and is often replaced by the fracture mechanics approach. Consequently, there are not advanced approaches to predict the allowable corrosion fatigue stress for values of stress ratio R≠-1.

As previously noted, following the FKM guideline, the value of mean stress sensitivity factor M_σ in Region II is much smaller than that calculated experimentally. In particular, using solely the FKM guide through parameters summarised in Table 5.6, there is no difference between the behaviour in air and in a corrosive environment. Alternatively, the mean stress sensitivity factor in Region II can be evaluated through the Schutz definition (5.1). However, even starting from this value, the allowable stress is Region III is different from experimental data. The FKM suggests a ratio of 3 between the slope of the two regions, but, as shown in Table 5.9, this ratio is different when calculated using experimental data and it is not constant during the corrosion fatigue life. Further, FKM defines the allowable stress amplitude in Region IV as a constant value, independent of the stress ratio, valid up to the ultimate strength of the material. However, it has been shown that the allowable stress is strongly decreasing with the increment of stress ratio. Therefore, the FKM model developed for material working in air is neither representative not conservative to be used as a reference to develop the Haigh diagram for S355J2 working in the freshwater solution.

Among the other main models available in the literature, the most of them suggest that, at high values of stress ratio, the allowable stress amplitude converges to the yield stress (i.e. Soderberg, Clemson and Bagci models) or to the ultimate stress (i.e. Goodman and Geber models). These approaches, because of their nature, are not suitable for prediction of behaviour in corrosive environments. As they converge to a specific point, they would not take into account the differences in the behaviour at different fatigue lives. The remaining approaches use a decreasing exponential shape to describe the relationship between stress amplitude and mean stress in the constant life diagram. In Figure 5.51 the three models, Kwofie, SWT, and Walker, are plotted in the Haigh diagram for a fatigue life of 15 million cycles. Extrapolation of experimental data, obtained from Basquin's law, is plotted on the same diagram for the same corrosion fatigue life. Stress amplitude at R=0.65 is obtained using the mean stress sensitivity factor, $M_{\sigma,4}$, from equation (5.6).

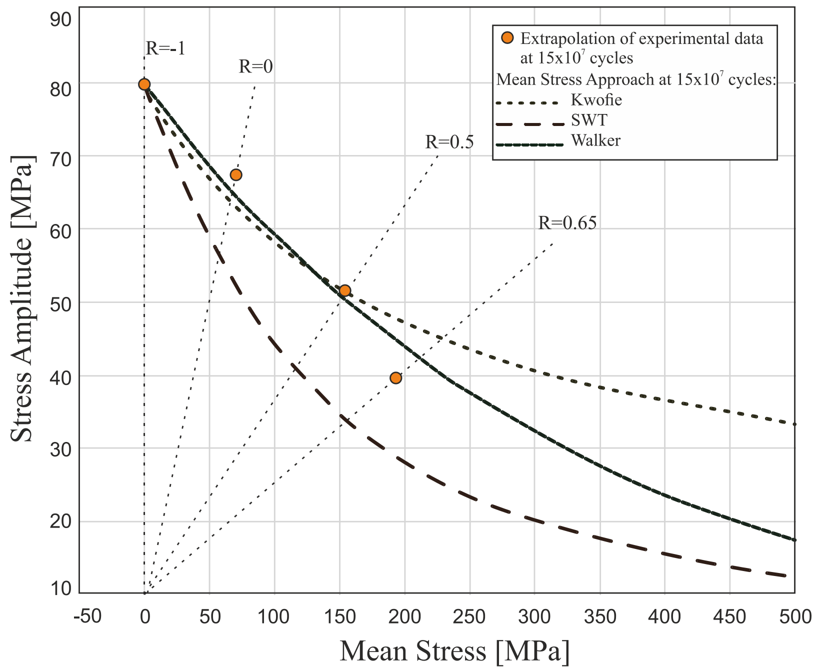

Figure 5.51: Haigh diagram at 15 million cycles. *Comparison of SWT, Walker and Kwofie approaches and experimental extrapolation of corrosion fatigue data obtained in AMRL at 15 million cycles.*

The SWT approach is independent of fitting parameters and cannot be scaled to fit the experimental data. Prediction based on this approach is extremely conservative and the effect of mean stress is identical to the behaviour in air. The more advanced version of SWT approach is the Walker equation, which depends on the fitting parameter γ, calculated as the best fit to experimental. The resulting value is reported in Table 5.13. Similarly, the Kwofie approach is dependent on a material constant, α, which is also calculated as the best fit to experimental data and its value reported in Table 5.13.

Table 5.13: Values of fitting parameter of Walker and Kwofie equations. *Data employed to calculate the allowable stresses at 15 million cycles.*

γ	α
0.685	1.523

Both the Walker and Kwofie approaches show the advantage of being dependant of a constant that allows the equation to be as close as possible to the experimental data. In addition, thanks to this dependence, these two approaches allow the representation of a slightly different behaviour compared to that in air. The evaluation of fitting parameters, for both approaches, is calculated at a fixed corrosion fatigue life, that means that the difference between experimental results and predicted allowable stress increases at different fatigue lives. To prevent this inaccuracy, the fitting parameter instead of being a constant value could be written as a function of the fatigue life. However, because of the shape of these equations, the effect of mean stress is under-estimated at values of stress ratio higher than R=0.5. Therefore, employing these equations in the prediction of allowable stress amplitudes would introduce an error in the evaluation of corrosion fatigue strength in Region IV and consequently a potential failure of components at a shorter fatigue life than expected.

5.4.4 Prediction of Haigh Diagrams in the Corrosive Environment at High Number of Cycles

The definition of the Haigh diagram through the use of mean stress sensitivity factors in the different regions can be considered a good approximation up to the validity of Basquin's laws, defined using experimental results of simultaneous effect of corrosion and fatigue.

The comparison between simultaneous corrosion fatigue tests and pre-corroded corrosion fatigue tests showed an intersection of the two S-N curves, in both stress ratio conditions. After this point, the proposal is that the corrosion fatigue life of S355J2 is described by the extrapolation of pre-corroded S-N curves. To evaluate the mean stress effect on corrosion fatigue life longer than the crossing point, pre-corroded results should be taken into account and the mean stress sensitivity factors should be calculated in the various regions based on pre-corroded results. However, only two stress ratios are available from the experimental investigation performed on pre-corroded specimens, R=-1 and R=0. Consequently, it is not possible to directly calculate the mean stress sensitivity factors using Basquin's laws from pre-corroded data and to design the Haigh diagram with the same procedure used with data from simultaneous corrosion fatigue. To derive this information to predict the behaviour of the material in the region of fatigue cycles between 10^7 and 10^9, some assumptions are required.

The first simplification is related to the fatigue life at which the S-N curves change trend. This condition happens around 10^7 cycles but it is not at the exact same length for both stress ratios. However, the difference in the fatigue life between the two conditions is within a small interval. The error in the stress amplitude prediction would be lower than 2 MPa if a different fatigue life is selected within the interval as the crossing-point between the two trends. A small error is introduced when the following simplification is adopted:

A1: Under the same conditions of corrosive solution and loading frequency, the transition between the two trends of S-N curve happens at the same value of corrosion fatigue life $\widetilde{N}$ regardless of the stress ratio conditions.

Based on this approximation, values of stress amplitude are defined in each point of the Haigh diagram at the corrosion fatigue life $\widetilde{N}$ equals 1.61 x10^7 cycles, the exact number of experimental cycles where transition at R=-1 happens. A generalisation of this leads to the following assumption. At this fatigue life, stress amplitude at R=-1 and R=0.5 comes from pre-corroded experimental data, whereas the stress amplitude at R=0 is calculated from simultaneous corrosion fatigue data. The stress amplitude at R=0.65 is evaluated solving the equation (5.6), using $\sigma_{a,R=0.5}$ from pre-corroded set, and the equation (5.5).

All values of mean stress sensitivity factor, at fatigue life of $\widetilde{N}$, are summarised in Table 5.14.

Table 5.14: Mean stress sensitivity factors in the positive mean stress regions. *Data calculated at the fatigue life equivalent to the transaction between the two main behaviours.*

M_σ	$M_{\sigma,3}$	$M_{\sigma,4}$
0.180	0.169	0.364

The second assumption is related to the mean stress sensitivity factors in Region II, between R=-1 and R=0. Trends of data obtained in the fatigue life up to 10^7 cycles showed that the mean stress sensitivity factors in this region decrease with increasing fatigue life, for both set cases performed in AMRL and Exova. This means that the line that joins the stress amplitude at R=-1 with R=0 is less steep with increasing fatigue life. Similar behaviour is also expected for corrosion fatigue life longer than 10^7. However, as there are no experimental results at R=0 for pre-corroded specimens, a direct calculation is not possible. Therefore, to predict the behaviour in Region II of the Haigh diagram at fatigue lives longer than $\widetilde{N}$, the following assumption is made:

A2: the mean stress sensitivity factor M_σ is independent of the fatigue life at high number of cycles and its constant value is that calculated at corrosion fatigue life $\widetilde{N}$.

This is a conservative assumption since if the value of mean stress sensitivity factor increased with increasing of corrosion fatigue life, the area of Region II would grow. Using this approximation, the resulting value of stress amplitude at stress ratio R=0 is lower, compared to that expected based on the observed trend at lower cycles. From assumption A2, the mean stress sensitivity factor is defined regardless of the fatigue life. Consequently, stress amplitude at R=0 can be calculated at any fatigue life.

The third assumption pertains to Region IV of the Haigh diagram, where no experimental data are available. To define the behaviour of the material in these stress ratio conditions, the following simplification is proposed:

A3: the stress amplitude at stress ratio R=0.65 is obtained from the same calculation as for lower numbers of cycles.

This means that the transition between the two main trends on the corrosion fatigue life is not taken into account in this region. It would be reasonable to expect that a transition in S-N curve would occur also for stress ratio higher than 0.5 and, in the same way as occurred for lower stress ratios, the second part of the curve would present a gentler slope. This would allow a higher corrosion fatigue strength at elevated number of cycles, which, reported on the Haigh diagram, would mean a much higher allowable stress in Region IV. However, based on the experimental data available, prediction of the change of slope of the S-N curve after the transition would not be accurate. To avoid potentially catastrophic consequence on the application of Haigh diagram, it is therefore assumed that no transition would occur in the region of high positive mean stress. Consequently, the approach employed to calculate the mean stress sensitivity factor at fatigue cycles lower than $\widetilde{N}$ is used.

Figure 5.52 shows the progression of allowable stress on the Haigh diagram at various fatigue lives. Values of stress amplitude required to calculate the mean stress sensitivity factors in each region are summarised in Table 5.15, for the corrosion fatigue lives shown in Figure 5.52.

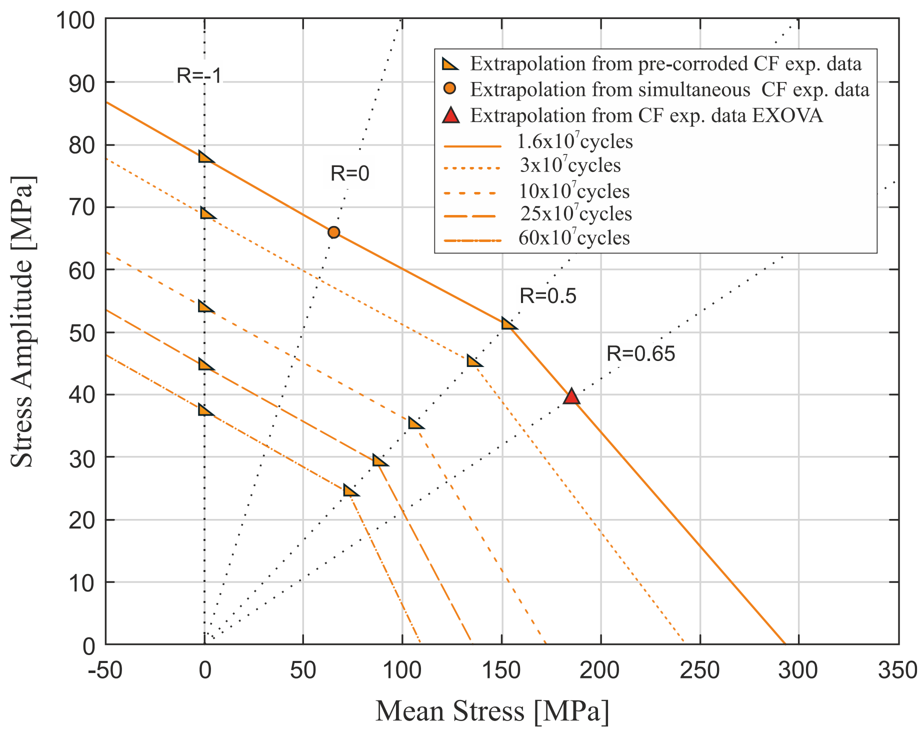

Figure 5.52: Prediction of the Haigh diagram at high number of cycles based on pre-corroded experimental data.

In Region III, mean stress sensitivity factors tend to increase with increasing of number of cycles, similar to the behaviour at shorter corrosion fatigue lives, but the rate of increase is slight, almost imperceptible. This trend can be explained by the fact that in the high-cycle region the value of mean stress sensitivity factor $M_{\sigma,3}$ is affected by assumption A2. If the changing of M_σ with corrosion fatigue life were taken into account, this would have affected the values of $\sigma_{a,R=0}$ and consequently the slope of the lines between R=0 and R=0.5. The values of $M_{\sigma,3}$ would be influenced both for the progressive decrease of $\sigma_{a,R=0.5}$ with fatigue life and for the progressive change of $\sigma_{a,R=0}$.

Table 5.15: Stress amplitudes and mean stress sensitivity factors used for the construction of the Haigh diagram in Figure 5.52.

Cycles	$\sigma_{a,R=-1}$ MPa	$\sigma_{a,R=0}$ MPa	$\sigma_{a,R=0.5}$ MPa	$\sigma_{a,R=0.65}$ MPa	M_σ	$M_{\sigma,3}$	$M_{\sigma,4}$
$3x10^7$	68.7	58.1	45.0	34.1	0.180	0.170	0.417
$10\ x10^7$	53.8	45.5	35.2	26.0	0.180	0.172	0.524
$25\ x10^7$	44.6	37.8	29.1	21.3	0.180	0.174	0.602
$60x10^7$	37.4	31.6	24.3	17.6	0.180	0.176	0.672

Basquin's law obtained from experimental data in corrosive environment at high frequency is used to extrapolate the value of stress amplitude to 10^9 cycles, the fatigue design life of GEHO pumps. This result is plotted in the Haigh diagram at 10^9 cycles, shown in Figure 5.53. The extrapolation of experimental data lies inside the allowable stress area, the differences between experimental data and the prediction, at R=0.3, is lower than 2.5 MPa. Although the prediction is non-conservative, the error prediction is relatively low, giving the model a good approximation

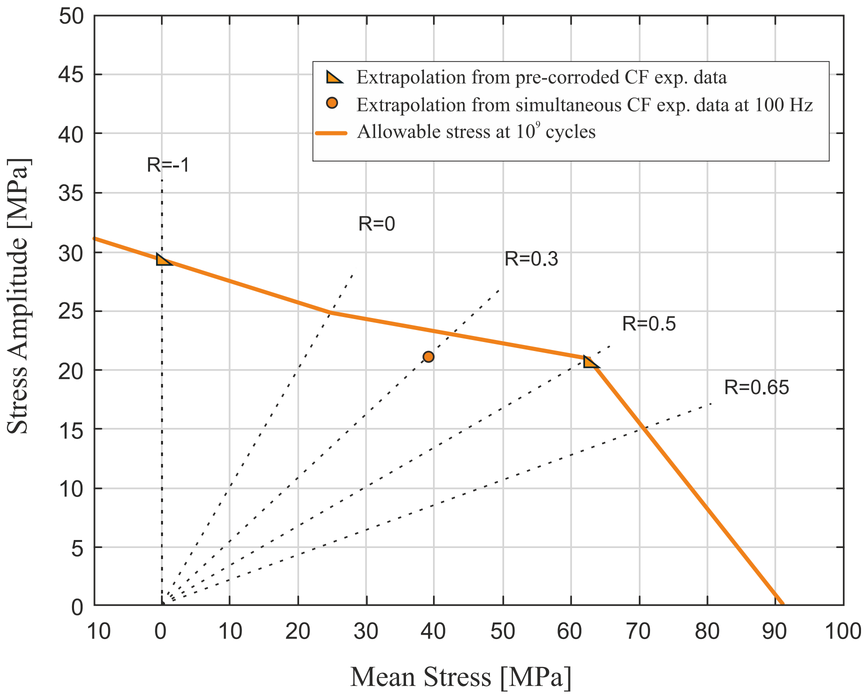

Figure 5.53: Prediction of the Haigh diagram at 10^9 cycles in the corrosive environment.

5.5 Summary

Specimens of S355J2 low carbon steel were tested in air and in the freshwater solution under different stress ratios. From each set of data, the least square method was used to calculate the best-fit parameters of Basquin's law to describe the S-N curves.

Experimental results showed a tangible decrease in fatigue strength due to the corrosive environment and a continuous decrease of fatigue strength with increment of fatigue lives. Compared to the fatigue behaviour in air, fatigue strength in the aqueous environment decreases over 50% at a fatigue life of 6 million and more than 62% when tested at stress ratio R=0.5. Moreover, from tests run at higher loading frequency, it was observed that cracks propagated at stress amplitude far below the in-air fatigue limit, leading the specimen to fracture.

An interesting characteristic was found by comparison of S-N curves obtained from tests performed in two different facilities, AMRL and Exova, which differ in the corrosive cell that enclosed the specimen during corrosion fatigue tests. Although tests were performed at the same stress ratio and under the same corrosive environment, because of the different flow distribution, the material reacts differently in terms of fatigue life. Particularly, at low stress amplitudes the fatigue behaviour of low carbon steel S355J2 is highly influenced by the variation of corrosive solution flow conditions.

Fractography analysis of fracture surfaces of specimens tested in air and in corrosive environment showed that in the corrosive environment multiple cracks develop and final fracture is characterised by their coalescence, particularly in the fatigue life region up to 10 million cycles. From the analysis of the external specimen surface, the degradation caused by corrosive solution effect was evaluated by measuring pits depth. Overall results show good agreement with the corrosion tests discussed in Chapter 3: after an initial non-steady phase, where the dimensions of defects grew continuously, corrosion affected the specimens in a steady manner and surface roughness and pit depth remained unchanged, although material loss was continuously occurring. Therefore, it is concluded that corrosion fatigue strength of low carbon steel S355J2 is particularly sensitive to the corrosive effects during the initial phase of the fatigue life.

The mean stress effects of corrosion fatigue life are evaluated by construction of Haigh diagrams based on experimental results. To account for the reduction of allowable stress due to mean stress at stress ratios higher than zero, new parameters were proposed, based on the physical meaning of the mean stress sensitivity factor. These proposed parameters, together with the mean stress sensitivity factor, allow the definition of allowable stresses in the three regions of positive mean stress in the Haigh diagrams. Comparison of Haigh diagram obtained from experimental results in air and in the corrosive environment showed as a general trend that the effect of positive mean stress is more severe on the fatigue strength in corrosive environment and, in particular, the material is more sensitive to mean stress at stress ratios R higher than zero.

Predictive models for mean stress effect available in the literature were compared with experimental data. However, none of these approaches gave an appropriate fit to experimental data and consequently, to predict the allowable stress at high number of cycles, a modified FKM approach, based on the proposed parameters, was employed to evaluate the behaviour up to 10^9 cycles.

Chapter 6

Industry Scale Testing

In this chapter, the corrosion fatigue life assessment procedure is applied to industry scale pressure test specimens, designed to be representative of Fluid End components in GEHO pumps, tested under corrosion fatigue loading.

The specimens were tested in the Weir Minerals NL dynamic pressure test rig. These non-standard tests required modifications to the test rig and compatible design of test specimens. Strict requirements related to the safe performance of the testing system were specified and adhered to during the design and development of the test system. Two validation tests, representative of two loading conditions of direct interest in GEHO pump corrosion fatigue assessment, were designed and performed. In the first case, the industry scale specimen was subject to cycling pressure, with nominal load ratio value R almost equal to zero. In the second case, the specimen was designed to incorporate a shrink-fit component to create a state of residual stress in the specimen. After this procedure, the specimen was tested under cycling pressure. Through to the combination of the assembly procedure and the cyclic pressure testing, a condition of a tensile mean stress, representative of a bolted connection in a GEHO Fluid End component was tested.

6.1 Testing System Characterisation and Industry Scale Specimens Design

6.1.1 Dynamic Pump Test Rig Modification

The Weir Minerals NL dynamic pump test rig is shown schematically in Figure 6.1.

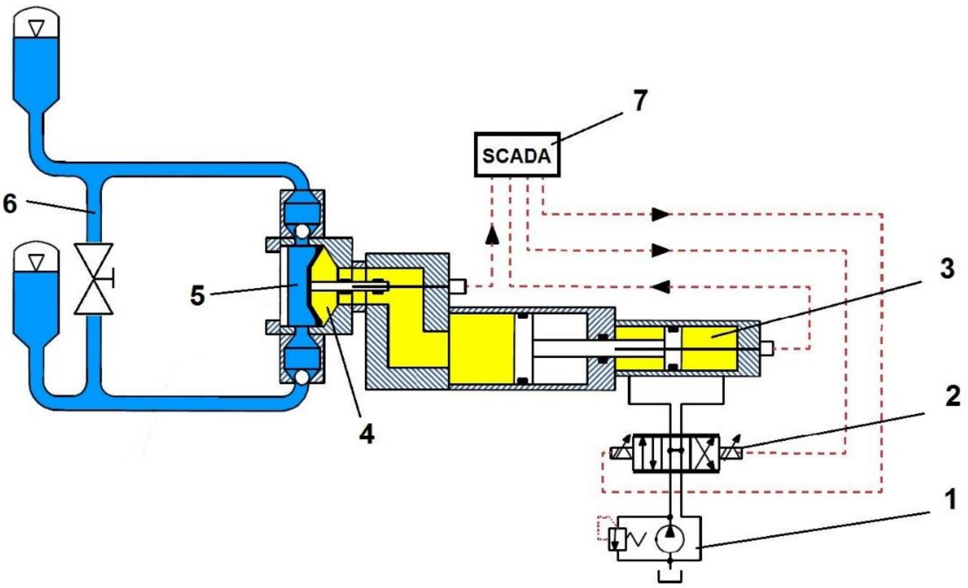

Figure 6.1: Sketch of test rig available in Weir Mineral NL. *Modified [8].*

The rig consists of a hydraulic power unit (1) which supplies hydraulic power to a high response proportional valve (2). The proportional valve drives a 500 mm stroke, 63 mm piston and 45 mm rod hydraulic cylinder (3). The hydraulic cylinder drives a 400 mm piston, that displaces propelling fluid in and out of the pump chamber (4). One end of the chamber is sealed a diaphragm which moves under the action of the propelling fluid. The other side of the diaphragm defines the border of the diaphragm chamber (5), often called the “pump chamber”. Self-acting non-return valves connect the diaphragm chamber to the water loop (6) and enable a positive displacement pump action. The water loop consists of DN125 steel piping with PN16 flanges and suction and discharge air vessels of 300 litres nominal volume each. A Supervisory Control and Data Acquisition (SCADA) system, which consists of Programmable Automation Controller and desktop PC, provides supervisory control of the individual devices and performs data acquisition of relevant signals.

The standard test rig configuration was modified to incorporate a corrosion fatigue test capability. Between the pumps chamber and the discharge vale, an additional unit, called the *External Chamber unit*, was added to enclose the industry scale specimen during the test and allow the safe use of the rig. The external chamber was designed to accommodate the specimen dimensions without constraining the specimen during the pressure testing.

Schematic drawings of the modified testing system, including the External Chamber unit and the Specimen are shown in Figure 6.2.

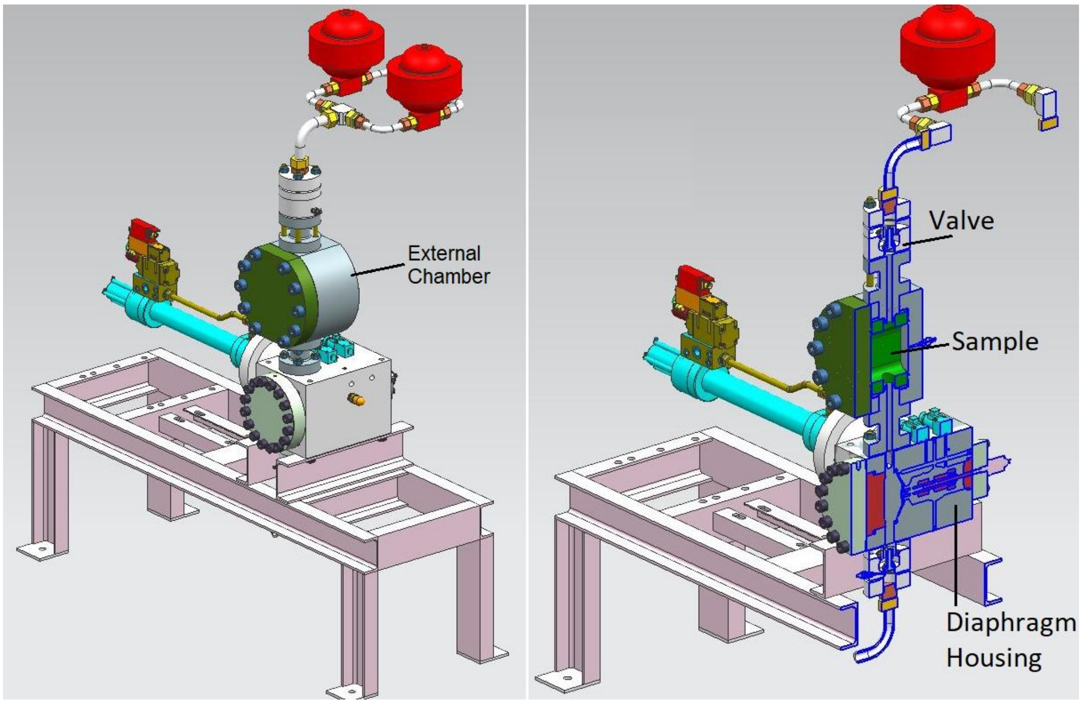

Figure 6.2: Schematic representation of modified test rig. *(Left) full view of the rig. (Right) section of the rig.*

The External Chamber has the pump chamber on one side and the discharge valve on the other, and is hermetically sealed to the external environment avoiding leakages of the pressured fluid. This is fundamental both for the operation of the testing system and for safety reasons.

The specimen, detailed in section 6.1.2, has a hollow shape to allow the pumped fluid to pass through it. The pumped fluid was required to circulate only in the internal part of the specimen and not be in contact with the external chamber, during the test.

To fulfil these requirements, specific o-rings were developed, in collaboration with an external company, tested and used during corrosion fatigue tests. Axial o-rings were placed to connect the bottom and top part of specimen to the pump chamber and to the discharge valve respectively. Radial o-rings were used to seal the connection in between the specimen and its casing (the external chamber).

The modified testing system, including the External Chamber unit and details of the assembled axial o-ring to the connecting equipment is shown in Figure 6.3.

Figure 6.3: Modified testing system for industry scale testing. *Left in the green box) External Chamber unit. Right in the red box) detail of assembled axial o-ring.*

The pressure in the External Chamber is the same as in the pump chamber, except for small losses. When the piston is at its minimum length and when the pump chamber is in its maximum volume configuration, the pressure in the External Chamber and in the pump chamber is at its minimum value, just below the Suction Pressure. This allows the suction valve, situated below the pump chamber, to open and consequently the fluid transition. Conversely, when the piston is at its maximum extension and the pump chamber is in its minimum volume configuration, the pressure in the pump chamber and in the External Chamber is at its maximum value in the cycle, which is slightly higher than the Discharge pressure. The difference between these two values of pressure allows the opening of the discharge valve, situated above the External

Chamber, and the fluid to transit. The load cycle to which the specimen is subjected is therefore identified by these two values of pressure.

Required parameters for the setting, entered from the PC, used as the Human Machine Interface, are the following:

- Percent of Stroke Volume;
- Suction and Discharge pressure;
- Strokes per minute.

Through to the SCDA system and the use of various sensors, the main signals monitored during the test are:

- Suction and Discharge Pressure;
- Cylinder pressure;
- External Chamber Pressure;
- Frequency;
- Position of Piston.

Characteristics of the test rig, on the base of which industry scale specimens were developed, are reported in Table 6.1.

Table 6.1: Maximum performance of testing system.

Parameter	Maximum Value
Suction Pressure	5 bar
Discharge Pressure	200 bar
Stroke Rate	300 rpm

The main limitations affecting the design of corrosion fatigue specimens were associated with the maximum stroke rate and the maximum value of suction pressure. The maximum stroke rate, around 5 Hz, prevented the execution of a fatigue test in the very high cycle fatigue regime, as the test time would be too long and prohibitively expensive. The maximum attainable value of suction pressure imposed a limitation on the minimum load during the pressure cycles. This is significant as using the sole effect of pressure variation, the load ratio is limited to the neighbourhood of zero. Therefore, to simulate different conditions of mean load, other solutions had to be defined.

6.1.2 Specimens Description

The aim of industry scale testing is to apply the fatigue life procedure to a real-life scale component. The industry scale specimens had to represent the Fluid End components and be suitable to fail under corrosion fatigue loading at a fatigue life at least of $5x10^5$ cycles.

To create representative testing conditions, two loading cases were of particular interest. One is represented by the single effect of cyclic pressure which load ratio is R=0. This case is representative of Fluid End components which are only subjected to the loading by the pressured fluid. The second case aims to represent the combined effect of pressure cycles and static tensile stress induced by bolt pretension, which is a typical condition in Fluid End components such as diaphragm houses. In this case, the load ratio is greater than zero. It was not possible to perform the second loading case using the sole effect of the pressure as the maximum suction pressure, the test rig could achieve and maintain for the length of the tests, is not high enough. It was necessary to create a state of tension on the specimen prior to being subjected to cyclic pressure. After considering possible approaches, shrink fit of an interference component inducing a constant tension state on the specimen was selected.

The design of specimens was related to the design of the External Chamber unit, as discussed in the previous section. To avoid using two external chambers, which increases not only the cost of production but also the time of dissembling and assembling to the testing system, the specimens for the two loading conditions had to fit the same external chamber. The two types of specimen were therefore required to have the same overall dimensions.

Two industry scale specimen configurations were developed, one for each loading case. Both configurations shared the overall dimensions of 200x140x240 mm, to be encased into the same external chamber. Specimens are characterised by a particular shape of double notched block, which represents the diaphragm house critical geometry. Each configuration is characterised by a through 44 mm diameter hole in the axial direction, which is the direction of the flow. In addition, an oval-shaped through notch typifies the transversal direction of both configuration specimens. The specimens for the pure cycling pressure test, defined *Specimen 1*, engineering drawing shown in Figure 6.4, was manufactured as a single block. To simulate positive load ratio condition, the second specimen, *Specimen 2*, has an interference coupling fit between the central core of the specimen, which has the same overall characteristic of Specimen 1. Two lateral blocks are assembled to the central core through the shrink-fit procedure. Engineering drawings of the central core of this specimen and of the shrink-fit block are shown in Figure 6.5 and Figure 6.6 respectively.

The through-hole along the axial direction is fundamental to allow the flow of the corrosive solution from the pump chamber to the discharge valve, which in turn is responsible to the pressure cycles on the specimens. At the two extremities of the hole, sealing gaskets are placed to guarantee the tightness. The lateral oval-shaped notched has a dual function: its intersection with the axial through hole creates a geometry representative of the Diaphragm House, increasing the stress in the region around the hole. In addition, due to the through notch, it was possible to create higher stress state distribution, at the same working cycling pressure, compared to the case in which no transversal hole is present. This is an important aspect, to avoid extremely long fatigue testing, due to the limited maximum pressure which the test rig is able to produce. Two radial seals are placed on each lateral sides of the specimens, around the oval-shaped notch, in contact with the External Chamber, on one side, and its cover, on the other side. Due to the presence of these sealing gaskets, the level of pressure in the internal part of the specimens is guaranteed and no leakage occurred for the whole length of the corrosion fatigue tests.

The material used for the specimen manufacture is low carbon steel S355J2, from the same block used for the production of uniaxial fatigue specimens, described in Chapter 3.

Figure 6.7 shows the view of Specimen 1, after manufacturing, from the lateral side and frontal side.

Figure 6.8 shows the lateral view of Specimen 2, after manufacturing, and four lateral blocks, two of which are assembled in the lateral pockets.

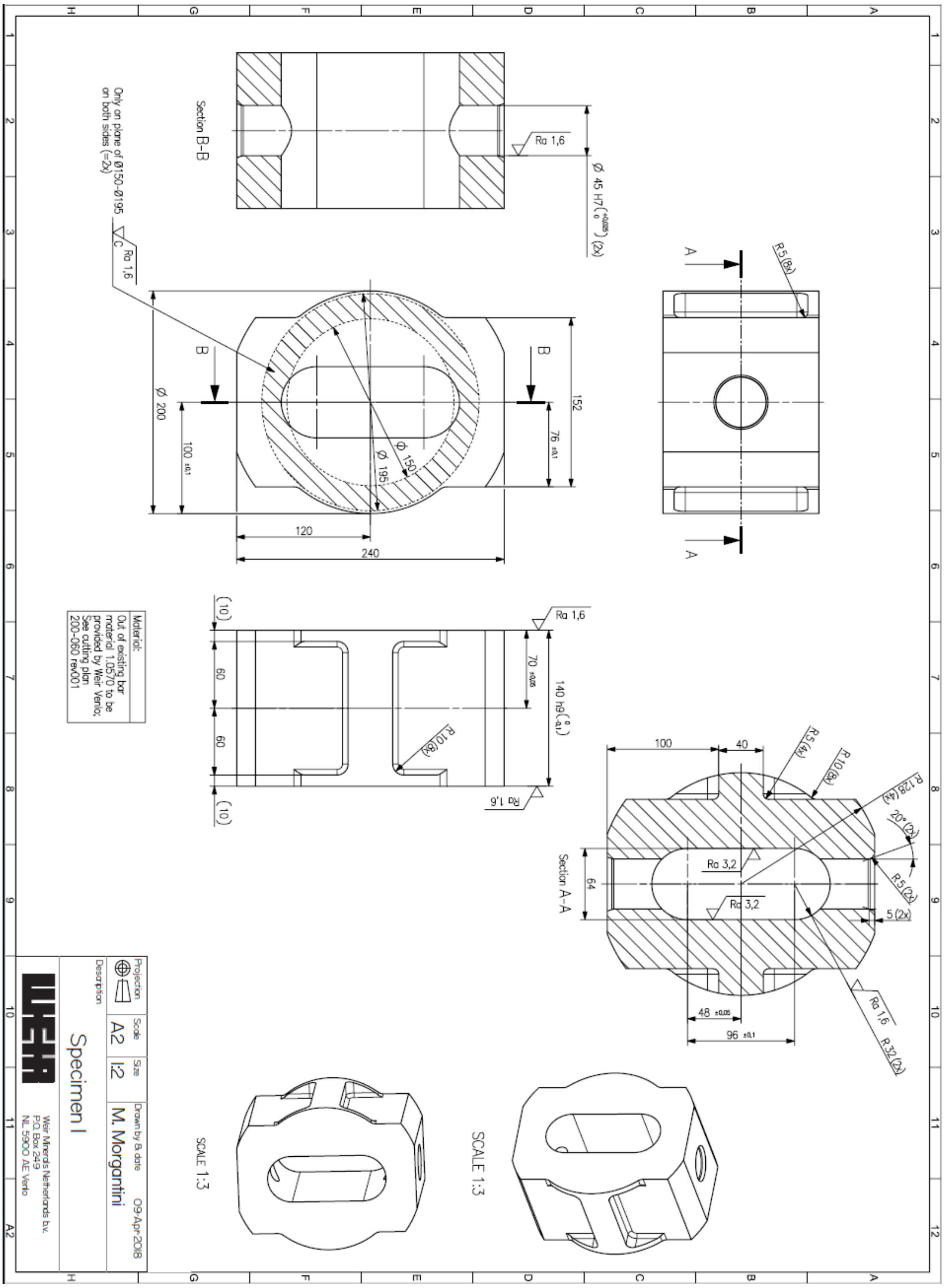

Figure 6.4: Technical drawing of Specimen 1. *Dimensions are expressed in mm.*

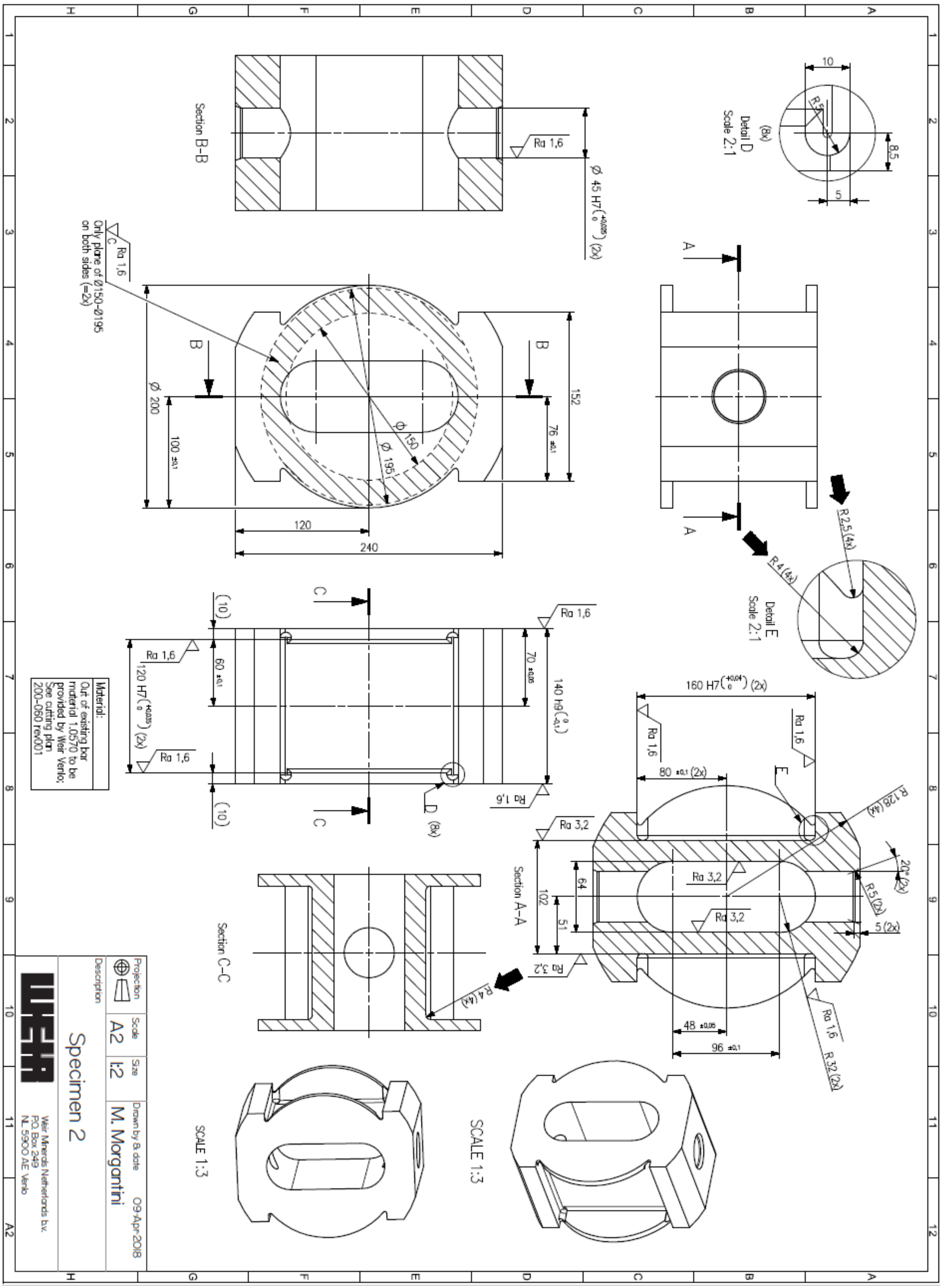

__Figure 6.5: Technical drawing of Specimen 2 .__ Dimensions are expressed in mm.

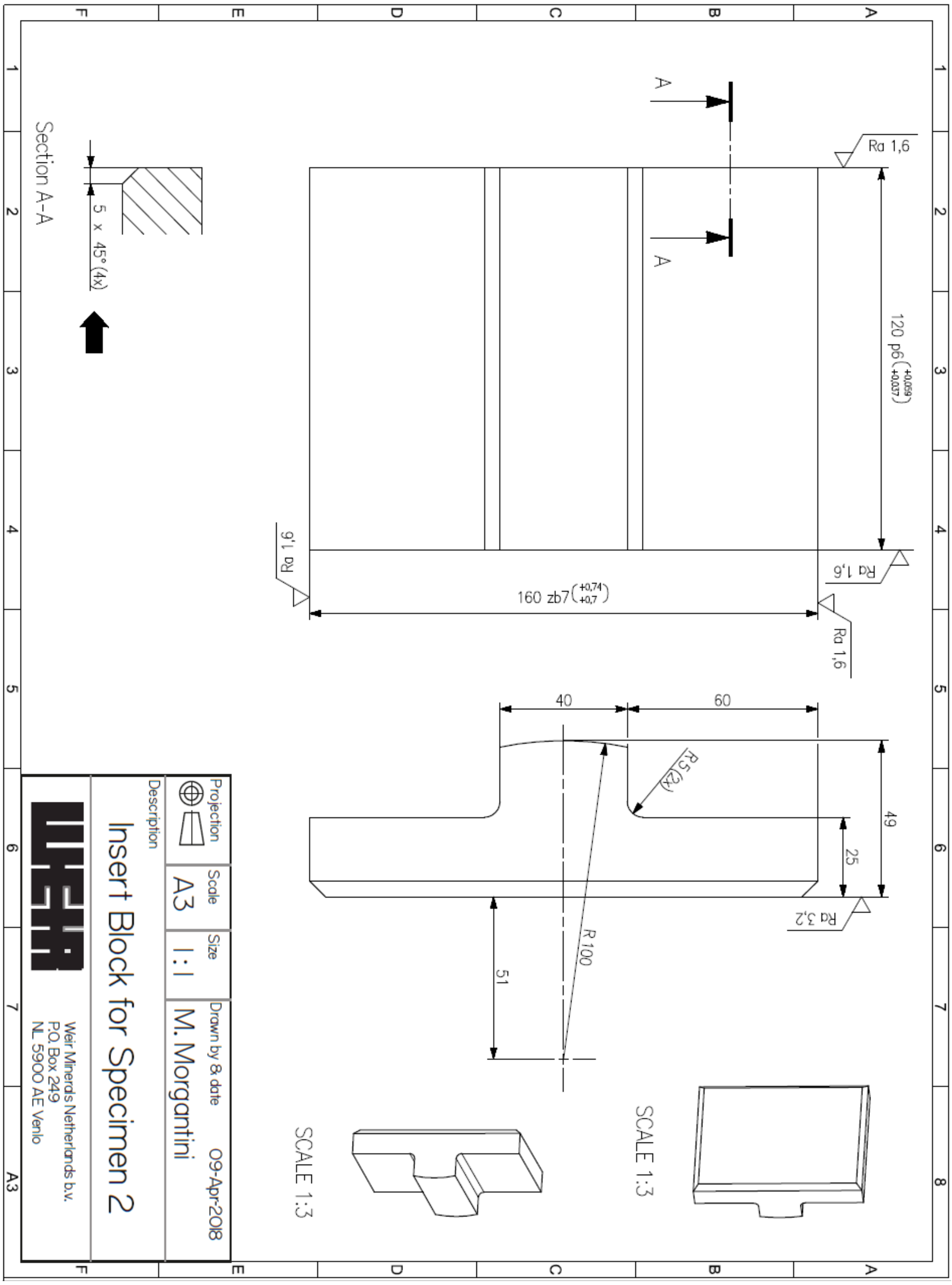

Figure 6.6: Technical drawing of the block to be assembled to the central core of Specimen 2. *Dimensions are expressed in mm.*

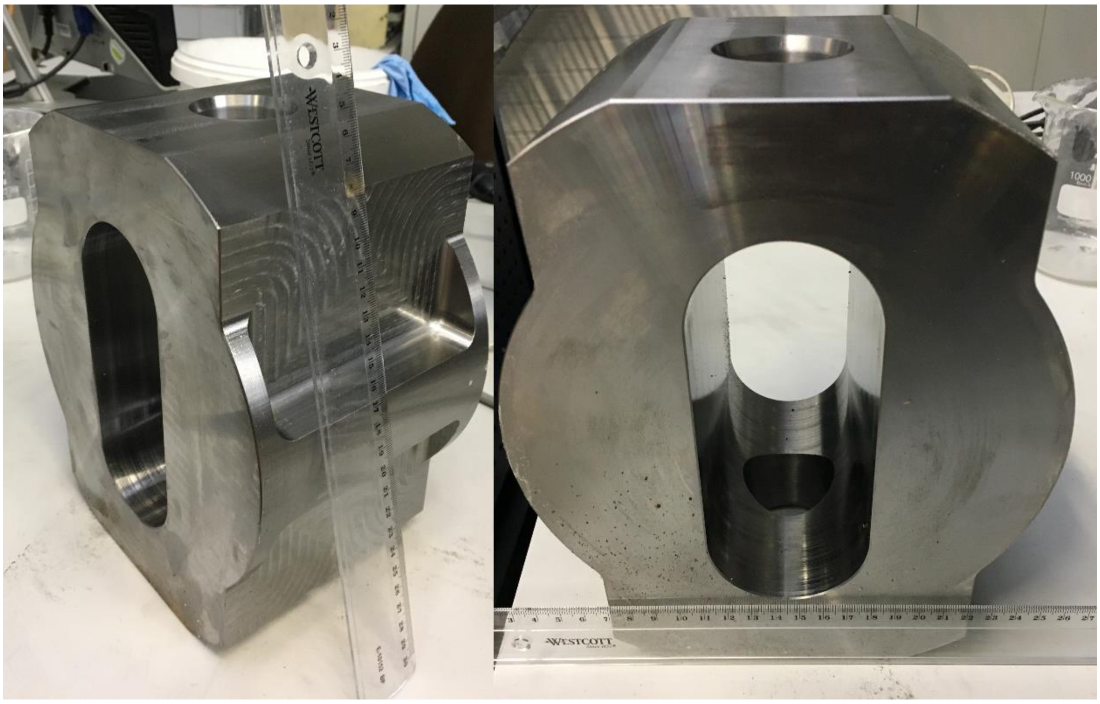

Figure 6.7: Specimen 1. *Lateral and frontal side after manufacturing.*

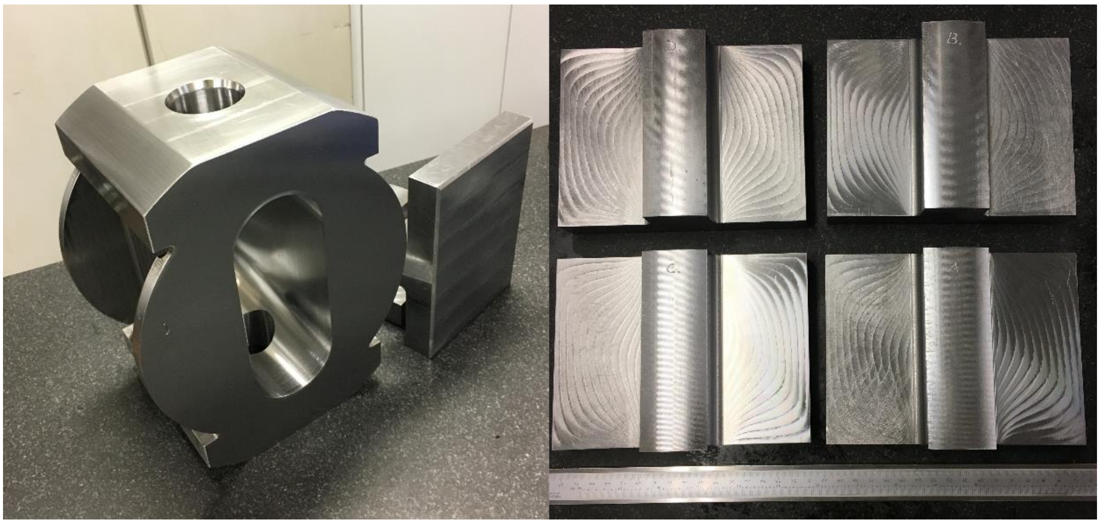

Figure 6.8: Specimen 2. *Lateral side after manufacturing (left) and manufactured blocks to be assembled (right).*

6.1.3 Shrink Fit Process

Shrink fit process is a joining method, often employed in mining industries, as well as in motor vehicle and in general mechanical engineering [141]. It is usually used to connect a shaft to a hub or ring, but the principle can be employed in many different situations, where an interference coupling fit is required. The shrink fit process can be hot, cold or a combination of the two. The hot shrink fit process consists of the heating the hub, or the component that has the function of encasing, to make the component expand. Then, the fitting element is located in the desired position and, as the heated component cools down, it contracts and it holds the other firmly in place. The cold shrink fit process is similar except that the component to be fitted is cooled so it contracts, after which it is placed in position. It then warms back up and expands, making a secure joint. In the case of a combination process, both components are thermally treated: the component which is to be fitted in the hole is cooled down, in order to contract, whereas the other component is heated up, to be expanded. This combination is inevitably more expensive, as it required the treatment of both components, therefore it is employed only when a big interference is required, to ensure the success of the coupling.

To assemble the two blocks to the central part of Specimen 2, a combination of the hot and cold shrink fit process was employed. The coupling between the three components is considered particularly challenging because of its geometry: the absence of coaxiality makes the insert of the block inside the designed pocket more difficult. In addition, the two blocks were required to be inserted at the same time to avoid creating different stress distribution on the two sides of the specimens. For the challenging characteristics of the coupling, the higher the temperature at which the process is performed, the higher the achievable deformation of the specimen and consequently, the easier the coupling. However, from a microstructural point of view, if the temperature is too elevated, above 650º C [142], the material may show a variation in its microstructure and consequently in its mechanical properties.

To meet both requirements, the linear expansion equation (6.1) was used to calculate the minimum temperature needed to achieve an expansion equal to the maximum interference.

$$\Delta L = \alpha L_0 \Delta T \tag{6.1}$$

Where L_0 is the initial dimension, ΔT is the difference between the maximum temperature applied and the room temperature, and α is the coefficient of linear expansion which value for the low carbon steel is $1.2x10^{-5}\,{}^{o}C^{-1}$. From this calculation, the minimum temperature required to achieve an expansion of $\Delta L = 0.74mm$ is $T = 410^{\circ}C$.

To assure the coupling, the Specimen 2 was heated up to 500º C. In addition, the cold shrink-fit procedure of the two lateral blocks was also included to create an extra margin in the process. In this case, the temperature was related to the

Dimensions of the two lateral holes and of each of the two blocks, to be assembled to the core of the specimen, taken before the cooling for the shrink fit process, are reported in Table 6.2.

Table 6.2: Dimensions of the Specimen 2. *Dimensions of the lateral holes, called A and B, on Specimen 2 before shrink fit and dimensions block 1 and 2, to be assembled to Specimen 2. Dimensions are expressed in mm.*

	A	B	Block 1	Block2
Width	159.98	160.00	160.62	160.62
Height	120.02	120.02	120.04	120.03

The interference coupling fit between the two blocks and the core of Specimen 2 were performed using the facility of *Hauck Heat Treatment Venlo B. V.*. The two blocks were cooled at -92ºC using carbon dioxide, commonly called dry ice. The core of the specimen was heated up to 500ºC using an oven available in *Hauck Heat Treatment* facility.

The assembly of the specimen, thus the performing of the shrink fit process, is shown in Figure 6.9.

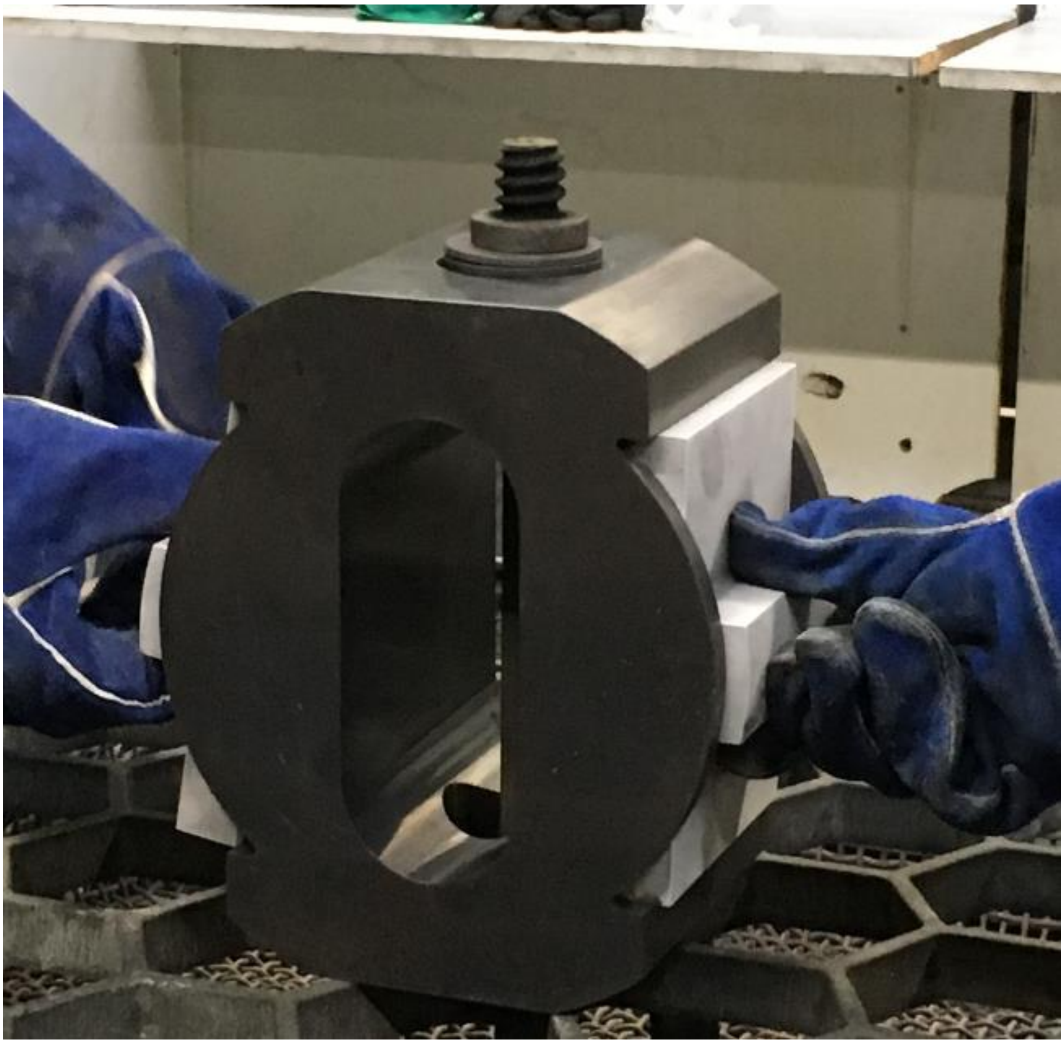

Figure 6.9: Assembly of Specimen 2 through the shrink fit process.

The shrink-fit process succeeded and the two blocks were firmly connected to the body of Specimen 2. However, the blocks were not inserted entirely on the holes and a small portion of each block remained outside the hole. This characteristic, which is highlighted in Figure 6.10, didn’t compromise the efficiency of the fit, but it had to be considered in the calculation of the distribution of stress, since it may affect it.

Figure 6.10: Specimen 2 after shrink fit. *Details of position of a blocks into the designated hole.*

To evaluate the stress distribution induced by the interference coupling fit, a non-linear contact simulation was performed using ANSYS Workbench FEM Software (2018). The frictional contact option was chosen to describe the connection between the blocks to the central body [143]. To calculate the stress state caused by the shrink-fit, the kinematic hardening model was preferred to the isotropic one, because of its capability of including the Bauschinger effect [144]. Multilinear kinematic hardening model was selected among the ANSYS options. Values of Stress versus Plastic Strain were entered based on experimental findings obtained by tensile tests on S355J2 low carbon steel specimens described in Chapter 4, [112]. The resulting Stress-Plastic Strain curve is shown in Figure 6.11.

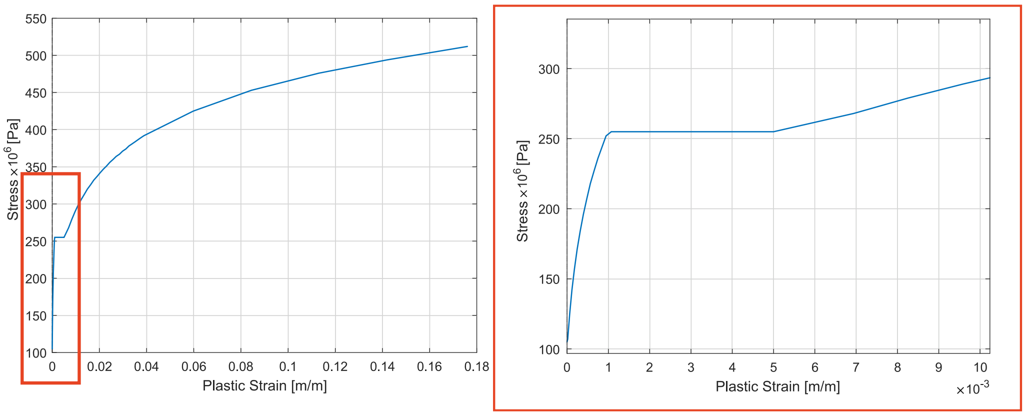

Figure 6.11: True Stress-Strain curve. *Data obtained by tensile tests [112].*

Due to symmetry, only one-eighth of the total body, shown in Figure 6.12, was used to simulate the contact problem. The geometry is composed of two bodies which geometries included the interferences, measured before the shrink fit and reported in Table 6.2. The model, composed by the portion of specimen and the portion of the block, was assembled and the interference included before being imported in the FEM. To characterise the contact and simulate pressure realised by the process, the frictional option was selected, using a friction coefficient equals to 0.2 [143]. Only two faces are in contact, as shown in Figure 6.12, and a gap was left on purpose between the back of the block and the hole to reproduce the real assembly. The body was meshed by higher-order tetrahedral elements, as shown in Figure 6.13, with a refinement to surfaces in contact and sizing to the vertex of double notch, where there is the main interest in the solution. The resulting mesh was chosen based on previous evaluations to avoid any dependency between the mesh distribution and results. Displacement perpendicular to each of the symmetry surfaces was imposed equal to zero as boundary condition to the problem. The *Auto Time Stepping* was enabled to allow a gradual increment of the contact pressure. In addition, *Large Deflection* was enabled, as the nature of the problem is non-linear.

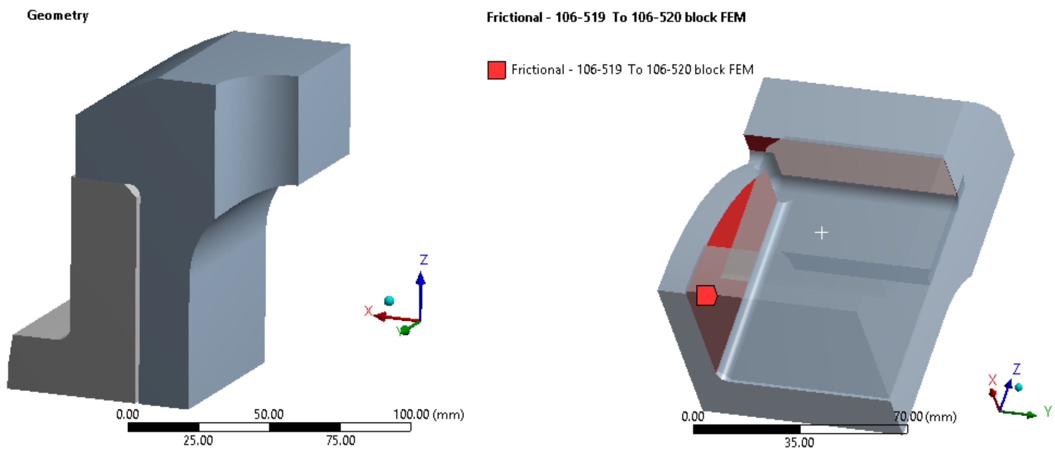

Figure 6.12: One eighth of Specimen 2 model and contact surfaces details.

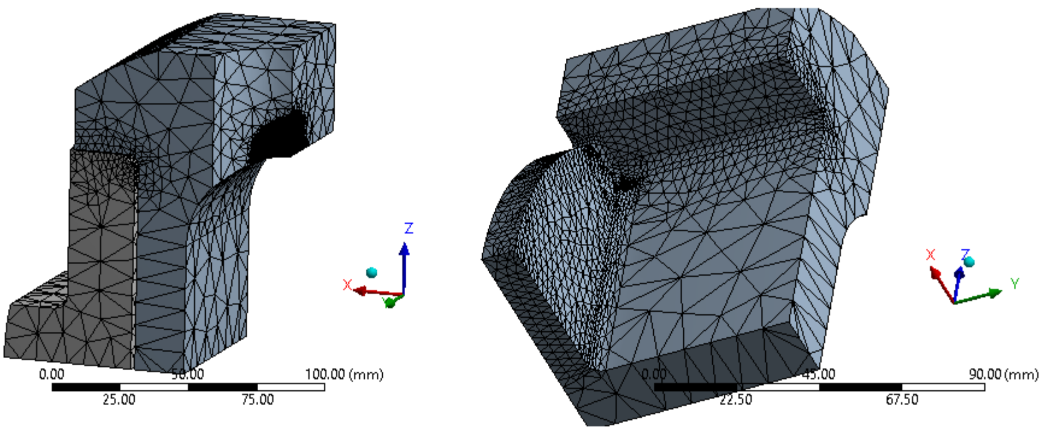

Figure 6.13: Details of mesh distribution on Specimen 2 model.

Figure 6.14 shows results of FEM simulation in terms of von Mises Equivalent Stress (Figure 6.14a) and in terms of Normal Stress, perpendicular to the plane of the corner of intersecting bore (Figure 6.14b) caused by the contact pressure generated through the interference coupling fit. Maximum values of Equivalent Stress, as well as of the Normal Stress, are mainly located around the corner of bores intersections, which is the area of main interest since it is representative of the critical area of Diaphragm Houses.

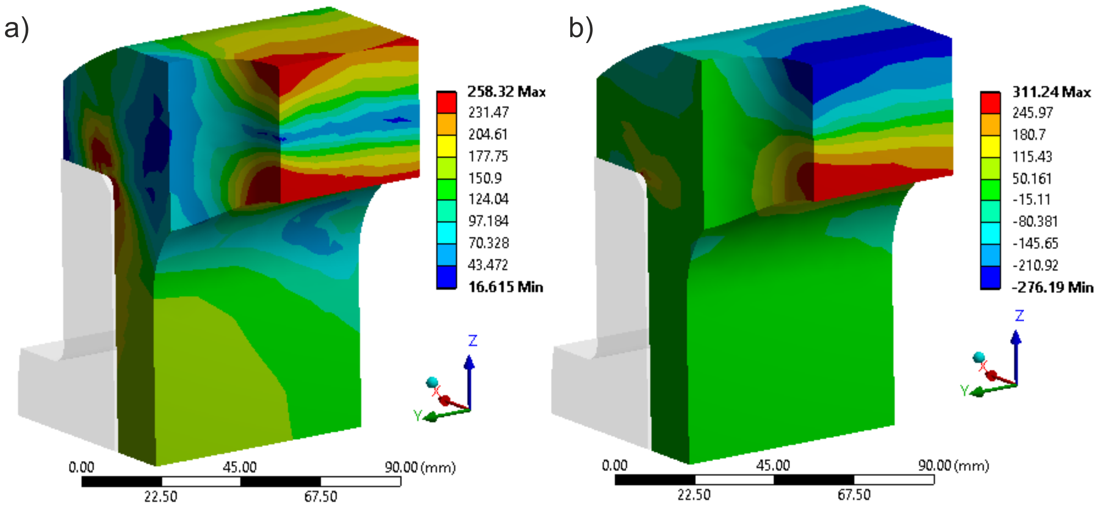

Figure 6.14: FEM calculation colour plot of the shrink fit process. *a) von Mises Equivalent Stress distribution, due to the interference coupling fit; b) Normal Stress distribution in the x-direction, due to the interference coupling fit.*

To verify that the FEM simulation closely represents the interference coupling fit problem, measurements of the oval-shaped holes were taken before and after the shrink-fit process. Because of the high temperature at which the shrink-fit was performed, it was not possible to measure the deformation caused by the coupling during the shrink-fit process through the use of strain gauges. A less precise methodology was employed to extract information related to the deformations of the specimen. The distance between the two parallel faces of the oval hole was measured, in both of the two faces of the specimen, before and after the process to evaluate the displacement. Distances between the two faces were measured in three different points along the oval shape: one measurement was taken from the middle and the other two from the two opposite extremities, as shown in Figure 6.15a. The measured displacements in the three points for both sides of the specimens, reported in Table 6.3, are the results of the difference between the mean value of measurement after the shrink fit and the mean value of measurements before the process. These values were compared with *directional deformation* obtained from the FEM simulation, shown in Figure 6.15b.

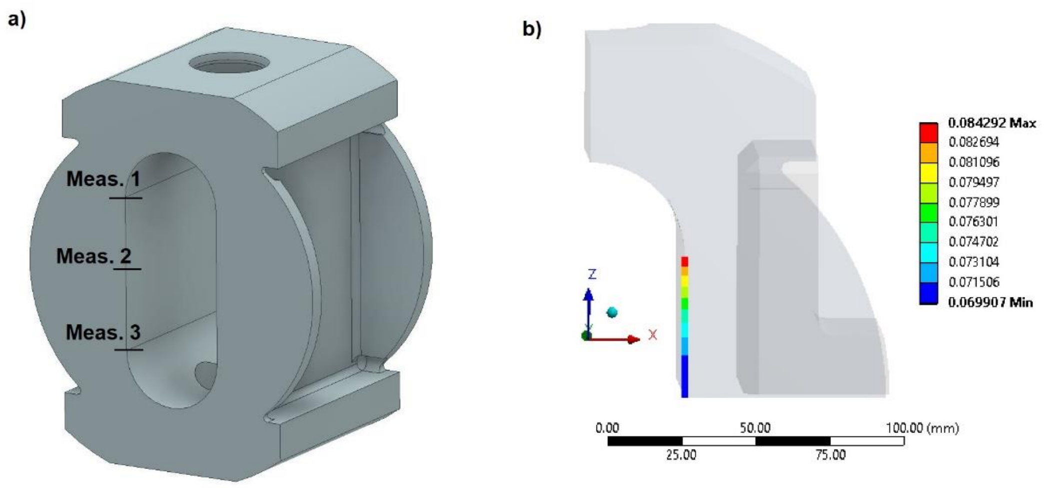

Figure 6.15: Displacement caused by the shrink fit. *a) Schematic drawing of the central part of Specimen 2 where the three measurement took place; b) FEM simulation colour plot in the area of interest showing the deformation caused by the contact pressure, measured in mm.*

Table 6.3: Measured displacement of oval-shaped hole, caused by shrink fit process.

	Displacement 1	Displacement 2	Displacement 3
Side A	0.17	0.14	0.17
Side B	0.18	0.14	0.18

From the FEM simulation, the maximum deformation along the x-direction, expressed in the form of displacement, occurs in point A and C, whereas the minimum displacement occurs in B. The FEM results are in line with measurements taken from the specimen. It is important to note that the deformation obtained from FEM analysis is related to the half portion of the real model. Therefore, the displacements connected to the entire model are two times the values showed in Figure 6.15b. Although values of measurements are not extremely precise, displacements obtained from FEM simulation match well, showing differences of the same order as the precision of the measurement equipment.

6.1.4 Test Conditions

Two industry scale tests were performed, one for each specimen configuration.

Nominal values of Suction pressure, Discharge pressure and Stroke per Minute, selected as the conditions for the tests through the desktop PC of the SCADA system as test conditions for Specimen 1 and for Specimen 2, are reported in Table 6.4.

Table 6.4: Nominal conditions selected for industry scale tests.

Test	Suction Pressure (bar)	Discharge Pressure (bar)	Frequency (rpm)
Specimen 1	3	160	250
Specimen 2	3	150	250

The aqueous solution, used in the test rig to be circulated during the activity of the pump, consisted of fresh tap water with the addition of *NaCl* in a concentration of 884 ppm. The characteristics of the aqueous solution were selected according to characteristics of the corrosive solution used for uniaxial testing, reported in Table 4.7.

Through the SCADA system the values of Suction, Discharge, External Chamber and Cylinder pressure were monitored during the entire test and values of almost 50 cycles every 30 minutes were recorded.

Each test lasted until the failure of the block, which is characterised by the growth of one or multiple cracks. When the length of the crack became large enough to allow passage of cycled corrosive solution out of the sealed area, a leakage occurs and consequently values of pressure decrease. The SCADA system was set to cut off the hydraulic power unit, and consequently to interrupt the test, when values of pressure decrease. Due to the introduction of this limit, the test was stopped in a short interval after its fracture, avoiding leakage and additional cycle loads applied to the component.

6.2 Test Results

6.2.1 Cycling Pressure Condition

The industry scale test performed using Specimen 1, representative of the pure cycling pressure condition, ran overall for almost 71 hours. The test conditions, obtained from data acquisition, are reported in Table 6.5. The values of Suction and Discharge pressure, as well as the value of frequency, are the arithmetic means of all the sets of data saved every thirty minutes, each of which includes almost 50 cycles. The values of minimum and maximum pressure are the absolute minimum and maximum values among all data sets saved during the test. The difference between the absolute maximum pressure and the arithmetic mean value of maximum pressure, as well as between the absolute minimum and the mean value of minimum pressure, is in the neighbourhood of 0.2 bar. Therefore, the range of all cycles can be considered constant, as well as the damage each single cycle caused to the final fracture. According to the arithmetic mean of the frequency, the overall corrosion fatigue life of Specimen 1 resulted to be 1.06 million cycles.

Table 6.5: Measured data during the test on Specimen 1.

Suction Pressure (bar)	Discharge Pressure (bar)	Max. chamber Pressure (bar)	Min. chamber Pressure (bar)	Frequency (rpm)	Fatigue life (cycles)
2.4	160.9	168.6	0	250.8	$1.06\text{x}10^6$

A typical pressure cycle, registered during the test, is shown in Figure 6.16, which includes Suction, Discharge and External Chamber pressure variations. The abscissa represents the overall stroke length of the cylinder, expressed in degree, which determines an entire cycle, whereas values of pressure, expressed in bar, are represented on the ordinate. Suction pressure and Discharge pressure are almost constant during the entire cycles, fluctuating around the nominal values selected in the set up. The load cycles acting on the specimen were determined by the variation of the pressure measured in the external chamber. Within one cycle, the minimum value of the pressure registered in the chamber is below the value of Suction pressure, almost zero. The maximum value of pressure, measured during a cycle, is always above the Discharge pressure, almost reaching 169 bar.

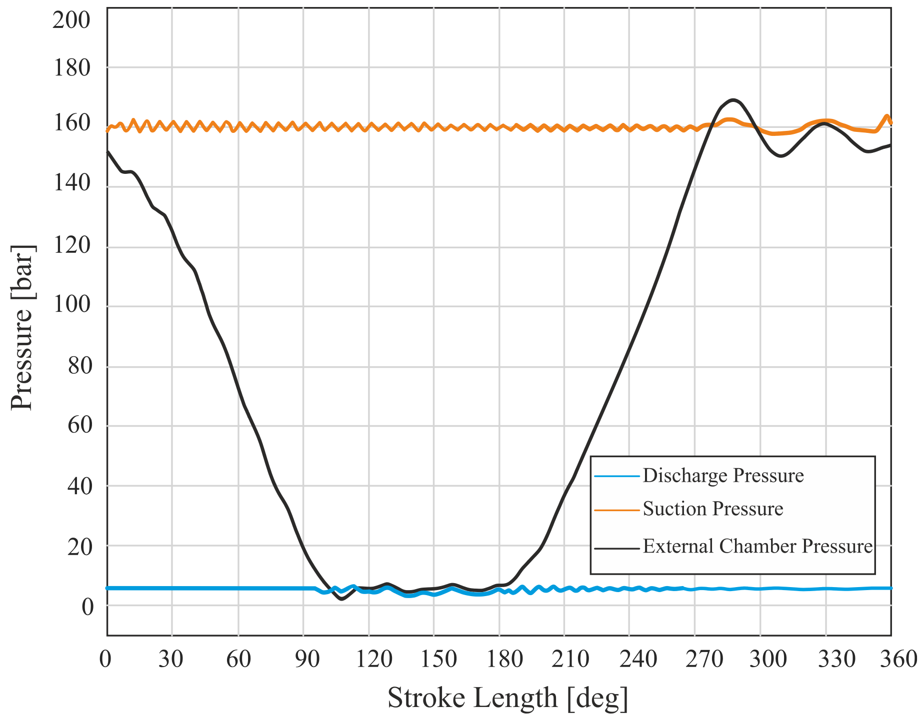

Figure 6.16: Variation of pressure values during one load cycle of test on Specimen 1.

The test stopped when the pressure dropped off and small leakage occurred. When the External Chamber was opened, the specimen was not entirely fractured, but cracks long enough to be visible by eye were present around the holes, in the transversal direction, on the top and bottom regions. Based on the lengths of cracks, it was estimated that, if the test started again at the same pressure level, the velocity of propagation would completely break the block in a short time. Therefore, the test was considered finished and number of cycles calculated accordingly.

To assess the positions of cracks and their precise extension, the block was cut, as shown in Figure 6.17, isolating the areas where cracks propagated. In this way, the four corners at the intersecting bores, where maximum stress distributions were expected, were extracted. A non-destructive method, liquid penetrate inspection, was undertaken to evaluate the crack extension on each of the four blocks. Figure 6.18 shows the four corner blocks, after the application of the penetrating liquid, which clearly highlighted the extension of cracks in both transverse and axial directions.

Figure 6.17: Cutting plan of Specimen 1 after corrosion fatigue test.

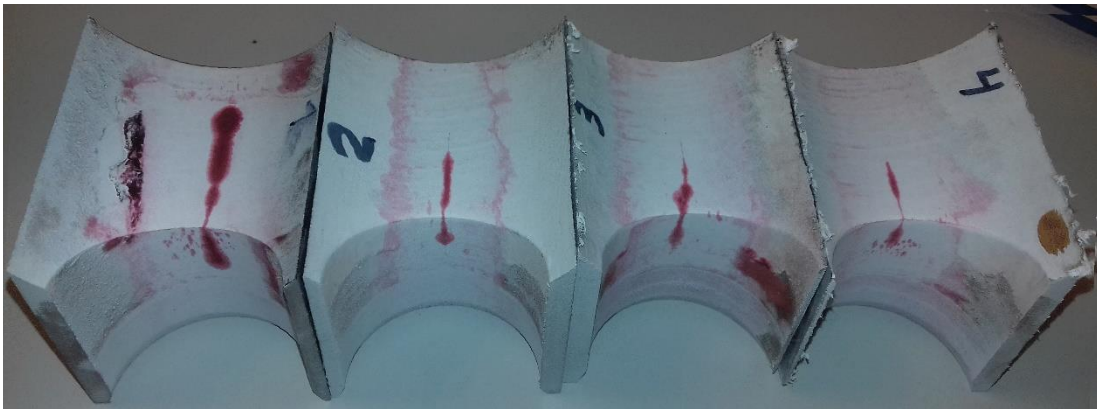

Figure 6.18: Liquid penetrate inspection on each of the four corners of intersecting bores of Specimen 1.

The longest crack occurred on corner 1, which transversal extension, measured through ImageJ®, is approximately 36 mm, almost 75% of the total length. The cracks didn't propagate exactly from the centre of the cross-bore intersection, where, theoretically, the maximum stress concentration occurs. This behaviour may be related to the degradation caused by corrosion effects: in a corrosive environment cracks mainly propagate from a corrosion defect, such as pits, which are developed on the surface. It was shown that the higher the stress amplitude, the more corrosion pits formed [145]. However, in the area where the stress amplitude is higher, pits development, and consequently cracks initiation, can be affected by different factors, including the microstructure and local composition of material [146]. Therefore, if crack initiation criterion is satisfied, thus to say the stress is sufficiently high, cracks can initiate also from other places where pits are already developed.

To estimate the stress distribution caused by the cyclic pressure on the specimen, an FE simulation was performed on a one-eighth of the model of Specimen 1. The Multilinear Kinematic Hardening model was selected, using the same material setting described in 6.1.3 for the shrink-fit analysis. The body was meshed by higher-order tetrahedral elements, as shown in Figure 6.19a). The size of elements for the mesh was previously checked to avoid any undue influence in the results. The model was constrained by imposing zero displacement perpendicular to the symmetrical surfaces and it was loaded by pressure acting on the internal surfaces, as shown in Figure 6.19b). Multiple steps were included in the analysis, to simulate the variation of pressure: from the minimum to the maximum values measured during the test, which are 0 to 16.86 MPa, whereas displacement constraints were constant, equal to zero, during all the steps. It was noted that, after 4 steps, results, in terms of distributions of stress, converge, showing differences between two consecutive couple of steps less than 0.5 MPa, whereas in the initial steps the difference is around 2 MPa. Therefore, for the fatigue analysis, the stress distributions, obtained after the convergence, are taken into account.

Figure 6.20 shows FEM results in terms of distribution of equivalent stress with application of the maximum pressure, 16.68 MPa, and the minimum pressure, 0 MPa, respectively in Figure 6.20a and Figure 6.20b, and the distribution of Normal Stress along x-axis, which is perpendicular to the cross-bores corner surface, in the maximum and minimum pressure configuration, in Figure 6.20c and Figure 6.20d respectively.

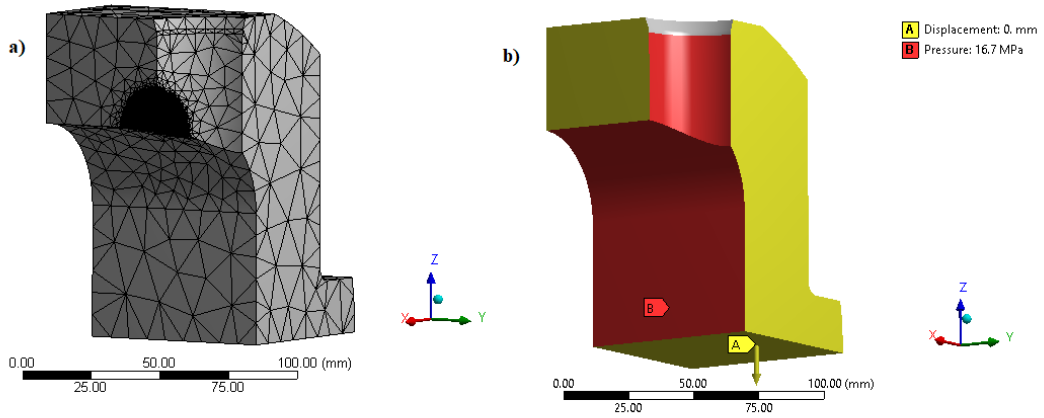

Figure 6.19: FEM model of one-eighth of Specimen 1. *a) detail of mesh distribution. b) analysis setting.*

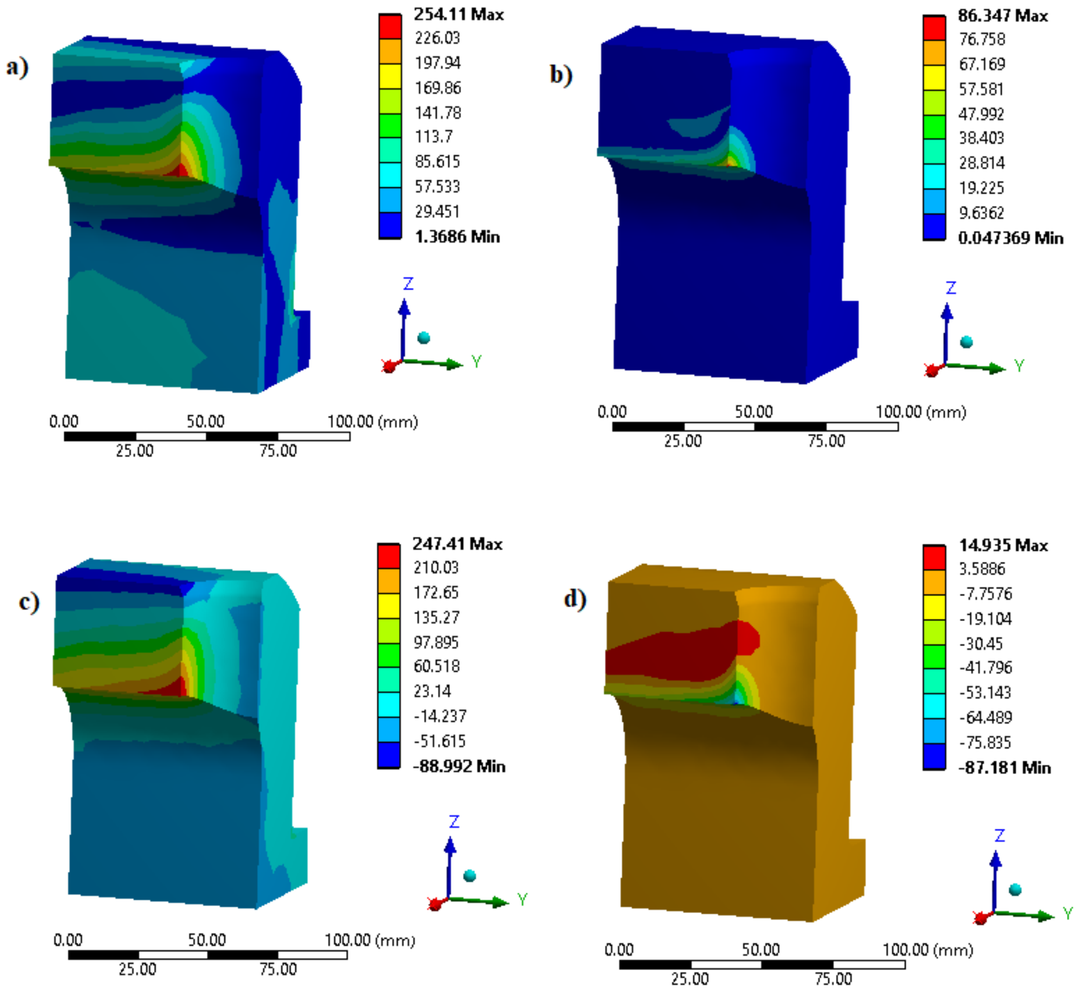

Figure 6.20: FEM calculation colour plot of Specimen 1*. a) von Mises Equivalent stress at 16.86 MPa of operational pressure, step 3; b) von Mises Equivalent stress at 0 MPa of operational pressure, step 4; c) Normal Stress (x-axis) at 16.86 MPa of operational pressure, step 3; d) Normal Stress (x-axis) at 0 MPa of operational pressure, step 4.*

The maximum Equivalent stress and the maximum Normal Stress occur when the maximum pressure is applied. Because of the predominance of the component along x-axis, for the fatigue analysis purpose, the multiaxial stress state can be reduced to a uniaxial stress state [147].

As shown by the FEM plot in Figure 6.20, the stress distribution on the fracture surface of Specimen 1 is not uniform, meaning that theoretically each point is subjected to a different fatigue cycle. Therefore, to assess the fatigue life of the entire component, the most critical stress range condition is evaluated and the analysis is based on this condition. The most critical condition occurs at the corner of the cross-bore intersection, and values of the maximum and minimum stress, calculated in the condition of maximum and minimum applied pressure respectively, are reported in Table 6.6. From these values, stress amplitude, mean stress and stress ratio were calculated and their values are summarised in Table 6.6.

Table 6.6: Values of stress at the cross-bore corner obtained by FEM simulation on Specimen 1.

$\sigma_{\max}$ (MPa)	$\sigma_{\min}$ (MPa)	σ_a (MPa)	σ_{mean} (MPa)	R
247	-87.1	165.1	78	-0.35

Although the nominal load ratio, defined as the ratio between the minimum applied load and the maximum applied load, is zero, the stress ratio at the most critical point of the specimen is different. This is due to the residual stress caused by the yielding in the area around the corner. In fact, during the first application of the maximum pressure, the stress in this area reaches the yield stress value, causing local plastic deformation. Because of the geometry, when the maximum load is released, a permanent deformation occurred leading to compressive residual stress, the absolute maximum value of which is the minimum stress. This is why, at the critical condition, the stress ratio is equal to R=-0.35.

6.2.2 Test on Specimen 2: Pressure Loading and Mean Stress

The cycling pressure test performed on the specimen assembled through the shrink-fit process, described in Section 6.1.3, ran for almost 38 hours continuously. The test performances, acquired during the test by the SCADA system and evaluated as described in section 6.2.1, are summarised in Table 6.7.

Representative pressure variations during a cycle, recorded during the test, are shown in Figure 6.21. Values of Suction pressure are almost constant during the entire cycle with small fluctuations around the mean value, which is actually lower than the nominal one, immediately after the opening of the Suction valve. A similar trend is shown in Discharge pressure values, which present fluctuations around the mean value, immediately after the Discharge valve opening.

Table 6.7: Measured data during the test on Specimen 2.

Suction Pressure (bar)	Discharge Pressure (bar)	Max. chamber Pressure (bar)	Min. chamber Pressure (bar)	Frequency (rpm)	Fatigue life (cycles)
0.6	150.2	161.2	0	250.28	5.7×10^5

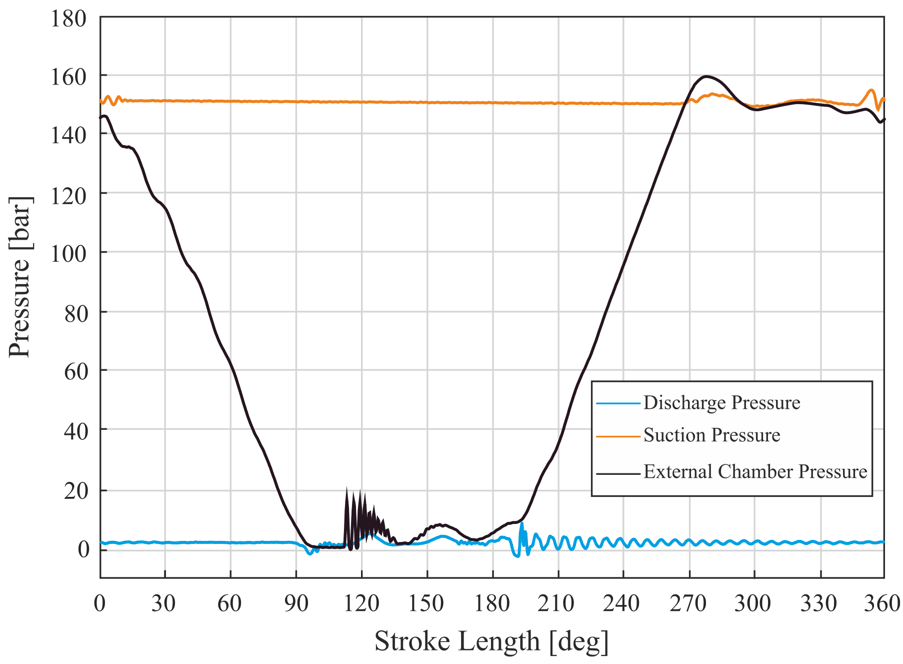

Figure 6.21: Variation of pressure values during one load cycle of test on Specimen 2.

The pressure measured in the external chamber, as described for tests on Specimen 1, varies during each cycle from the minimum value, occurring immediately before the suction valve opening, to the maximum value, occurring immediately before the Discharge valve opening. Values of maximum and minimum pressure in the external chamber define the range of pressure at which the industry scale specimen is subjected to every cycle.

The test on Specimen 2 was automatically shut down by the SCADA because of dropping pressure values. Cracks occurred at each of the four cross-bore corners and, in the two bottom corners, cracks propagated throughout the transversal thickness. The test concluded when it was stopped. Figure 6.22 shows Specimen 2 assembled in the external chamber, immediately after the conclusion of the test, and a detail of the propagated bottom crack.

To analyse the area where cracks propagated, the specimen was cut to extract the bottom and top area around the axial and the transversal holes, as shown in Figure 6.23. From the bottom, both of the two cracks, which developed from the opposite side of the central hole, propagated throughout the transversal direction.

From the top area, cracks initiated from both sides and propagated along the transversal direction but, in both cases, didn't achieve the external border.

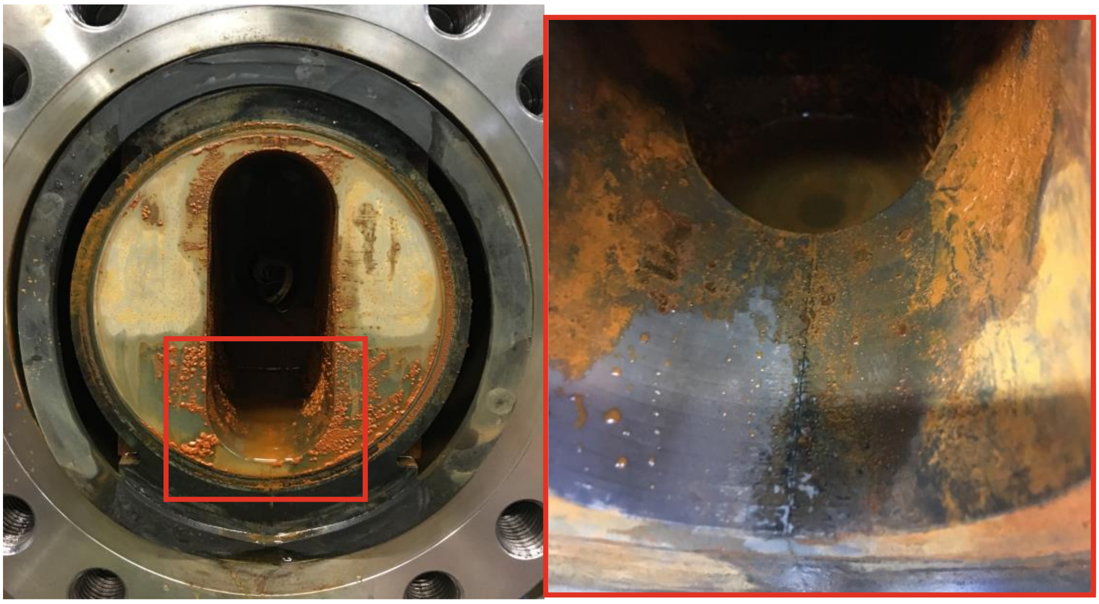

Figure 6.22: Specimen 2 after corrosion fatigue tests. *Details of propagated crack at the bottom corner.*

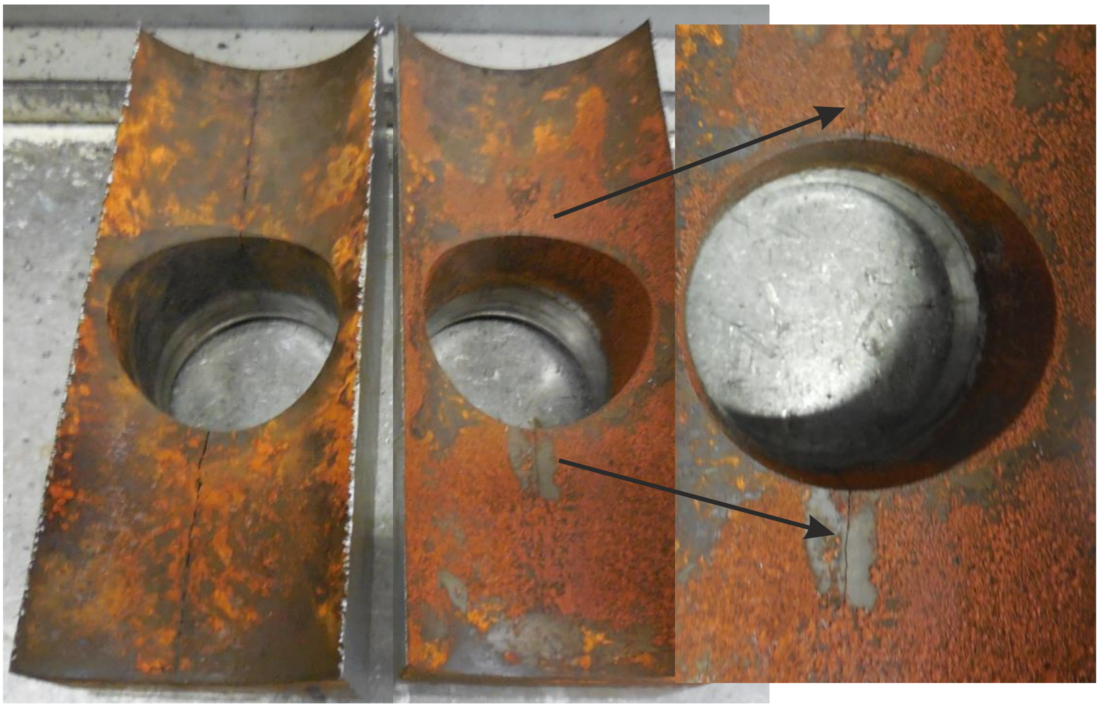

Figure 6.23: Detail of Specimens 2 after the test. *Isolated bottom (left) and top (right) area around the axial hole, highlighting extension of propagated cracks from the hole.*

Each of the two blocks was then divided into two halves, along the diameter of the hole perpendicular to the direction of the crack, obtaining four blocks. Lastly, each block was split in two following the propagated crack path, causing a static fracture on the remaining portion. Figure 6.24 and Figure 6.25 show the fracture surfaces of the two bottom areas, Corner 1 and Corner 2 respectively. Cracks propagated from Corner 2 reached the rounding of the hole, in the axial direction, and the external side of the specimen in the transversal direction. Cracks propagated from Corner 1 developed, in the transversal direction, up to the external side of the specimen, and, in the axial direction, almost at the rounding of the hole. Both cracks contributed to the leaking of the fluid, and consequently to the end of test. Based on the extension of the fractured surface, Figure 6.25, it is believed that the crack from Corner 2 started to propagate early. Figure 6.26 and Figure 6.27show fracture surfaces caused by cracks propagated from Corner 3 and Corner 4 respectively, both placed on the top of Specimen 2 during the pressure test. In both cases, the cracks didn't propagate deep enough to reach the external surface or the rounding of the hole. A common feature, visible in all the four fractured surfaces of Specimen 2, is the presence of multiple secondary cracks, caused by the effect of corrosion.

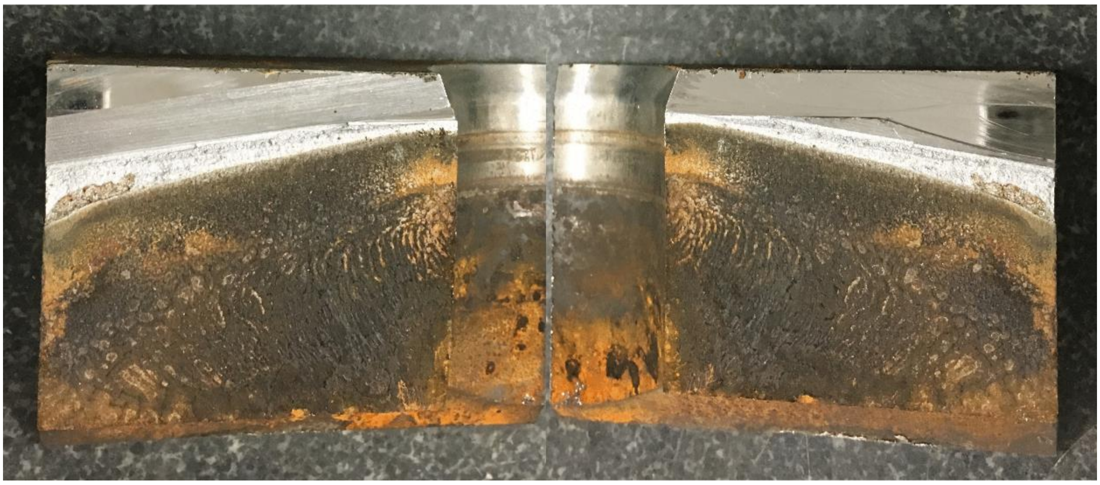

Figure 6.24: Detail of Corner 1, split along the propagated crack.

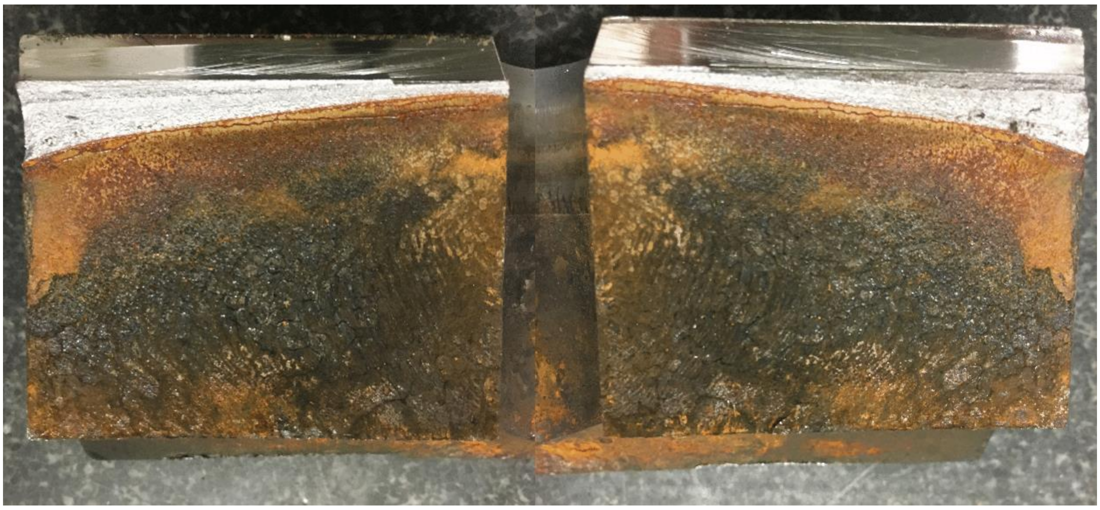

Figure 6.25: Detail of Corner 2, split along the propagated crack.

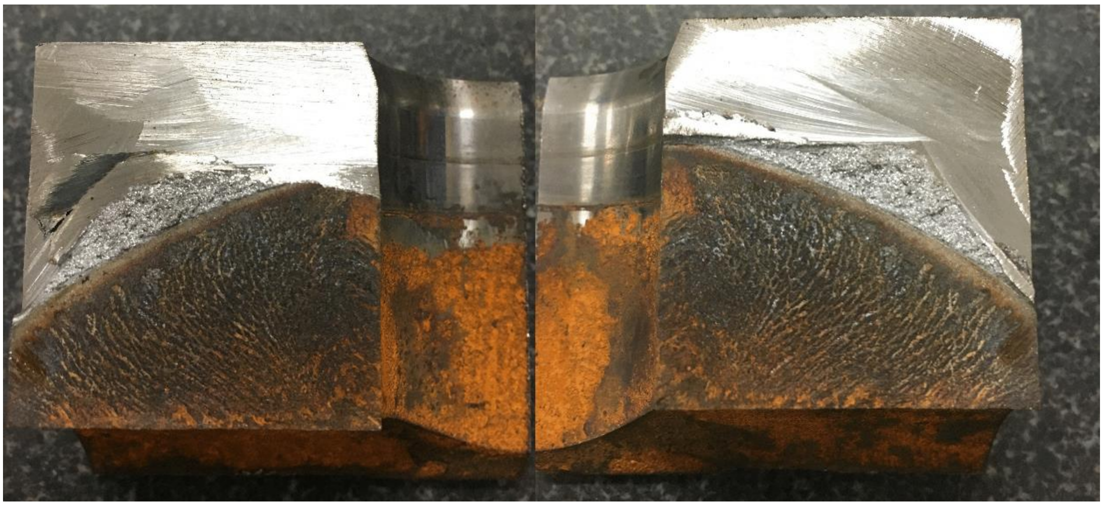

Figure 6.26: Detail of Corner 3, split along the propagated crack.

Figure 6.27: Detail of Corner 4, split along the propagated crack.

An FEM simulation was performed to calculate the stress distribution on the industry scale specimen, based on the pressure load cycle obtained from the measurements during the test. To simulate all the testing conditions, the combination of the shrink-fit process, described in section 6.1.3, and the cycling pressure problem, described in section 6.2.1, was reproduced. To assess and evaluate the stress state distribution, it is fundamental to include the static stress induced by the interference coupling fit. The same model described for the shrink fit process analysis, shown in Figure 6.12, with the same constraints, and the same mesh, Figure 6.13, are selected. In addition to the contact problem, the model is loaded by pressure, acting on the internal surface, as shown for Specimen 1 in Figure 6.19 b). In the first step of the simulation, only the load caused by the contact problem is imposed and the value of pressure is set to zero. After the first step, the effect of pressure is introduced and, at each consequent step, the value of pressure changes from the maximum, equal to 16.12 MPa, to the minimum, equal to 0 MPa.

FEM results in terms of von Mises equivalent stress distribution, both in the configuration of maximum and minimum applied pressure, are shown in Figure 6.28a and Figure 6.28b respectively. For the same pressure conditions, results in term of Normal Stress distribution along the x-axes, perpendicular to the fracture surface, are shown in Figure 6.28c and Figure 6.28d respectively. The main component of stress distribution, similarly to simulation on Specimen 1, is along the x-direction and, as this component is dominant, for the fatigue analysis purpose the multiaxial loading is reduced to a uniaxial state stress.

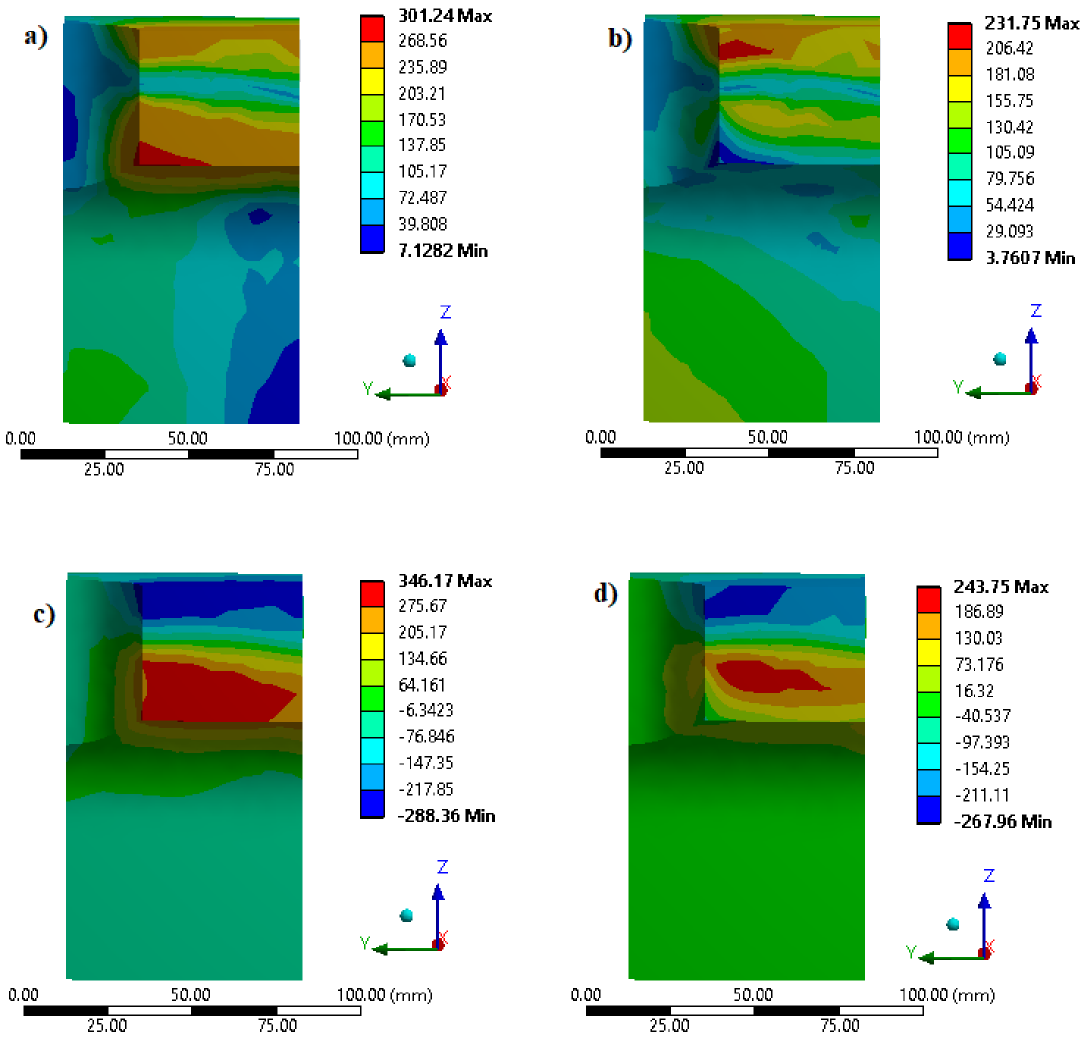

Figure 6.28: FEM calculation colour plot of Specimen 2. *a) von Mises Equivalent stress at 16.12 MPa of operational pressure, step 3; b) von Mises Equivalent stress at 0 MPa of operational pressure, step 4; c) Normal Stress (x-axis) at 16.86 MPa of operational pressure, step 3; d) Normal Stress (x-axis) at 0 MPa of operational pressure, step.*

To assess the range of stress the specimen was subjected to, the same procedure described for FEM analysis of Specimen 1, was used, identifying the most critical condition. The values of the maximum and minimum Normal stress along x, calculated respectively in the condition of maximum and minimum applied pressure, are reported in Table 6.8.

Table 6.8: Values of stress at the cross-bore corner resulted from FEM simulation on Specimen 2.

$\sigma_{\max}$ (MPa)	$\sigma_{\min}$ (MPa)	σ_a (MPa)	σ_{mean} (MPa)	R
291.7	-56.2	173.9	117.7	-0.19

Due to the constant stress induced by the interference coupling fit, the stress ratio, at the corner of intersection cross bore, is increased compared to the previous test. However, because of the residual stress caused by yielding, the minimum stress is still negative, leading to a negative value of stress ratio R. In other words, it was not possible to simulate a problem of fluctuation of stress entirely in the positive range.

6.3 Stress Life Prediction

6.3.1 Comparison of Pressured Industry Scale Test Results and Haigh Diagram Prediction

In this section, Stress Life prediction is used to estimate the corrosion fatigue life of the two industry scale specimens. In addition, a comparison with the Haigh diagram, developed at the fatigue life obtained from the two tests, using the procedure described in Chapter 5, is presented to highlight the limitation of Stress Life Prediction to design components in corrosive environment.

The first step to assess the corrosion fatigue life of the two blocks is considering, for each problem, the critical values in terms of stress amplitude and mean stress, obtained from the FEM analysis, reported in Table 6.6 and Table 6.8 for Specimen 1 and Specimen 2 respectively. These components were evaluated, for each specimen, using the maximum Normal x stress component in the configuration of maximum applied pressure and the minimum Normal x stress in the configuration of minimum applied pressure at the same geometrical point.

For both specimens, at the critical point, the value of stress ratio lies in Region II of the Haigh diagram, between R=-1 and R=0. The mean stress sensitivity factor in Region II is acquired from the evaluation of mean stress in corrosive environment as a function of the stress amplitude, using the approach proposed in section 5.4.2. The relation is shown in the equation (6.2)

$$M(\sigma_a) = 0.2179\ln(\sigma_a) - 0.772 \tag{6.2}$$

From this relationship, the values of mean stress sensitivity factor are generated at various levels of stress amplitude. Using the Schutz definition of mean stress sensitivity factor in Region II, reported in (6.3), it is possible to generate values of stress amplitude $\tilde{\sigma}_a$ at the stress ratio R representative for the critical conditions of each industry scale test, as a function of the number of cycles.

$$M_\sigma = \frac{\sigma_{a,R=-1} - \tilde{\sigma}_a}{\tilde{\sigma}_a (1+R)/(1-R)} \tag{6.3}$$

Then, using the linear regression analysis, Basquin's relations are found for the two loading conditions, with constants summarised in Table 6.9. Consequently, using the maximum amplitude stress, the corrosion fatigue life of each component is estimated, based on simultaneous corrosion fatigue testing on uniaxial specimens. The estimated fatigue life and the mean stress sensitivity factor value at the estimated fatigue life are summarised in Table 6.10 for the two testing conditions.

Table 6.9: Constant values defining Basquin's equations at R=-0.35 and R=-0.19.

Type of Stress	$\sigma_f^{'}$, (MPa)	b
R=-0.35	7213.7	-0.2666
R=-0.19	5936.4	-0.2572

Table 6.10: Estimated corrosion fatigue life and mean stress sensitivity factor for industry scale tests.

Configuration	Type of Stress	M_σ	Predicted fatigue life
Specimen 1	R=-0.35	0.37	7.11×10^5
Specimen 2	R=-0.19	0.40	4.56×10^5

To graphically show the difference between the Stress Life prediction and the experimental results, the allowable amplitude stress at the fatigue life obtained by the experimental tests is shown, for each condition, in the Haigh diagram. Representations of Haigh diagrams for Specimen 1 and Specimen 2 are shown in Figure 6.29 a and Figure 6.29 b respectively. In both cases, the experimental result lies outside the allowable amplitude stress area, which means under the Haigh diagram predictions, the combination of amplitude and mean stress should be lower to achieve the corrosion fatigue life. For both testing conditions, the Stress-Life prediction is slightly more conservative than the experimental results.

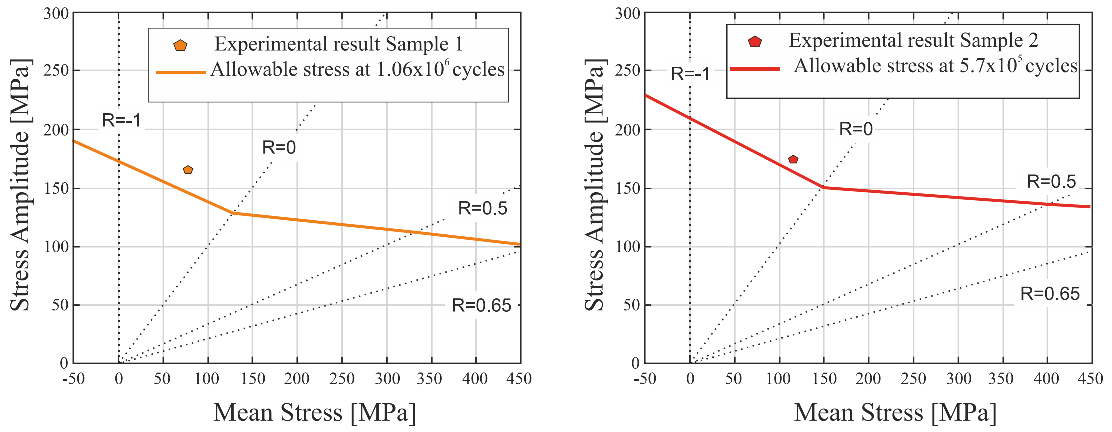

Figure 6.29: Haigh diagrams of industry scale specimens. *Allowable stresses calculated at the fatigue life of Specimen 1 (left) and Specimen 2 (right) respectively.*

6.3.2 Discussion

The Stress Life prediction, used to estimate the corrosion fatigue life of industry scale problems, shows a good agreement with experimental results in term of number of cycles. The same trend is also highlighted in the representations of the Haigh diagrams for both testing conditions at the number of cycles obtained from the experimental investigation. The difference between the calculated stress amplitude obtained from the FEM simulation, and the allowable stress, predicted through the Haigh diagram, at the same fatigue life, is less than 10% in the case of specimens subjected to the sole effect of cycling pressure and around 5% in the configuration with residual stress. For both tests, the prediction obtained using the stress-life analysis is conservative in comparison to the corrosion fatigue life obtained experimentally. The number of cycles at which both industry scale experimental tests ended are higher than those predicted by the model. This is seen in the Haigh diagram where, for both loading configurations, the allowable stress predicted by the model is lower than the experimental stress conditions and consequently the experimental stress configuration lies outside the allowable stress limits on the Haigh diagram.

This difference between the predictive corrosion fatigue life based on Stress Life analysis and corrosion fatigue life of industry scale components can be explained by the different portion of life spent in the crack initiation and the crack propagation stages. It is proposed that cracks in the uniaxial stress field propagate faster compared to cracks at the cross bore corners in the industry scale specimens when compared for the same stress at the surface. The difference in crack propagation under the same surface stress conditions may happen because of the different stress gradient. In uniaxial specimens, the stress distribution is constant thought the section of the specimens and the only variations in local stress distribution are caused by the propagation of the crack that changes the local geometry of the specimen. Differently, at the cross bore corner, around which the stress distribution is not constant, the crack, initiated from the surface at high stress equal to uniaxial conditions, slows down in the field of decreasing stress. In this case, because of the lower stress, the crack growth is lower and consequently, the corrosion fatigue life of the component longer.

The same trend is showed by Okorokov *et al*. [148] in the comparison of fatigue strength of double notched S355J2 specimens, under loading ratio of the applied remote load R=0, and uniaxial specimens, both tested in corrosive environment. There, the difference in corrosion fatigue strength prediction between the double notched test results and the Stress Life analysis is even bigger than in the case of industry scale components, as the geometry of double notched specimen induced a bigger stress gradient.

Chapter 7

Conclusion

The research work proposed in this thesis aimed to improve the fatigue assessment currently used by WMNL for the design of Fluid End components of the GEHO pumps family. The main research questions which motivated this work are:

- How does the fatigue strength of low carbon steel S355J2 change in corrosive environment with increasing fatigue lives? In particular, what is the corrosion fatigue strength at 10^9 cycles in the freshwater environment?
- What is the effect of positive mean stress on the corrosion fatigue proprieties of low carbon steel S355J2?

The fatigue and corrosion fatigue behaviours of low carbon steel S355J2 were experimentally investigated and a predictive model on positive mean stress effect for various ranges of fatigue life proposed, aimed at improving the corrosion fatigue design methodology for Fluid End components of GEHO pumps.

To understand the fatigue behaviour of S355J2 in air and in the freshwater environment three major groups of experimental tests were designed and performed:

- Uniaxial fatigue tests in air, to characterise the fatigue in air at different stress ratios and to use this information to be compared with the behaviour in corrosive environment.
- Corrosion testing on unloaded specimens exposed to freshwater flow in a corrosion cell, to evaluate the effect of corrosion overtime on surface properties of S355J2 low carbon steel.
- Uniaxial fatigue tests in corrosive environment on virgin specimens and on pre-corroded specimens under various stress ratios and load frequencies, to evaluate how the corrosion fatigue strength of S355J2 low carbon steel decreases with increasing fatigue life under the different testing conditions.

Analyses of experimental data, in terms of fatigue strength and fractography of specimens tested under different conditions led to the development and implementation of a predictive model. The model describes the corrosion fatigue strength of S355J2 in the freshwater environment, predicting the behaviour up to 10^9 cycles and describing how the corrosion fatigue strength is affected by the positive mean stress, at various ranges of fatigue life. The practical application of this model is the design of Fluid End components of GEHO pumps. To validate the model, industry scale specimens were designed and manufactured to be representative of the geometry of GEHO's diaphragm houses that are one of the most critical component among the Fluid End section. Tests were performed under cyclic pressure, with and without the application of additional static loads to simulate different mean stress conditions.

7.1 Key Findings

The following conclusions may be drawn:

- Results of fatigue testing in air show that the fatigue strength of S355J2 low carbon steel can be represented by a power law equation, up to approximately 2 million cycles. At this fatigue life, the strength is around 80% and 70% of the material's yield when tested at R=-1 and R=0 respectively. A plateau in the S-N diagram is identified for fatigue life longer that 2 million cycles.
- Fatigue tests in air are not affected by the different types of fatigue machines used in the experiments. Results are in within the scatter.

- Corrosion testing on unloaded specimens in the freshwater solution identified general corrosion attack on the material surface. Microscopic examinations and surface roughness measurements showed an unsteady corrosion effect during the initial phase of corrosion exposure. After approximately 15 days of corrosion exposure, surface properties such as pit depth and surface roughness stabilise, exhibiting a steady corrosion effect.
- Fatigue life is significantly reduced under corrosion fatigue conditions in a freshwater environment at load frequency 10 Hz compared to fatigue lives obtained in air. At a fatigue life of 10^6 cycles, the corrosion fatigue strength is 79% of the fatigue strength in air and the difference increases at longer fatigue lives, achieving the 40% of the fatigue strength in air at 10^7 cycles.
- Fractography on corrosion fatigue tested specimens showed the presence of multiple cracks both on the fracture surface of the specimens and on the lateral surfaces. This characteristic is in contrast with the typical behaviour occurring in fatigue in air, where usually only one crack develops and grows during the fatigue life of the sample.
- The corrosion fatigue lives of S355J2 specimens tested in a freshwater environment are strongly influenced by the flow conditions around the material during the fatigue test. Microscopic analysis of specimen surfaces, tested using two different corrosion chambers, which induced two different flow distributions, showed changes in the deterioration of samples. Variations were quantified through surface roughness measurements. At a stress amplitude of 90 MPa, under the same loading conditions and the same chemical environment, the difference in fatigue life is a factor of 3.
- The exposure of specimens to a corrosive environment before corrosion fatigue testing had a stronger effect at shorter fatigue lives. Comparison with simultaneous corrosion fatigue results performed on virgin specimens, under the same testing conditions, suggested that after an initial phase, where general surface degradation occurs on virgin specimens, the characteristics of the two families of tests are aligned. Consequently, after this initial phase, the corrosion fatigue life of virgin and pre-corroded specimens is found to be the same.
- High frequency corrosion fatigue results, obtained in the region between $5x10^7$ and $5x10^8$ cycles, confirmed the hypothesis that the corrosion fatigue

behaviour in that region can be described by the extrapolation of pre-corroded experimental data.

- The corrosion fatigue behaviour of S355J2 in between 10^6 and 10^9 cycles in the freshwater environment can be ideally schematised by two different power law equations, in log-log S-N diagrams. The transition between the two behaviour can be identified with the time in which surface degradation, caused by the corrosion effect, becomes steady. The first region is mainly driven by the corrosion effect and is time dependant. Conversely, the second region is driven by the loading condition and is cycles dependant.
- No fatigue limit is observed in the fatigue behaviour of S355J2 in a freshwater environment. In a corrosive environment failures occurred even below the fatigue limit in air.
- The literature review of existing models taking account of the mean stress effect on fatigue behaviour in air showed that the model that best predicts the effect of mean stress is the Walker approach. This approach requires experimental information for at least two loading conditions to be defined. A good agreement with this approach was also shown by experimental results obtained from S355J2 specimens fatigued in air.
- The comparison between Haigh diagrams in air obtained from experimental results and the FKM procedure showed that parameters employed to design the latter are not representative of the low carbon steel S355J2 behaviour resulting in a non-conservative diagram, with an error of around 15%.
- The analyses of mean stress effects on the behaviour of S355J2 in the freshwater solution were performed through the development of Haigh diagrams at different fatigue lives. The Schutz definition of mean stress sensitivity factor was employed to evaluate the effects of positive mean stress for load conditions between R=-1 and R=0. Modified Schutz parameters were defined in the thesis and employed to evaluate the effects at higher stress ratio conditions in the Haigh diagrams.
- Experimental results showed that the material is more sensitive to mean stress at higher values of stress ratio. This means that the reduction of corrosion fatigue strength is higher at higher stress ratios, in absolute terms. This trend is opposite to what is proposed by FKM guidelines in air, which suggested a decrease of sensitivity with increasing stress ratio.

- A comparison between the different flow conditions showed that at the same loading conditions, the material presented the same mean stress sensitivity factor.
- The design and manufacture of the industrial scale samples and modifications to the WMNL test rig succeeded in the safe performance of industrial scale tests. The shrink-fit process was successfully performed, allowing the generation of residual stress in the specimen.
- The results of the industry scale tests showed good agreement with the number of cycles to failure calculated using the methodology proposed in the thesis.

7.2 Further Work and Discussion

The following has been identified as potential future work:

Corrosion fatigue experimental tests on pre-corroded specimens at high loading frequency.

The comparison between corrosion fatigue results on virgin and pre-corroded specimens showed that the two S-N curves, plotted in a logarithmic scale, crossed each other at fatigue life around $2x10^7$. Based on the analyses presented in Section 5.3, it was found that the pre-corrosion process affects the corrosion fatigue life of S355J2 only up to a certain extent, which is roughly around $2x10^7$ cycles. An experimental investigation on pre-corroded specimens under corrosion fatigue conditions in the fatigue life range around 10^8 cycles would better define the effect of the initial degradation and would help in defining the material behaviour investigation in the very high cycle fatigue regime. In particular, the following hypothesis could be experimentally confirmed: the corrosion fatigue behaviour at elevated number of cycles may be represented by the extrapolation of S-N curve of pre-corroded specimens obtained in the region between 10^6 and $2x10^7$ cycles.

Investigation of the effect of flow distribution on corrosion fatigue behaviour. Experimental results, obtained from the two corrosion cell designs, showed that the effect of corrosive flow velocity and distribution around the fatigued specimen plays an important role on the corrosion fatigue life. This is a significant finding could be used in the design of Fluid End components but requires further investigation. It would be interesting to determine to what extent the flow distribution affects the corrosion fatigue life both in the freshwater environment and in a more aggressive environment, such as seawater. Results would help in the design of corrosion fatigue test rigs and in the definition of Standard guideline to accurately perform, interpret and use experimental information. In addition, it would be interesting to study from a fluid dynamic prospective the flow distribution inside the two corrosion chambers, employed in this thesis, and to compare the results with the flow distribution inside the Diaphragm House. In particular, it would be useful to understand if the internal flow of the Diaphragm House can be modified to be closer to the condition occurred in Exova corrosion cell.

Industry scale testing.

The design of the industrial scaled testing, which included both the conceiving of specimens and of loading application in conjunction with the implementation of the test rig, succeed in the performance of corrosion fatigue testing on industrial scale specimens. However, improvements can be applied for future industrial scale tests, which are planned by WMNL, to represent higher stress ratio conditions. The use of the shrink fit process to introduce static tension in the sample was found to be limited in the maximum tensile stress that could be induced. In other words, it is not possible to achieve high value of stress ratio with the current arrangement. The implementation of different specimen design could allow testing condition which simulate higher stress ratio conditions to be achieved. This would require the modification of the Chamber and all attached connections and seals. Alternatively, a modification of the pump system could allow the realisation of higher suction pressure, which in turn would simulate a loading condition at higher stress ratio.

References

1. Weir, G.; Available from: https://www.global.weir/products/product-catalogue/geho-zpm/.
2. Akid, R., *Corrosion fatigue*, in *Shreir's Corrosion*. 2010. p. 928-953.
3. Hagn, L., *Life prediction methods for aqueous environments.* Materials Science and Engineering, 1988. **103**(1): p. 193-205.
4. 3, E., *Design of Steel Structures. Part 1.9: Fatigue*, in *EN-1993-1-9*. 2009.
5. Hänel, B., et al., *FKM-Richtlinie: Rechnerischer Festigkeitsnachweis für Maschinenbauteile aus Stahl, Eisenguss-und Aluminiumwerkstoffen.* Aufl. Forschungskuratorium Maschinenbau, Frankfurt/Main, 2003.
6. Standard, D.-G., *DNV-OS-J101 Design of Offshore Wind Turbine Structures*. 2014.
7. Standard, D.G., *DNVGL-ST-0126 Support structures for wind turbines*. 2016.
8. van Rijswick, R., *Fluid structure interaction in piston diaphragm pumps*. 2017, Delft University of Technology.
9. van Rijswick, R., *Alcan gove pulsation and vibration analysis* V.r.W.M.N. b.v., Editor. 2008.
10. Engineers, T.A.o.G., *Systematic calculation of high duty bolted joints* in *VDI 2230*. 2003.
11. Standardization, G.I.f., *Preferred Numbers and Series of Preferred Numbers* in *DIN 323-2* 1974: Germany.
12. Haibach, E., *Rechnerischer Festigkeitsnachweis für Maschinenbauteile (Analytical Strength Assessment of Components in Mechanical Engineering)* F. Guideline, Editor. 2003: Frankfurt Main.
13. Haigh, B.P., *Experiments on the fatigue of brasses.* Journal of the Institute of Metals, 1917. **18**: p. 55-86.
14. Dowling, N. and Thangjitham, S., *An Overview and Discussion of Basic Methodology for Fatigue*, in *An Overview and Discussion of Basic Methodology for Fatigue*. 2000. p. 3-36.
15. Wöhler, A., *Über die Festigkeitsversuche mit Eisen und Stahl.* Zeitschrift für Bauwesen, 1870. **20**: p. 73-106.
16. Dowling, N.E., *Mechanical Behaviour of Materials*, in *Engineering Methods for Deformation, Fracture, and Fatigue* Pearson, Editor. 2013.
17. R. I. Stephens, A.F., R. R. Stephens, H. O. Fuchs, *Metal Fatigue in Engineering*, J.W. Sons, Editor. 2001: Canada p. 74-78.

18. Hou, S.-q. and Xu, J.-q., *Relationship among S-N curves corresponding to different mean stresses or stress ratios.* Journal of Zhejiang University-SCIENCE A, 2015. **16**(11): p. 885-893.
19. Milella, P.P., *Fatigue and Corrosion in Metals*, Springer, Editor. 2013.
20. Bathias, C., Paris, P.C.,, *Gigacycle Fatigue in Mechanical Practice*. 2005, New York Mercel Dekker.
21. Neuber, H., *Theory of Notch Stresses: Principles for Exact Stress Calculation*. 1946: Edwards, J.W. .
22. Pilkey, W., *Peterson's Stress Concentration Factors*. Second ed. 1997.
23. Wehner, T. and Fatemi, A., *Effects of mean stress on fatigue behaviour of a hardened carbon steel.* International Journal of Fatigue, 1991. **13**(3): p. 241-248.
24. Geber, W.Z., *Bestimmung der zulässigen Spannunger in Eisenstructures.* Z Bayer Archit Ing, 1874. **6**: p. 101-110.
25. Goodman, J., *Mechanics Applied to engineering.* 1899.
26. Coffin Jr, L.F., *A study of the effects of cyclic thermal stresses on a ductile metal.* Transactions of the American Society of Mechanical Engineers, New York, 1954. **76**: p. 931-950.
27. Manson, S. and Hirschberg, M., *Fatigue: an interdisciplinary approach.* Syracuse University Press, Syracuse, NY, 1964: p. 133.
28. Zehnder, A.T., *Lecture notes on fracture mechanics.* Cornell University, 2007. **20**: p. 22.
29. Newman, I. and Raju, I., *Stress Intensity Factor Equations for Cracks in Three-Dimensional Finite Bodies Subjected to Tension and Bending Loads*. Vol. 85. 1984.
30. Tada, H., Paris, P.C., and Irwin, G.R., *Two-Dimensional Stress Solutions for Various Configurations with Cracks*, in *The Stress Analysis of Cracks Handbook, Third Edition*, H. Tada, P.C. Paris, and G.R. Irwin, Editors. 2000, ASME: New York, NY.
31. Murakami, Y., *Stress intensity factors*. 1987: Pergamon Books Inc.,Elmsford, NY; None. Medium: X; Size: Pages: 1566.
32. Vasudevan, A.K. and Sadananda, K., *Analysis of fatigue crack growth under compression–compression loading.* International Journal of Fatigue, 2001. **23**: p. 365-374.
33. Rice, J.R., *A Path Independent Integral and the Approximate Analysis of Strain Concentration by Notches and Cracks.* Journal of Applied Mechanics, 1968. **35**(2): p. 379-386.
34. Hu, H.-j., et al., *A new cyclic J-integral for low-cycle fatigue crack growth.* Applied Mathematics and Mechanics, 2006. **27**(2): p. 149-160.
35. Paris, C.P., Gomez, P.Mario, Anderson, E. William, *A Rational Analytic Theory of Fatigue* The trend in Engineering, 1961. **13**: p. 9-14.
36. Paris, P. and Erdogan, F., *A Critical Analysis of Crack Propagation Laws.* Journal of Basic Engineering, 1963. **85**(4): p. 528-533.
37. Elber, W., *Fatigue crack closure under cyclic tension.* Engineering Fracture Mechanics, 1970. **2**: p. 37.
38. Elber, W., *The Significance of Fatigue Crack Closure.* Damage Tollerance in Aircraft Structures ASTM STP 486, 1971: p. 230-242.
39. Zerbst, U., et al., *About the fatigue crack propagation threshold of metals as a design criterion – A review.* Engineering Fracture Mechanics, 2016. **153**: p. 190-243.

40. Lawson, L., Chen, E.Y., and Meshii, M., *Near-threshold fatigue: a review*. International Journal of Fatigue, 1999. **21**: p. S15-S34.
41. Suresh, S., *Fatigue of Materials*. Second ed. 2001.
42. Tanaka, K., *4.04 - Fatigue Crack Propagation*, in *Comprehensive Structural Integrity*, I. Milne, R.O. Ritchie, and B. Karihaloo, Editors. 2003, Pergamon: Oxford. p. 95-127.
43. Lancaster, J., *Engineering Catastrophes: Causes and Effects of Major Accidents*, W. Publishing, Editor. 1996: Cambridge.
44. G.H. Koch, M.P.H.B., N.G. Thompson, Y.P. Virmani, and J.H. Payer., *Corrosion Costs and Preventive Strategies in the United States.* NACE International.
45. Xie, Y., et al., *Corrosion behavior of novel 3%Cr pipeline steel in CO2 Top-of-Line Corrosion environment.* Materials & Design (1980-2015), 2012. **36**: p. 54-57.
46. Xu, L.Y. and Cheng, Y.F., *Experimental and numerical studies of effectiveness of cathodic protection at corrosion defects on pipelines.* Corrosion Science, 2014. **78**: p. 162-171.
47. Alamilla, J.L., et al., *Failure analysis and mechanical performance of an oil pipeline.* Materials & Design, 2013. **50**: p. 766-773.
48. Bordbar, S., Alizadeh, M., and Hashemi, S.H., *Effects of microstructure alteration on corrosion behavior of welded joint in API X70 pipeline steel.* Materials & Design, 2013. **45**: p. 597-604.
49. E647-15, A., *Standard Test Method for Measurement of Fatigue Crack Growth Rates*, in *ASTM E647-15*. 2015, ASTM.
50. Endo, K., Komai, K., and Nakamuro, N., *ESTIMATION OF CORROSION FATIGUE STRENGTH BY CORROSION RESISTANCE AND NOTCH SENSITIVITY OF MATERIALS.* Bull JSME, 1970. **13**(61): p. 837-846.
51. Imhof, E.J. and Barsom, J.M., *FATIGUE AND CORROSION-FATIGUE CRACK GROWTH OF 4340 STEEL AT VARIOUS YIELD STRENGTHS.* ASTM Special Technical Publication, 1972: p. 182-205.
52. Mansor, N.I.I., et al., *A review of the fatigue failure mechanism of metallic materials under a corroded environment.* Engineering Failure Analysis, 2014. **42**: p. 353-365.
53. Akid, R., *2.12 - Corrosion Fatigue**, in *Shreir's Corrosion*, B. Cottis, et al., Editors. 2010, Elsevier: Oxford. p. 928-953.
54. Larrosa, N.O., Akid, R., and Ainsworth, R.A., *Corrosion-fatigue: a review of damage tolerance models.* International Materials Reviews, 2018. **63**(5): p. 283-308.
55. Pook, L., *Metal Fatigue*, Springer, Editor. 2007: London.
56. Forrest, P.G., *CHAPTER I - INTRODUCTION*, in *Fatigue of Metals*, P.G. Forrest, Editor. 1962, Pergamon. p. 4-14.
57. Miller, K.J., *THE TWO THRESHOLDS OF FATIGUE BEHAVIOUR.* Fatigue & Fracture of Engineering Materials & Structures, 1993. **16**(9): p. 931-939.
58. Ritchie, R.O. and Lankford, J., *Small fatigue cracks: A statement of the problem and potential solutions.* Materials Science and Engineering, 1986. **84**: p. 11-16.
59. McAdam, D.J., *Stress-strain relationships and the corrosion-fatigue of metals.* Proc. ASTM, 1926. **26**: p. 224-254.
60. Gough, H.J.J., *Corrosion-Fatigue in Metals.* Institute of Metals, 1934. **1**(11).

61. Nicholas, T., *Chapter 3 - Accelerated Test Techniques*, in *High Cycle Fatigue*, T. Nicholas, Editor. 2006, Elsevier Science Ltd: Oxford. p. 70-142.
62. Nikolin, E.S. and Karpenko, G.V., *Effect of loading frequency upon the corrosion-fatigue strength of carbon steel.* Soviet materials science : a transl. of Fiziko-khimicheskaya mekhanika materialov / Academy of Sciences of the Ukrainian SSR, 1966. **1**(5): p. 368-370.
63. Endo, K. and Miyao, Y., *Effects of cycle frequency on the corrosion fatigue strength.* Bulletin of JSME, 1958. **1**(4): p. 374-380.
64. Rolfe, S.T. and Barsom, J.M., *Fracture and fatigue control in structures: Applications of fracture mechanics*. 1977: ASTM International.
65. Barsom, J.R., S.,, *Fracture and Fatigue Control in Structures: Applications of Fracture Mechanics,*. Third ed. 1999.
66. Forrest, P.G., *CHAPTER III - FATIGUE STRENGTH OF METALS*, in *Fatigue of Metals*, P.G. Forrest, Editor. 1962, Pergamon. p. 56-92.
67. Speidel, M., *Corrosion fatigue*, in *Fracture 84*. 1984, Elsevier. p. 379-398.
68. Ragab, A., Alawi, H., and Sorein, K., *CORROSION FATIGUE OF STEEL IN VARIOUS AQUEOUS ENVIRONMENTS.* Fatigue & Fracture of Engineering Materials & Structures, 1989. **12**(6): p. 469-479.
69. Rollins, V., Arnold, B., and Lardner, E., *Corrosion fatigue in high carbon steel.* British Corrosion Journal, 1970. **5**(1): p. 33-40.
70. Palin-Luc, T., et al., *Fatigue crack initiation and growth on a steel in the very high cycle regime with sea water corrosion.* Engineering Fracture Mechanics, 2010. **77**(11): p. 1953-1962.
71. Murtaza, G. and Akid, R., *Empirical corrosion fatigue life prediction models of a high strength steel.* Engineering Fracture Mechanics, 2000. **67**(5): p. 461-474.
72. Masahiro, G., *Corrosion fatigue behavior of a heat-treated carbon steel and its statistical characteristics.* Engineering Fracture Mechanics, 1992. **42**(6): p. 893-909.
73. Murtaza, G. and Akid, R., *Corrosion fatigue short crack growth behaviour in a high strength steel.* International Journal of Fatigue, 1996. **18**(8): p. 557-566.
74. Ebara, R., Kai, T., and Inoue, K., *Corrosion-Fatigue Behavior of 13Cr Stainless Steel in Sodium-Chloride Aqueous Solution and Steam Environment*, in *Corrosion-Fatigue Behavior of 13Cr Stainless Steel in Sodium-Chloride Aqueous Solution and Steam Environment*. 1978.
75. Ebara, R., *Long-term corrosion fatigue behaviour of structural materials.* Fatigue and Fracture of Engineering Materials and Structures, 2002. **25**(8-9): p. 855-859.
76. Ebara, R., et al., *Fractographic Analysis of Corrosion Fatigue Cracking of 13 Cr Stainless Steel in NaCl Aqueous Solution.* Journal of the Society of Materials Science, Japan, 1978. **27**(292): p. 64-68.
77. Forrest, P.G., *CHAPTER IV - THE INFLUENCE OF STRESS CONDITIONS ON FATIGUE STRENGTH*, in *Fatigue of Metals*, P.G. Forrest, Editor. 1962, Pergamon. p. 93-127.
78. Soderberg, C.R., *Workig Stresses.* ASME Applied Mechanics Division 1933. **1**(3).
79. Morrow, J., *Fatigue Properties of Metals*, in *Fatigue Design Handbook*, S.o.A. Engineers, Editor. 1968.
80. Landgraf, R.W., *The resistance of metals to cyclic deformation. Achievement of High Fatigue Resistance in Metals and Alloys.* ASTM, 1970: p. 3-36.

81. Watson, P., *The effect of mean stress and overstrain on the fatigue behaviour of structural components*. 1971, University of Waterloo Canada.
82. Dowling, N.E., *Mean stress effects in stress-life and strain-life fatigue.* SAE Technical Papers, 2004.
83. Kececioglu, D., Chester, L.B., and Dodge, T.M., *Combined Bending-Torsion Fatigue Reliability of AISI 4340 Steel Shafting With Kt = 2.34.* Journal of Engineering for Industry, 1975. **97**(2): p. 748-760.
84. Kececioglu, D., et al., *Fatigue Reliability With Notch Effects for AISI 4130 and 1038 Steels.* Journal of Engineering for Industry, 1975. **97**(1): p. 359-370.
85. Sekercioglu, T., *A new approach to the positive mean stress diagram in mechanical design.* Materialwissenschaft und Werkstofftechnik, 2009. **40**(9): p. 713-717.
86. Bagci, C., *Fatique design of machine elements using the "Bagci line" defining the fatigue failure surface line (mean stress diagram).* Mechanism and Machine Theory, 1981. **16**(4): p. 339-359.
87. Orthwein, W.C., *Estimating fatigue dueto cyclic multiaxial stress.* Journal of Vibration and Acoustics, Transactions of the ASME, 1987. **109**(1): p. 97-102.
88. Wang, S.-J., et al., *The Clemson Limit Stress Diagram for Ductile Parts Subjected to Positive Mean Fatigue Loading.* Journal of Mechanical Design, 2000. **122**(1): p. 143-146.
89. Kwofie, S., *An exponential stress function for predicting fatigue strength and life due to mean stresses.* International Journal of Fatigue, 2001. **23**(9): p. 829-836.
90. Papuga, J., et al. *Mean stress effect in stress-life fatigue prediction re-evaluated*. in *MATEC Web of Conferences*. 2018.
91. Smith, K.N., Watson, P., and Topper, T.H., *Stress- strain function for the fatigue of metals.* J Mater, 1970. **5**(4): p. 767-778.
92. Bergmann, J., Seeger, T.,, *On the influence of cyclic stress-strain curves, damage parameters, and various evaluation concepts in the life prediction by the local approach.* Proc 2nd European Coil on Fracture, 1978: p. 270-285.
93. Roberts, R. and Erdogan, F., *The effect of mean stress on fatigue crack propagation in plates under extension and bending.* Journal of basic engineering, 1967. **89**(4): p. 885-892.
94. Walker, K., *The Effect of Stress Ratio During Crack Propagation and Fatigue for 2024-T3 and 7075-T6 Aluminum*, in *The Effect of Stress Ratio During Crack Propagation and Fatigue for 2024-T3 and 7075-T6 Aluminum*. 1970.
95. Nihei, M., Heuler, P., Boller, Ch., Seeger, T., *Evaluation of mean stress effect in fatigue life by use of damage parameters.* International Journal of Fatigue, 1986. **8**(No 3): p. 119-126.
96. Dowling, N.E., *Mean stress effects in strain-life fatigue.* Fatigue and Fracture of Engineering Materials and Structures, 2009. **32**(12): p. 1004-1019.
97. Haibach, E., *Fatigue strength in service.* VDI-Verlag GmbH, Düsseldorf, 1989.
98. Lee, Y.-L. and Taylor, D., *4 - STRESS-BASED FATIGUE ANALYSIS AND DESIGN*, in *Fatigue Testing and Analysis*, Y.-L. Lee, et al., Editors. 2005, Butterworth-Heinemann: Burlington. p. 103-180.
99. Kœchlin, S., *FKM Guideline: Strengths, Limitations and Experimental Validation.* Procedia Engineering, 2015. **133**: p. 309-319.

100. McKelvey, S.A., Lee, Y.-L., and Barkey, M.E., *Stress-Based Uniaxial Fatigue Analysis Using Methods Described in FKM-Guideline.* Journal of Failure Analysis and Prevention, 2012. **12**(5): p. 445-484.
101. Burger, R. and Lee, Y., *Assessment of the Mean-Stress Sensitivity Factor Method in Stress-Life Fatigue Predictions.* 2013.
102. Boiler, C.H.R. and Seeger, T., *Materials Data for Cyclic Loading*, in *Materials Science Monographs*, C.H.R. Boller and T. Seeger, Editors. 1987, Elsevier.
103. Ukrainetz, P.R., *The effect of the mean stress in the endurance limit* in *Mechanical Engineering* 1960, University of British Columbia: Vancouver.
104. ASTM, *Standard Practice for Conducting Force Controlled Constant Amplitude Axial Fatigue Tests of Metallic Materials*. 2007.
105. Standardization, I.O.f., *Metallic Materials--Fatigue Testing--Axial Force-controlled Method*. 2006, International Organization for Standardization.
106. Adedipe, O., Brennan, F., and Kolios, A., *Review of corrosion fatigue in offshore structures: Present status and challenges in the offshore wind sector.* Renewable and Sustainable Energy Reviews, 2016. **61**: p. 141-154.
107. Maiya, P.S. and Busch, D.E., *Effect of surface roughness on low-cycle fatigue behavior of type 304 stainless steel.* Metallurgical Transactions A, 1975. **6**(9): p. 1761-1766.
108. ASTM, *Standard Practice for Corrosion Fatigue Testing of Metallic Implant Materials*, in *F1801-97(2014)* 2014.
109. ISO, *11782-1:1998(en)-Corrosion of metals and alloys — Corrosion fatigue testing*, in *Part 1: Cycles to failure testing*. 1998.
110. ISO, *ISO 9227:2017, Corrosion tests in artificial atmospheres- salt spray tests* 2017.
111. ASTM, *Standard Test Methods for Tension Testing of Metallic Materials*. 2016.
112. Okorokov, O., *Investigation of Air and Corrosion Fatigue Enhanced via Compressive Residual Stress*, in *Mechanical and Aerospace Engineering*. 2019, Univeristy of Strathclyde.
113. Loveday, M.S., Gray, T., and Aegerter, J., *Tensile testing of metallic materials: A review.* Final report of the TENSTAND project of work package, 2004. **1**.
114. EN10025, B., *Hot rolled products of non-alloy structural steels.* Brussels: European Committee for Standardisation, 1990.
115. Chen, G.S., et al., *Transition from pitting to fatigue crack growth - Modeling of corrosion fatigue crack nucleation in a 2024-T3 aluminum alloy.* Materials Science and Engineering A, 1996. **219**(1-2): p. 126-132.
116. DuQuesnay, D.L., Underhill, P.R., and Britt, H.J., *Fatigue crack growth from corrosion damage in 7075-T6511 aluminium alloy under aircraft loading.* International Journal of Fatigue, 2003. **25**(5): p. 371-377.
117. Hoeppner, D.W., *MODEL FOR PREDICTION OF FATIGUE LIVES BASED UPON A PITTING CORROSION FATIGUE PROCESS.* ASTM Special Technical Publication, 1979(675): p. 841-870.
118. Kondo, Y., *Prediction of Fatigue Crack Initiation Life Based on Pit Growth.* CORROSION, 1989. **45**(1): p. 7-11.
119. Sankaran, K.K., Perez, R., and Jata, K.V., *Effects of pitting corrosion on the fatigue behavior of aluminum alloy 7075-T6: Modeling and experimental studies.* Materials Science and Engineering A, 2001. **297**(1-2): p. 223-229.
120. Alcántara, J., et al., *Marine atmospheric corrosion of carbon steel: A review.* Materials, 2017. **10**(4): p. 406.

121. ASTM, *Standard Practice for Conducting Force Controlled Constant Amplitude Axial Fatigue Tests of Metallic Materials*, in *E466-15*. 2015, ASTM INTERNATIONAL.
122. Jakubowski, M., *Influence of Pitting Corrosion on Fatigue and Corrosion Fatigue of Ship and Offshore Structures, Part II: Load - Pit - Crack Interaction.* Polish Maritime Research, 2015. **22**(3): p. 57-66.
123. Evans, U.R., Simnad, M.T., and Gough, H.J., *The mechanism of corrosion fatigue of mild steel.* Proceedings of the Royal Society of London. Series A. Mathematical and Physical Sciences, 1947. **188**(1014): p. 372-392.
124. Linder, J. and Blom, R., *Development of a method for corrosion fatigue life prediction of structurally loaded bearing steels.* Corrosion, 2001. **57**(5): p. 404-412.
125. Melchers, R.E., *Development of new applied models for steel corrosion in marine applications including shipping.* Ships and Offshore Structures, 2008. **3**(2): p. 135-144.
126. Beretta, S., et al., *Corrosion–fatigue of A1N railway axle steel exposed to rainwater.* International Journal of fatigue, 2010. **32**(6): p. 952-961.
127. Anagnostakis, A., *Corrosion fatigue of low alloy and stainless steels*, in *Mechanical and Aerospace Engineering* 2019 University of Strathclyde
128. Evripidis, T., *Investigation of Coatings and Cathodic Protection Systems and Development of Design Rules for Enhanced Corrosion Fatigue Life in Pd Pumps*. 2019, University of Strathclyde.
129. Nicholas, T., *Chapter 2 - Characterizing Fatigue Limits*, in *High Cycle Fatigue*, T. Nicholas, Editor. 2006, Elsevier Science Ltd: Oxford. p. 27-69.
130. Kondo, Y., *Prediction of fatigue crack initiation life based on pit growth.* Corrosion, 1989. **11**(4): p. 280.
131. Li, S.-X. and Akid, R., *Corrosion fatigue life prediction of a steel shaft material in seawater.* Engineering Failure Analysis, 2013. **34**: p. 324-334.
132. Ebara, R., *Corrosion fatigue crack initiation behavior of stainless steels.* Procedia Engineering, 2010. **2**(1): p. 1297-1306.
133. Bathias, C. and Paris, P.C., *Gigacycle fatigue in mechanical practice*. 2004: CRC Press.
134. Ebara, R., *Corrosion fatigue phenomena learned from failure analysis.* Engineering Failure Analysis, 2006. **13**(3): p. 516-525.
135. El May, M., et al., *Effect of corrosion on the high cycle fatigue strength of martensitic stainless steel X12CrNiMoV12-3.* International Journal of Fatigue, 2013. **47**: p. 330-339.
136. Turnbull, A., *6.04 - Environment-assisted Fatigue in Liquid Environments*, in *Comprehensive Structural Integrity*, I. Milne, R.O. Ritchie, and B. Karihaloo, Editors. 2003, Pergamon: Oxford. p. 163-210.
137. Zerbst, U., et al., *Defects as a root cause of fatigue failure of metallic components. III: Cavities, dents, corrosion pits, scratches.* Engineering Failure Analysis, 2019. **97**: p. 759-776.
138. Jenkin, C.F. and Ewing, J.A., *High-frequency fatigue tests.* Proceedings of the Royal Society of London. Series A, Containing Papers of a Mathematical and Physical Character, 1925. **109**(749): p. 119-143.
139. Morrissey, R.J. and Nicholas, T., *Fatigue strength of Ti–6Al–4V at very long lives.* International Journal of Fatigue, 2005. **27**(10): p. 1608-1612.
140. Schütz, W., *Über eine beziehung zwischen der lebensdauer bei konstanter und bei veränderlicher beanspruchungsamplitude und ihre anwendbarkeit auf die*

bemessung von flugzeugbauteilen. Zeitschrift für Flugwissenschaften, 1967. **15**(11): p. 407-419.
141. Denton, T., *Motor vehicle engineering*. 2002: Cengage Learning EMEA.
142. Callister Jr, W.D. and Rethwisch, D.G., *Fundamentals of materials science and engineering: an integrated approach*. 2012: John Wiley & Sons.
143. Eyercioglu, O., Kutuk, M.A., and Yilmaz, N.F., *Shrink fit design for precision gear forging dies.* Journal of Materials Processing Technology, 2009. **209**(4): p. 2186-2194.
144. Jahed, H., Farshi, B., and Karimi, M., *Optimum Autofrettage and Shrink-Fit Combination in Multi-Layer Cylinders.* Journal of Pressure Vessel Technology, 2005. **128**(2): p. 196-200.
145. Zhang, X.-Y., Li, S.-X., and Liang, R. *Effect of corrosion pits on fatigue life and crack initiation*. in *ICF13*. 2013.
146. Sankaran, K.K., Perez, R., and Jata, K.V., *Effects of pitting corrosion on the fatigue behavior of aluminum alloy 7075-T6: modeling and experimental studies.* Materials Science and Engineering: A, 2001. **297**(1): p. 223-229.
147. Zenner, H., *Multiaxial fatigue – methods, hypotheses and applications.* Materials Testing, 2005. **47**(5): p. 249-254.
148. Okorokov, V., et al., *Corrosion Fatigue of Low Carbon Steel under Compressive Residual Stress Field.* Procedia Engineering, 2018. **213**: p. 674-681.

Annexes

The technical drawings of the corrosion cell used in Exova facility to perform the corrosion fatigue tests are shown in Figure A1.

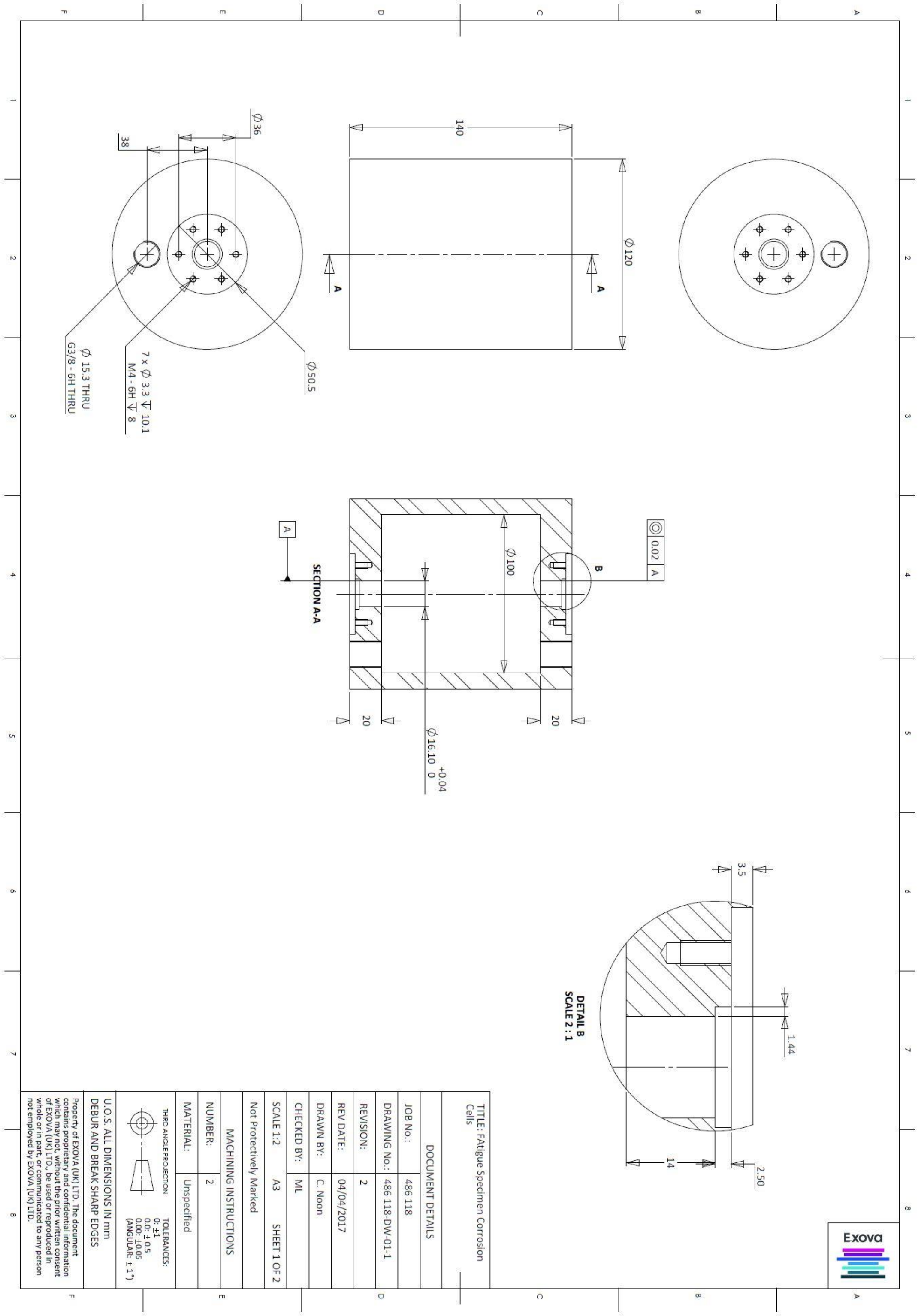

Figure A1: Technical drawing of corrosion cell used in Exova. *Continued to next page.*

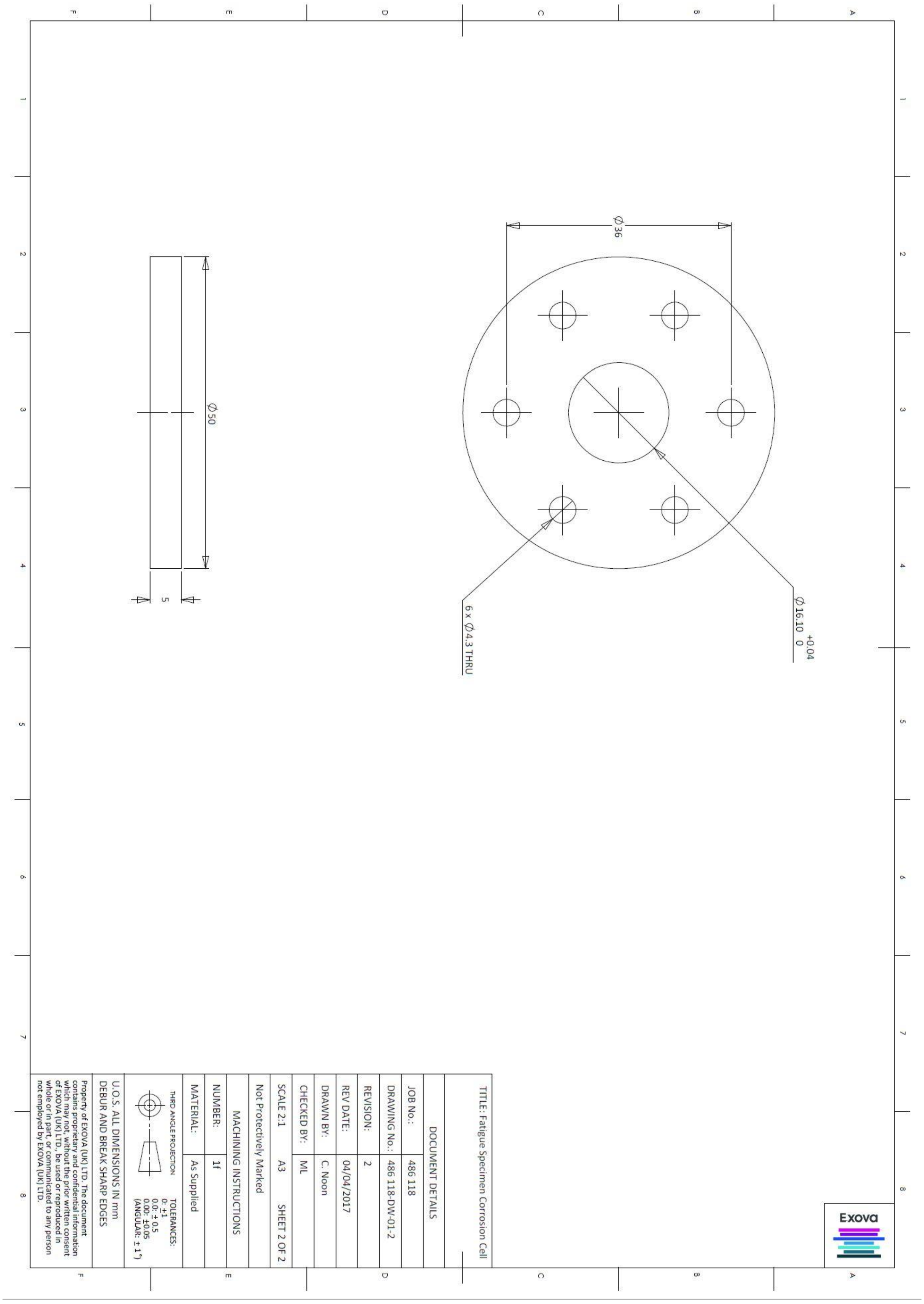

Figure A1: Technical drawing of corrosion cell used in Exova.